Investigation of Structure-Property Relationships of Cerium Oxide-Based Catalysts for CO Oxidation

Von der Fakultät Chemie der Universität Stuttgart
zur Erlangung der Würde eines
Doktors der Naturwissenschaften (Dr. rer. nat.)
genehmigte Abhandlung

Vorgelegt von

Jan Simon Florenski
aus Esslingen am Neckar

Hauptberichter	Prof. Dr.-Ing. Elias Klemm
Mitberichter	Prof. Dr.-Ing. Ulrich Nieken
Prüfungsvorsitzender	Prof. Dr. rer. nat. Thomas Schleid

Tag der mündlichen Prüfung: 08.12.2023

Institut für Technische Chemie der Universität Stuttgart
2023

Erklärung über die Eigenständigkeit der Dissertation

Ich, Jan Simon Florenski, versichere, dass ich die vorliegende Arbeit mit dem Titel ”Investigation of Structure-Property Relationships of Cerium Oxide-Based Catalysts for CO Oxidation” selbständig verfasst und keine anderen als die angegebenen Quellen und Hilfsmittel benutzt habe; aus fremden Quellen entnommene Passagen und Gedanken sind als solche kenntlich gemacht.

Declaration of Authorship

I, Jan Simon Florenski, hereby certify that the dissertation entitled ”Investigation of Structure-Property Relationships of Cerium Oxide-Based Catalysts for CO Oxidation” is entirely my own work except where otherwise indicated. Passages and ideas from other sources have been clearly indicated.

Name: Jan Simon Florenski

Signature: ....

Date: 04.09.2023

Acknowledgments

The research for this work was conducted at the Institute of Technical Chemistry of the University of Stuttgart between April of 2019 and April of 2023.

First and foremost I want to thank Prof. Dr.-Ing. Elias Klemm for the opportunity to conduct my research at the Institute of Technical Chemistry. I want to thank him especially for his trust that aside from all adversity facing one in such a complicated and well researched and competitive topic I would be able to complete this project successfully. This trust resulted in a scientific freedom for which I am very grateful as it enabled me to grow as a scientist. I also want to thank him for the detailed correction of the presented work.

The presented work here would not have been possible without my students, whom I supervised during their bachelor thesis, research internship as well as master thesis. Noah Schellander, contributed a lot to this work, especially in the catalyst preparation. Also, my other students, Tobias Schuchardt (FP, MA), Ferdinand Ertmann (BA) and Isabell Benner (FP) all contributed to this work in some way. I want to thank them for their hard work and dedication to go along with everything I envisioned. During the supervision I learned a lot and came out smarter and hope to have helped you to gain a glimpse into my passion that is heterogeneous catalysis.

I want to thank the people with whom I collaborated during my time at the ITC. Most importantly I want to express my gratitude to Indro Biswas from the DLR. Without his influence and guidance during my studies, I would not be at this point. My time at the DLR really shaped me as an independent researcher, while also showing me how much fun chemistry can be when you do not have to do column chromatography. Aside from that he of course always helped me out with XPS and *Raman* spectroscopy measurements during my PhD. Bruna and Carlos Lobo from the University of Bayreuth I want to thank for tirelessly trying to measure my low-loaded platinum samples at the synchrotron, where measurement time is hard to come by. With the help of Michael Haumann from the Freie Universität Berlin they succeeded in getting useful XAS data, enabling us to draw conclusions about our catalysts, which were essential. I want to thank Hongguang Wang from the MPI-FKF, as well as Helena Solodenko and Guido Schmitz for electron microscopy measurements of my samples. Thomas Heim, Wadih Yared and Frank Kern from the IFKB of the University of Stuttgart I want to thank for the support in, although not presented in this work, the development of a spray coating technique with viscosity, particle size, surface roughness as well as the preparation of the $CeAlO_3$ XPS standard. I want to thank Paul Rößner of the

IPV for enabling us to use their laser scan microscope during the development of the spray coating technique.

Of course I want to also thank my colleagues who practically supported this work. Ann-Katrin Beurer, Dorothea Häussermann, Michael Benz and Faeze Tari for countless nitrogen physisorption measurements. Paul Rößner and Joachim Hildebrand I have to thank for TEM measurements as well, while Max Schmidt helped me out with REM measurements. I want to thank Heike Fingerle for ICP-OES measurements. Although my catalysts turned out to be a challenge, she always found a way to get my many samples measured. Special thanks goes to Andreas Stieber who helped me to convert any unrealistic idea of mine into reality through his ingenuity and practical skills. This was also demonstrated by Max Schmidt and Armin Löwe who 3D printed many parts I did and did not need for my research. I also want to thank Ines Lauerwald for the support I got during designing, building and commissioning of my experimental setup. Especially Paul Rößner, Ann-Katrin Beurer and Max Schmidt helped me aside from their scientific contribution through very tough times, which I am very grateful for. I want to also extend my thanks to all my (former) ITC colleagues who made the last four years fly by and made them what they were: a blast!

I want to thank Lisa Mewes for supporting me during the time of my doctorate and keeping me from loosing myself in this work. Especially in challenging times you've helped me get out of my head and supported me unconditionally at every point. Thank you very much! Above all I want to thank my brothers and my mother for the support you gave me during my studies as well as during my PhD. This wouldn't have been possible without your unwavering support! And of course my friends I want to thank for completing the support network I had and knew I could rely on.

A big thank you to you all! Let the next chapter begin!

Abstract

Platinum-loaded ceria catalysts are important industrial catalysts, due to their use in the emission abatement of internal combustion engine cars. Knowledge-based development and improvement of new catalysts is necessary to comply with new, ever more strict exhaust gas norms. However, it is difficult to derive structure-property relationships based on the material properties of ceria in platinum-loaded systems since the platinum-ceria interface is highly dynamic under process conditions. As the $\mathrm{Pt{-}O{-}Ce}$ perimeter dictates the reactivity of such catalytic systems, deriving reliable structure-property relationships is challenging and yet not sufficiently discussed in literature.

To tackle this, different ceria materials were prepared using precipitation. By variation of the precipitation and calcination temperatures, materials with different properties were prepared. It was observed, that with increasing precipitation temperature, smaller crystallites and larger BET surface areas were obtained. Using pH measurements this was traced back to an increased nucleation rate. It was also observed that higher precipitation led to an increase in lattice defects as observed by *Raman* spectroscopy. This increase in defect concentration could be related to an increase in sinter resistance.

Ceria materials are used because of their unique redox properties. After material preparation, the influence of the material properties on the redox parameters was probed by Temperature Programmed Reduction (TPR) and O_2 pulse chemisorption. It was shown that the amount of reversibly releasable oxygen does not directly correlate with the BET surface area derived from nitrogen physisorption measurements. Using *in situ* Diffuse Reflectance Infrared Fourier Transform Spectroscopy (DRIFTS) experiments, H_2-Temperature Programmed Desorption (TPD), X-Ray Diffraction (XRD) coupled with Rietveld refinement and Transmission Electron Microscopy (TEM), this was traced back to small crystallites not being capable of releasing oxygen upon reduction. This is probably caused by $\mathrm{Ce}_{\mathrm{Ce}}'$ point defects. The fact that not the entire surface can release oxygen has implications for the investigation of structure-property relationships of ceria materials, because a simple normalization using the BET surface area is not sufficient. Instead, the Mars-van-Krevelen (MvK) active surface area has to be used. Crystallite size, D, derived from Rietveld refinement calculation of XRD patterns allows to approximate the MvK active surface area.

Afterwards, CO oxidation experiments were carried out to derive structure-property relationships for unloaded and platinum-loaded ceria. Strong Electrostatic Adsorption (SEA)

was employed to prepare materials with atomic dispersion, which where successively analyzed by CO-DRIFTS, X-Ray Absorption Spectroscopy (XAS) and High-Angle Annular Dark-Field Imaging (HAADF)-Scanning Transmission Electron Microscopy (STEM) imaging. It was shown that in the as-synthesized state isolated platinum ions are present on the surface, which are also stable under the lean reaction conditions used in this work. When applying harsh reduction treatment, however, they are reduced. From the presented data it is not clear whether they are still isolated or form metallic clusters. Since these materials are stable under reaction conditions they can be used to derive structure property relationships for platinum-loaded ceria.

Using these materials, it was shown that the activity of unloaded ceria can be described using the defect concentration extracted by *Raman* spectroscopy. Not only the activation energy but also the Turnover Frequency (TOF) could be described as a function of the intensity ratio between the defect related band and the breathing mode of oxygen ions in the ceria lattice. Through kinetic modeling and simulation of the partial pressure dependency of CO reaction rates, it was found that CO_2 adsorption probably limits the reaction rate of ceria materials through retardation of reoxidation rate. Although CO_2 desorption measurements did corroborate these findings, more data is required to derive reliable conclusion about the CO_2 inhibition.

Prepared and stable isolated platinum ions on ceria were selected as a way to circumvent the problem of changing Pt$-$O$-$Ce perimeter under reaction conditions. Through that the role of ceria in determining the reaction rates of different ceria materials could be investigated. By using light-off curves with dry and wet feeds it was shown that, although platinum is present, the mechanism still follows the MvK mechanism as the CO light-off is still linked to the reduction onset of the materials. Water was found to enhance the reaction rate while decreasing the slope of the light-off curve. Accordingly, steady-state kinetic investigations showed high activation energies of around $100\,\mathrm{kJ\,mol^{-1}}$ for feeds without water, whereas roughly $30\,\mathrm{kJ\,mol^{-1}}$ lower values were obtained when water was present in the feed. This is in line with Density Functional Theory (DFT) calculations suggesting the reaction of adsorbed CO and lattice oxygen as the Rate Determining Step (rds). The similar activation energies between the different materials are probably relatable to the similar active sites between the material coupled with the limited activation of CO on the isolated, ionic platinum ions. After adding water to the reaction feed it was however observed that deviations of reactivity between the materials did increase. Also, variations of the activation energy were now apparent. This might be explained by the change in transition state, which was proposed to include a carboxylic species when water and hydroxyl groups are present in the vicinity of the platinum ions. No clear trend of the activation energy with any of the material parameters could be found, the reason probably being that different processes are involved in determining the reaction rate. Thorough model-based analysis of partial pressure dependencies is necessary to derive material-based activity descriptors here. TOF values for the different platinum-loaded oxides could be described as a function of the bulk defect concentration again, similar to the unloaded ceria materials. However, not a linear relationship was obtained but a parabolic one, which was similar when dry or wet feeds were used. This points towards the conclusion that similar processes determine the reactivity of platinum-loaded ceria materials in dry as well as wet feeds. These results show that it is indeed possible to use Pt_1-CeO_2 catalysts using very low loading to derive structure-property relationships for platinum-loaded catalysts, which should enable a better knowledge-based catalyst design in the future as well as the derivation of descriptors to improve kinetic models used for online catalysts control. However, more measurements are needed, especially partial pressure dependencies of the reaction rates.

Zusammenfassung

Platinbeladene Ceroxidkatalysatoren sind durch ihre Verwendung im Bereich der Autoabgaskatalyse ein industriell wichtiges Katalysatorsystem. Da die Abgasregulierungen immer strenger werden, ist hier eine wissensbasierte Katalysatorentwicklung von Nöten, um die Grenzwerte weiter einhalten zu können. Allerdings ist die Ableitung von Struktur-Wirkungsbeziehungen auf Basis der Materialeigenschaften von Ceroxiden im platinbeladenen Zustand schwierig, da sich die Platin-Ceroxidfläche unter Betriebsbedingungen dynamisch ändert. Da diese $\mathrm{Pt{-}O{-}Ce}$ Grenzfläche aber die Reaktivität des Katalysators bestimmt, macht dies die Ableitung von Struktur-Wirkungsbeziehungen sehr herausfordernd und führt dazu, dass diese noch nicht genau verstanden sind.

Um dies anzugehen, wurden durch Fällung verschiedene Ceroxide hergestellt. Durch die Variation der Fällungs- und Kalzinierungstemperaturen wurden hierbei die Materialeigenschaften variiert. Es konnte beobachtet werden, dass mit steigender Fällungstemperatur kleiner Kristallite und größere BET Oberflächen erhalten werden. Durch pH Messungen wurde eine gesteigerte Nukleationsrate bei höheren Temperaturen als mögliche Erklärung ausgemacht. Die höhere Fällungstemperatur führte auch zu Materialien mit einer höheren Konzentration an Defekten, was durch *Raman* Spektroskopie bestimmt wurde. Diese höhere Defektivität konnte auch mit einer höheren Sinterstabilität korreliert werden.

Ceroxide werden auf Grund ihrer einzigartigen Redoxeigenschaften verwendet. Nach der Herstellung der Materialien wurde daher der Einfluss der Materialeigenschaften auf das Redoxverhalten durch TPR und O_2 Pulschemisorption untersucht. Es konnte gezeigt werden, dass die Menge an freisetzbarem Sauerstoff nicht direkt mit der BET Oberfläche korreliert. Mit Hilfe von *in situ* DRIFTS, H_2-TPD, XRD mit Rietveldverfeinerung und TEM wurde dies auf kleine Kristallite zurückgeführt, welche kein Sauerstoff freisetzen können, sondern unter Hydroxylgruppenbildung reduziert werden. Dies wird vermutlich durch $\mathrm{Ce}'_{\mathrm{Ce}}$ Punktdefekte hervorgerufen. Die Tatsache, dass nicht die gesamte Oberfläche Sauerstoff freisetzen kann, hat wichtige Implikationen für die Ableitung von Struktur-Wirkungsbeziehungen von Ceroxiden, da Reaktivitäten in der katalytischen Testung meist über die BET Oberfläche normiert werden. Dies ist jedoch nicht ausreichend. Daher muss die MvK aktive Oberfläche verwendet werden. Mit Hilfe der Kristallitgröße, welche durch Rietveldverfeinerung der Röntgendiffraktogramme erhalten werden kann, kann diese Größe angenähert werden.

CO-Oxidationsexperimente wurden anschließend durchgeführt, um die Struktur- Wirkungs-

beziehungen von unbeladenen und platinbeladenen Ceroxiden zu untersuchen. Um eine atomare Dispersion der Platinspezies auf der Oberfläche zu erzeugen, wurde SEA zur Platinbeladung verwendet. Die beladenen Materialien wurden anschließend mit Hilfe von CO-DRIFTS, XAS und HAADF-STEM untersucht. Es konnte gezeigt werden, dass im Frischzustand eine atomare Dispersion der Platinspezies vorhanden ist, welche auch unter den mageren Bedingungen der katalytischen Experimente stabil ist. Wenn die Proben allerdings stark reduzierenden Bedingungen ausgesetzt werden, werden die Platinionen reduziert. Es ist allerdings nicht klar, ob die Platinspezies im reduzierten Zustand aggregieren oder weiterhin isoliert vorliegen. Aufgrund der Stabilität der Materialien unter den mageren Bedingungen, konnten diese im Anschluss jedoch verwendet werden, um den Einfluss der Materialeigenschaften auf die katalytische Funktion zu untersuchen.

Es konnte gezeigt werden, dass im unbeladenen Zustand die Aktivität der Ceroxide in der CO-Oxidation von der, aus *Raman* Spektroskopiemessungen abgeleiteten, Defektkonzentration abhängt. Hierbei konnte nicht nur die Aktivierungsenergie, sondern auch die TOF als Funktion der Defektkonzentration beschrieben werden. Mit Hilfe von kinetischer Modellierung und Simulation von Partialdruckabhängigkeiten der Reaktionsgeschwindigkeiten konnte anschließend auch herausgefunden werden, dass das gebildete CO_2 vermutlich produktinhibierend wirkt, indem es die Reoxidationsrate verlangsamt. CO_2 Desorptionsexperimente bestärkten diese Vermutung. Allerdings sind hier noch weitergehende Untersuchungen notwendig, um diese Vermutung zu untermauern.

Isolierte Platinatome auf Ceroxid wurden verwendet, um die Problematik der sich dynamisch veränderten Platin-Ceroxidfläche zu umgehen. Hierdurch konnten die Unterschiede in der katalytischen Aktivität zwischen den Materialien auf die oxidischen Träger zurückgeführt werden. Mit Hilfe von Light-Off Experimenten mit trockenem und feuchtem Gasstrom konnte gezeigt werden, dass auch im platinbeladenen Zustand die Reaktion einem MvK Mechanismus folgt, da das Reaktionsonset weiterhin an das Reduktionsonset des Trägers gebunden ist. Es konnte beobachtet werden, dass Wasser zu einer höheren Katalysatoraktivität führt, während die Steigung der Light-Off Kurven abnahm. Anschließend konnten kinetische Untersuchungen im dynamischen Gleichgewicht zeigen, dass die Materialien, unabhängig vom oxidischen Träger, Aktivierungsenergien von ungefähr $100\,\mathrm{kJ\,mol^{-1}}$ bei trockenem Gasstrom aufwiesen, während für wasserhaltige Feedgasströme Aktivierungsenergien erhalten wurden, die ca. $30\,\mathrm{kJ\,mol^{-1}}$ niedriger waren. Diese Beobachtung stimmt mit Literaturdaten überein. Die experimentellen Ergebnisse deuten auf eine Veränderung des Übergangszustandes hin, der durch das Vorhandensein von Wasser hervorgerufen wird. Es wurde in der Literatur auf Basis von theoretischen Berechnungen beschrieben, dass im Beisein von Wasser die Reaktion über einen Carboxylübergangszustand abläuft, was die Aktivierungsenergie herabsetzt. Dies deckt sich mit den Ergebnissen dieser Arbeit. Es konnten allerdings keine Trends zwischen den Oxideigenschaften und der katalytischen Aktivität von Pt_1-CeO_2 Katalysatoren gefunden werden. Der Grund hierfür liegt vermutlich bei sich überlagernden Prozessen, die eine modellbasierte Analyse der Partialdruckabhängigkeiten voraussetzt, um diese zu entschlüsseln. Es konnte aber gezeigt werden, dass es möglich ist, Pt_1-CeO_2 Katalysatoren zu verwenden, um Struktur-Wirkungsbeziehungen von platinbeladenen Ceroxiden abzuleiten. Diese Herangehensweise und die daraus abgeleiteten Wirkzusammenhänge können anschließend dazu beitragen eine bessere wissensbasierte Katalysatorentwicklung zu ermöglichen. Weiterhin könnte dies ermöglichen, Modelle auf Basis der Eigenschaften der Ceroxide aufzustellen, um so eine bessere modellbasierte Katalysatorkontrolle über die Lebenszeit sicher zu stellen.

Contents

Abbreviations

AFM	Atomic Force Microscopy
ALD	Atomic Layer Deposition
AP	Ammonia-Based Precipitation
BET	Brunauer-Emmett-Teller
BJH	Barrett-Joyner-Halenda
CNT	Classical Nucleation Theory
CVD	Chemical Vapor Deposition
DFT	Density Functional Theory
DLR	German Aerospace Center (Deutsches Zentrum für Luft und Raumfahrt e.V.)
DLS	Dynamic Light Scattering
DRIFTS	Diffuse Reflectance Infrared Fourier Transform Spectroscopy
EELS	Electron Energy Loss Spectroscopy
ER	Eley-Rideal
EXAFS	Extended X-Ray Absorption Fine Structure
FID	Flame Ionization Detector
FT-IR	Fourier-Transform Infrared Spectroscopy
GC	Gas Chromatograph
HAADF	High-Angle Annular Dark-Field Imaging
HC	Unburned Hydrocarbons
HSA	High Surface Area
HUP	Hydrothermal Urea-Based Precipitation

ICP-MS	Inductively Coupled Plasma Mass Spectrometry
ICP-OES	Inductively Coupled Plasma Optical Emission Spectroscopy
IMTCCC	Institute of Manufacturing Technologies of Ceramic Components and Composites
IR	Infrared
IW	Incipient Wetness
LH	Langmuir-Hinshelwood
LR	Langmuir-Rideal
LSA	Low Surface Area
MARI	Most Abundant Reaction Intermediate
MFC	Mass Flow Controller
MS	Mass Spectrometer
MvK	Mars-van-Krevelen
NC	Nanocubes
NIST	National Institute of Standards and Technology
NO	Nanooctahedrons
NP	Nanoparticles
NR	Nanorods
OSC	Oxygen Storage Capacity
OSM	Oxygen Storage Materials
PM	Precious Metal
PSD	Particle Size Distribution
PXRD	Powder X-Ray Diffraction
PZC	Point Of Zero Charge
rds	Rate Determining Step

SAC	Single Atom Catalyst
SCR	Selective Catalytic Reduction
SEA	Strong Electrostatic Adsorption
SET	Single Electron Transfer
SL	Surface Loading
SRM	Standard Reference Material
STEM	Scanning Transmission Electron Microscopy
STM	Scanning Tunneling Microscopy
STP	Standard Temperature And Pressure
STY	Space-Time-Yield
TAPN	Tetraammineplatinum(II) Nitrate
TCD	Thermal Conductivity Detector
TEM	Transmission Electron Microscopy
TGA	Thermogravimetric Analysis
TOF	Turnover Frequency
TON	Turnover Number
TOSC	Total Oxygen Storage Capacity
TPD	Temperature Programmed Desorption
TPO	Temperature Programmed Oxidation
TPR	Temperature Programmed Reduction
TPx	Temperature Programmed Methods
TWC	Three-Way Catalytic Converter
UP	Urea-Based Precipitation
UV-VIS	Ultraviolet-Visible
WGS	Water-Gas Shift

XANES	X-Ray Absorption Near Edge Structure
XAS	X-Ray Absorption Spectroscopy
XP	X-Ray Photoelectron
XPS	X-Ray Photoelectron Spectroscopy
XRD	X-Ray Diffraction

List of Latin Symbols

Symbol	Description	Unit
a	Cubic lattice parameter	m
A	Area	$\mathrm{m^2}$
c_i	Concentration of compound i	$\mathrm{mol\,m^{-3}}$
D	Crystallite size	nm
D_0	Free diffusion coefficient	$\mathrm{m^2\,s^{-1}}$
d_{cat}	Catalyst particle diameter	m
D_{eff}	Effective diffusion coefficient	$\mathrm{m^2\,s^{-1}}$
E	Pore shape exponent	-
E_{A}	Activtivation energy	$\mathrm{kJ\,mol^{-1}}$
J	Nucleation rate	$\mathrm{mol\,s^{-1}}$
k	Equilibrium constant	-
k_0	Preexponential factor	-
$K_{\mathrm{ads},i}$	Adsorption constant of component i	$\mathrm{Pa^{-1}}$
$\mathrm{k_B}$	*Boltzmann* constant	$1.38 \times 10^{-23}\,\mathrm{J\,K^{-1}}$
m	Mass	g
M_i	Molar mass of compound i	$\mathrm{g\,mol^{-1}}$
n	Amount of substance	mol
$\mathrm{N_A}$	*Avogadro* constant	$6.022 \times 10^{23}\,\mathrm{mol^{-1}}$
$\dot{n}_i$	Molar flow rate of component i	$\mathrm{mol\,s^{-1}}$
n_{i}	Reaction order for compound i	-
p	Pressure	Pa

Symbol	Description	Unit
P	Shape factor	-
p_i	Partial pressure of component i	Pa
R	Universal gas constant	$8.314\,\mathrm{J\,mol^{-1}\,K^{-1}}$
Re	Reynolds number	-
r	Reaction rate	$\mathrm{mol\,s^{-1}}$
r_{cat}	Particle radius of catalyst	m
r_{v}	Volume-specific reaction rate	$\mathrm{mol\,m^{-3}\,s^{-1}}$
r_{A}	Area-specific reaction rate	$\mathrm{mol\,m^{-2}\,s^{-1}}$
r_{m}	Mass-specific reaction rate	$\mathrm{mol\,g^{-1}\,s^{-1}}$
$r_{\mathrm{intrinsic}}$	Intrinsic reaction rate	$\mathrm{mol\,g^{-1}\,s^{-1}}$
r_{obs}	Measured reaction rate	$\mathrm{mol\,g^{-1}\,s^{-1}}$
r_i	Ionic radius of element i	m
S_{A}	Mass-specific surface area (universal)	$\mathrm{m^2\,g^{-1}}$
S_{BET}	Specific BET surface area from physisorption	$\mathrm{m^2\,g^{-1}}$
SD_{A}	Area-specific site density	$\mathrm{mol\,m^{-2}}$
SD_{m}	Mass-specific site density	$\mathrm{mol\,g^{-1}}$
S_{Hg}	Specific surface area from Hg porosimetry	$\mathrm{m^2\,g^{-1}}$
SL	Surface loading	$\mathrm{m^2\,l^{-1}}$
S_{MvK}	Mars-van-Krevelen active surface area	$\mathrm{m^2\,g^{-1}}$
t	time	s
T	Temperature	K/°C
$T_{\mathrm{Hüttig}}$	*Hüttig* temperature	K/°C
T_{melt}	Melting temperature	K/°C

Symbol	Description	Unit
TOF	Turnover frequency	s^{-1}
$TOSC_T$	Total oxygen storage capacity at temperature T	$\mathrm{mol\,g}^{-1}$
$u_{\text{broundary}}$	Fluid velocity in the boundary layer	$\mathrm{m\,s}^{-1}$
u_{fluid}	Fluid velocity in the bulk fluid	$\mathrm{m\,s}^{-1}$
V	Volume	m^3
$\dot{V}$	Volumetric flow rate	$\mathrm{m}^3\,\mathrm{s}^{-1}$
V_{Hg}	Total specific pore volume from Hg intrusion porosimetry	$\mathrm{m}^3\,\mathrm{g}^{-1}$
z	Oxidation state	-
w	Rel. remaining mass	-
X_i	Conversion of compoonent i	-
y	Oxygen deficiency	-
Y_i	Yield of component i	-

List of Greek Symbols

Symbol	Description	Unit
β_1	Mass transfer coefficient	$\mathrm{m\,s}^{-1}$
χ_i	Molar fraction of compound i	-
δ	Cerium reduction degree	-
Δ	Difference	
ΔG	Gibb’s free energy	$\mathrm{kJ\,mol}^{-1}$

Symbol	**Description**	**Unit**
ΔH	Reaction enthalpy	$\mathrm{kJ\,mol^{-1}}$
ϵ	Porosity	-
γ	Surface energy	$\mathrm{J\,m^{-2}}$
η	Catalyst effectiveness factor	-
μ_i	Chemical potential of component i	$\mathrm{J\,mol^{-1}}$
ν	Vibrational frequency	$\mathrm{cm^{-1}}$
Ψ	*Weisz-Prater* criterion value	-
ρ_i	Density of compound i	$\mathrm{g\,ml^{-1}}$
$\rho_{\mathrm{Hg,mod}}$	Bulk density from Hg intrusion porosimetry	$\mathrm{g\,ml^{-1}}$
τ	Tortuosity	-

Part I.

Introduction

Catalysis plays an important role in many different aspects of modern life. From large scale production of platform chemicals, to synthesis of medicine, to sustainable catalysis, focusing on converting harmful substance into harmless products. The term catalysis, while first described by Johann Wolfgang Döbereiner in 1823, was coined by Swedish chemist Berzelius in 1835.[1] According to Berzelius, "*Catalysis is the acceleration of a slow chemical process by the presence of a foreign material*"[1].[2] A catalyst is defined as a material, which enhances reaction rates without changing the thermodynamics through lowering the activation energy by splitting the reaction path into different elementary steps. Although catalysts are part of the reaction, they are regenerated during each catalytic cycle, thus not being consumed.[3,4] Catalysis is present when the turnover number (TON), the number of times the active site goes through the active cycle, is larger than one.[5]

Today, more than 80 % of industrial processes are of catalytic nature.[6] One of the most widely employed catalytic processes is the emission abatement of internal combustion engine cars.[7,8] These systems are employed in order to reduce emissions of harmful substances stemming from the combustion process of fuels.[9] Through incomplete conversion, unburned hydrocarbons (HC) as well as CO are formed, whereas the high temperatures in the engine lead to oxidation of N_2 to nitric oxides NO_x.[10] Due to the simultaneous removal of these three compounds the term three-way catalytic converter (TWC) was coined in case of *Otto* engines. While removal of CO and HC is done by oxidation, the simultaneous removal of NO_x is a reduction. Thus, different oxygen stoichiometry dependencies are observed for the oxidation and reduction reaction, with oxidation reactions showing ever increasing conversion with higher oxygen stoichiometry, while reduction of NO_x becomes less favorable at high oxygen contents. This yields an optimal operating window as a function of oxygen content in the exhaust gas.[11] This is represented by the λ-value, which is the ratio between present and required oxygen. Mixtures with $\lambda > 1$, so oxygen surplus, are called lean feed mixtures, whereas oxygen deficient feeds with $\lambda < 1$ are defined as rich feed mixtures.[10] Typical TWCs consist of a monolithic carrier, mostly made from cordierite or steel and the washcoat, which is a porous γ-alumina structure, containing ceria-based materials as well as precious platinum-group metals.[8] Precious metals are used to decrease light-off temperature through better reactant activation and the alumina is used

---

[1] "Katalyse ist die Beschleunigung eines langsam verlaufenden chemischen Vorgangs durch die Gegenwart eines fremden Stoffes"

to increase surface area. The main role of ceria-based materials in TWCs is to keep the oxygen stoichiometry at $\lambda \approx 1$. This is achieved through redox cycling of the Ce^{IV}/Ce^{III} redox couple. Ceria materials are reduced under rich feed conditions, thus oxygen is released, while they are reoxidized under lean feed conditions, which led to the term oxygen storage materials (OSM) being used for these materials. Through this buffering behavior of ceria, the operating regime, in which the conversion of all three harmful pollutants is maximized, is broadened.[12] Ceria-based materials also improve the water-gas shift (WGS) activity, stabilize precious metal dispersion, improve stability of the γ-Al_2O_3 washcoat as well as improve activity of the precious metal at the precious metal ceria interface.[13]

Although ceria materials have been intensely investigated for their use in environmental catalysis for over 30 years with 24800 papers published and close to 1600 in 2020 alone[2], there are still questions about the direct link between preparation conditions and ceria material properties as well as the role of these material properties in catalysis in the presence of precious metals. This is especially important as model-based catalyst controls are employed. These models are currently fitted empirically to new catalytic systems, making it difficult to describe the catalyst performance over its lifetime. Instead of applying empirical models, formulating the models with material-based descriptors would allow to account for catalyst aging in a better way. To be able to develop material-based models these material-based reactivity descriptors have to be found.

Part II.
Theory

1. General Aspects in Heterogeneous Catalysis

Most industrial processes employ catalysts to increase yield, decrease the amount of side-products formed as well as decrease cost and increase space-time-yield (STY). This is achieved by decreasing the activation barrier of reactions by elementary steps that favor formation of the desired product.Therefore, although the thermodynamics of a reaction is not changed, its kinetics is altered significantly. By catalyst design and adjustment of process conditions it is possible to alter the conversion and selectivity and with it the yield of the desired product. The field of catalysis was historically divided into three

---

[2] According to webofscience.com; publications containing ”ceria”, accessed 9.4.2023.

different fields: homogeneous catalysis, heterogeneous catalysis and biocatalysis. In the last decades however, this clear distinction started to get blurred by interdisciplinary approaches applying immobilized organometallic complexes[14] or immobilized enzymes[15] to benefit from the advantages of heterogeneous catalysis, the ease of which the product is separated from the catalyst, while circumventing disadvantages such as ill-defined structures, low selectivities and site-specific turnover rates. Still, most large industrial processes are gas-phase processes employing solid catalysts, making the field of heterogeneous catalysis one of the most industrially important catalysis fields.[6]

1.1. Heterogeneous Catalysis in Gas-Solid Systems

Heterogeneous catalysis describes a reaction of a reactant that is in a different phase compared to the catalyst. Most frequently this refers to gas-solid or liquid-solid reactions. However, also phase-separated liquid-liquid systems may be considered heterogeneous. The advantage of heterogeneously catalyzed processes using solid catalysts is the easy separation of the catalyst from the product stream as well as low price, high thermal stability and high density of active sites. However, the site-specific activity as well as selectivity is often lower compared to enzymatic or homogeneously catalyzed processes.[16] For a reaction to be catalyzed by a porous solid catalyst, the reactants have to get to the active site on the surface of the solid. This means the reactant has to undergo several steps before the actual reaction can occur. When a solid particle is introduced into a fluid with velocity u_{fluid} a boundary layer around the particle is formed. Because the flow in the boundary layer of the catalyst particle is laminar no turbulent lateral mixing occurs. Therefore, to reach the catalyst the reactant has to diffuse through this stagnant boundary layer (step 1). After passing through the boundary layer, the reactant has to diffuse through the pores of the catalyst powder to the active site (step 2). In the next step the reactant reaches the catalyst surface where adsorption and activation can occur (step 3). The chemisorption of the reactants enables the actual reaction (step 4). Subsequently the formed product will desorb (step 5), diffuse back through the pores (step 6) and through the boundary layer (step 7) to reach the bulk fluid again. Out of these seven steps, each one can be limiting, making it necessary to carefully evaluate obtained kinetic data when structure-property relationships are derived.[17]

1.2. External Mass Transport Limitation

When the mass transport through the film is limiting, a gradient between the bulk fluid reactant concentration and the reactant concentration at the phase boundary between the catalyst particle and the fluid occurs. Since most reactions are highly sensitive towards the reactant concentration the observable reaction rate will differ strongly from the reaction rate when no external mass transport limitation occurs. Because the temperature sensitivity of physical processes like diffusion is usually lower compared to the intrinsic chemical reaction, at severe limitations very low ($\approx 5\,\mathrm{kJ\,mol^{-1}}$) activation energies are obtained.[18] Since thickness of the boundary layer is a function of the fluid velocity, the temperature at which external mass transport limitation will occur depends on the velocity chosen.

To probe whether external mass transport is limiting different approaches are described in literature. Experimentally, the dependency of the boundary layer thickness on the fluid velocity can be exploited. Comparing the measured reaction rates at different flow rates at constant modified residence times yields, in the absence of external mass transport limitation, identical values for the reaction rate r_m. In the case of external mass transport limitation the reaction rate is expected to increase at higher flow rates as the thickness of the boundary layer is decreased. However, it was also discussed by Chambers et al. that at low Reynolds values usually used in laboratory catalyst tests (*Re* < 10) this test may not yield a reliable proof for the absence of mass transport limitations since the mass and heat transfer coefficient may not strongly depend on the *Re*-number to lead to a measurable change in conversion.[19]

Mears proposed a theoretical equation to test for the absence of external mass transport limitation which is known today as the *Mears-criterion*[20] and is shown in eq. (1).

$$\frac{r_\mathrm{A,obs}}{\beta_1 \cdot c_{1,0}} < \frac{0.05}{|n|} \tag{1}$$

where $r_\mathrm{A,obs}$ represents the measured area-specific reaction rate, β the mass transfer coefficient, $c_{1,0}$ the reactant concentration in the bulk of the fluid and $|n|$ is the absolute value of the reaction order. It is generally assumed that external mass transport limitation plays a subordinate role for porous solid catalysts.[17]

1.3. Internal Mass Transport Limitation

Compared to external mass transport limitation, internal mass transport limitation is more probable for porous catalysts.[17] This is especially true for very fast reactions and/or small pore diameters. For internal mass transport limitation the ratio between the intrinsic reaction rate and diffusion rate is an important parameter. If the rate of diffusion is significantly higher than the intrinsic reaction rate no diffusion limitation is observable. However, if they are in a comparable range, starvation of active sites in the center of the pore system occurs. The more centers are starved (for example by an increase in reaction rate through changes in temperature), the more the measured reaction rate r_{obs} will deviate from the intrinsic reaction rate $r_{\text{intrinsic}}$ without internal mass transport limitation. This can be described by the catalyst effectiveness factor η which is defined as shown in eq. (2).

$$\eta = \frac{r_{\text{obs}}}{r_{\text{intrinsic}}} \tag{2}$$

Since the reaction still occurs despite internal diffusion limitations the activation energy is decreased to a fraction of the actual activation energy. It is reported that the effective, meaning the measured activation energy is approximately half of the actual activation energy in case of strong internal mass transport limitation.[18]

Similar to the external mass transport limitation discussed in chapter 1.2, different approaches for the investigation of the presence of internal mass transport limitation are proposed.

The empirical test involves testing the catalyst at the same conditions while changing the secondary particle size. If no mass transport limitation is present the observed reaction rate r_{obs} is not a function of the particle diameter. However, if internal mass transport limitation is present, the observed reaction rate r_{obs} will behave inversely proportional to the particle diameter.[17] Weisz et al. also proposed a criterion to check whether internal diffusion might limit the reaction. The so-called *Weisz-Prater Criterion* shown in eq. (3) is fulfilled when no internal mass transport limitation is present:

$$\frac{(0.5\, d_{\text{cat}})^2}{D_{\text{eff}}} \frac{1}{c_1} r_{\text{v,obs}} \leq 1 \tag{3}$$

Here d_{cat} is the diameter of the catalyst particle, D_{eff} is the effective diffusion coefficient in the pore system and $r_{\text{v,obs}}$ represent the reaction rate per volume of catalyst.[21] If this criterion is fulfilled, the catalyst effectiveness factor η is larger than 0.95 ($\eta > 0.95$).

Under confined geometries diffusion is hindered. Weissberg showed that the diffusion coefficient in a porous solid D_{eff} and the free, unrestricted diffusion coefficient D_0 are connected by the porosity ϵ and the tortuosity τ as shown in eq. (4):[22]

$$D_{\text{eff}} = \frac{D_0 \cdot \epsilon}{\tau} \tag{4}$$

The free diffusion coefficient D_0 is a function of the temperature T and the pressure p as well as the gas matrix in which diffusion occurs. However, data on diffusion coefficients in ternary mixtures are very scarce. *Blanc's law*,[23] initially developed for the mobility of ions in gases, can be used to calculate the diffusion coefficient, $D_{i,(\chi_{\text{j}},\chi_{\text{k}})}\,(T,p)$, at a given temperature T and pressure p in a matrix of substances j and k with a molar fraction χ_{j}, χ_{k} on the basis of diffusion coefficients in the pure matrix components $D_{i,j}\,(T,p)$ and $D_{i,k}\,(T,p)$ as shown in eq. (5).[24]

$$D_{i,(\chi_{\text{j}},\chi_{\text{k}})}\,(T,p) = \left[\frac{\chi_j}{D_{i,j}\,(T,p)} + \frac{\chi_k}{D_{i,k}\,(T,p)}\right]^{-1} \tag{5}$$

The diffusion coefficients of component i in pure matrix components at various temperatures T can be calculated based on their values reported at standard temperature and pressure (STP) $D_{i,j}\,(0\,^{\circ}\text{C}, 1\,\text{bar})$[25] according to eq. (6):

$$D_{i,j}\,(T,p) = D_{i,j}\,(0\,^{\circ}\text{C}, 1\,\text{bar}) \cdot \left(\frac{p_0}{p}\right) \cdot \left(\frac{T}{T_0}\right)^{1.81} \tag{6}$$

The other factor in eq. (4) is the porosity ϵ which represents the void volume fraction of a solid while the third one, tortuosity τ, is considered to be the ratio between fluid flow path through a porous medium compared to its mean free path.[26] The concept of tortuosity was first reported by Carman in 1937 who calculated a fixed value of $\sqrt{2}$.[27] In a later publication the term *tortuosity* was coined.[28] Carniglia proposed a simple equation based on *Fick's first law*[30] to calculate tortuosity τ with the help of mercury intrusion measurements, which is still used and referred to when calculating tortuosities to this day. *Carniglia's expression* for systems in which cylindrical pores do not prevail is shown in eq. (7).[29]

$$\tau = \left(2.23 - 1.13 V_{\mathrm{Hg}} \cdot \rho_{\mathrm{Hg,bulk}}\right) \left(0.92 y\right)^{1+E} \tag{7}$$

With $y = S_{\mathrm{Hg}}/S_{\mathrm{BET}}$ representing the pore shape factor, V_{Hg} is the total specific pore volume, which is the cumulative intruded pore volume at the maximal experimental pressure, while $\rho_{\mathrm{Hg,bulk}}$ is the bulk particle density and E is the pore shape exponent. If $y \leq 1.1$, meaning cylindrical pores are dominant in the material, τ can be calculated by the simplified form of the *Carniglia's expression* shown in eq. (8).

$$\tau = 2.23 - 1.13 V_{\mathrm{Hg}} \cdot \rho_{\mathrm{Hg,bulk}} \tag{8}$$

These equations are still used frequently to calculate tortuosities up to this day due to their simplicity.[31–35] However, it was also pointed out that *Carniglia's expression* fails to describe the connectivity of void volumes and void pore volumes adequately.[36,37] If the material can be assumed to consist of agglomerated spheres an expression proposed by Comiti and Renaud can be used.[38] This model assumes the pores to be void space between agglomerated particles, which was developed for packed beds and is shown in eq. (9).

$$\tau = 1 - P \ln(\epsilon) \tag{9}$$

Where ϵ is the porosity while P represents the shape factor. It was shown by Barrande, Bouchet, and Denoyel that this equation can also be used for materials with non-porous primary particles that are aggregated by using a shape factor P of $P = 0.49$.[26]

1.4. Kinetic Descriptions of Reactions Catalyzed by Solids

When neither external and internal mass transport rates, reactant adsorption and product desorption are limiting, the intrinsic activity of the catalyst can be measured. The description and fit of experimentally obtained intrinsic reaction rates (*i.e.* $\eta = 1$) can usually be accomplished in an empiric, non-mechanistic way by so-called power law descriptions of the reaction rate r which is shown in eq. (10).[17,18]

$$r = k \prod_{i=1}^{N} p_i^{n_\mathrm{i}} \tag{10}$$

Eq. (10) describes the rate of a reaction based on the partial pressures p_i of the involved reactants i and the so-called reaction order n_i. The latter representing to which extend the concentration of a reactant i will influence the overall reaction rate. k is the equilibrium constant, which is temperature dependent according to the *Arrhenius*-equation shown in eq. (11).

$$k = k_0\,\mathrm{e}^{\frac{-E_\mathrm{A}}{\mathrm{R}T}} \tag{11}$$

With k_0 being the preexponential factor, representing the maximum equilibrium constant at infinite temperatures, E_A the activation energy, R the universal gas constant ($8.314\,\mathrm{J\,mol^{-1}\,K^{-1}}$) and T being the absolute temperature.[39]

This empirical description, however, may not satisfy more complex dependencies since it is not mechanism-specific. Especially when reaction orders become temperature dependent a simple power law approach is not able to describe such reactions. Therefore mechanism-based descriptions of kinetics were developed early on. Langmuir postulated three different types of reactions on solid catalysts[40] in 1922:

1. Reaction between an adsorbed and non-adsorbed species
2. Reaction between two adsorbed species on adjacent sites
3. Reaction between an adsorbed species and the catalyst surface

1.4.1. Reaction of an Adsorbed Species With a Non-Adsorbed Species — The *Eley-Rideal* Mechanism

The first type of reaction is frequently referred to as the *Eley-Rideal (ER)*-mechanism resulting from the work of Eley and Rideal on *para*-hydrogen activation on tungsten.[41,42] However, since Langmuir was the first to postulate such a reaction it is also referred to as

Langmuir-Rideal (LR)-mechanism.[43] Such a reaction between reactants A and B can be described by the following reactions 1-3.

$$\mathrm{A} + * \rightleftharpoons \mathrm{A}{-}* \qquad [\mathrm{R}\ \mathbf{1}]$$

$$\mathrm{A}{-}* + \mathrm{B} \longrightarrow \mathrm{BA}{-}* \qquad [\mathrm{R}\ \mathbf{2}]$$

$$\mathrm{BA}{-}* \rightleftharpoons \mathrm{BA} + * \qquad [\mathrm{R}\ \mathbf{3}]$$

A reactant A does adsorb on the active site $*$ to form the adsorbed and activated surface species A$-*$. This activated surface species can react with the second reactant directly from the gas phase to form the adsorbed product BA$-*$, which subsequently can desorb to form BA and regenerate the active site $*$. When the surface reaction (reaction 2) is assumed to be the rds and irreversible the kinetic expression can be written, using the *Langmuir* isotherm[44] to describe the adsorption, using eq. (12)

$$r = r_{\mathrm{rds}} = k\frac{K_{\mathrm{ads},1}p_1p_2}{1+\sum_{i=1}^{N}K_{\mathrm{ads,i}}p_{\mathrm{i}}} \tag{12}$$

Since in the ER mechanism only one of the reactants is activated, the ER is usually only found with simple reactions with a low activation energy such as the gas phase selective catalytic reduction (SCR) of NO with ammonia.[45]

1.4.2. Reaction of Two Adsorbed Species — The *Langmuir-Hinshelwood* Mechanism

In his book *The Kinetics of Chemical Change in Gaseous Systems* Hinshelwood first used the *Langmuir* isotherm to describe kinetics of a reaction of two adsorbed species giving the mechanism.[43,44,46] The original *Langmuir-Hinshelwood (LH)* mechanism is formulated for a catalyst exhibiting one adsorption site $*$, which can be described by the following reaction scheme.

$$\mathrm{A} + * \rightleftharpoons \mathrm{A}{-}* \qquad \text{[R \textbf{4}]}$$

$$\mathrm{B} + * \rightleftharpoons \mathrm{B}{-}* \qquad \text{[R \textbf{5}]}$$

$$\mathrm{A}{-}* + \mathrm{B}{-}* \longrightarrow \mathrm{AB}{-}* + * \qquad \text{[R \textbf{6}]}$$

$$\mathrm{AB}{-}* \rightleftharpoons \mathrm{AB} + * \qquad \text{[R \textbf{7}]}$$

On a monofunctional catalyst two different reactants A and B adsorb on the same active site $*$ leading to competitive adsorption. Two adsorbed surface species $\mathrm{A}{-}*$ and $\mathrm{B}{-}*$ subsequently react to form the adsorbed product $\mathrm{AB}{-}*$, which desorbs to regenerate the active site $*$ and the product AB. The most prominent example for such a reaction in which two species compete for the same adsorption site while following the LH mechanism is the CO oxidation catalyzed by platinum on alumina.[47,48] This reaction was formerly reported to follow the ER-mechanism.[49] Considering the reaction network 4-7 the reaction rate can be described by eq. (13) considering the surface reaction (reaction 6) is the rate determining step (rds).

$$r = r_{\mathrm{rds}} = k \frac{K_{\mathrm{ads,1}} p_1 \cdot K_{\mathrm{ads,2}} p_2}{\left(1 + \sum_{i=1}^{N} K_{\mathrm{ads,i}} p_{\mathrm{i}}\right)^2} \tag{13}$$

It can also be envisioned that for multifunctional catalysts both reactants can adsorb on different active sites $*_1$ and $*_2$. This leads to a different rate expression, which is shown in eq. (14).[50,51]

$$r = r_{\mathrm{rds}} = k \frac{K_{\mathrm{ads,1,}*_1} p_1 \cdot K_{\mathrm{ads,2,}*_2} p_2}{\left(1 + \sum_{i=1}^{N} K_{\mathrm{ads,i,}*_1} p_{\mathrm{i}}\right)\left(1 + \sum_{i=1}^{N} K_{\mathrm{ads,i,}*_2} p_{\mathrm{i}}\right)} \tag{14}$$

In the latter case, no competitive adsorption of the reactants occurs, because they occupy different active sites.

1.4.3. Reaction of an Adsorbed Species with the Catalyst — The *Mars-van-Krevelen* Mechanism

The described reaction of a reactant with the catalyst by Langmuir is the first step in the so called Mars-van-Krevelen (MvK) mechanism, which was described by Mars and van Krevelen for the oxidation of hydrocarbons with reducible oxides.[52] Generally reactions following the MvK mechanism can be described by reactions 8-11 .

$$\mathrm{A} + * \rightleftharpoons \mathrm{A}{-}* \qquad [\mathrm{R}\ \mathbf{8}]$$

$$\mathrm{A}{-}* + \mathrm{O}_{\mathrm{lattice}} \longrightarrow \mathrm{AO}{-}* + \mathrm{v}_{\mathrm{O}} \qquad [\mathrm{R}\ \mathbf{9}]$$

$$\mathrm{AO}{-}* \rightleftharpoons * + \mathrm{AO} \qquad [\mathrm{R}\ \mathbf{10}]$$

$$\mathrm{v}_{\mathrm{O}} + 0.5\,\mathrm{O}_2 \longrightarrow \mathrm{O}_{\mathrm{lattice}} \qquad [\mathrm{R}\ \mathbf{11}]$$

The reactant A adsorbs on the catalysts surface and reacts with a lattice oxygen to form the oxidation product AO. In the process the catalyst is reduced, leading to the formation of an oxygen vacancy v_{O}. After desorption of the product the oxygen vacancy is healed through adsorption and reduction of the gas phase oxidant. Aside from the oxidation reactions the MvK mechanism was initially proposed for, it can also be used to describe deoxygenations and desulfurization reactions.[53]

The rate expression Mars and van Krevelen derived can be expressed by eq. (15).[52]

$$r = \frac{k_1 k_2 p_1 p_{\mathrm{O}_2}^n}{k_1 p_1 + k_2 p_{\mathrm{O}_2}^n} \tag{15}$$

Although it was argued by Vannice that this kinetic rate expression is flawed,[51] many kinetic models based on the MvK mechanism for different but mainly oxidation reactions are derived to this day.

2. Cerium-based Oxides - Properties and Preparation

Cerium and cerium-based oxides are broadly employed materials in biomedical and nanomedical applications due to their antioxidant and enzyme-mimetic properties,[54–56] in photocatalysis,[57–60] fuel cells,[61–64] and most prominently in redox catalysis.[65–67] The intrinsic redox properties make cerium oxide a good redox catalyst, with the exhaust gas aftertreatment being the most prominent application. Due to the importance of emission abatement in the individual transportation sector, numerous publications dealt with the investigation of preparation, characterization and testing of cerium-based catalysts.

Stoichiometric cerium oxide crystallizes in a cubic CaF_2 structure. In this structure cerium ions span a face centered cubic structure while the oxygen ions fill up the tetrahedral interstitial sites.[67] Thus, cerium ions exhibit a coordination number of eight leading to an ionic radius of $r_{\mathrm{Ce^{IV}}} = 0.097\,\mathrm{nm}$, whereas oxygen ions have four nearest neighbors, resulting in an ionic radius of $r_{\mathrm{O^{2-}}} = 0.138\,\mathrm{nm}$.[68,69] This structure is shown in figure 1.[70]

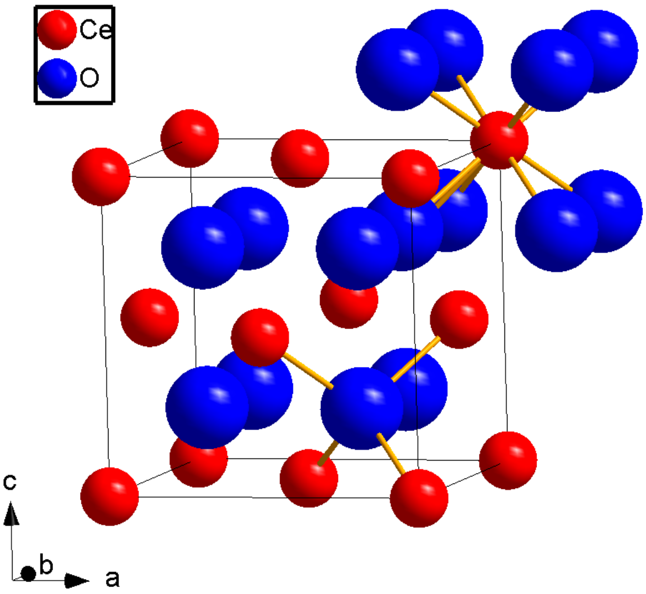

Figure 1: Crystal structure of stoichiometric CeO_2

2.1. Redox Properties of Cerium Oxides

The broad application spectrum of cerium oxide materials stems from the low oxygen vacancy formation energy. This is caused by the fact that no phase transformation is necessary during reduction over a wide range y in CeO_{2-y}. The reduction of cerium oxide was shown to produce oxygen vacancies rather than cerium shifting to interstitial sites.[71] Therefore, the reduction of cerium oxide can be written using the *Kröger-Vink* notation as follows:[67]

$$2\,\mathrm{Ce}_{\mathrm{Ce}}^{\mathrm{x}} + \mathrm{O}_{\mathrm{O}}^{\mathrm{x}} \rightleftharpoons 2\,\mathrm{Ce'}_{\mathrm{Ce}} + 0.5\,\mathrm{O}_2 + \mathrm{v}_{\mathrm{O}}^{\bullet\bullet} \qquad [\mathrm{R}\ \mathbf{12}]$$

The *Kröger-Vink* notation is frequently used in defect chemistry of oxides. The index represents the element that occupies the lattice position in question in an ideal, defect free lattice. The relative charge to the ideal lattice is represented by the symbols ’ for a relative negative charge, • for one relative positive charge and ^{x} for zero net charge in comparison to the host ion. $\mathrm{Ce'}_{\mathrm{Ce}}$ therefore represents a $\mathrm{Ce}^{\mathrm{III}}$ on the lattice position of $\mathrm{Ce}^{\mathrm{IV}}$ in CeO_2, having a net-charge of -1. $\mathrm{v}_{\mathrm{O}}^{\bullet\bullet}$ refers to the formed oxygen vacancy on the oxygen lattice position having a net-charge of +2.

Density functional theory (DFT) calculations suggest that the charge density is localized at the two neighboring $\mathrm{Ce}^{\mathrm{III}}$ sites rather than being delocalized over the whole crystal.[72] The reduction degree of cerium-based materials is frequently described by the oxygen deficiency y in literature. However, since cerium-based materials are frequently doped to alter the material properties in a way that is beneficial for the desired operation, the oxygen deficiency has to be normalized by the amount of ceria present as these dopants may not take place in the reduction process, distorting the meaning of y in such systems. Therefore, the cerium reduction degree δ will be used in this work to describe the non-stoichiometry in ceria materials. δ represents the fraction of $\mathrm{Ce'}_{\mathrm{Ce}}$ of all sites occupied by cerium ions and can therefore be calculated as shown in eq. (16)

$$\delta = \frac{x_{\mathrm{Ce}'_{\mathrm{Ce}}}}{x_{\mathrm{Ce}'_{\mathrm{Ce}}} + x_{\mathrm{Ce}^{x}_{\mathrm{Ce}}}}. \tag{16}$$

For undoped CeO_2 materials the oxygen deficiency y is given by $y = 0.5\ \delta$.[73]

As mentioned before the low oxygen vacancy formation energy in cerium oxides is caused by the fact that ceria can undergo severe reduction without a phase transition. The upper limit for a phase-transitionless reduction is reported to be around $\delta = 0.572$.[73] Up to this point however, a continuum of unordered, fluorite-type oxygen deficient structures $\mathrm{CeO}_{2\text{-}\mathrm{y}}$ is formed, commonly referred to as the α-phase. Oxygen vacancy association and clustering occurs during heating leading to the formation of reduced ceria superstructures. Atomic force microscopy (AFM) and Scanning tunneling microscopy (STM) studies showed triangular and linear defect structures when annealing reduced ceria, suggesting a stabilizing effect by vacancy clustering.[74,75] Above a reduction degree of $\delta = 0.572$

phase transition occurs and a body-centered Ce_2O_{4-2y} cubic structure is formed, referred to as σ-phase.[67,73]

Under operation conditions of redox catalysis only mild reduction occurs. This means the phase transition from the non-stoichiometric α-phases to σ does not usually occur. When staying beneath the reduction degree limit of $\delta = 0.572$, it was found that the lattice parameter a increases linearly with the reduction degree δ. This can be explained by describing the partially reduced cerium oxide as a solid solution of fluorite type Ce_2O_3 with oxygen vacancies in place of every fourth oxygen ion and bare cerium oxide according to *Vegard's law*,[76] which describes the lattice parameter of a mixed oxide crystal as a linear relationship between the molar fraction of the dopant and host crystal system following eq. (17)

$$a_{\mathrm{CeO_{2-y}}} = (1-\delta)\ a_{\mathrm{CeO_2}} + \delta\ a_{\mathrm{CeO_{1.5}}}. \tag{17}$$

Cerium oxide and fluorite analogues are reported to follow *Vegard's law* (*c.f.* eq.(17)) over a wide dopant concentration range.[71] One challenge is the fact that the cubic lattice parameter of reduced cerium oxide $a_{\mathrm{CeO_{1.5}}}$ is not easily accessible because of the aforementioned phase transformation to a *bcc* structure. There are different approaches to this challenge, two of which shall be discussed here. Kim formulated empiric equations to calculate the lattice parameter of doped cerium oxides of different fluorite-type oxides, while they circumvent the previously mentioned problem of not knowing the lattice parameter of cubic $CeO_{1.5}$.[77] The equation to calculate the lattice parameter $a_{\mathrm{CeO_{2-y}}}$ of reduced cerium oxide CeO_{2-y} according to *Kim* is shown in eq. (18).

$$a_{\mathrm{CeO_{2-y}}} = 0.5413\,\mathrm{nm} + \sum_{k}^{3} (0.0220\Delta r_{\mathrm{k}} + 0.00015\Delta z_{\mathrm{k}})\,\delta \tag{18}$$

with Δr_{k} being the difference between the ionic radius of the k-th dopant $r_{\mathrm{k}} = r_{\mathrm{Ce^{III}}} = 0.114\,\mathrm{nm}$ and the host cation radius $r_{\mathrm{h}} = r_{\mathrm{Ce^{IV}}} = 0.097\,\mathrm{nm}$ giving a value for partially reduced ceria of $\Delta r_{\mathrm{k}} = r_{\mathrm{k}} - r_{\mathrm{h}} = 0.017\,\mathrm{nm}$. Δz_{k} represents the charge difference between the kth dopant and the host cation, and therefore gives a value of $\Delta z_{\mathrm{k}} = z_{\mathrm{k}} - z_{\mathrm{h}} = -1$ for reduced ceria. x_{k} represents the mole fraction of the kth dopant in mole percent. Thus, the lattice parameter of partially reduced, undoped cerium oxide CeO_{2-y} can be calculated based on the reduction degree $\delta = 0.01x_{\mathrm{k}}$ using eq. (19),

$$a_{\mathrm{CeO_{2-y}}} = 0.5413\,\mathrm{nm} + 0.0224\,\mathrm{nm}\,\delta. \tag{19}$$

Compared to the pure empirical nature of *Kim*'s approach, *Hong and Virkar* constructed an equation to assess the lattice parameter based on geometric considerations.[71] Based on the equation for the lattice parameter a of an ideal cubic lattice structure (eq.(20)) they formulated eq. (21), which for the case of partially reduced cerium oxide $\mathrm{CeO_{2-y}}$ with a cerium reduction degree of δ yields eq. (22)

$$a = \frac{4}{\sqrt{3}}\left(r_{\mathrm{cation}} + r_{\mathrm{anion}}\right) \tag{20}$$

$$a = \frac{4}{\sqrt{3}}\left[x r_{\mathrm{k}} + (1-x)\,r_{\mathrm{h}} + (1-0.25x)\,r_{\mathrm{O^{2-}}} + 0.25 x r_{v_{\mathrm{O}}}\right] \times 0.9971 \tag{21}$$

$$= \frac{4}{\sqrt{3}}\left[\delta r_{\mathrm{Ce^{III}}} + (1-\delta)\,r_{\mathrm{Ce^{IV}}} + (1-0.25\delta)\,r_{\mathrm{O^{2-}}} + 0.25\delta r_{v_{\mathrm{O}}}\right] \times 0.9971 \tag{22}$$

using the ionic radius of $\mathrm{Ce^{IV}}$ and $\mathrm{Ce^{III}}$ as well as the ionic radius of tetrahedral coordinated oxygen $r_{\mathrm{O^{2-}}} = 0.1380\,\mathrm{nm}$ and the oxygen vacancy radius $r_{v_{\mathrm{O}}} = 0.1164\,\mathrm{nm}$. The empiric factor of 0.9971 was introduced to fit the lattice parameter of undoped cerium oxide to the literature value of $a_{\mathrm{CeO_2}} = 0.5411\,\mathrm{nm}$.

From both equations (19) and (22) it is evident that the lattice parameter is expected to increase with increasing reduction degree due to the larger ionic radius of $\mathrm{Ce^{III}}$. Since the lattice parameter a can be easily determined from reflection positions in X-Ray Diffraction (XRD) patterns, the bulk reduction degree can be calculated using equations (23) and (24)

$$\delta_{\mathrm{Kim}} = \frac{a_{\mathrm{CeO_{2-y}}} - 0.5413\,\mathrm{nm}}{0.0224\,\mathrm{nm}}, \tag{23}$$

$$\delta_{\mathrm{Hong-Virkar}} = \frac{4\left(a_{\mathrm{CeO_{2-y}}} - \frac{3.9884}{\sqrt{3}}\left(r_{\mathrm{Ce^{IV}}} + r_{\mathrm{O^{2-}}}\right)\right)}{\frac{3.9884}{\sqrt{3}}\left(4r_{\mathrm{Ce^{III}}} - 4r_{\mathrm{Ce^{IV}}} - r_{\mathrm{O^{2-}}} + r_{v_{\mathrm{O}}}\right)}. \tag{24}$$

Since the lattice parameter calculated from *Kim*'s formula for totally oxidized $\mathrm{CeO_2}$ does not match the reported value, calculation of the reduction degree from XRD data δ_{XRD} will be done using eq. (24) in the following work.

Table 4: Surface energies E^{surf}[72] and oxygen vacancy formation energies E^{vac}[79] for low index ceria facets

Facet	$E^{\mathrm{surf,unrelaxed}}$ / eV[72]	$E^{\mathrm{surf,relaxed}}$ / eV[72]	E^{vac} / eV[79]
Bulk	-	-	3.390
(111)	0.690	0.680	2.600
(110)	1.260	1.010	1.990
(100)	2.050	1.410	2.270

2.2. Structure Sensitivity of Cerium Oxides

Since catalysis is a surface process, it was already early on suggested from density functional theory (DFT) calculations, that the type of exposed surface facet has a significant impact onto the activity of cerium oxides in catalysis.[78] Commonly cerium oxide materials expose (111), (110) and (100) facets. Facets with higher indices usually undergo restructuring rather easily due to the higher thermodynamic stability of the low index facets.

It was also reported that the low index crystal facets exhibit different stabilities. Nolan et al. used DFT-U to assess the stability of low-index facets of ceria.[72] Their results, *c.f.* table 4, show that the stability which is inverse proportional to the surface energy follows the trend: (111) > (110) > (100). The amount of surface relaxation ($E^{\mathrm{surf,unrelaxed}}$ - $E^{\mathrm{surf,relaxed}}$) also is consistent with experimental results that showed that the (111) facet is simply oxygen terminated,[75] whereas (110) facets exhibit a stoichiometric capping layer[80] and the (100) facets have to undergo severe restructuring to relax the perpendicular dipole moment, which makes surfaces unstable. When looking at the vacancy formation energies E^{vac} it is again evident, that the reduction of the surface is more favorable compared to oxygen vacancy formation in the bulk. But also between the different facets there is a significant difference. As demonstrated in table 4, the oxygen vacancy formation energy increases with (110), (100) to (111) surface facets, suggesting higher activity for MvK-type reactions.

2.3. Preparation of Cerium Oxides

Many different methods can be applied in synthesizing cerium oxides: From simple precipitation, to sol-gel and hydrothermal synthesis to high energy ball milling as well as flame-spray pyrolysis or combustion synthesis.[81] Due to its simplicity precipitation is a frequently used method for preparation of metal oxide catalysts. Since it is also used in this work, a detailed discussion of the precipitation process follows.

2.3.1. The Precipitation Process

Mullin states that although precipitation is used frequently literature still lacks an unambiguous definition. It is generally regarded as a fast crystallization process. However, these processes and the developed models to describe crystallization are assuming equilibrium. This is not the case for precipitation. Usually supersaturation is achieved via a chemical reaction between a precursor salt and a precipitation agent forming an insoluble compound. Thus, equilibrium processes like in classical crystallization play a less important role during precipitation.[82] Nevertheless, precipitation follows the same processes as classical crystallization which are

1. Creating supersaturation
2. Nucleation
3. Particle growth.

In the following each step will be discussed in more detail.

Creating Supersaturation

Supersaturation can be described on basis of the chemical potentials μ of a molecule or ion in solution μ_s and in the solid or crystal phase μ_c as shown in eq. (25).[83]

$$\Delta\mu = \mu_\mathrm{s} - \mu_\mathrm{c} \tag{25}$$

A solution is defined as undersaturated when $\Delta\mu < 0$, saturated when $\Delta\mu = 0$ and supersaturated when $\Delta\mu > 0$. Therefore, a supersaturated system is thermodynamically unstable, enabling the formation of nuclei. Saturated and undersaturated systems are stable, meaning nucleation and therefore precipitation can not occur.[83]

Supersaturation can be achieved via different routes. In classical crystallization it is usually achieved by changing the temperature. For endothermic dissolution processes the temperature is altered to reach supersaturation and with it nucleation and crystal growth.

As mentioned in the introduction, precipitation for catalyst preparation is usually done by adding a precipitation agent. For metal oxides the precipitation agent is usually a base since transition metal hydroxides tend to have very low solubility limits. Metallic particles can also be precipitated by adding a reducing agent, producing insoluble metal particles.[84] In both cases supersaturation is achieved very rapidly, since the solubility product that has to be considered is no longer the one of the soluble metal salt but the compound formed by the reaction with the precipitation agent. Therefore, the yield Y is no longer limited by the thermodynamic equilibrium of a highly soluble salt as in classical crystallization and it is possible to achieve yields close to $Y = 1$.

After reaching supersaturation the system is thermodynamically unstable, leading to nucleation.[85] Although thermodynamically unstable, it was reported that nucleation is a kinetically controlled process.[86] Thus, in many systems a short induction time can be observed. For some systems short range ordering in solution was already observed as well.[85]

Nucleation

Nucleation is a process that is still under scientific scrutiny more than 100 years after the development of the ground breaking work of Volmer et al., Becker et al. and Frenkel and is known today as classical nucleation theory (CNT).[87–89] Due to its simplicity CNT is still used today to describe, in words as well as mathematically, the process of nucleation and growth of nanoparticles from solution although it was initially developed for vapor condensation. It is based upon thermodynamic considerations regarding the stabilizing effect of bonds formed in the bulk and destabilizing effect from surface energy γ. For a spherical nucleus, the thermodynamic most favorable geometry considering the lowest surface-to-volume ratio, the free energy of the particle ΔG is described by eq. (26).[90]

$$\Delta G = \underbrace{-\frac{4}{3}\pi r^3 \left|\Delta G_{\mathrm{pc}}\right|}_{\Delta G_{\mathrm{v}}} + \underbrace{4\pi r^2 \gamma}_{\Delta G_{\mathrm{s}}} \tag{26}$$

The first summand of eq. (26) represents the stabilizing contribution of the bulk ΔG_{v} as a function of the particle radius r and ΔG_{pc} the change in free energy due to the phase change. The latter summand describes the destabilizing effect of the surface ΔG_{s} caused by the surface tension γ. From eq. (26) it is evident that the stabilizing bulk contribution scales with $\Delta G_{\mathrm{v}} \sim -r^3$ whereas the surface contribution scales in a quadratic manner

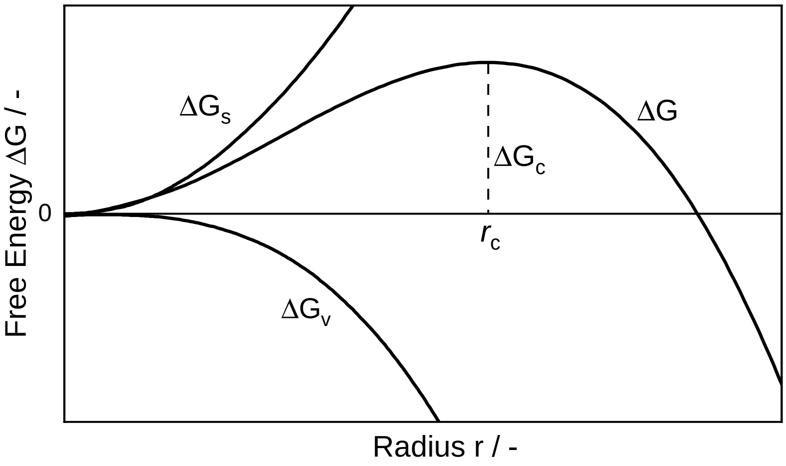

Figure 2: Free energy of the formation of a particle as function of the particle radius adapted from Kaščiev[91]

with the particle radius $\Delta G_\mathrm{s} \sim r^2$. This leads to a maximum in the particle free energy ΔG_c at a radius r_c known as the critical radius. From this radius on, particles gain stability, i.e. reduce their free energy with an increase in particle radius r. This is exemplified in figure 2.

Nucleation in CNT is therefore considered a solely thermodynamic process of the first-order phase transition.[92] The initial formation of nuclei is thought of as following the fluctuation theory. Since the critical radius has the largest ΔG value, the probability of forming a cluster with radius r_c is least probable. Therefore the rate for the unprobable, spontaneous formation of a nucleus with size r_c governs the overall nucleation rate according to CNT. This nucleation rate J is given by eq. (27)

$$J = A \cdot \mathrm{e}^{\frac{-\Delta G_\mathrm{c}}{\mathrm{k_B} T}} \tag{27}$$

where $\mathrm{k_B}$ is the *Boltzmann* constant and ΔG_c is the free energy change at the critical radius r_c. Thus the second term in eq. (27) describes the probability according to fluctuation theory of a nucleus of size r_c being formed. It is also evident from eq. (27) that nucleation is an activated process and higher temperatures are suggested to lead to a higher nucleation rate.[86]

Although it is frequently employed, CNT has several assumptions that limit its quantitative applicability outside of its original vapor to liquid transition of weak binding systems. These are outlined in a detailed review[85,93] and will only be shortly listed here:

- The formed nucleus is thought as of having the same physical properties as the stable phase after crystal growth.

- The formed nuclei are entirely spherical and there is a sharp phase boundary between nucleus and supersaturated fluid.

- The phase boundary is entirely planar, introducing large deviations for small nuclei sizes.

Crystal Growth

After nucleation occurred the formed nuclei will grow into crystallites. There are many proposed mechanisms for the growth of crystallites after nucleation, which are meticulously described and listed by Whitehead et al. in their critical review about the most cited kinetic description of particle growth kinetics, the *LaMer* model[94] from 1950.[85] The underlying mechanism used in the initial nucleation and growth model as well as earlier ones like the one of Farkas published in 1927,[95] describe particle growth as a series of successive attachments and detachments of monomers to formed nuclei[83,93–95]

$$\mathrm{M} + \mathrm{M_n} \rightleftharpoons \mathrm{M_{n+1}} \xrightleftharpoons[\text{-M}]{\text{+M}} \mathrm{M_{n+2}} \xrightleftharpoons[\text{-M}]{\text{+M}} \mathrm{M_{n+3}} \xrightleftharpoons[\text{-M}]{\text{+M}} \ldots.$$

The assumption of only monomers attaching to a formed nuclei is a very simplified representation of a very complex process. It entirely omits the possibility of merging of nuclei and smaller particles which from a thermodynamic standpoint would seem very plausible. As depicted in figure 2 surface area acts thermodynamically destabilizing to a particulate systems. Thus, small particles tend to merge, leading to a decrease in surface-to-bulk ratio. This effect is known as *Ostwald ripening*. Especially for polydisperse particle size distributions the driving force for agglomeration is large.[96] However, although *Ostwald ripening* plays an important role in particle growth kinetics, especially in the aging state, it is entirely omitted in the CNT-based *LaMer* model. Another problem with the early models is that it was assumed that instantaneous burst nucleation occurs, making nucleation and crystal growth two separate processes. This time separation of nucleation and crystal growth was shown to be one of the major drawbacks of the kinetic models of LaMer et al. as pointed out by Whitehead et al..[85,93] Modern kinetic models trying to describe the nucleation and crystal growth process use more complex and realistic assumptions to describe this complex and poorly understood process.

2.4. Preparation of Cerium Oxides by Means of Precipitation - Influence of Preparation Parameters

Literature describes many ways of preparing cerium oxide materials. From the frequently employed methods such as precipitation,[97–101] sol-gel synthesis,[57,102–104] hydrothermal synthesis[105–107] to more niche methods like solution combustion,[108–110] high energy ball milling[111–113] and microwave assisted synthesis[114–116] various approaches to prepare materials with different properties are employed. Since this work will focus on the preparation by precipitation process and processes derived therefrom, this will be the focus of the following section.

Precipitation of cerium oxides and cerium-based oxides is usually carried out by adding a precipitation agent to an aqueous solution of cerium ions. Since the solubility of cerium hydroxides is very low[117] usually bases like aqueous solutions of ammonia,[107] sodium hydroxide[118] or ammonium bicarbonate[119] are used to create a high degree of supersaturation.[82,85] Resulting from the low solubility of the formed precipitates the yield of precipitation is essentially $Y = 1$. By employing multiple metal precursors that have similar solubility products it is also possible to prepare mixed cerium-based oxides via co-precipitation.[120]

The properties of the final obtained products are known to be highly sensitive to the conditions present during precipitation.[121] Therefore, different experimental setups are proposed for carrying out precipitations. From adding a precipitation agent into the metal salt solution, to adding metal salt solution to the precipitation agent to adding both at the same time. These differences are mostly to reduce the inherent inhomogeneities during the precipitation process, which stem from finite mixing times when mixing two solutions.[17] These inhomogeneities are present in temperature as well as in concentration. One way to circumvent this challenge is the use of substances that can release the precipitation agent slowly through a chemical reaction. The most prominent example is urea. Urea decomposes readily at higher temperature in aqueous media[122] according to the following proposed two-step reaction.[123,124]

$$\mathrm{CO(NH_2)_{2(aq)}} \longrightarrow \mathrm{NCO^-_{(aq)}} + \mathrm{NH^+_{4(aq)}} \qquad [\mathrm{R}\ \mathbf{13}]$$

$$\mathrm{NCO^-_{(aq)}} + \mathrm{NH_4{\equiv}_{(aq)}} + 3\,\mathrm{H_2O} \longrightarrow \mathrm{CO_{2(g)}} + 2\,\mathrm{NH^+_{4(aq)}} + 2\,\mathrm{OH{-}_{(aq)}} \qquad [\mathrm{R}\ \mathbf{14}]$$

This means hydroxide ions are released through dissociation of urea homogeneously throughout the whole solution volume. It was reported that the urea-based precipitation (UP) process leads to a very narrow size distribution when precipitating metal hydroxides from aqueous solution.[125] This process is frequently used to prepare cerium oxide materials.[99,126–130] To homogenize precipitated materials hydrothermal synthesis is also used in the preparation of cerium oxide. In a typical synthesis the precipitated hydroxide is placed into an autoclave and treated above 100 °C at elevated pressure. At higher temperatures dissolution processes are more prominent, leading to a change in material properties with changing treatment conditions.[105,107] Lastly, the hydrothermal urea-based precipitation (HUP) should be mentioned. It is a combination of UP and hydrothermal synthesis. In a typical preparation the metal precursors and urea are dissolved and placed into an autoclave before the reaction solution is treated under hydrothermal conditions.[106,131] The latter is reported to prepare materials with higher crystallite strain compared to the other methods. This might be a result of the carbon dioxide formed in reaction 14 not being able to escape, leading to the formation of bulk carbonates.[132]

After precipitation and aging is carried out the precipitated hydroxides are generally separated from the solution and are dried and calcined. Although the drying process was reported to have a negligible effect on material properties the effect of calcination is severe. Literature is congruent about the decrease in surface area with a simultaneous increase in crystallite size. It was shown that the crystallite size increases slowly between 300 °C to 700 °C, before increasing rapidly thereafter.[102] It was also shown that calcination time had a limited effect at 500 °C and below, whereas significant effects were observed for temperatures above that..[133] Since sintering is strongly dependent on the mobility of surface atoms it is related to the semi-empirical *Hüttig* temperature ($T_{\text{Hüttig}} = 0.3 \times T_{\text{melt}}$) which for ceria is $T_{\text{Hüttig,CeO}_2} \sim 590\,°\text{C}$. However, it has to be mentioned that the rate of sintering is highly dependent on the particle size and is faster for nanoparticles due to their higher chemical potential.[134] It was also noted by Perrichon et al. that increased oxygen mobility, caused by defect concentration may lead to a decrease in temperature stability.[135]

3. Cerium Oxide as a Redox Catalyst

3.1. Reduction and Oxidation Mechanism of Cerium Oxides

As mentioned before the redox properties play an important role in the application of cerium oxides. Therefore, it is of paramount importance to look into the mechanism of ceria reduction depending on the reducing agent.

3.1.1. Reduction of Cerium Oxide with Hydrogen

H_2-temperature programmed reduction (TPR) is an important tool for the evaluation of redox catalysts. It is used to qualitatively and quantitatively assess the temperature dependent reducibility of redox catalysts[136–140] However, the reduction of cerium-based materials with H_2 also has implications in the application of TWC as it was found that after rich-to-lean transitions hydrogen is formed by the reduction of water.[141] This hydrogen can subsequently interact with ceria again.

Cerium oxide reduction with H_2 is believed to occur via two different processes. The first being the formation and desorption of water and an oxygen vacancy accompanied by the reduction of two neighboring Ce^{IV} atoms.[142,143] The second process is believed to occur through hydrogen chemisorption and formation of a hydroxyl group which is not eliminated to form an oxygen vacancy.[144,145] It was shown using magnetic susceptibility measurements in a series of studies by Bernal et al. that the second reduction process is reversible by applying vacuum to the sample.[146,147] It was also reported that these two mechanisms persist even if the activation of hydrogen is catalyzed by the presence of a precious metal followed by hydrogen spillover.[148] However, for pure cerium oxide the irreversible reduction, i.e. the formation of an oxygen vacancy accompanied by a desorption of water, is prevalent, whereas for precious metal containing catalysts the reversible reduction plays a more important role, due to the lower temperatures employed during reduction.[147]

Reduction of Cerium Oxide with Carbon Monoxide

CO is one of the important pollutants which have to be removed during exhaust gas aftertreatment. CO acts as a σ-electron donor while backbonding can occur into the π^* orbital, thus weakening the C-O bond. Many studies concerned themselves with the adsorption of CO on ceria-based catalysts.[80,119,149–154] Fourier-transform infrared spectroscopy (FT-IR) was used to distinguish between different adsorbed species upon CO exposure.[149,150] After exposure to CO it is reported that different species are formed. A linear adsorption on top of exposed cerium ions was observed, which however is not stable and can be easily removed via evacuation. Other formed species are monodentate and bidentate carbonate species as well as inorganic carboxylates.[149] Similar species were also visible when investigating the adsorption of CO_2 pointing towards a slight reduction of ceria at room temperature upon CO adsorption. These findings were later also corroborated by theoretical studies from Nolan et al..[80] As with the oxygen vacancy formation energy it was already proposed in 1992 by Sayle et al. that the adsorption and with it the CO oxidation activity is dependent on the exposed crystal facets.[78] This was later confirmed by various experimental and theoretical studies.[155] It was shown that CO adsorption on (111) is a linear adsorption mode on top of the metal ion, similar to the reported weak adsorbing mode proposed by Li et al..[80,149] For (110) and (100) facets it was found that strong chemisorption in a bridging conformation occurs, leading to a carbonate-like species.[156] It was also predicted that an occupied band gap state in ceria is formed upon adsorption, indicating cerium reduction. This was also in line with a transfer of 1.7 and 1.8 electrons for the (110) and (100) facet, respectively.[80] The adsorption of CO was calculate to have a facet dependent adsorption energy of $-25\,\mathrm{kJ\,mol^{-1}}$ for the (111) facet,$-188\,\mathrm{kJ\,mol^{-1}}$ for the (110) facet and $-310\,\mathrm{kJ\,mol^{-1}}$ for the (100) facet. These trends were also validated in experimental studies looking at the structure sensitivity of CO oxidation over materials with preferred exposed crystal planes such as nanorods (NR), nanocubes (NC) and nanooctahedrons (NO).[119,154]

Reoxidation of Ceria

For the catalytic cycle to continue according to the MvK mechanism the material has to be reoxidized. Between molecular oxygen O_2,[152,153,157–166] nitrous oxides NO and N_2O[167–170] as well as water[141,171,172] in accordance to process condition of the TWC, different oxidizing agents are used in the testing of ceria materials.

In a laboratory setting oxygen is frequently employed as an oxidizing agent. Reoxidizing the surface with molecular oxygen requires dissociative adsorption, which was reported to follow the modified general oxygen reduction scheme[173,174]

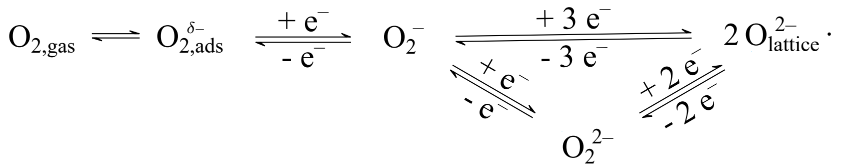

$$\begin{tikzcd}
O_{2,\mathrm{gas}} \arrow[r, shift left, harpoon] & O_{2,\mathrm{ads}}^{\delta-} \arrow[l, shift left, harpoon] \arrow[r, shift left, "+ e^-"] & O_2^- \arrow[l, shift left, "- e^-"] \arrow[rr, shift left, "+ 3 e^-"] \arrow[dr, shift left, "+ e^-"] & & 2\,O_{\mathrm{lattice}}^{2-}\,. \arrow[ll, shift left, "- 3 e^-"] \arrow[dl, shift left, "- 2 e^-"] \\
& & & O_2^{2-} \arrow[ul, shift left, "- e^-"] \arrow[ur, shift left, "+ 2 e^-"] &
\end{tikzcd}$$

Upon adsorption on the ceria surface a partially charged molecular oxygen species $O_{2,\mathrm{ads}}^{\delta-}$ is formed. Successive electron transfers from the reduced oxide to the adsorbed oxygen molecule lead to the formation of superoxide O_2^- and peroxide O_2^{2-} surface species. Further reduction of the oxygen species leads to the formation of lattice oxygen $O_{\mathrm{lattice}}^{2-}$.[175–178] All of these species were observed using vibrational spectroscopy while also being predicted theoretically.[179] It was reported from experimental as well as theoretical studies that oxygen adsorption on stoichiometric ceria surfaces is slightly endothermic.[174,176,180] Equivalent to the activation of reducing agents it was also reported in several studies that oxygen activation is a structure-sensitive process.[181] It was reported to follow the same order compared to CO activation, meaning the weakest activation was observed and predicted at the (111) facet, followed by the (110) and (100) facet.[178] The authors also found that for the (111) facet the vacancies are diffusing into a the sub-surface oxygen layer, limiting oxygen activation even more on the (111) facets.[178] When oxygen adsorbs on a $\mathrm{Ce^{III}}$ ion close to a vacancy, Zhao et al. calculated that oxygen coordinates into the oxygen vacancy, forming a peroxide by two single electron transfer (SET) from Ce$4f$ to the $\pi 2p^*$ orbital of oxygen. On the other hand if oxygen adsorbs on an isolated $\mathrm{Ce^{III}}$ site, only a single SET occurs, leading to the formation of a superoxide.[177]

3.2. Defect Chemistry of Cerium Oxide

Redox active metal oxides are known for their complex defect chemistry, whose understanding is paramount, as defects play a big role in changing reactivity of such redox active metal oxides.[182,183] Generally four different types of defects can be distinguished in pure ceria, along with any other metal oxide, not considering impurities:[184]

- Ceria with cerium deficiency (cerium vacancies; $v_{\mathrm{Ce}}^{''''}$)
- Ceria with cerium excess (metal on interstitial sites; $\mathrm{Ce}_i^{\bullet\bullet\bullet\bullet}$)
- Ceria with oxygen deficiency (oxygen vacancies; $v_{\mathrm{O}}^{\bullet\bullet}$)
- Ceria with oxygen excess (oxygen on interstitial sites; $\mathrm{O}_i^{''}$)

In order to adhere to overall charge neutrality, defects usually occur in defect pairs, which are known as *Schottky* ($v_{\mathrm{Ce}}^{''''} - 2v_{\mathrm{O}}^{\bullet\bullet}$), *Frenkel* ($v_{\mathrm{Ce}}^{''''} - \mathrm{Ce}_i^{\bullet\bullet\bullet\bullet}$) and *anti-Frenkel* ($v_{\mathrm{O}}^{\bullet\bullet} - \mathrm{O}_i^{''}$) defects.[185] In redox active oxides an oxygen vacancy does not have to coincide with a change in cation position, but can simply be compensated by a change in oxidation state of the metal. Although materials tend to have a prevalent type of defect, all of the above mentioned defects may be present in an oxide. For ceria it was found that the most prominent type of defect are oxygen vacancies with theoretical calculation suggesting a roughly 20 fold higher concentration compared to the aforementioned other defect types.[186,187] These defects may occur isolated on a single lattice site or may associate through stabilizing effects. The former are called point defects, or unassociated defects, whereas the latter are referred to as associated defects or defect clusters.[183]

3.3. Cerium Oxides as Catalysts for the CO Oxidation

Oxidation of CO is one of the important reactions in emission abatement in exhaust gas aftertreatment. Although activation of CO occurs *via* a precious metal (PM) in the actual TWC, CO oxidation over bare cerium oxides is frequently used as a model reaction to assess the oxygen release properties of different oxide supports.[188]

It is generally accepted that the CO oxidation follows the MvK mechanism, as described in chapter 1.4.3 whose elementary reactions steps are shown below in reactions 15-18.[189,190]

$$
\begin{aligned}
\mathrm{CO}_{(g)} + * &\longrightarrow \mathrm{CO}{-}* && \text{[R }\mathbf{15}\text{]}\\
\mathrm{CO}{-}* + \mathrm{O}_\mathrm{O}^\mathrm{x} &\longrightarrow \mathrm{CO}_2{-}\mathrm{v}_\mathrm{O}^{\bullet\bullet} && \text{[R }\mathbf{16}\text{]}\\
\mathrm{CO}_2{-}\mathrm{v}_\mathrm{O}^{\bullet\bullet} &\longrightarrow \mathrm{CO}_{2(g)} + \mathrm{v}_\mathrm{O}^{\bullet\bullet} && \text{[R }\mathbf{17}\text{]}\\
0.5\,\mathrm{O}_{2(g)} + \mathrm{v}_\mathrm{O}^{\bullet\bullet} &\longrightarrow \mathrm{O}_\mathrm{O}^\mathrm{x} && \text{[R }\mathbf{18}\text{]}
\end{aligned}
$$

After CO adsorption on a *Lewis*-acid site $*$ (i.e. $\mathrm{Ce^{III}}$, $\mathrm{Ce^{IV}}$) (c.f. reaction 15) CO is oxidized *via* a lattice oxygen ion $\mathrm{O}_\mathrm{O}^\mathrm{x}$ (reaction 16). Successively the formed $\mathrm{CO_2}$ is desorbed (reaction 17) and the created oxygen vacancy $\mathrm{v}_\mathrm{O}^{\bullet\bullet}$ is reoxidized by an oxidation agent, such as $\mathrm{O_2}$ (reaction 18). However, as already discussed in the previous chapter 3.1, it is also possible that especially on isolated sites $\mathrm{v}_\mathrm{O}^{\bullet}$, every other converted CO can react via the LH mechanism according to reactions 19-21.[191]

$$
\begin{aligned}
\mathrm{O}_{2(g)} + \mathrm{v}_\mathrm{O,iso}^{\bullet} &\longrightarrow \mathrm{O}_2^{-}{-}\mathrm{v}_\mathrm{O,iso}^{\bullet\bullet} && \text{[R }\mathbf{19}\text{]}\\
\mathrm{O}_2^{-}{-}\mathrm{v}_\mathrm{O,iso}^{\bullet\bullet} + \mathrm{CO}{-}* &\longrightarrow \mathrm{CO}_2{-}* + \mathrm{O}_\mathrm{O,iso}^\mathrm{x} && \text{[R }\mathbf{20}\text{]}\\
\mathrm{CO}_2{-}* &\longrightarrow \mathrm{CO}_{2(g)} + * && \text{[R }\mathbf{21}\text{]}
\end{aligned}
$$

Here molecular oxygen adsorbs on an isolated, not associated vacancy site $\mathrm{v}_\mathrm{O,iso}^{\bullet}$ to form a adsorbed superoxide species $\mathrm{O}_2^{-}{-}\mathrm{v}_\mathrm{O,iso}^{\bullet\bullet}$ (reaction 19) as discussed in the previous chapter 3.1. Afterwards a CO molecule adsorbed at a *Lewis* acid site $\mathrm{CO}{-}*$ (reaction 15) can react with the superoxide species to form $\mathrm{CO}_2{-}*$ while reoxidizing the isolated vacancy site to $\mathrm{O}_\mathrm{O,iso}^\mathrm{x}$ (reaction 20).[177] Afterwards $\mathrm{CO_2}$ can desorb (reaction 21).[192] The LH mechanism is more dominant at low temperatures since vacancy association and surface mobility of oxygen species is an activated process.[176] This leads to a shift in the equilibrium of adsorbed oxygen in direction of the lattice species $\mathrm{O_{lattice}}$ discussed in chapter 3.1.1.[193]

CO oxidation onset over CeO_2 catalysts is reported by several researcher to be directly linked to the surface reducibility of the employed catalyst, assessed by TPR experiments.[154] Thus it was reported that the rds in CO oxidation in the temperature range of 200 °C to 500 °C is the electron transfer from the oxide to CO.[194] Resulting from the structure sensitivity of vacancy formation, as discussed in chapter 3.1.1, the CO oxidation activity shows the same behavior with regards to exposed crystal facets.[119,194] It was reported that bare ceria is only reduced at temperature $T > 200\,°\mathrm{C}$. This is also evident from the light-off temperatures reported by several research groups. A list of different values reported in literature are given in table 5.

It is evident from the literature data reported in table 5 that values for light-off behavior in literature differ significantly. However, one can see that generally speaking lower light-off temperatures are observed for NR compared to other materials. NRs are reported to exhibit mostly (110) surface facets, having the lowest oxygen vacancy formation energy (c.f. tab. 4[79]). Also a shift of T_{50} to lower temperature with increasing specific surface area S_{A} and decreasing crystallite size D can be extracted from the light-off data reported.[119] This can be explained by the lower surface-to-bulk ratio decreasing the mass specific active site density SD_{m}. Therefore it is very difficult to derive structure-activity relationships from light-off experiments since the separation of these two factors is difficult. Especially since light-off curves are usually carried out with a dynamic temperature ramp, not ensuring the catalyst to reach dynamic equilibrium.

Although there are plenty reports on light-off behavior of CO oxidation catalyzed by ceria (c.f. table 5), a comprehensive study on structure-property relationships of polycrystalline cerium oxide is missing. There are a few studies that looked at activation energies of cerium oxides. Breyesse et al. published a thorough kinetic investigation of carbon monoxide oxidation via polycrystalline ceria, measuring an activation energy of $84\,\mathrm{kJ\,mol^{-1}}$ for a polycrystalline ceria sample $\left(S_{\mathrm{A}} = 27\,\mathrm{m^2\,g^{-1}}\right)$ as well as CO and O_2 reaction orders of $n_{\mathrm{CO}} = 0.84$ and $n_{\mathrm{O_2}} = 0$.[189] Slightly lower but similar activation energies are found by other authors, reporting values between $44\,\mathrm{kJ\,mol^{-1}}$ to $75\,\mathrm{kJ\,mol^{-1}}$ while the lower values were mostly obtained for facet enriched oxides.[119,140,165,199] It also has to be mentioned that resulting from the high activity of cerium-based catalysts in CO oxidation, diffusion limitations can be present and have to be ruled out.[119,189] This, however, was not the case for some of the investigations reporting activation energies for mesoporous ceria which might explain the very low values obtained by Lykaki et al. and Konsolakis et al.[140,198–200]

Table 5: Literature data for CO oxidation light-off over bare ceria catalysts

Author	Experimental conditions	$T_{50}/°C$
Aneggi et al.[119]	$2\,\%$ CO, $1\,\%$ O_2 ; 1×10^{-4} g s ml^{-1} nanoparticles (NP) S_A =5 m^2 g^{-1} to 140 m^2 g^{-1} D =7 nm to 51 nm	340 to 495
Boaro et al.[195]	$2\,\%$ CO, $1\,\%$ O_2; 1×10^{-4} g s ml^{-1} S_A =10 m^2 g^{-1} to 97 m^2 g^{-1}	365
Lykaki et al.[140]	$0.2\,\%$ CO, $1\,\%$ O_2; 8×10^{-4} g s ml^{-1} NR, NP S_A = 50 m^2 g^{-1} to 100 m^2 g^{-1} D =9 nm to 15 nm	325 to 465
Wu et al.[194]	$0.5\,\%$ CO $3.75\,\%O_2$; 1.25×10^{-3} g s ml^{-1} NR, NC and NO S_A =(93, 29 and 12) m^2 g^{-1}	295 to 355
Zhou et al.[154,196]	$1\,\%$ CO, $16\,\%$ O_2 2×10^{-3} g s ml^{-1} NR, NP, $S_A \sim$ 50 m^2 g^{-1}	180 and 227
Lykaki et al.[197,198]	$0.2\,\%$ CO, $1\,\%$ O_2; 2.5×10^{-5} g s ml^{-1} NR, NC and NP S_A =(92, 40 and 100) m^2 g^{-1} D_{Scherrer} =(11.6, 19.2 and 9.6) nm	320 to 385
Lee et al.[199]	$1.8\,\%$CO, $2.3\,\%$ O_2; 1.4×10^{-4} g s ml^{-1} mesoporous CeO_2 S_A = 125 m^2 g^{-1} D_{Scherrer} = 4.1 nm	287
Zhou et al.[200]	$0.5\,\%$ CO, $10\,\%$ O_2, 1×10^{-3} g s ml^{-1} mesoporous CeO_2, NP S_A =80 m^2 g^{-1} to 106 m^2 g^{-1}	307 to 397
Cui et al.[201]	$3\,\%$ CO, $12\,\%$ O_2, 3.75×10^{-3} g s ml^{-1} Nanospheres $S_A \sim$ 25 m^2 g^{-1}	298,321
Tschope et al.[202,203]	$2\,\%$ CO, $16\,\%$ O_2; 9×10^{-2} g s ml^{-1} NR, NP S_A = (57 and 35) m^2 g^{-1} $D_{\text{Scherrer}} \sim$ 10 nm	200, 380
Li et al.[204]	$1\,\%$ CO, $1\,\%$ O_2; 5×10^{-3} g s ml^{-1} NR S_A =93 m^2 g^{-1} to 123 m^2 g^{-1}	187 to 260

4. Platinum-loaded Cerium Oxides for Catalytic Applications

4.1. CO-Oxidation over Platinum-loaded Cerium Oxides

Precious metals are used to increase the low-temperature activity of ceria-based redox catalysts. It is known that the activity of precious metal-loaded ceria catalysts is highly dependent on the particle size of the precious metal.[205] This effect is often traced back to different precious metal-ceria perimeters caused by changing particle sizes, which also holds true for platinum-loaded ceria catalysts.[160] This is in line with findings, that even in the platinum-loaded state a MvK mechanism is prevalent, with CO adsorbing on the platinum atoms at the Pt-ceria perimeter, and getting oxidized through ceria lattice oxygen.[206] This also explains the difference to Pt alumina catalysts, where at lower temperatures below 150 °C the platinum is CO poisoned and oxygen is diminished.[207]

It is described in literature that platinum in its metallic form is significantly more active compared to ionic PtO_x.[208] While in the oxidized state, light-off temperatures above 100 °C are usually observed, light-off temperatures well below 100 °C are observed when the platinum species on the surface are reduced.[160,208,209] This trend can also be observed when looking at the activation energies of platinum-loaded ceria systems. Whereas activation energies of $60\,\mathrm{kJ\,mol^{-1}}$ to $70\,\mathrm{kJ\,mol^{-1}}$ in the as-synthesized state are reported, the activation energies after reduction are lower and usually in the range of $40\,\mathrm{kJ\,mol^{-1}}$ to $50\,\mathrm{kJ\,mol^{-1}}$. Studies by Meunier et al. however showed that while other authors proposed neutral platinum being more active, oxidized species might also be involved in the reaction mechanism in platinum nanoparticle loaded ceria.[210] This would be in line with the study by Wang et al. who showed that ionic Pt−O−Pt clusters exhibited very high activity, without the presence of metallic Pt species on the surface.[165] Gänzler et al. showed that, in line with other studies investigating the role of the Pt−O−Ce interface,[211] an ideal Pt particle size is present, which maximizes the Pt−O−Ce interface while at the same time keeping the metallic nature of the nanoparticles. They proposed an optimal particle size of 1.4 nm.[205] It was however also found when comparing materials with similar nanoparticle size, that the strength of interaction between the platinum particles and the oxide support plays an important role in the activity of precious metal-loaded ceria catalysts.[212]

One very important aspect of platinum-loaded ceria is the high mobility of platinum ions and particles on ceria. A series of studies showed, that while in reductive treatment, platinum tends to aggregate and form large nanoparticles, under oxidative treatment at high temperatures, the opposite happens. When oxidative conditions at temperatures above 400 °C are applied, platinum redisperses on the support.[205,213] This can be explained by formation of highly mobile PtO_x species which migrate to the support where they are bound due to strong interactions with ceria.[214–216] The dynamic nature of platinum on ceria is also exemplified by the fact that solely through CO adsorption at room temperature the platinum ions are being moved out of the ceria lattice.[209] This high mobility leads to dynamic changes in the platinum-ceria perimeter during catalysis. The contact area, however, does as discussed above dictate the activity. This makes it difficult to derive reliable structure-property relationships for the oxides support from kinetic data obtained.

4.2. Isolated Platinum Ions on Ceria as Model Catalysts

The high cost of precious metals drives research to aim for maximum dispersion and with it utilization in precious metal catalysts. It was found that ceria can stabilize platinum in its atomically dispersed state.[217] Different synthetic procedures were subsequently described, from atomic layer deposition (ALD),[171,218] to surface atom trapping[219,220] to strong electrostatic adsorption (SEA).[165,221]

Different coordination geometries for Pt single atoms were proposed in literature. Their presence was reported for different ceria facets, surface steps and bulk solid solutions. DFT calculations, coupled with X-ray absorption spectroscopy (XAS) experiments, showed that loading of ceria after preparation leads to surface decoration rather than bulk integration of platinum species.[217] It was also reported that the stability given by the adsorption strength of Pt^{2+} on ceria is a function of the exposed surface facet and is increasing from CeO_2 (111), to (110) to (100). This can be traced back to the increase in oxygen coordination, which also follows the same trend. This is consistent with theoretical studies on Pt_1-CeO_2, showing that a four-fold square planar coordination is the only stable coordination environment for Pt-SAC catalysts on ceria.[222] The authors then argued that since this coordination is only possible for the (100) facet or surface steps, platinum single atoms are only present on these surface facets or on surface defects. It was, however, also reported that treating platinum-loaded ceria hydrothermally at 800 °C leads to stabilization of atomically dispersed platinum species even at high platinum loadings.[217,219] Investigations of the coordination environments of the atomically dispersed platinum species using extended X-ray absorption fine structure (EXAFS) showed, that this high temperature treatment leads to a surface restructuring and to the stable square-planar coordination environment of Pt^{II} usually only observed for the (100) facet.[217] Resasco et al. also showed that it is possible to obtain atomic dispersion of platinum on ceria without high temperature treatment using a SEA approach, by reducing the surface specific loading to a value lower than 0.03 atoms/nm^2.[221] Thus atomic dispersion can be ensured in two different ways: The first one being a hydrothermal treatment of the prepared materials which according to the authors can stabilize atomic dispersion up to a loading of 3 wt. % The second one aims at lowering the Pt loading to a point where surface steps and defects can be populated with platinum ions.[223] This is exemplified by the comparison of three different studies. Ye et al. prepared materials with 1.3 wt. % using ALD without post treatment,[218] whereas Maurer et al. prepared 0.94 wt. % Pt on ceria by impregnation with a successive high temperature treatment according to Jones et al.[217,219] while Resasco et al. prepared materials with loadings of 0.05 wt. % using SEA.[221] Although the surface area is not reported by Ye et al., the synthesis of nanorods usually yields ceria materials with surface areas between 60 m^2 g^{-1} to 100 m^2 g^{-1}, giving comparable surface specific loadings to the study by Maurer et al. Whereas the materials investigated in the study of Ye et al. showed platinum aggregates after reduction at temperatures already at 150 °C, the atomic dispersion was still observable in the materials of Maurer et al. after reaction at 500 °C. This difference can be attributed, as also discussed by the authors, to the more stable coordination environment of the $\mathrm{Pt^{II}}$ ions after high temperature treatment through surface restructuring.[217] Comparing these findings to the results reported by Resasco et al. who did not use a high temperature treatment but rather lowered the surface specific loading (Maurer et al. $SD_\mathrm{A} = 1.2$ atoms/nm^2; Resasco et al. $SD_\mathrm{A} = 0.03$ atoms/nm^2) were also able to stabilize the atomic dispersion up to reduction temperatures of 500 °C.[221]

4.2.1. Characterization of Platinum Single Atom Catalysts (SAC) on Ceria

Proving the presence of atomically dispersed active sites is an important step when working with single atom catalyst (SAC). Due to low loading the analysis of such systems suffers from inherently low signal-to-noise ratio. However, a complementary approach of several techniques can help to show that the precious metal is atomically dispersed on the support. These techniques include high-angle annular dark-field imaging (HAADF)-scanning transmission electron microscopy (STEM), XAS, X-Ray photoelectron spectroscopy (XPS), CO-diffuse reflectance infrared fourier transform spectroscopy (DRIFTS), Raman spectroscopy, and XRD.

Analysis Based on Oxidation State

It is reported that platinum when atomically dispersed is stabilized in its ionic $\mathrm{Pt^{II}}$ state. Thus, as soon as platinum is reduced to its metallic $\mathrm{Pt^{0}}$ state, aggregation of the platinum species occurs. Therefore, the absence of metallic Pt^0 is frequently used to indirectly show that atomic dispersion is present. This is usually either done by XPS or X-ray absorption near edge structure (XANES). Platinum can be present in the oxidation states IV, II and 0. As most preparation procedures involve a calcination and oxidative nitrate precursors are used, the as-prepared materials usually exhibit an oxidation state of Pt of IV, which can be easily reduced to Pt^{II}.[217,221] As discussed before, upon further reduction to Pt^0, platinum aggregation and particle formation are usually observed.

Using the Pt4f XPS spectra, these species can be distinguished. With Pt^{IV}4f showing its doublet peak at 74.3 eV, Pt^{II} at 72.9 eV while 71.4 eV is usually observed for metallic Pt species. The Pt4f spectra is additionally accompanied by a peak splitting due to spin-orbit coupling between the $Pt4f_{7/2}$ and $Pt4f_{5/2}$ electrons of 3.3 eV.[217] The surface sensitive nature of XPS also enables the measurement of samples with a very low loading. The XANES spectra of platinum show a decrease in white-line intensity with decreasing oxidation state and also a red-shift of the white line from Pt^{II} to Pt^0.

It, however, has to be stressed that analysis of the as-prepared materials is usually not sufficient when trying to propose that single-sites are present under reaction conditions. Therefore, it is important to either use *operando* techniques or artificially age the samples by reduction to investigate whether or not isolated platinum species are present on the surface at reaction conditions. Studies by Maurer et al. additionally revealed that despite before and after reaction isolated platinum ions are present, some might form only during light-off through partial reduction even under oxidizing atmosphere.[217]

4.2.2. Analysis of the Position of Platinum Species

When discussing PM-SAC per definition there is no other PM-ion in close vicinity to the others. Thus, methods that can provide this proof are used complementary to the analysis of the oxidation state to show that the precious metal is dispersed atomically. The most straight forward way is using imaging techniques. By using STEM imaging, the absence of platinum clusters can be observed. To increase the contrast between cerium ions and platinum HAADF-STEM is usually employed.[221] However, electron microscopy always only shows a small section of the catalyst surface. Another method being highly sensitive towards the coordination environment of platinum is EXAFS. By comparing the interatomic distances of the first coordination sphere with platinum foil, the presence of Pt-Pt coordination can be excluded. However, when employing a calcination step, particles on the surface usually are oxidized, as discussed above, which is the reason why the second coordination sphere has to be analyzed. However, due to the low loading the intensities are very low, which is the reason why this analysis is difficult. This can also be avoided by employing a reducing step beforehand, as a reduced sample would show, if platinum clusters are present which would get reduced during reductive treatment, Pt-Pt scattering paths in the first shell which can be analyzed better.

Another surface sensitive technique that is frequently employed to investigate the coordination environment of platinum ions is CO-DRIFTS.[152,164,224,225] The CO stretching vibration is very sensitive to the nature of the adsorption site. Whereas unadsorbed CO shows an infrared (IR) band associated with the CO stretching vibration at 2143 cm^{-1}, upon adsorption this frequency is red-shifted depending on the amount of backbonding from the adsorption site into the $\pi^\star$ orbital of CO, which weakens the C-O bond.[152] Therefore, the higher the electron density of the Pt species CO is adsorbed at, the stronger the back bonding and the larger the red-shift.[224] It was proposed and widely accepted that CO adsorbed on $\mathrm{Pt}^{\delta+}$ shows a red-shift of 28 cm^{-1} compared to unadsorbed CO, whereas CO adsorbed on metallic Pt^0 species show a larger red-shift of 53 cm^{-1} to 73 cm^{-1} corresponding CO stretching vibrations between 2070 cm^{-1} to 2090 cm^{-1}.[224] CO adsorption on nanoparticles usually leads to a broadening of CO bands since nanoparticles allow the adsorption in other configuration other than linear adsorption. Happel et al. did a thorough study of CO adsorption on Pt nanoparticles supported on $\mathrm{CeO_2}$ and suggested that the IR band observed at around 2070 cm^{-1} can be attributed to the on-top adsorption on Pt^0 edges and steps, whereas modes around 2081 cm^{-1} to 2097 cm^{-1} were attributed to CO adsorbed on-top of Pt(111) facets. Another feature the authors detected was a bridged CO(η_2) species showing a vibrational frequency of 1850 cm^{-1} to 1875 cm^{-1}.[226] The latter one is inherently absent in catalysts only showing isolated platinum ions. On platinum nanoparticles different adsorption modes can be distinguished. For isolated $\mathrm{Pt}^{\mathrm{II}}$ species on ceria, the stretching vibration of adsorbed CO is shifted to 2095 cm^{-1} compared to lower frequencies observed for CO adsorbed on metallic Pt clusters. This is in line with the lower activity in the CO oxidation observed for ionic platinum species. Both bi- and tridentate coordination geometries are not possible in case of only isolated Pt species being present on the catalyst. Using CO-DRIFTS to proof the presence of nanoclusters or oxidation states of platinum is difficult as discussed thoroughly by Aleksandrov et al. and Meunier.[227,228]

Two lesser used methods are Raman spectroscopy which enables the investigation of the Pt-O-Ce band and XRD which can be used to exclude large platinum particles.

4.2.3. Pt-Single Atom Catalysts (SAC) in CO Oxidation

Pt-SAC loaded on ceria are of great interest for applications, as they can maximize the utilization of the expensive precious metal. However, stability and low activity are a challenge. That is why there are many studies focusing on improving the activity of Pt_1-CeO_2 catalysts for CO oxidation. As discussed above two different approaches in obtaining atomic dispersion are usually followed to obtain stable isolated platinum ions. While the first employs high loadings and uses support restructuring to stabilize single platinum ions, the other method uses low platinum loadings to suppress platinum agglomeration. Maurer et al. reported that, although high dispersions might be present at the start and end of a light-off cycle, the catalyst might form clusters during CO light-off.[217] The presence of small platinum clusters, which are known to exhibit higher activity, makes the comparison of published kinetic data challenging. It is generally accepted that CO oxidation catalyzed by Pt-SAC on CeO_2 follows the MvK mechanism.[165,217] When CO adsorbs on Pt^{II} sites σ-bonding from CO is strengthened while π back bonding is weakened compared to adsorption of Pt-NP. Thus, the activation of CO is lowered compared to metallic nanoparticles. Afterwards oxygen is transferred from the ceria lattice, leading to CO_2 formation, similar to platinum nanoparticle-loaded ceria discussed in chapter 4.1. Subsequently the formed oxygen vacancy is reoxidized with oxygen from the gas phase.[229] Su et al. reported DFT calculations showing that the most abundant reaction intermediate (MARI) is highly dependent on the coordination environment of the single platinum atoms. For species where platinum ions are adsorbed on steps of ceria crystals, the MARI is adsorbed CO, whereas platinum present on the $CeO_2(111)$ facet showed that adsorbed CO is the MARI only at high temperatures, whereas CO_2 is the MARI at low temperatures.[229] The above mentioned difficulty to prove whether isolated platinum ions are present, or whether clusters or nanoparticles cause the activity is also evident when comparing light-off data published in literature. An excerpt of published literature values are shown in tab. 6.

Table 6: Literature data for CO oxidation light-off over Pt-single atom catalysts as well as two studies focusing on nanoparticle loaded ceria

Author	Pt loading	Experimental conditions	$T_{50}/°C$
Jones et al.[219]	1 wt. %	2 % CO, 1.3 % O_2 in He; $\tau_{\text{mod}} = 0.39\,\text{g min l}^{-1}$	275 °C to 290 °C
Maurer et al.[217]	0.94 wt. %	0.1 % CO, 8 % O_2; 60000 $\text{l g}^{-1}\,\text{h}^{-1}$ (Pt)	194 °C
Maurer et al.[209]	(1, 2.3 and 4.5) wt. %	0.1 % CO, 8 % O_2; 60000 $\text{l g}^{-1}\,\text{h}^{-1}$ (Pt)	ox: (365, 282 and 195) °C red: (103, 90 and 86) °C
Ye et al.[218]	1.2 wt. % to 4 wt. %	1 % CO, 20 % O_2; $\tau_{\text{mod}} = 0.028\,\text{g s l}^{-1}$	dry: 189 °C to 232 °C wet: 84 °C to 232 °C
Wang et al.[165]	0.11 wt. % to 0.27 wt. %	0.1 % CO, 5 % O_2 in N_2; 2400 $\text{l g}^{-1}\,\text{h}^{-1}$	226 °C
Nie et al.[166]	1 wt. %	0.4 % CO, 10 % O_2; 200000 $\text{ml g}^{-1}\,\text{h}^{-1}$	310 °C
Jiang et al.[164]	1 wt. %	1 % CO, 10 % O_2; 200000 $\text{ml g}^{-1}\,\text{h}^{-1}$	288 °C
Pereira-Hernández et al.[212]	1 wt. %	1.9 % CO, 1.3 % O_2 in He; 232500 $\text{ml g}^{-1}\,\text{h}^{-1}$	assyn: (250 and 265) °C red: (56 and 92) °C
Gatla et al.[208]	2.5 wt. %	0.6 % CO, 10 % O_2 in N_2; $GHSV = 50000\,\text{h}^{-1}$	ox: 191 °C red: 43 °C to 57 °C
Cargnello et al.[160]	0.5 wt. %	1 % CO, 4 % O_2 in N_2; 150000 $\text{mL g}^{-1}\,\text{h}^{-1}$	70 °C to 110 °C

It can be observed, that while very low values are reported by Ye et al., most of the values lie between 200 °C to 300 °C which is significantly higher than values obtained for metallic nanoparticles, which, as shown in table 6, can reach values below 100 °C. The list shows that values obtained do differ strongly between the materials. Another aspect that is obvious when looking at the published data is that comparing materials between different studies is very difficult, since not only the measurement parameters do change but the materials do as well. This holds also true when comparing different steady-state, differential kinetic investigations and calculated activation energies. An overview over published data is shown in figure 3.

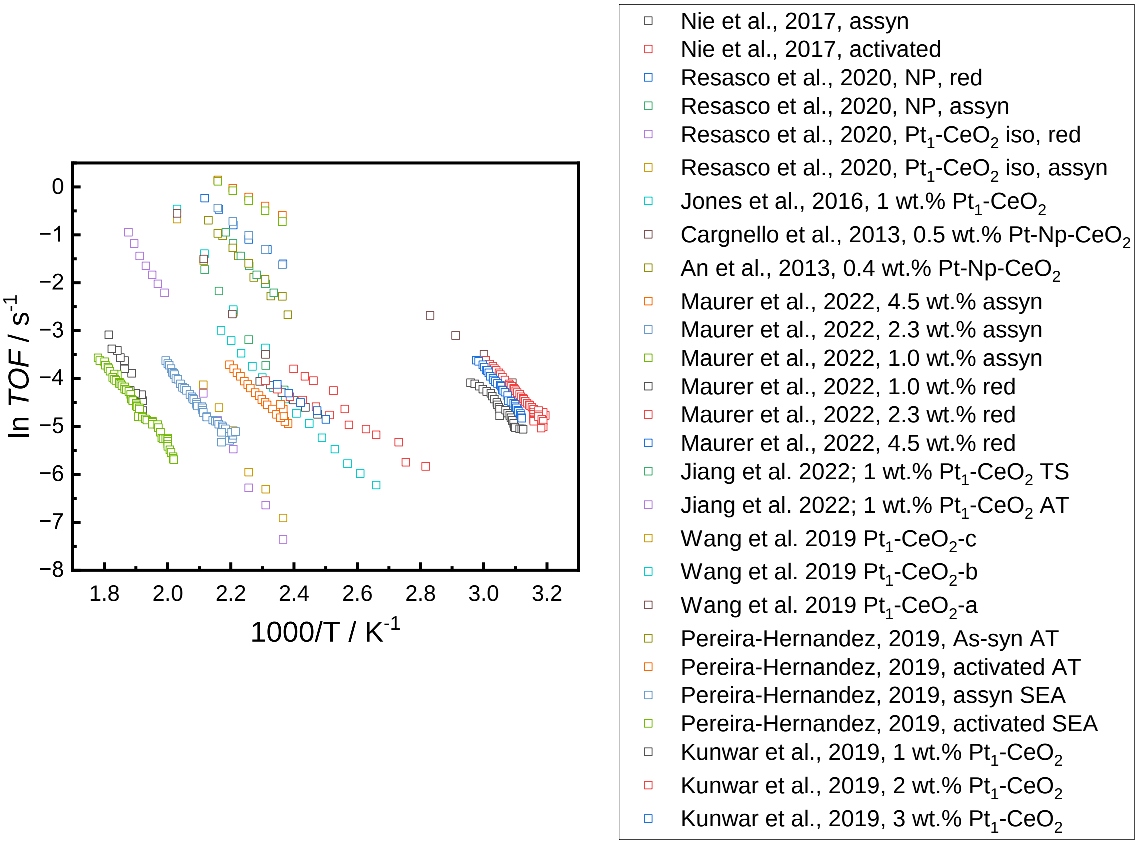

Figure 3: Arrhenius plot of literature published studies on Pt_1-CeO_2 materials whose analysis results are also listed in tab. 7.

When comparing kinetic data published for Pt_1-CeO_2 materials the same trend as shown with the light-off temperatures is visible. The published data scatters over a wide range of activities. However, when activation energies are compared, materials with different activities can be classified into three different groups based on the authors' approach. First, studies that focus on ensuring atomic dispersion also under reaction conditions, such as the study by Resasco et al., second materials with comparatively high catalyst loading, which was shown to form metal clusters under reaction conditions[217] such as studies by

Maurer et al. and Ye et al.[217,218] third studies directly focusing on the Pt−O−Ce perimeter of nanoparticles like Cargnello et al. and An et al.[160,230] This is also represented in the activation energies reported for Pt-CeO_2 catalysts shown in tab. 7.

Table 7: Kinetic data reported for Pt_1-CeO_2 catalysts

Author	Loading	Conditions	Activation energies
Resasco et al.[221]	0.05 wt. %	0.5 % CO, 10 % O_2 in He	95 kJ mol^{-1}
Nie et al.[166]	1 wt. %	0.4 % CO, 10 % O_2 200000 ml g^{-1} h^{-1}	105 kJ mol^{-1}
Resasco et al.[221]	0.05 wt. %	0.5 % CO, 10 % O_2 in He	assyn: 84 kJ mol^{-1} red: 45 kJ mol^{-1}
Nie et al.[166]	1 wt. %	0.4 % CO, 10 % O_2 200000 ml g^{-1} h^{-1}	42.5 kJ mol^{-1}
Jones et al.[219]	1 wt. %	2 % CO, 1.3 % O_2 in He $\tau_{\mathrm{mod}} = 0.39\,\mathrm{g} \times \mathrm{min}/\mathrm{l}$	56 kJ min^{-1}
Wang et al.[165]	0.11 wt. % to 0.27 wt. %	0.1 % CO, 5 % O_2 in N_2 2400 l g^{-1} h^{-1}	86.3 kJ mol^{-1}
Pereira-Hernández et al.[212]	1 wt. %	2 % CO, 1.25 % O_2 in H2	53.5 kJ mol^{-1}
Maurer et al.[209]	1 wt. %	0.1 % CO, 10 % O_2 in N_2	assyn: 67 kJ mol^{-1} red: 32 kJ mol^{-1}
Wang et al.[171]	0.22 kJ mol^{-1}	1 % CO, 20 % O_2 in N_2	62 kJ mol^{-1}
Cargnello et al.[160]	0.5 wt. %	1 % CO, 4 % O_2 in Ar	42 kJ min^{-1} to 63 kJ min^{-1}
An et al.[230]	0.3 wt. % to 0.5 wt. %	5 % CO, 10 % O_2 in He	63 kJ mol^{-1}

Using theoretical calculations different authors tried to unravel the mechanism of the CO oxidation catalyzed by Pt_1-CeO_2. Generally they assume that CO oxidation is governed by the MvK mechanism. However, they deviate in the consideration of the two-center LH mechanism, where adsorbed CO reacts with an oxygen vacancy adsorbed superoxide.[165,166] Whereas the reaction of activated CO adsorbed to a platinum ion with adsorbed and activated molecular oxygen was included in Nie et al.'s calculation, it was neglected in the calculations of Wang et al. In the latter calculation the authors assumed that two oxygen vacancies are formed, before they are refilled by dissociative adsorption of O_2.[165] Since platinum ions are four-fold coordinated in the Pt_1-CeO_2 catalysts, it is difficult to envision that two vacancies are formed in lose vicinity of the Pt ion before reoxidation occurs. The difference in the proposed mechanisms also leads to different calculated activation energies. For splitting the oxygen bond to heal two formed oxygen vacancies, the activation barrier was calculated to be $150\,\mathrm{kJ\,mol^{-1}}$, making it the largest barrier in the cycle.[165] The second largest barrier from the calculation would be the surface reaction of adsorbed CO and a lattice oxygen with an activation barrier of $105\,\mathrm{kJ\,mol^{-1}}$. In the calculations of Nie et al. the reaction of CO with the adsorbed $O_2^{*}{-}v_0$ has a lower barrier compared to the dissociative adsorption. The highest barrier in this study is the reaction of adsorbed CO with a lattice oxygen. Close to the value of the previously discussed calculation the value was calculated to be $122\,\mathrm{kJ\,mol^{-1}}$. A similar mechanism was also proposed by Wang et al.[171]

It is known that the presence of water does influence the CO oxidation rate of Pt-CeO_2 catalysts. This was also studied using Pt_1-CeO_2 catalysts. It was found that the presence of hydroxyl groups in the vicinity of the platinum center decreases the activation barrier of the surface reaction.[166] These hydroxyl groups lead, according to DFT calculations, to a carboxyl transition state. While water pretreatment can lead to more hydroxyl groups, also healing an oxygen vacancy through water reduction can form hydroxyl groups.[171] It is reported that reaction barriers are lowered by around $30\,\mathrm{kJ\,mol^{-1}}$ if vicinal OH groups are present.[165,166] This was also proven by experiments.[165,171] At temperatures above 200 °C the WGS activity is one reaction pathway which can lead to increased CO conversion.[141] Distinguishing the water-mediated MvK mechanism from the WGS mechanism requires separate kinetic testing without oxygen in the gas feed.[171]

Part III.

Motivation and Objectives

Platinum-loaded ceria catalysts are important materials in environmental catalysis, especially in the emission abatement of internal combustion vehicles. The legislation on limiting harmful components CO, NOx and HC , becomes ever tighter. Modern internal combustion vehicles use kinetic model-aided engine and catalyst control to predict the activity of the catalyst and change the ratio of injected fuel accordingly. These models, however, are of empirical nature. While this makes the models somewhat simple, it makes the description of aging effects difficult. This leads to increased emission of harmful pollutants over the catalyst lifetime. Basing kinetic models on material parameters of the catalyst requires knowledge about suitable descriptors. The complexity of the employed catalytic system and reaction network involved makes this very challenging. This is especially true for the ceria-based oxygen storage component, as the dynamic of precious metals under process conditions complicates the derivation of activity descriptors. This is the reason why well-defined material-based descriptors for ceria in precious metal loaded ceria are still scarce in literature.

The overarching objective of this work was therefore to derive structure-property relationships of different ceria materials in their precious metal loaded state for the exhaust gas aftertreatment. In order to keep the parameter space as small as possible, ceria materials loaded with isolated platinum ions were used as a model catalyst systems, while using the CO oxidation as a model reaction.

In order to do that, different challenges have to be addressed first. In order to derive structure-reactivity descriptors, it has to be investigated how the preparation conditions can influence the material properties of ceria materials. While precipitation is frequently used to prepare such materials, there is no common knowledge about how preparation conditions do influence the material parameters.

In a second step a method has to be developed with which the contribution of precious metal and ceria support can be separated. This is especially important when trying to trace back any changes in reactivity between the different materials to a change in the oxide support. The reported high mobility of platinum species has to be accounted for.

This enables the subsequent development of structure-reactivity relationships for ceria in the unloaded and platinum-loaded state. These structure-reactivity relationships, coupled with the derived reactivity descriptors, are important to parameterize kinetic models for exhaust gas aftertreatment systems. One aspect that should be investigated, is how the material parameters of ceria do influence the increase in reaction rate in the presence of water, which inherently is present in the exhaust gas but is frequently neglected in studies focusing on the catalytically active material.

Altogether this study aims for a deeper understanding of the role of the ceria oxygen storage material in precious metal loaded ceria systems and how the specific material parameters influence the reactivity of such systems. This should enable a parametrization of kinetic models using ceria material parameters.

Part IV.

Practical Section

5. Materials Used in This Work.

The materials used in this work are listed in table 8.

Table 8: Materials used in the experiments

Material/Chemical	Supplier	Purity	Use case
$(NH_4)_2Ce^{IV}(NO_3)_6$	Carl Roth	99 %	Preparation
$ZrO(NO_3)_2$	Sigma-Aldrich	99 %	Preparation
$(NH_2)_2CO$	Carl Roth	99.9 %	Preparation
$NH_{3(aq)}$ (10 wt. %)	Carl Roth	99 %	Preparation
C_2H_5OH	Merck KGaA	99.8 %	Preparation
$Pt^{II}(NH_3)_4(NO_3)_2$	Sigma-Aldrich	99.999 %	Preparation
$HClO_4$	Carl Roth	70 % (w/w)	pH experiments
NaOH	Carl Roth	99 %	pH experiments
CeO_2-HSA	Solvay	-	Reference material.
CeO_2-LSA	STREM	99.995 %	Reference for XRD, XPS
$CeAlO_3$	Sigma-Aldrich	99.9 %	Ce^{III} standard for XPS
CuO	Sigma-Aldrich	99.999 %	Standard for TPR calibration
LaB_6 (NIST 660c)	NIST	-	Standard for XRD
γ-Al_2O_3	Sasol	-	PZC measurements
γ-Al_2O_3	Baikoski	-	Preparation of $CeAlO_3$
SiO_2	Evonik	-	PZC measurements
TiO_2	Aldrich	99.9 %	PZC measurements

6. Material Preparation

The material properties of cerium-based oxides are highly dependent on the preparation methods and conditions. To prepare materials with different properties, preparation methods and conditions were successively changed to elucidate the role preparation conditions play as well as to prepare materials with different properties to elucidate structure-property relationships.

6.1. Preparation of the Oxide Support

6.1.1. Ammonia-based Precipitation (AP)

Ammonia-based precipitation (AP) is one of the most frequently used methods to prepare metal oxides. In a typical experiment $0.1\,\mathrm{mol\,l^{-1}}$ metal salt solution was prepared by dissolving cerium ammonium nitrate in bidistilled water. Due to the hygroscopic nature of the precursor salts, the actual cerium content was measured using inductively coupled plasma optical emission spectroscopy (ICP-OES) to ensure constant molarities across all preparations through adjusting the mass of precursor accordingly. In a double walled stirred tank reactor ($V = 1\,\mathrm{l}$) connected to a thermostat (*F12-MC* from *Julabo*), the reaction solution ($V_\mathrm{solution} = 0.6\,\mathrm{l}$) was tempered to the desired precipitation temperature T_prec under stirring using a KPG paddle stirrer with 300 rpm. To ensure constant temperature in the reaction solution a waiting time of 1 h was introduced. Subsequently, using a piston pump (*REGLO-CPF Digital* from *ISMATEC*), 10 wt. % ammonia solution was added with $5\,\mathrm{ml\,min^{-1}}$ until a pH of 10 was reached. The formed precipitate was then aged for an hour before filtration and washing with 2 l bidistilled water and 0.2 l ethanol, respectively. Drying at 80 °C before calcination at T_calc yielded the as-prepared material.

To follow the precipitation process, pH titration experiments were additionally carried out. Metal salt solutions were prepared in the same way as for the AP preparations. Subsequently, 5 ml of $1\,\mathrm{mol\,l^{-1}}$ NaOH solution was added. After sodium hydroxide addition, the solution was stirred for 2 min before measuring the pH value using an *InLab Power Pro-ISM (Mettler Toledo)* pH electrode with a *SevenCompact S210 (Mettler Toledo)*. This was repeated until the pH did reach a stationary level. For blind measurements, sodium chloride was used instead of the cerium salt in order to ensure sufficient conductivity. The amount of OH^- consumed was calculated from the difference between sample and blind measurement. These experiments were carried out at 5 °C, 25 °C and 50 °C.

6.1.2. Urea-based Precipitation (UP)

Reaction solutions were prepared in a flask by dissolving under stirring appropriate amounts of $(NH_4)_2Ce(NO_3)_6$ and urea to yield a metal salt concentration of $0.1\,\mathrm{mol\,l^{-1}}$ and a molar ratio Ce^{IV}:urea of 1:15. The reaction solution was refluxed at 100 °C for 4 h during which precipitation occurred. Afterwards the precipitate was separated and washed with 2 l of bidistilled water and 0.2 l ethanol, respectively. Drying overnight at 80 °C and calcining the material at T_{calc} gave the as-prepared material.

6.1.3. Urea-based Precipitation Under Hydrothermal Conditions (HUP)

For the preparation under hydrothermal conditions steel autoclaves with 0.12 l Teflon liners were used. Reaction solutions were prepared in the same way as for the urea-based precipitation. 0.08 l were filled into a Teflon liner before placing the liner into the autoclave, which was subsequently closed. The autoclaves were placed into a rotary oven with a rotary frequency of $10\,\mathrm{min^{-1}}$ at 140 °C for 24 h. Afterwards the autoclaves were cooled down using an ice bath before opening them and separating the precipitate using centrifugation at 12000 rpm before washing twice with water and once with ethanol. The washed precipitate was dried at 80 °C overnight before calcination at T_{calc}.[106] As the reaction volume is restricted by the volume of the autoclave, six autoclaves were used in parallel to increase the amount of product obtained. To reduce deviations between the different autoclaves, each autoclave was filled with aliquotes from the same metal salt solution and placed into the oven at the same time. In the centrifugation process the precipitates from the different autoclaves were combined and analyzed as one.

6.2. Platinum Loading

As described previously precious metals are used to decrease light-off temperatures and increase the activity of commercial three-way catalysts. In this work, platinum was loaded using a SEA and an incipient wetness (IW) approach.

6.2.1. Loading with Platinum Using Strong Electrostatic Adsorption (SEA)

Loading using SEA is based upon the coulombic attraction between metal salt and oxide surface. Loading was carried out using tetraammineplatinum(II) nitrate (TAPN)

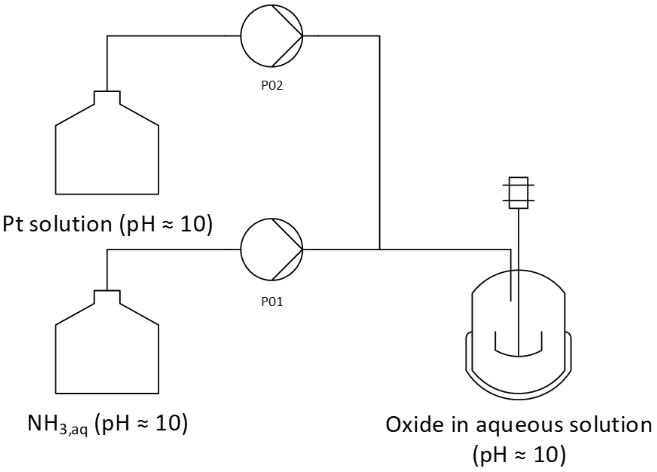

Figure 4: Flow chart of the Pt loading setup with P01 being a peristaltic pump (*reglo digital (Ismatec)*) and P02 a syringe pump (*PHD Ultra (Harvard Apparatus)*).

($Pt(NH_3)_4(NO_3)_2$), thus a negative charge of the oxide surface is necessary to obtain attractive forces between the oxide surface and $Pt(NH_3)_4^{2+}$ complex. Knowledge about the point of zero charge (PZC) enables the charging of the surface via the solution pH. As a negative surface charge is needed, one has to increase the pH value above the PZC of the oxide. This was achieved by dispersing the different ceria materials in bidistilled water, whose pH was adjusted beforehand with 10 wt. % ammonia to pH ≈ 10.

Loadings were carried out in the setup shown in figure 4, while using a constant surface loading (SL), which is a measure for oxide surface per volume of dispersion,[231] between the different preparations. With it and the mass of oxide m_{Ox} and its specific surface area from nitrogen physisorption experiments S_{BET} the solution volume after addition $V_{\mathrm{final,SL}}$ can be calculated.

$$V_{\mathrm{final,SL}} = \frac{m_{\mathrm{Ox}} \cdot S_{\mathrm{BET}}}{SL} \tag{28}$$

All loadings were carried out using a SL of $SL = 2900\,\mathrm{m^2\,l^{-1}}$. In a typical experiment, 3 g of oxide was degassed at 150 °C overnight in nitrogen. The degassed mass of the oxide was determined before dispersing it in the initial volume, V_{initial}, of an aqueous pH-adjusted (pH=10) solution. An aqueous TAPN stock solution was prepared using diluted ammonia solution so the pH was approximately 10. Afterwards, the Pt concentration was determined using ICP-OES. The necessary volume of this solution needed to reach the desired surface specific platinum loading SD_{A}, calculated using eq. (29), was diluted to $V_{\mathrm{Pt-solution}} = 5\,\mathrm{ml}$ using an aqueous ammonia solution with pH = 10.

$$n_{\mathrm{TAPN}} = \frac{m_{\mathrm{ox}} \cdot S_{\mathrm{BET}} \cdot SD_{\mathrm{A}}}{\mathrm{N_A}}. \tag{29}$$

In the loading process, the diluted TAPN solution was pumped using a syringe pump (P02) with a constant flow rate of $\dot{V}_{\mathrm{TAPN-solution,P02}} = 0.015\,\mathrm{ml\,min^{-1}}$ into a constant flow of pure ammonia solution (pH = 10) of $\dot{V}_{\mathrm{NH_3,aq,\ P01}} = 0.06\,\mathrm{ml\,min^{-1}}$ pumped using a peristaltic pump. This was done in order to dilute the TAPN solution further before addition it into the reaction vessel over a duration of $t_{\mathrm{loading}} = 330\,\mathrm{min}$. During the addition, the oxide dispersion was stirred using a magnetic stirrer. Over the course of an experiment, $V_{\mathrm{dil.TAPN-solution}} = 5\,\mathrm{ml}$ of diluted TAPN solution was added using the syringe pump while $V_{\mathrm{NH_3solution}} = 20\,\mathrm{ml}$ of ammonia solution was added through the peristaltic pump. After the entire TAPN solution was added, the syringe used for the TAPN solution was purged twice with $V_{\mathrm{rinsing}} = 5\,\mathrm{ml}$ of ammonia solution (pH = 10) to make sure all TAPN was added to the oxide dispersion.

Thus, the inital volume can be calculated according to eq. (30)

$$V_{\mathrm{initial}} = V_{\mathrm{final,SL}} - V_{\mathrm{dil.TAPN-solution}} - V_{\mathrm{NH_3solution}} - 2V_{\mathrm{rinsing}}. \tag{30}$$

After the TAPN addition water was slowly evaporated at 70 °C under stirring. Subsequently the samples were calcined at 450 °C for 4 h in a syn. air flow of $100\,\mathrm{l\,h^{-1}}$.

6.2.2. Measurement of Point of Zero Charge (PZC) for SEA Loading

Before PZC analysis the oxides were dispersed in 10 wt. % ammonia solution and sonicated for 30 min to remove any surface adsorbates. Afterwards the powder was separated by centrifugation (4000 rpm; 20 min) before decanting and washing with bidistilled waster and ethanol. The washed solids were dried for 3 h at 80°C before placing them into an oven at 450 °C for 5 h in nitrogen atmosphere to desorb any surface adsorbates. Sodium perchlorate solutions (0.01 M) were adjusted to different pH values ($\mathrm{pH_{initial}}$) using $HClO_4$ and NaOH before placing them in centrifugation tubes. By bubbling Ar through the solution an inert gas atmosphere was ensured. Afterwards the cleaned oxides were added while still hot with as little contact to ambient air as possible to the different solutions with a SL of $SL = 500\,\mathrm{m}^2\,\mathrm{l}^{-1}$. The tubes were subsequently closed and placed on a vibrating plate for 24 h. Afterwards the solid was separated using centrifugation (10000 rpm, 30 min) and the pH of the supernatant solution was measured at 25 °C ($\mathrm{pH}_{\mathrm{final}}$) using an *InLab Power Pro-ISM (Mettler Toledo)* pH electrode coupled with a *SevenCompact S210 (Mettler Toledo)*. The electrode was calibrated using National Institute of Standards and Technology (NIST) pH standards ($\mathrm{pH}_1 = 1.679$, $\mathrm{pH}_2 = 4.006$, $\mathrm{pH}_3 = 6.865$ and $\mathrm{pH}_4 = 10.012$) before every measurement. The pH difference ΔpH was calculated according to eq. (31)

$$\Delta\mathrm{pH} = \mathrm{pH}_{\mathrm{final}} - \mathrm{pH}_{\mathrm{initial}}. \tag{31}$$

The plot of the pH difference ΔpH as a function of the initial pH $\mathrm{pH}_{\mathrm{initial}}$ gives the PZC as the intersection of the linear fit with the x-axis.[232]

6.2.3. Loading with Platinum using Incipient Wetness (IW)

IW loadings of different oxides were carried out to compare them with the samples prepared by SEA, since IW is known to produce NPs. To load m_{ox}, the volume of metal salt solution was calculated from the total pore volume $V_{\mathrm{pore,m}}$ obtained through nitrogen physisorption experiments as shown in eq. (32)

$$V_{\mathrm{IW}} = V_{\mathrm{pore,m}} \cdot m_{\mathrm{Ox}}. \tag{32}$$

The amount of TAPN needed was calculated based on the desired platinum weight fraction ω_{Pt} according to eq. (33)

$$n_{\mathrm{TAPN}} = \frac{\omega_{\mathrm{Pt}} \cdot m_{\mathrm{ox}}}{M_{\mathrm{Pt}}}. \tag{33}$$

The oxide was degassed at 150 °C overnight in nitrogen. The calculated amount of TAPN n_{TAPN} was subsequently dissolved in the calculated volume V_{IW} under sonication. Afterwards the entire impregnation solution was added slowly to the oxide which was agitated using a magnetic stirrer during the process to ensure homogeneous distribution. Afterwards the loaded oxide was stirred for 1 h before drying the solid at 80 °C overnight and calcination at 450 °C for 4 h in a flow of $100\,\mathrm{l\,h^{-1}}$ of syn. air.

7. Material Characterization

After preparation, the samples were characterized for their elemental composition using ICP-OES and inductively coupled plasma mass spectrometry (ICP-MS). Analysis of the crystal structure was done by XRD coupled with *Rietveld* refinement. Surface area and pore volumes/pore size distributions were collected using N_2 physisorption and Hg porosimetry. Mass loss during degassing was quantified using thermogravimetric analysis (TGA). For the spectroscopic characterization of the samples *Raman* spectroscopy, DRIFTS, XAS and XPS were applied. The redox and adsorption/desorption properties were characterized using temperature programmed methods (TPx), while the performance of the prepared catalysts was determined in a self-built catalyst testing apparatus.

7.1. Inductively Coupled Plasma optical emission spectroscopy/mass spectrometry

To quantify the platinum content of the prepared samples, ICP-OES measurements were carried out. For this approximately 30 mg of loaded oxide was dissolved in 5 ml concentrated nitric acid in a lab microwave at 200 °C to 210 °C before dilution to 50 ml using bidistilled water. The solutions were measured using an *Avio 200 (Perkin Elmer)* spectrometer. Sample preparation as well as measurements were carried out by Heike Fingerle and Nağme Ay. For samples having a concentration below the quantification limit of the ICP-OES instrument, ICP-MS measurements were carried out at the *Fraunhofer* Institute for Interfacial Engineering and Biotechnology by Katharina Wasmer.

7.2. X-ray Diffraction

Analyzing the crystal structure of ceria is paramount in deriving structure-property relationships for ceria-based catalysts. For this reason X-ray diffractograms were measured using a *D8 Advance (Bruker)* equipped with a *Vantec PSD* and a Cu source ($\lambda = 0.1541$ nm) operated with a voltage of 35 kV. A zero background sample holder was used to limit contributions of the sample holder to the diffraction patterns. Diffraction patterns were collected in the range of $2\theta = 15°$ to $110°$ with a step size of $0.036\,°\,\mathrm{s}^{-1}$.

Quantitative analysis was carried out using *GSAS-II*.[233] To assess and quantify the instrument contribution to reflex position and measured line shape, a standard reference material (SRM) was purchased from NIST (SRM660c (LaB_6); $a = (0.4156826 \pm 0.0000008)\,\mathrm{nm}$, $D = 0.8\,\mu\mathrm{m}$). This material was measured and used to create the instrument profile using the supplied values for lattice parameter and size while assuming the strain to be zero as specified in the standard's documentation. This calibration was done four times a year over the course of this work. A exemplary diffractogram of the LaB_6 NIST-SRM660 is shown in figure 50 in the appendix. For *Rietveld* calculations a $Fm\bar{3}m$ structure was used with Ce atoms at the position (0, 0, 0) and O on the lattice position (1/4, 1/4, 1/4). During the refinement, lattice parameter a, crystallite size D and strain ϵ were refined, while occupancy factor and atomic positions were held constant.

7.3. N_2 Physisorption

Physisorption measurements were carried out to assess the surface area and pore size of the prepared samples. Using an *Autosorb 3B (Quantachrome Instruments)* and *Autosorb iQ (Anton-Paar)* the isotherms were measured. Samples were degassed at 300 °C overnight *in vacuo*. Measurements were conducted at 77 K. Surface areas were determined using the Brunauer-Emmett-Teller (BET) theory while pore volume values were calculated with the Barrett-Joyner-Halenda (BJH) method.

Physisorption experiments were carried out by Dorothea Häussermann, Ann-Katrin Beurer, Faeze Tari and Michael Benz at the Institute of Technical Chemistry. A validation experiment was carried out at the Institute of Polymeric Chemistry measured by Dr. Felix Ziegler using an *Autosorb iQ (Anton-Paar)*. During the validation experiment the same value at all three instruments was obtained and matched the value reported by the supplier of the material. Values deviated not more than $\pm\ 5\,\mathrm{m}^2\,\mathrm{g}^{-1}$ between the measurements on different instruments.

7.4. Hg Porosimetry

Mercury porosimetry measurements were carried out to investigate the porosity and tortuosity of the catalyst powders to assess presence of diffusional limitations. Measurements were conducted using a low-pressure (*Pascal 140 (CE Instruments)*) and high-pressure (*Pascal*

440 (CE Instruments)) instrument. In a usual experiment 0.3 g of catalyst powder was placed into a volume calibrated dilatometer. After degassing, pressure was continuously increased to 375 kPa in the low pressure unit before placing the Hg filled dilatometer into the high-pressure unit and steadily increasing the pressure to 400 MPa.

Measurements were performed at the Institute of Manufacturing Technologies of Ceramic Components and Composites (IMTCCC) of the University of Stuttgart under the guidance of Thomas Heim.

7.5. Transmission Electron Microscopy

Transmission electron microscopy (TEM) measurements were carried out at the Institute for Material Science in the Department for Materials Physics of the University of Stuttgart using a *CM200 FEG (Philips)* at 200 kV by Helena Solodenko and Guido Schmitz. HAADF-STEM images were collected by Dr. Hongguang Wang at the MPI-FKF.

Sample preparation was done by dispersing the sample in isopropanol under ultrasonication before applying it dropwise to a copper grid. After drying the copper grids overnight, the samples were analyzed. Sample preparation was carried out by Faeze Tari.

7.6. Thermogravimetry

Thermogravimetric measurements were carried out to investigate mass loss of the different samples during degassing as well as to verify the oxidation state of the employed CuO standard.

Determination of Mass Loss During Degassing

To rectify the sample mass in catalytic experiments and high-temperature TPx experiments, the mass loss of samples during degas was determined using TGA.

For these measurements between 20 mg to 100 mg were used for analysis, depending on the specific surface area S_{BET} of ther material. The samples were heated in a flow of 50 ml min^{-1} synthetic air to 300 °C with a heating rate of 10 K min^{-1}. Afterwards the samples were held at that temperature for 3 h. Measurements were corrected using blind measurements with the same measurement protocol. The relative remaining mass after degassing w_{degas} was later used for data analysis.

Oxidation State Analysis

Reduction of redox active oxides can be monitored gravimetrically by following the corresponding mass loss.

For that purpose samples (usually 20 mg to 100 mg) were degassed first at 300 °C in a flow of 50 ml min^{-1} of synthetic air for 3 h before cooling down to 50 °C. Afterwards the atmosphere was switched to Ar and after 2 h of isothermal treatment the degassed sample mass was recorded $m_{\mathrm{T,0,Ar}}$. Thereafter, premixed 5 % H_2/N_2 with a flow rate of 50 ml min^{-1} was selected and the sample was heated to 600 °C with a heating ramp of 10 K min^{-1}. Afterwards the sample was cooled down to 50 °C before switching to argon again. After isothermal equilibration at 50 °C for 2 h the reduced sample mass $m_{\mathrm{T,\,red,\,Ar}}$ was recorded. During the experiment a constant flow of 20 ml min^{-1} argon was used as protective gas for the balance. The relative remaining mass w after reduction was calculated using eq. (34) without a blind measurement

$$w = 1 - \frac{m_{\mathrm{T,\,red,\,Ar}}}{m_{\mathrm{T,0,Ar}}}. \tag{34}$$

The oxidation state ox of the measured $\overset{\mathrm{ox}}{\mathrm{M}}_{\mathrm{n}}\overset{-\mathrm{II}}{\mathrm{O}}_{\mathrm{m}}$ can be calculated from the measured relative remaining mass w under the assumption of homogeneous reduction to a defined compound (e.g. in the case of copper oxide reduction to elemental copper is assumed while for ceria the reduction is assumed to yield Ce_2O_3) with the molecular mass of M_{red} and the molecular mass of oxygen M_{O} using equation (35)

$$ox = 2\frac{\left(\frac{M_{\mathrm{red}}}{w}\right) - M_{\mathrm{red}}}{M_{\mathrm{O}}}. \tag{35}$$

7.7. Raman Spectroscopy

XRD is insensitive towards changes in oxygen sublattice of ceria materials due to the large mass difference and related scattering contribution between Ce and O nuclei. *Raman* spectroscopy can act as a complementary method to investigate changes in the oxygen sublattice.

Therefore, *Raman* spectra were recorded using a *LabRamHR (Horiba)* in the range of 100 cm^{-1} to 1000 cm^{-1} with a spectral resolution of 1 cm^{-1}. A 100 mW laser with a wavelength of $\lambda = 532$ nm was used. To circumvent saturation of the detector a filter was employed to attenuate the laser to 1 % to 20 % of its full power depending on the sample. The laser was focused onto the sample with a 50x objective while the detector was a CCD sensor. Spectra were generally measured with an accumulation time of 3 s while the spectra were averaged over 50 scans. Measurements were carried out with the equipment of the Electrochemical Energy Technology group in the Institute of Engineering Thermodynamics of the German Aerospace Center (Deutsches Zentrum für Luft und Raumfahrt e.V.) (DLR).

7.8. Diffuse Reflectance Infrared Fourier Transform Spectroscopy

DRIFTS measurements were carried out using a *Nicolet iS50 (ThermoFisher)* FT-IR spectrometer equipped with a *praying mantis (Harrick)* accessory employing a liquid nitrogen cooled $Mg_{1-x}Cd_xTe$ detector with a spectral resolution of 4 cm^{-1} and accumulation of 64 scans. Before the sample measurement a background was recorded with KBr, degassed at 300 °C under constant nitrogen flow of 15 ml.

Reduction Experiments

Before the measurement the samples are degassed at 300 °C for 3 h in 15 ml min^{-1} nitrogen. Subsequently, the sample is cooled down to 100 °C in nitrogen before measuring a spectrum. Then the gas is changed to 10 vol. % H_2 in N_2 and the sample is equilibrated for 1 h before a spectrum is measured. Subsequently the sample is heated to 200 °C, 300 °C, 400 °C and 500 °C equilibrating the sample for 1 h at each temperature before measuring a spectrum. Afterwards the sample is cooled down to 100 °C before taking the final spectrum. The experiment is repeated in a flow of 15 ml min^{-1} of dry N_2 to investigate the hydrogen desorption behavior.

CO Adsorption Measurements

Samples are degassed at 300 °C for 3 h in a flow of 15 ml min^{-1} dry nitrogen. After cooling down the sample to 25 °C a spectrum is measured. The gas is changed to 10 vol. % of CO in N_2 purging the sample for 1 h before measuring a second spectrum. Changing the gas to N_2 the sample is subsequently purged for 1 h to remove CO from the DRIFTS cell so only adsorbed CO is visible in the spectrum.

In a second step the same sample is reduced in a flow of 15 ml min^{-1} of 5 % H_2 in N_2 at 300 °C for 3 h. The sample is cooled down to 25 °C before changing the gas to N_2 before a spectrum is measured after 1 h of purging. The sample is subsequently loaded with CO in the same way as the first CO loading. Then CO is again purged from the DRIFTS cell as previously described before measuring the last spectrum.

Spectra are reported as differences between the spectrum after degassing and after CO loading and N_2 purging. In order to remove any metal carbonyls formed in the gas cyliner, a dry ice cool trap was employed between the mass flow controller (MFC) and the sample cell.

7.9. X-ray Absorption Spectroscopy

XAS measurements were conducted at the KMC-3 beamline at *Berliner Elektronenspeicherring-Gesellschaft für Synchrotronstrahlung m.b.H.* in three separate measurement sessions (10.2022, 01.2023 and 03.2023) by Michael Haumann of the Physics Department of the FU Berlin in collaboration with Bruna Lobo from the University of Bayreuth. Aside from the samples, Pt foil and PtO_2 were measured as standards. Data analysis was also done by Michael Haumann.

7.10. X-ray Photoelectron Spectroscopy

XPS can give important insights into the oxidation state of different elements, which are of outstanding importance in catalysis. X-ray photoelectron spectra were recorded in a high vacuum system with a base pressure of 2×10^{-13} bar in an *ESCALAB Xi+(FEI/ThermoFisher Scientific)* using a monochromated Al Kα source with an excitation energy of 1486.74 eV using a hemispherical analyzer. Using an ion-etched silver surface the energy axis of the instrument was calibrated and adjusted. Due to the insulating nature of the samples, charge compensation was done by means of a low energy Ar plasma.

Of each sample a survey spectrum was collected before collecting high resolution spectra for the elements of interest. The measurement parameters for each element are listed in table 9.

Table 9: Measurement parameters of measured X-ray photoelectron spectra

Type	Measurement range		Scans	Dwell time	Step	Pass Energy
	max / eV	min / eV	-	/ ms	/ eV	/ eV
survey	1350	0	5	50	0.50	100
Ce3d	965	850	30	100	0.10	30
O1s	575	500	30	100	0.10	30
C1s	310	270	30	100	0.10	30
Pt4f	84	60	1000	100	0.10	30

The spectra were fitted using CasaXPS. A U2 Tougaard background was employed to describe the contribution of the secondary electrons to the measured spectrum. Peaks were described as convoluted *Lorentzian* and *Gaussian* peak functions. The photoelectron spectra of mixed valent cerium consists of five doublet peaks. This makes the mathematical description in a physical meaningful way very challenging. According to literature, a linear combination approach was employed using the spectra of a Ce^{IV} standard, CeO_2-LSA (STREM, 99.995 %), as well as a self synthesized Ce^{III} standard, a $CeAlO_3$ perovskite.

Preparation of the Ce^{III} standard $CeAlO_3$

For the preparation of $CeAlO_3$, commercial CeO_2 (99.9 %) and Al_2O_3 (Baikowski Baikalox CR30F) were mixed in ethanol using a ball mill with ZrO_2 grinding balls. Afterwards, the mixture was dried overnight, before it was pressed into discs of 16 mm diameter. Successively they were sintered in dry hydrogen. After a purging time of 30 min, the sample was heated to 800 °C with a heating ramp of 5 K min^{-1}, before lowering the heating rate to 2 K min^{-1} to 1450 °C at which the sample was held for 2 h before cooling down to 20 °C with a cooling rate of 10 K min^{-1}.[238]

The preparation was done at the IMTCCC with Frank Kern. After preparation the standard was analyzed using XRD and XPS.

7.11. Temperature Programmed Methods

TPR measurements are frequently employed to assess the reducibility of redox active catalysts. These measurements were carried out using an *Autosorb iQ-c (Quantachrome Instruments)*. Prior to TPR measurements the samples were pressed, crushed and sieved to a particle size fraction of 200 µm to 500 µm to limit the pressure drop during measurement. All samples were degassed at 450 °C in 30 ml min^{-1} of 10 % O_2 in He for one hour before cooling down in 30 ml min^{-1} helium to the desired starting temperature.

7.11.1. Measurement of TPR Profiles

After the degassing procedure samples were heated from 50 °C with a heating rate of 10 K min^{-1} in 10 % H_2 / N_2 to 1000 °C. The hydrogen consumption was measured using a thermal conductivity detector (TCD) while the water formed during reduction was condensed from the effluent gas stream using a dry ice/acetone cold trap in front of the detector.

The TCD signal was calibrated by measuring different amounts of a copper(II) oxide standard. Since the inbuilt temperature measurement showed large deviations due to sensor aging, a separate thermocouple was added to the outside of the sample cell at the sample position. The values measured by the additional thermocouple were used to correct the temperature values given by the instrument.

7.11.2. Total Oxygen Storage Capacity (TOSC) Measurements

The total oxygen storage capacity $(\mathrm{TOSC})_\mathrm{T}$ is an important value for ceria materials as it represents the amount of reversibly releasable oxygen. TOSC values were measured by means of O_2 pulse chemisorption because it was observed that oxygen is mainly consumed rather than only adsorbed.[234] After degassing the samples were heated to the desired analysis temperature T at which the TOSC should be analyzed with a heating ramp of 10 K min^{-1} in a flow of 30 ml min^{-1} of 10 % H_2 in N_2. After reaching the desired analysis temperature the sample was held at this temperature for 1 h to ensure complete reduction. Afterwards, the cell was purged with 30 ml min^{-1} of helium for 1 h before injecting $V_\mathrm{SL} = (66 \pm 1)$ µl of pure oxygen 16 times every five minutes using a sample loop. The amount of injected oxygen $n_{\mathrm{O_2,inj}}$ was calculated with eq. (36) assuming ideal gas conditions.

$$n_{\mathrm{O_2,inj}} = \frac{p_{\mathrm{SL}} V_{\mathrm{SL}}}{\mathrm{R} T_{\mathrm{SL}}} \tag{36}$$

with p_{SL} being the pressure in the sample loop, R being the universal gas constant and T_{SL} the temperature at the sample loop.

Oxygen flow through the sample loop was chosen in a way to limit pressure buildup in the sample loop ($\dot{V}_{\mathrm{O_2,SL}} \approx 5\,\mathrm{ml\,min^{-1}}$) because ambient pressure was assumed in the sample loop for the calculations ($p_{\mathrm{SL}} = 1.013\,\mathrm{bar}$) while the temperature at the sample loop T_{SL} was measured every second using a thermocouple.

The injected amount of oxygen was subsequently used to calculate the TOSC_T value according to eq. (37)

$$TOSC_T = \frac{\sum_0^{16} \left(n_{\mathrm{O_2,inj}} - n_{\mathrm{O_2,det}} \right)}{m_{\mathrm{cat}}} \tag{37}$$

where $n_{\mathrm{O_2,det}}$ is the detected amount of unreacted oxygen, quantified using an one point calibration with the area of the injections where total oxygen breakthrough occurred, i.e. the sample was totally reoxidized.

7.11.3. CO_2 Desorption Experiments

The basicity of an oxidic surface can be probed by means of CO_2 desorption experiments. These are especially relevant for CO oxidation, since the reaction can be limited by product desorption.

To assess the CO_2 desorption characteristics, the samples were cooled down after degassing to 50 °C before adsorbing CO_2 on the sample by flowing $30\,\mathrm{ml\,min^{-1}}$ of pure CO_2 (99.996 %, Westfalen AG) over the sample for an hour. Afterwards an isothermal desorption step was carried out for an hour in $30\,\mathrm{ml\,min^{-1}}$ of He. Using a TCD the CO_2 desorption was followed whilst applying a heating ramp of $10\,\mathrm{K\,min^{-1}}$ to 1000 °C.

The TCD signal was calibrated using a sample cell equipped with a septum, through which defined amounts of pure CO_2 were injected into a stream of $30\,\mathrm{ml\,min^{-1}}$ with an analytical syringe. The resulting detector signal is plotted as a function of the injected amount of CO_2, $n_{\mathrm{CO_2}}$, yielding the calibration curve that is shown in figure 53 in the appendix.

7.12. Catalyst Testing

Kinetic investigations were carried out in a home-built apparatus. The flowchart of which is shown in figure 5.

Nitrogen (*Westfalen AG*, 99.999 %), oxygen (*Westfalen AG*, 99.999 %) and 10 % carbon monoxide in nitrogen (*Westfalen AG*, 99.997 %, 99.999 %) were used without purification. It was also possible to feed water through a saturator (*S01*) or an evaporator (*E01*), respectively. Flow rates of the permanent gases were controlled by MFCs of the type *EL-Flow prestige (Bronkhorst)*. Variations of residence time as well as changes in partial pressure were done by altering the flow rates of the reactants. The reactor was a stainless steel tube of 3/8” OD placed in a heating block heated by two 400 W heating cartridges. The pressed, crushed and sieved catalyst (100 µm to 200 µm) was diluted with 2 g of commercial acid washed silicon oxide spheres (150 µm to 212 µm). On a stainless steel mesh, a piece of quartz wool and 1.5 g of acid washed glass beads (212 µm to 300 µm), the diluted catalyst bed was filled and densified through tapping the reactor on the bench for approximately one minute. Afterwards 1 g of acid washed glass beads (212 µm to 300 µm) were packed above the diluted catalyst bed to ensure a homogeneous flow regime and to preheat the gas mixture and minimize temperature changes across the catalyst bed. The catalyst bed was secured in place by another plug of quartz wool on top. A thermocouple was placed in the first third of the diluted catalyst layer to obtain the catalyst temperature. The packed reactor was subsequently placed into the heating block and connected to the setup for catalytic experiments. The reactor could be switched into bypass operation mode using a 4-way valve (*4WV02*).

Pressure during experiments was measured by means of a pressure sensor upstream and downstream of the reactor. The whole system has to be heated to omit condensation of water. The pressure at the reactor inlet was controlled by a MFC connected to nitrogen whose flow is added downstream of the reactor in front of a needle valve. By adjusting its flow rate automatically with a control loop in the control software the overall pressure before the reactor is set to be 1.05 bar.

Product analysis was carried out using a gas chromatograph (GC)-mass spectrometer (MS) (*7850B-7977B (Agilent)*). A customized column switching system (s. appendix, figure 59) provided by *Teckso* was used to separate the gases. Pre columns were used to separate the permanent gases from higher boiling compounds (i.e. water) before separating CO and CO_2 from the other permanent gases. Afterwards the remaining permanent gases (H_2, O_2 and N_2) were separated using a molecular sieve column. CO and CO_2 were passed around the molecular sieve column to avoid damaging the column. Afterwards the gases

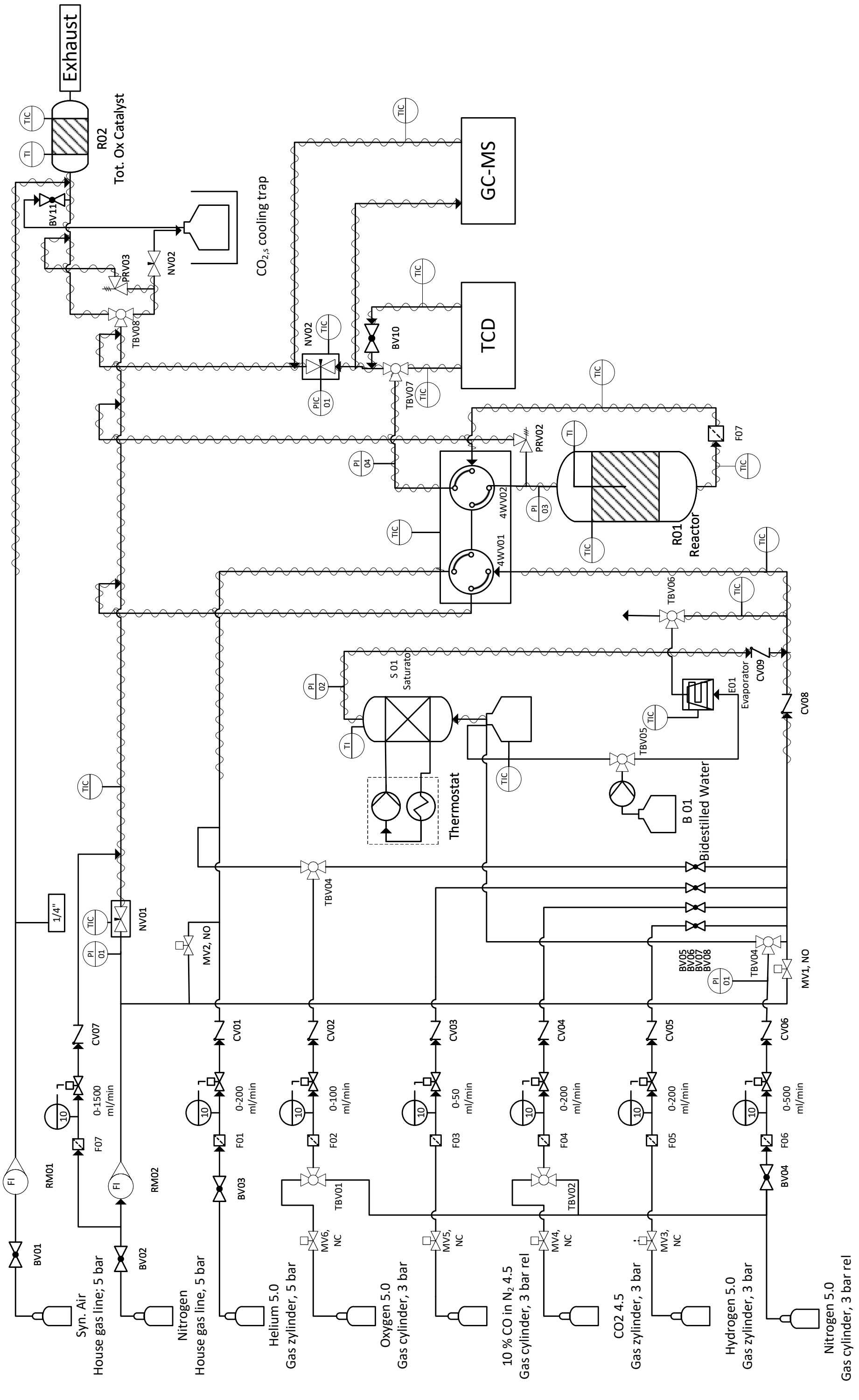

Figure 5: Flow chart of experimental setup used for catalyst testing

Table 10: Retention times t_R for each component and detector in the used GC-MS system, an exemplary chromatogram is shown in figure 60.

Compound	TCD/FID t_R / min	MS t_R / min
CO	12.4	6.5
CO_2	5.8	8.0
H_2O	-	13.5
N_2	8.8	6.5
O_2	6.5	6.6

passed through the TCD for detection. The non-destructive nature of a TCD enables the subsequent use of a methanizer to convert CO and CO_2 to methane before detecting them in the downstream flame ionization detector (FID). This enables a more accurate detection of CO and CO_2 at low concentrations. Higher boiling compounds were separated using a capillary column before detection by MS. The retention times of each compound are shown in table 10.

The GC-MS system was calibrated over the course of the work when the measured concentration of a 10 % CO in N_2 mixture did deviate from the value given by the supplier. A typical calibration and derived calibration factors are shown in the appendix in figure 61.

After detection the reaction gases are diluted using nitrogen supplied by a rotameter (*RM01*, $\dot{V}_{\mathrm{RM01,N_2}} \approx 1\,\mathrm{l\,min^{-1}}$) before adding syn air to the gas mixture (*RM02*, $\dot{V}_{\mathrm{RM02},syn.air} \approx 0.6\,\mathrm{l\,min^{-1}}$) and passing it over a total oxidation catalysts to oxidize any CO being still in the gas feed.

7.12.1. Light-Off Measurements

Light-off measurements were carried out to assess the activity as a function of temperature. In a typical experiment 100 mg of catalyst is introduced into the reactor as described before. The total flow rate was fixed to 50 ml min^{-1} during experiment, corresponding to a modified residence time τ_{mod} of $\tau_{\mathrm{mod}} = 120\,\mathrm{kg\,s\,m^{-3}}$.

Before the experiments the catalysts were degassed in 20 % of O_2 in N_2. The temperature was ramped within an hour to 300 °C where the catalyst was held for 3 h before cooling down to 50 °C for platinum containing materials and 150 °C for platinum free catalysts.

Afterwards the gas was switched to a feed consisting of 5000 ppm CO and 10 % O_2 in nitrogen. When assessing the influence of water, 10 % of H_2O was additionally added via the saturator. After equilibration of the sample for 5 h the temperature was ramped with a heating rate of 0.5 K min^{-1} for platinum-containing and 1 K min^{-1} for pure ceria materials to 400 °C, which was again held for 1 h. During the experiment the gas phase composition was analyzed continuously using the GC-MS. Starting concentrations were measured after each experiment by bypass measurements. For that purpose, the reactor was switched to bypass operation mode before measuring the concentration five times. The obtained mean value for each compound i was used as the initial molar fraction $x_{\mathrm{i,0}}$ for data analysis described in chapter 7.12.4.

7.12.2. Kinetic Measurements

The investigation of the temperature dependency of the intrinsic reaction rate was carried out under differential operating conditions by keeping the conversion below $X < 0.15$. The total flow rate for the experiments was fixed to 100 ml min^{-1}. For unloaded ceria materials 10 mg of sample was weighed into the reactor as described before, giving a modified residence time τ_{mod} of $\tau_{\mathrm{mod}} = 6\,\mathrm{kg\,s\,m^{-3}}$. For platinum-containing samples the sample mass was adjusted in a way so the platinum related modified residence time of $\tau_{\mathrm{Pt,mod}} = 0.0032\,\mathrm{kg\,s\,m^{-3}}$ was held constant. Before measurements, as for the light off experiments described in section 7.12.1, the sample was degassed. Afterwards the sample was cooled down to the highest analysis temperature before switching to the reaction gas (5000 ppm CO, 10 % O_2 in N_2 (dry) or 5000 ppm CO, 10 % O_2 and 10 % H_2O in N_2 (wet)). The catalyst was equilibrated for 12 h before analysis was started. Subsequently each temperature was held for 5 h before lowering the temperature by 10 K. For analysis the last five measurements at each temperature were averaged. As for the light-off experiments bypass measurements were carried out to determine $x_{\mathrm{i,0}}$ for data analysis.

7.12.3. Kinetic Measurements with Change in Partial Pressures

Assessing the influence of catalyst properties on the reaction orders is of great importance. Experiments were carried out to investigate the reaction orders regarding CO and O_2. For this purpose, as described in section 7.12.2, 10 mg of catalyst were packed into the reactor. After degassing, the sample was cooled down to the reaction temperature before switching to the feed mixtures and equilibrating the catalyst for 12 h in the first feed mixture. The concentration of reactants was altered for CO from 0.1 % to 2 % and for oxygen from 1 % to 15 %. Each composition was measured for 3 h before switching. If partial pressure dependencies were analyzed for different temperatures the temperature was ramped to the next temperature, which was held for 5 h to ensure the catalyst reached steady state again before returning to the previously described measurement protocol.

After the measurements the concentrations were determined using bypass measurements. These were carried out for the maximum and minimum molar fractions of each reactant while the other molar fractions $x_{i,0}$ were interpolated from these measurements.

7.12.4. Data Analysis

Using the CO molar fractions measured during the catalytic measurements $x_{i,t}$ and the initial value $x_{i,0}$ obtained by bypass measurements as described in ch. 7.12.1, 7.12.2 and 7.12.3, the conversion was calculated according to eq. (38)

$$X_{\mathrm{CO}} = \frac{x_{\mathrm{CO},0} - x_{\mathrm{CO},t}}{x_{\mathrm{CO},0}}. \tag{38}$$

The degassed mass of catalyst $m_{\mathrm{cat,degas}}$ was calculated using the relative remaining mass w_{degas} obtained by TGA measurements described in section 7.6 and the weighed in hydrated sample mass $m_{\mathrm{cat,hyd}}$ according to equation (39)

$$m_{\mathrm{cat,degas}} = m_{\mathrm{cat,hyd}} \cdot w_{\mathrm{degas}}. \tag{39}$$

The degassed sample mass was used to calculate the mass specific reaction rate r_{m} with the molar inlet flow rate of CO $\dot{n}_{\mathrm{CO},0}$ following equation (40)

$$r_{\mathrm{m}} = \frac{X_{\mathrm{CO}}\ \dot{n}_{\mathrm{CO},0}}{m_{\mathrm{cat,degas}}}. \tag{40}$$

From the mass specific reaction rates r_{m} surface-specific reaction rates r_{A} and site-specific reaction rates (turnover frequencys (TOFs)) were calculated according to equation (41) and (42)

$$r_{\mathrm{A}} = r_{\mathrm{m}} \cdot \frac{1}{S_{\mathrm{BET}}}, \tag{41}$$

$$TOF = r_{\mathrm{m}} \cdot \frac{1}{S_{\mathrm{BET}}} \cdot \frac{1}{SD_{\mathrm{A}}}. \tag{42}$$

with S_{BET} being the BET surface area and SD_{A} the area specific site density. Since reduction of ceria at temperatures investigated in this work is mostly limited to the outer surface, the measured $TOSC_{500\,^{\circ}\mathrm{C}}$ can be used as a mass specific site density SD_{m}. Since $TOSC_{500\,^{\circ}\mathrm{C}}$ is given as $\mathrm{mol_{O_2}g^{-1}}$, the value has to be multiplied by two. Thus, the site-specific turnover rates for unloaded ceria materials was calculated using the measured $TOSC_{500\,^{\circ}\mathrm{C}}$ values following eq. (43)

$$TOF = r_{\mathrm{m}} \cdot \frac{1}{2 \cdot TOSC_{500\,^{\circ}\mathrm{C}}}. \tag{43}$$

Part V.

Results and Discussion

8. Preparation of Ceria-Based Catalysts

As discussed in chapter 2.3, ceria materials can be prepared via different routes. In this work, precipitation was used to prepare ceria materials exhibiting different properties. Method validation in this work was carried out using two different commercial ceria samples. A high surface area sample CeO_2-high surface area (HSA) kindly provided by *Solvay* and a low surface area sample CeO_2-low surface area (LSA) purchased from *STREM* were measured as reference to compare the prepared materials to these samples.

As described in chapter 2 ceria crystallizes in the cubic CaF_2 structure. With a lattice parameter of $a_{CeO_2} = 0.5411\,\mathrm{nm}$, the resulting diffractogram can be calculated and is shown in figure 6 alongside the measured diffractograms for CeO_2-HSA and CeO_2-LSA.

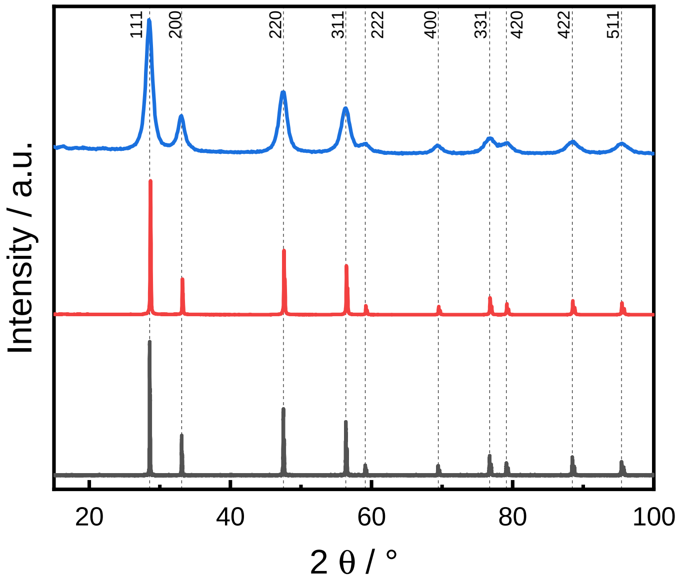

Figure 6: Diffractograms of CeO_2-HSA (——), CeO_2-LSA (——) and simulated diffractogram of ceria (——)

Figure 6 shows that the purchased ceria materials all exhibited the same cubic crystal structure. This crystal structure was also observed for every material prepared in this work. Reflection positions were very comparable, but small changes in the lattice parameter were observed. Comparing the diffractograms of the commercial CeO_2-HSA and LSA samples a difference in line shape is evident. Whereas the reflections of the LSA sample are sharp, line broadening can be observed for the HSA sample. This is caused by an non-infinite size of crystallites, leading to destructive interference not occuring anymore around the *Bragg* angle. The smaller the crystallites are, the more pronounced this phenomenon becomes and the broader the reflections in the powder X-ray diffraction (PXRD) appear. This phenomenon was first investigated and described by Scherrer who postulated the so called *Scherrer*-equation,[235] which is still used today to approximate domain sizes from PXRD.[236] During domain size analysis using the *Scherrer* equation line broadening caused by crystallite strain as well as by the instrument contribution are superimposed, which leads to an underestimation of the domain size if these are not accounted for.[237] For that reason *Rietveld* refinement with *GSAS-II*[233] was conducted to determine the samples crystallite size D and strain ϵ.

As described in chapter 3.1 the catalytic properties of ceria are linked to the redox cycle between Ce^{IV} and Ce^{III}. Therefore, the amount of Ce^{III}, stemming from lattice defects, in the fully oxidized, i.e. as-prepared, state is often used to derive structure-property relationships. The X-ray photoelectron (XP) Ce3d spectra of ceria, however, is characterized by three doublet peaks associated with Ce^{IV} and two doublets associated with Ce^{III}. Different approaches are described in literature to obtain a meaningful fit of the Ce3d region.[238,239] Aside from using literature values for line shape and peak position, the preparation of Ce^{III} standards can be used to quantify the contributions of Ce^{III} to the Ce3d spectra and thus to reduce the degree of freedom in the fit.[238] For this purpose, as Ce^{III} oxide is usually highly air sensitive, a $CeAlO_3$ reference compound in which cerium is stabilized in the Ce^{III} state was prepared as described in chapter 7.10. The resulting diffractogram and XP spectrum are shown in figure 7.

The synthesized $CeAlO_3$ shows the diffraction pattern of the *I4/mcm* space group, which is reported for the desired cerium aluminate perovskite.[238] Most importantly no reflections associated with the precursor CeO_2 are visible anymore. Looking at the XP spectrum, the obtained *Ce3d* spectrum can be described with two doublets, corresponding to the v_0 and u_0 as well as v' and u' components.[238,239] Thus, only Ce^{III} is present on the surface of the prepared $CeAlO_3$, showing that the preparation was successful, enabling the use as a line shape standard for other *Ce3d* spectra.

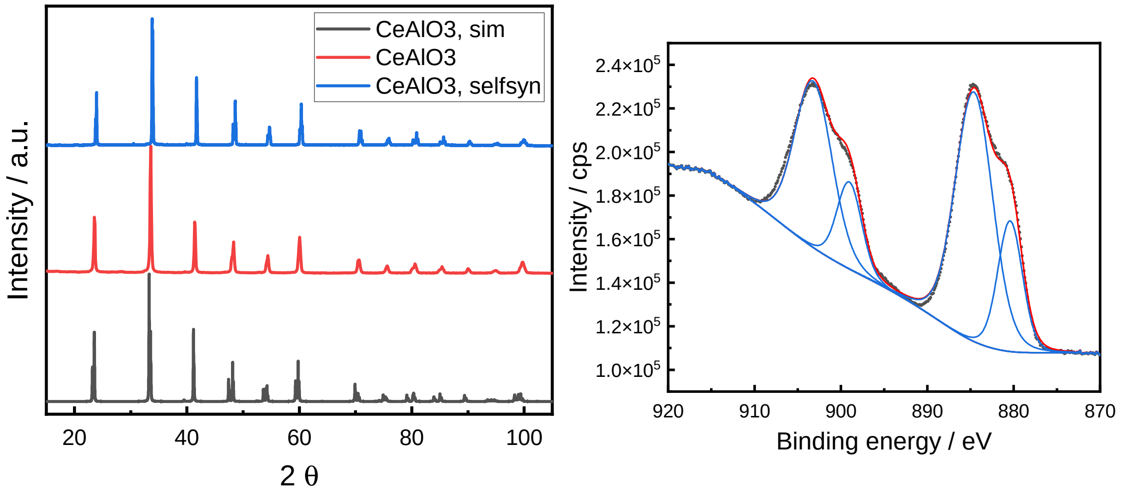

Figure 7: Simulated (——) and measured XRD pattern of self-synthesized (——) and commercial reference (——) $CeAlO_3$ (left) and Ce3d X-ray photoelectron spectra of self-synthesized $CeAlO_3$ with fit (right)

8.1. Influence of Precipitation Conditions on Ceria Material Properties

Metal oxide catalysts can be prepared via a plethora of routes, however, as discussed in chapter 2.4, precipitation is widely used due to its simplicity. Although carrying out precipitation processes is rather straight forward, the role of preparation parameters on the final precipitate is difficult to predict and has to be investigated for every system separately, as noted by Schüth et al..[121]

Using the temperature-calibrated stirred tank reactor with a calibrated piston pump (*c.f.* appendix chapter A), materials were prepared at different precipitation temperatures via ammonia-based precipitation (AP) as described in chapter 6.1, while keeping every parameter constant but the precipitation temperature T_{prec}. Ceria materials were also prepared using UP and HUP methods as described in sec 6.1.2 and 6.1.3. After preparation the materials were analyzed using N_2 physisorption, XRD coupled with *Rietveld* refinement and *Raman* spectroscopy.

The measured X-ray diffractograms of the samples prepared at different precipitation temperatures T_{prec} and their related *Rietveld* refinement fit are shown in figure 8.

All materials prepared showed the diffraction pattern of the cubic crystal structure expected for ceria samples. Qualitatively it could be observed, that with increasing precipitation temperature T_{prec} reflections became broadened and less intense for materials prepared using AP. Comparing the diffractograms of the UP and HUP sample, no qualitative difference was

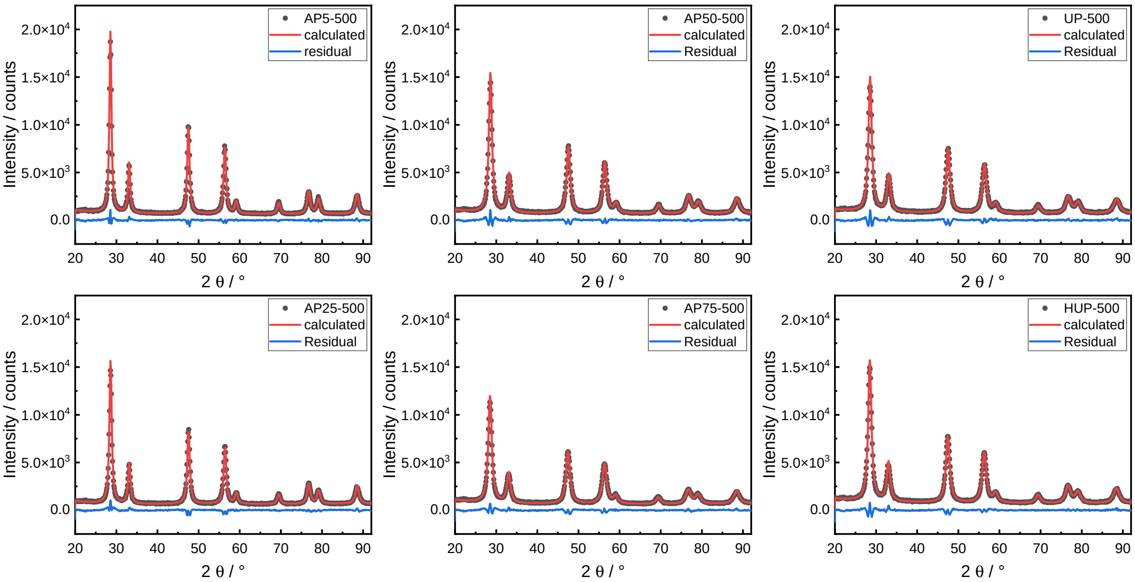

Figure 8: Measured X-ray diffractograms (●) and associated calculated diffraction pattern (——) and residuals (——) from *Rietveld* refinement for materials calcined at $T_{\mathrm{calc}} = 500\,°\mathrm{C}$, results of the structural refinement are listed in table 11.

observed. To quantify these differences, *Rietveld* refinement calculations were carried out using the $Fm\bar{3}m$ space group. The calculated diffraction patterns and the calculated residual are also plotted in figure 8, while the analysis results are summarized in table 11.

It can be observed that materials calcined at 500 °C show a slightly increased lattice parameter compared to the theoretical lattice value. This behavior is frequently observed in literature and suggested to be linked to the destabilizing effect of small crystallites and resulting higher concentration of defects.[119] Small crystallites are indeed present, since crystallite sizes D extracted during refinement range between 10 nm to 18 nm for materials calcined at 500 °C. Comparing crystallite sizes and BET surface areas extracted from N_2 physisorption experiments and listed in table 11 as a function of precipitation temperature yields figure 9.

From the plot in figure 9, a trend for the crystallite size as well as BET surface area S_{BET} can be observed with increasing precipitation temperature T_{prec}: the crystallite size decreases while the BET surface area increases with increasing precipitation temperature T_{prec}. This is in contrast to findings by Chen and Chang as well as Cui et al. who reported an increase in crystallite size D with increasing precipitation temperature.[97,98] Comparing the preparation approach with their work, the most prominent difference is the different cerium precursor. In this work $(NH_4)_2Ce(NO_3)_6$ was employed, whereas in the other two studies $Ce(NO_3)_3$ was used. Thus, this difference might be explained by the difference between a Ce^{III} and Ce^{IV} precursor. Literature reports that when precipitating Ce^{III} precursors a preceding

Table 11: Analysis Results of *Rietveld* Refinement of XRD patterns [a], N_2 physisorption experiments[b] and *Raman* spectra[c] for materials prepared at different precipitation and calcination temperature

Sample	T_{prec} / °C	T_{calc} / °C	a^a / nm	D^a / nm	ϵ^a / -	S^b_{BET} / $\text{m}^2\,\text{g}^{-1}$	$(I_{600}/I_{564})^c$ / -
AP5-500	5	500	0.54115(3)	18.07(3)	0.004(1)	26	0.0022
AP25-500	25	500	0.54118(5)	14.6(3)	0.0002(1)	37	0.0026
AP50-500	50	500	0.54114(6)	12.0(2)	0.008(1)	80	0.0051
AP75-500	75	500	0.54121(7)	10.3(2)	0.006(1)	90	0.0057
AP5-700	5	700	0.54104(1)	80(2)	0.002(1)	3	n.m.
AP25-700	25	700	0.54106(2)	73.3(2)	0.002(1)	3	n.m.
AP50-700	50	700	0.54102(2)	46.8(9)	0.002(1)	3	n.m.
AP75-700	75	700	0.54106(2)	34.3(6)	0.002(1)	3	n.m.
UP-500	100	500	0.54128(7)	11.3(3)	0.009(1)	107	0.0070
UP-700	100	700	0.54107(3)	23.7(4)	0.003(1)	39	n.m.
HUP-500	140	500	0.54127(6)	11.5(2)	0.009(1)	110	0.0065
HUP-700	140	700	0.54104(3)	24.1(4)	0.004(1)	39	n.m.

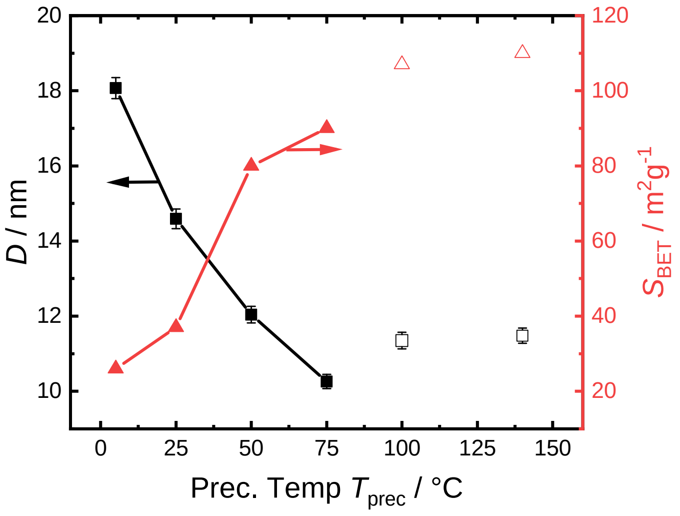

Figure 9: Crystallite size D (■) and BET surface area S_{BET} (▲) as a function of the precipitation temperature T_{prec} (solid) and UP and HUP reference materials (hollow) all calcined at $T_{\text{calc}} = 500\,°\text{C}$

oxidation step occurs before nucleation (1) and precipitation (2)[99] schematized below.

$$\mathrm{Ce^{III}}_{(aq)} \xrightleftharpoons[-\,e^-]{+\,e^-} \mathrm{Ce^{IV}}_{(aq)} \xrightleftharpoons{\;1\;} \mathrm{Ce^{IV}O_x(OH)_y}\ \text{nuclei} \xrightarrow{\;2\;} \mathrm{Ce^{IV}O_x(OH)_{y(s)}}$$

In chapter 2.3.1 it was discussed that the formation rate of nuclei, the nucleation rate, is a function of the supersaturation. In the case of precipitation of $\mathrm{Ce^{III}}$ precursors, the supersaturation is controlled by the preceding oxidation equilibrium before the nucleation step. Therefore, in the case of $\mathrm{Ce^{III}}$ precipitation the nucleation rate is probably lowered and the supersaturation is decreased because of the preceding oxidation step. This would then mean that the particle size is most likely controlled by crystal growth rather than nucleation. After the first particles are formed, nucleation is thermodynamically less favorable compared to crystal growth. This effect gets even more pronounced when surface catalytic oxidation of $\mathrm{Ce^{III}}$ species on the surface of particles occurs as some nucleation and growth models suggest.[93] Altogether the preceding oxidation equilibrium would lead to an increase in crystallite size with increasing precipitation temperature. In the case of $\mathrm{Ce^{IV}}$ precursors however, nucleation is not hindered and can proceed in a burst like fashion leading to a nucleation rate controlled crystallite size and thus a decrease in crystallite size with increasing precipitation temperature. This hypothesis is also supported by research on the precipitation of ceria-zirconia mixed oxides. Letichevsky et al. found that usage of $\mathrm{Ce^{III}}$ precursors does not lead to formation of homogeneous ceria-zirconia solid solutions.[120] Considering the aforementioned argument that the oxidation equilibrium hinders nucleation, it would be possible that first zirconia rich crystallites are precipitated before cerium-rich crystallites are formed. This could explain why the authors observed a zirconium-rich and a cerium-rich phase in PXRD possible pointing to core-shell-type precipitate. The same was observed for the UP method of preparation of $\mathrm{CeZrO_4}$ by which it was not possible to obtain phase homogeneity when using $\mathrm{Ce^{III}}$ precursors, whereas it was when using $\mathrm{Ce^{IV}}$.[129,130] Hirano and Kato also looked into the difference between precipitating $\mathrm{Ce^{III}}$ and $\mathrm{Ce^{IV}}$ precursors. In their study they found that hydrothermal treatment did not have a significant influence on the properties of the materials precipitated from $\mathrm{Ce^{III}}$ solution, whereas it had a distinct influence when precipitating from a $\mathrm{Ce^{IV}}$ solution, relining the possibility of faster crystal growth compared to the nucleation rate when using $\mathrm{Ce^{III}}$ precursors.[107]

High temperature calcination is frequently reported to decrease the BET surface area significantly while at the same time increasing the crystallite size. This process is often linked to the *Hüttig* temperature, leading to severe surface area loss above the *Hüttig* temperature which amounts to $T_{\text{Hüttig}} \approx 590\,°\mathrm{C}$ for ceria (*c.f.* chapter 2.4). To probe the sinter stability of the samples, they were also calcined at $T_{\text{calc}} \approx 700\,°\mathrm{C}$ as described in chapter 6.1. After calcination the samples were analyzed. The measured X-ray diffraction

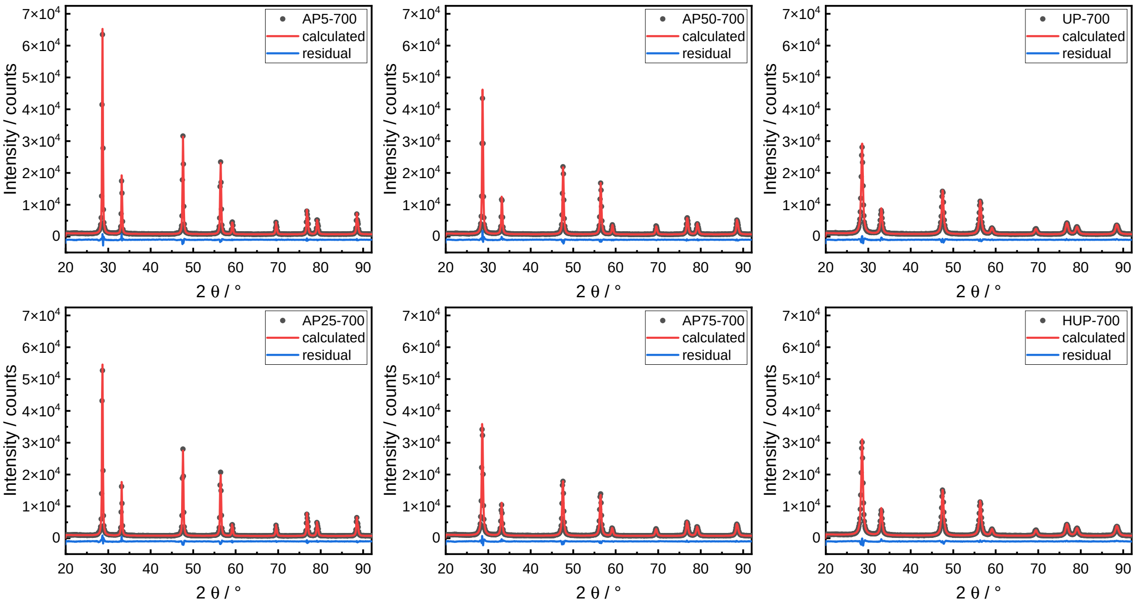

Figure 10: Measured X-ray diffractograms (●) and associated calculated diffraction pattern (——) and residuals (——) from *Rietveld* refinement for materials calcined at $T_{\text{calc}} = 700\,°\text{C}$, results of the structural refinement are listed in table 11.

patterns together with the calculated pattern and residual from the refinements are shown in figure 10.

Comparing the diffractograms shown in figure 8 and 10, it is evident that for all cases the line broadening did decrease when increasing the calcination temperature, caused by increased crystallite sizes due to sintering. This aligns well with the aforementioned steep increase in crystallite size when increasing calcination temperature above the *Hüttig* temperature. Comparing the BET surface areas after calcination one can also observe a significant decrease there, which again suggests an increase in crystallite size. The results of the refinements of the diffraction patterns corroborate the qualitative expectation of the formation of larger crystallites upon calcination above the *Hüttig* temperature.

Not only are the crystallites larger, but their lattices are also contracted compared to the sample calcined at 500 °C. The phenomenon is often observed when increasing calcination temperature.[240] Also the strain ϵ derived from the diffraction pattern did decrease through high temperature calcination. As the values are small and therefore the relative errors are large, results from *Raman* spectroscopy are used further. In order to evaluate the influence of precipitation temperature on sinter stability of the materials, the increase in crystallite size when increasing calcination temperature from 500 °C to 700 °C $\Delta D_{700\,°\text{C}-500\,°\text{C}}$ is plotted as a function of the precipitation temperature in fig.11.

It is evident that materials precipitated at higher temperatures using AP tend to retain

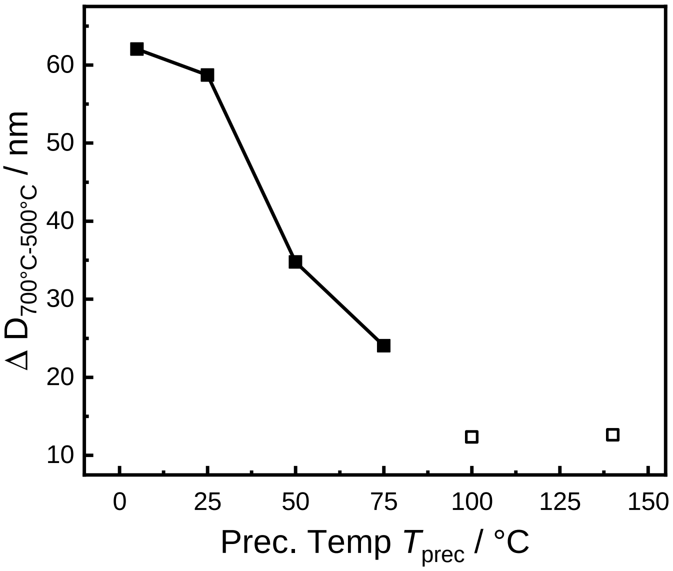

Figure 11: Difference in crystallite size after calcination at $T_{\text{calc}} = 700\,°\text{C}$ compared to calcination at $T_{\text{calc}} = 500\,°\text{C}$ $\Delta D_{700\,°\text{C}-500\,°\text{C}}$ as a function of precipitation temperature of AP materials (■) and UP and HUP reference materials (□)

smaller crystallite sizes after increasing the calcination temperature. The highest stability was obtained for the materials prepared via urea-based techniques, UP and HUP. These methods are known to yield more homogeneous precipitates. The higher the homogeneity the lower the thermodynamic driving force towards sintering via *Ostwald ripening*.[241]

Although PXRD is a powerful tool in analyzing ceria compounds the diffraction pattern is mostly dominated by the position of cerium ions because of their high atomic mass compared to the oxygen ions in the lattice. Thus, the X-ray diffraction patterns contain little information about the oxygen sublattice. For that reason *Raman* spectroscopy is often used as a complementary method in analyzing cerium-based materials because it is highly sensitive to changes in the oxygen sublattice through changes in the oxygen breathing mode.[178,242,243] Therefore *Raman* spectra were collected after calcination to investigate how the precipitation conditions influence the oxygen sublattice as this was correlated to activity in previous studies.[197,244] Normalized *Raman* spectra are shown in 12.

The measured *Raman* spectra are characterized by the strong F_{2g} mode, at $\nu_{\text{F2g}} = 464\,\text{cm}^{-1}$ which can be considered the oxygen breathing mode, usually observed for cubic ceria materials.[242] It can be seen, when juxtaposing the spectra of materials calcined at 500 °C and 700 °C, that this mode is narrower for the high temperature calcined materials. This is caused by an increase in crystallite size.[245,246] Additionally, in the material calcined at 500 °C a *Raman* active band can be observed around 600 cm^{-1}. This band is ascribed in literature to oxygen vacancy defects in the oxygen sublattice enabling the otherwise inactive

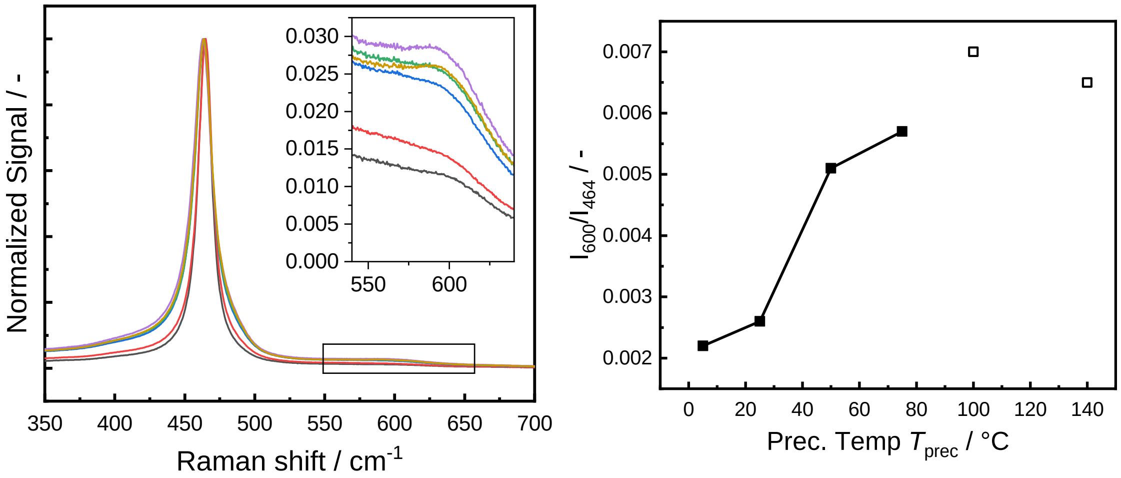

Figure 12: Raman spectra of precipitated samples AP5-500 (——), AP25-500 (——), AP50-500 (——), AP75-500 (——) and UP-500 (——) as well as HUP-500 (——) (left) and extracted peak intensity ratios between I_{600} and I_{464} (right), extracted values are added to table 11.

band.[242] In literature the intensity ratio between the defect related band at $\nu = 600\,\mathrm{cm}^{-1}$ and the F_{2g} mode is used to describe the concentration of oxygen vacancies in the lattice.[244] For this purpose the spectra were baseline corrected to account for the different peak widths due to altering crystallite sizes. The resulting peak heights after baseline subtraction gave, due to the preceding normalization to the F2g peak at 464 cm^{-1}, the intensity ratio I_{600}/I_{464}, which was subsequently plotted as a function of precipitation temperature T_{prec} in figure 12.

It can be seen that with increasing precipitation temperature the defect concentration increases for materials prepared via AP while UP and HUP did yield a higher concentration of defects. The defect concentration is often linked to higher catalytic activity of ceria materials due to their higher oxygen mobility.[197] It was also reported that introducing larger dopants, which Ce$^{\mathrm{III}}$ could be considered as one, limits diffusion processes which are necessary for particle growth during sintering.[247] When plotting the increase in crystallite size $\Delta D_{700\,^{\circ}\mathrm{C}-500\,^{\circ}\mathrm{C}}$ as a function of the defect concentration represented by I_{600}/I_{464} one obtains figure 13.

Figure 13 suggests a linear correlation between the sinter resistance of the samples and the defect concentration. This would mean that the reason for a higher sinter resistance of materials precipitated at higher temperatures is two-fold: First, more homogeneously precipitated materials are obtained when precipitating at higher temperatures which reduces the driving force of *Ostwald* ripening and thus increasing sinter resistance and second a higher oxygen defect concentration resulting from higher precipitation temperature which yields a higher sinter resistance as well.

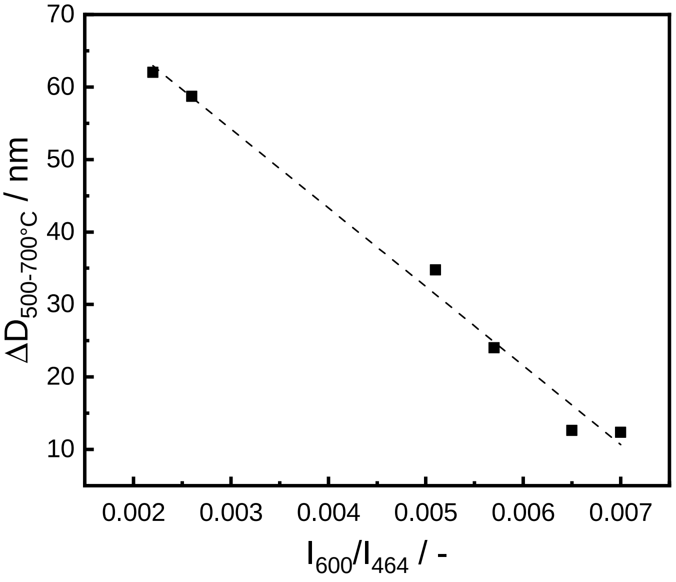

Figure 13: Increase in crystallite size when calcining the precipitates at 700 °C instead of 500 °C $\Delta D_{700\,°\mathrm{C}-500\,°\mathrm{C}}$ as a function of the intensity ratio between $\nu = 600\,\mathrm{cm}^{-1}$ and $\nu = 464\,\mathrm{cm}^{-1}$ I_{600}/I_{464}

8.2. pH Titration Experiments Probing the Effect of Higher Precipitation Temperatures

To investigate how the precipitation temperature influences the precipitation process, pH titration experiments were carried out. These experiments were conducted as described in chapter 6.1.1. The resulting pH curves for 5 °C, 25 °C and 50 °C as a function of the added amount of sodium hydroxide n_{OH^-} are shown in figure 14.

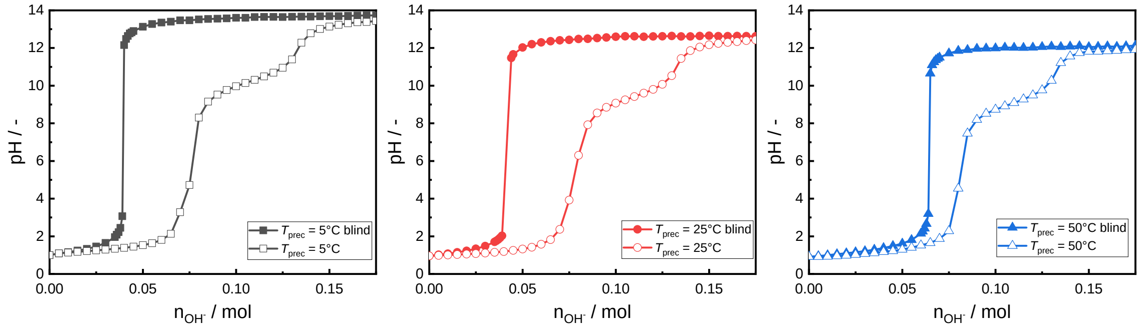

Figure 14: pH as a function of added n_{OH^-} from titration experiments at 5 °C (left), 25 °C (middle) and 50 °C (right) with blank run (—■—) and in presence of cerium ions (—□—)

The titration curves in figure 14 show that compared to the blank experiments the pH values at all temperatures did increase later when cerium ions are present. During precipitation cerium oxyhydroxides are formed, removing hydroxides from the solution, which otherwise would have led to an increase in pH. Thus, the difference in pH observed stems from hydroxide ion consumption due to nucleation and precipitation. Another thing that is evident is the temperature influence on the pH value due to changes in the water dissociation equilibrium. Although a pH sensor with an inbuilt temperature correction was used, temperature is known to alter the water dissociation equilibrium, leading to changes in pH with temperature, which is why the results will only be discussed qualitatively.

When subtracting the interpolated curve of the blank measurement from the sample measurement ΔpH can be plotted as a function of the added hydroxide ion amount which is shown in figure 15. However, since pH is a logarithmic scale, difference in ΔpH makes interpretation difficult. For this purpose, the amount of hydroxide ions that are not bound in the precipitate is calculated. Using the pH measured, the proton concentration at the starting point $n_{\mathrm{H^+},0}$ is calculated. Using this value and the pH measured after addition i, pH$_i$, to calculate $n_{\mathrm{H^+},i}$ or $n_{\mathrm{OH^-},i}$ depending on the pH, the amount of hydroxyide ions that after addition were not bound to the precipitated can be calculated. This has to be done for two different cases: for pH < 7 and pH > 7. While for pH values smaller than pH < 7, where the amount OH$^-$ that is not bound to the precipitate is represented by a decrease in H$^+$ concentration, the amount of "free OH$^-$" is given by equation 45.

$$\begin{aligned} n_{\mathrm{OH^-},\mathrm{free},i} &= n_{\mathrm{H^+},0} - n_{\mathrm{H^+},i} && (44) \\ &= 10^{-\mathrm{pH}_0} \cdot V_0 - 10^{-\mathrm{pH}_i} \cdot V_i && (45) \end{aligned}$$

For the case of the pH$_i$ being above 7, the value of added hydroxides that are not bound to the precipitate is obtained by the sum of protons present in the initial solution $n_{\mathrm{H^+},0}$ and the free hydroxide ions $n_{\mathrm{OH^-},i}$ as shown in equation 47.

$$\begin{aligned} n_{\mathrm{OH^-},\mathrm{free},i} &= n_{\mathrm{H^+},0} + n_{\mathrm{OH^-},i} && (46) \\ &= 10^{-\mathrm{pH}_0} \cdot V_0 + 10^{\mathrm{pH}_i-14} \cdot V_i && (47) \end{aligned}$$

After calculating the values $n_{\mathrm{OH^-},\mathrm{free},i}$ for every addition i for the sample and blank run the amount of OH$^-$ which is bound to the precipitate $n_{\mathrm{OH^-},\mathrm{bound},i}$ was calculated as the difference between blank $n_{\mathrm{OH^-},\mathrm{free,blank},i}$ and sample $n_{\mathrm{OH^-},\mathrm{free},i}$ run using equation (48).

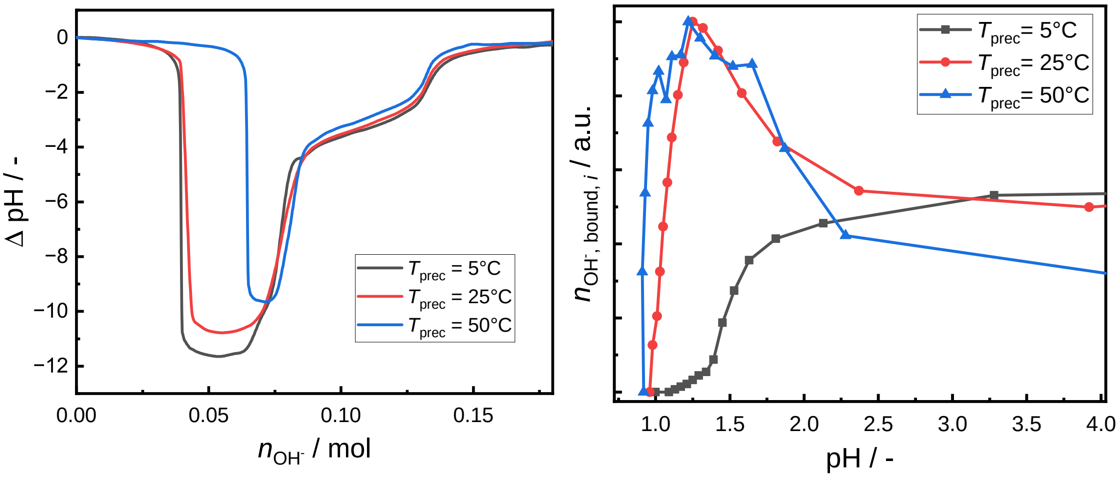

Figure 15: pH difference ΔpH as a function of the added amount of hydroxide ions $n_{\mathrm{OH^-}}$ for experiments at 5 °C (——), 25 °C (——) and 50 °C (——) (left) and the normalized amount of bound OH⁻, $n_{\mathrm{OH^-,bound},i}$, as a function of the pH for experiments at 5 °C (—■—), 25 °C (—●—) and 50 °C (—▲—) (right).

$$n_{\mathrm{OH^-,bound},i} = n_{\mathrm{OH^-,free,blank},i} - n_{\mathrm{OH^-,free},i} \tag{48}$$

These values are plotted as a function of the solution pH, the normalized values of which are shown in figure 15.

It can be observed, that the higher the precipitation temperature the faster $\mathrm{OH^-}$ ions are consumed. Precipitation, however, was only observed when the pH exceeded pH = 7. Thus, the consumption of $\mathrm{OH^-}$ may be attributable to the formation of nuclei, or the already in chapter 2.3.1 discussed preorientation of precursors prior to nucleation. Both effects would increase the number of nuclei formed with increasing temperature, which can explain the observed trend of decreasing crystallite size with increasing precipitation temperature.

9. Redox Properties of Ceria-Based Catalysts

Ceria materials are employed due to their redox properties, which were discussed in detail in chapter 3. In order to increase low-temperature activity (precious) metals are used in many applications to decrease the activation barrier of the reactants. However, the oxide still has an important contribution, since even with precious metal-loaded ceria materials a MvK mechanism was observed, with oxygen being supplied from the redox-active support.[160,205,209] Thus, understanding the structure-property relationships for the oxide

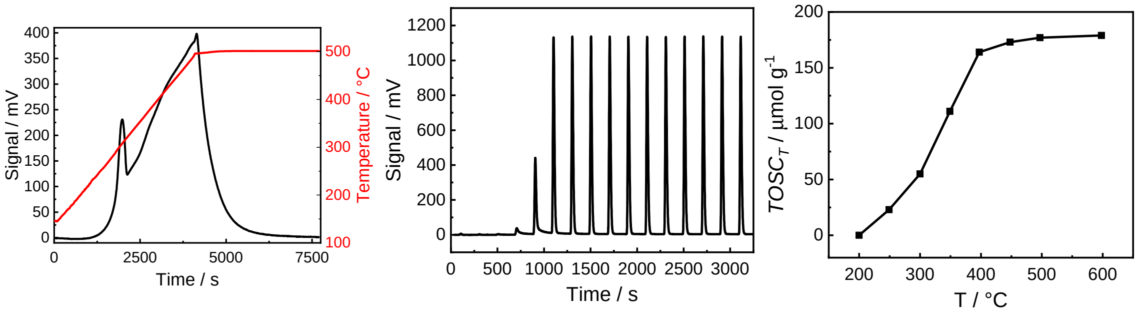

Figure 16: Exemplaric $TOSC_{500\,°C}$ determination. TCD signal (——) and temperature (——) during reduction (left), successive O_2 pulse chemisorption (middle) carried out at 500 °C and $TOSC_T$ as a function of temperature. (right).

support during reduction and oxidation is important as these also play an important role, even in the loaded state.

9.1. Redox Activity of Unloaded Cerium Oxides

The reduction profile of ceria materials during TPR experiments is characterized by two peaks, as discussed in chapter 3. The low temperature signal is related to surface oxygen species, whereas the high-temperature feature is caused by bulk reduction of the ceria materials because bulk diffusion of oxygen is enabled at higher temperatures.[248] As the bulk reduction requires oxygen solid state diffusion processes, which are slow compared to the surface reaction, for highly transient applications such as redox catalysis, the amount of oxygen releasable from the surface is important. The quantity of the entire releasable oxygen at a given temperature is commonly referred to as total oxygen storage capacity ($TOSC$).[249] Different quantification approaches are described in literature. In this work, pulse oxygen chemisorption was used. One exemplary experiment is shown in figure 16.

It can be observed that 1 h of isothermal reduction at 500 °C is enough to ensure that all ceria centers, which can be reduced at 500 °C are reduced. 500 °C was chosen as the analysis temperature in this work, because it can be observed, in figure. 16 that the measured $TOSC_T$ does not increase significantly above that temperature, which means the surface is totally reduced.

For the different prepared materials, whose material properties are listed in table 11, $TOSC_{500\,°C}$ values were measured and are shown in table 12 alongside their crystallite size D and BET surface area S_{BET}.

The amount of reducible centers at the surface is frequently assumed to correlate strictly in a linear manner with the specific surface area S_{BET} when normalizing kinetic data. This

Table 12: Analysis results of *Rietveld* refinement of XRD patterns ^{a}, N_2 physisorption experiments^b and from O_2 pulse chemisorption^c. for materials prepared at different precipitation temperatures

Sample	a^a / nm	D^a / nm	S^a_{cryst} / $m^2\,g^{-1}$	S^b_{BET} / $m^2\,g^{-1}$	$TOSC^c_{500\,°C}$ / $\mu mol_{O_2} g^{-1}$	S^c_{MvK} / $m^2\,g^{-1}$
AP5-500	0.54115	18.07	46	26	131	46
AP25-500	0.54118	14.6	57	37	146	52
AP50-500	0.54114	12.0	69	80	158	56
AP75-500	0.54121	10.3	81	90	n.m.	n.m.
AP5-700	0.54104	80	10	3	43	15
AP25-700	0.54106	73.3	11	3	45	16
AP50-700	0.54102	46.8	18	3	56	20
AP75-700	0.54106	34.3	24	3	n.m.	n.m.
UP-500	0.54128	11.3	73	107	204	72
UP-700	0.54107	23.7	35	39	98	35
HUP-500	0.54127	11.5	72	110	185	65
HUP-700	0.54104	24.1	40	39	93	33
HSA	0.54112	12.0	69	160	192	68

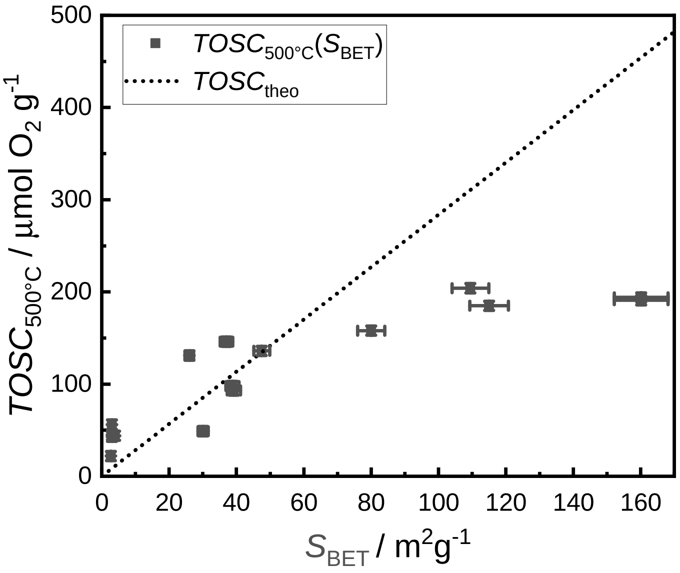

Figure 17: Measured $TOSC_{500\,°\mathrm{C}}$ values as a function of BET surface area S_{BET} (■) and theoretical oxygen storage capacity as function of surface area calculated with equation (49) (┈┈┈)

is done in order to compare the activity of materials exhibiting different surface areas. However, this assumes that the entire surface is redox-active and that the active site density is constant. The latter assumption however is known to be a simplification since different ceria crystal facets exhibit different oxygen densities.[250] The measured $TOSC_{500\,°\mathrm{C}}$ values listed in table 12 are plotted against their specific surface area S_{BET} in figure 17.

When the $TOSC_{500\,°\mathrm{C}}$ is plotted as a function of the specific surface area S_{BET} it becomes evident, that although the $TOSC_{500\,°\mathrm{C}}$ values increase with increasing S_{BET}, one can not observe the assumed linear relationship between S_{BET} and $TOSC_{500\,°\mathrm{C}}$. Theoretical $TOSC_{\mathrm{theo}}$ can be calculated based on the oxygen density which can be derived from the lattice parameter a. Using the lattice parameter a and a mass-specific surface area S_{BET}, $TOSC_{\mathrm{theo}}$ can be calculated with equation (49)[250–252]

$$TOSC_{\mathrm{theo}} = \frac{S_{\mathrm{BET}}}{2a^2 \cdot \mathrm{N_A}}. \tag{49}$$

Using the literature value for $a_{\mathrm{CeO_2}} = 0.5411\,\mathrm{nm}$, equation (49) is plotted in figure 17. Comparing the measured $TOSC_{500\,°\mathrm{C}}$ the diagram shows that at low S_{BET} values the measured $TOSC_{500\,°\mathrm{C}}$ scatter around the theoretically predicted line. With increasing BET surface areas however, the deviation between theoretically calculated $TOSC_{\mathrm{theo}}$ and the measured values of $TOSC_{500\,°\mathrm{C}}$ become larger. Since in this work reoxidation of the

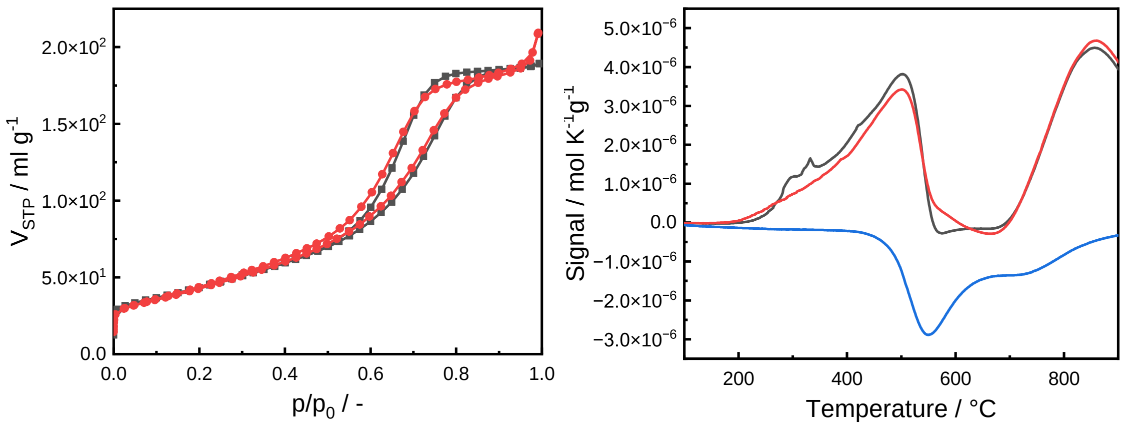

Figure 18: N_2 physisorption isotherms before (—■—) and after (—●—) $TOSC_{500\,°C}$ analysis (left) and H_2-TPR profile of pristine HSA material (——) and after $TOSC_{500\,°C}$ analysis (——) as well as H_2-TPD analysis (——) (right)

surface is used to estimate the amount of cerium centers reduced, the observed effect can be caused by two different mechanisms. Either irreversible reduction, meaning loss of redox-active surface area,[253–255] or reduction without oxygen release.[144] The former could be caused by overreduction, as observed in other redox catalysts[253,254] or surface area loss during the initial reduction processes,[255] whereas the latter would mean quantification is not possible through oxygen chemisorption. Both mechanisms however, would lead to a decrease in *Mars-van-Krevelen* active surface area S_{MvK}, i.e. surface area whose active sites can reversibly be reduced under oxygen release.

In order to investigate this further nitrogen physisorption experiments were carried out after the initial $TOSC_{500\,°C}$ analysis. Comparing the surface area S_{BET} before and after reduction is an indicator as to whether sintering is causing the large difference in theoretical TOSC $TOSC_{\mathrm{theo}}$ and the measured values $TOSC_{500\,°C}$. The two isotherms are shown in figure 18.

Comparing the isotherms for the HSA material obtained before and after $TOSC_{500\,°C}$ analysis plotted in figure 18 shows that there is a negligible difference. This is also represented in the extracted BET surface area S_{BET} before, $S_{\mathrm{BET,pristine}}$, and after $TOSC_{500\,°C}$ analysis, $S_{\mathrm{BET,after}\ TOSC_{500\,°C}}$, ($S_{\mathrm{BET,pristine}} = 160\,\mathrm{m^2\,g^{-1}}$; $S_{\mathrm{BET,after}\ TOSC_{500\,°C}} = 164\,\mathrm{m^2\,g^{-1}}$) which points towards the fact that the difference in measured $TOSC_{500\,°C}$ is not caused by a loss of surface area.

Using different TPR methods it was attempted to investigate this further. As mentioned before, a possible explanation for this phenomenon can be irreversible reduction. Whether irreversible reduction is present was probed by measuring a TPR after $TOSC_{500\,°C}$ analysis. The reduction profile is shown in figure 18. Although there are slight differences between the reduction profiles between the pristine material and the material after $TOSC_{500\,°\mathrm{C}}$, the integral of the reduction feature related to the surface did not change in a way to explain the large deviation between measurement and theoretically predicted $TOSC$ value. Since Bernal et al. suggested that a fraction of the surface might not be reducible under oxygen release due to vacancy formation but rather hydroxyl group formation, H_2-temperature programmed desorption (TPD) experiments were carried out to investigate the amount of bound H_2.[144] As a desorption step was introduced between reduction and O_2 chemisorption in the $TOSC_{500\,°\mathrm{C}}$ measurement, these species would not contribute to the measured value. The H_2-TPD profile is shown in figure 18.

The diagrams shows an intense desorption feature with an onset at 425 °C. Although the TCD used is unselective, the experimental conditions were chosen in a way to conclude that desorption is hydrogen. As described in chapter 7.11, the desorption experiments were carried out in N_2. Thus possible carbonates that might decompose at those temperatures would have a negligible influence to the TPD profile. Also, a cold trap cooled with a dry ice/acetone bath (-78 °C) was used to condense any water formed during reduction. Thus, the observed signal in the TCD is most probably neither from CO_2 nor from H_2O. This makes the most probable explanation for the observed feature in the TPD profile to be desorbed H_2. Integrating the desorption feature and calculating the amount of adsorbed $n_{\mathrm{H_2,ads}}$ gives a value of 498 $\mu\mathrm{mol}_{\mathrm{H_2}}/\mathrm{g}$. As a result of the stoichiometry, this correlates to 249 $\mu\mathrm{mol}_{\mathrm{O_2}}/\mathrm{g}$. Using equation (49), the theoretical *TOSC* of the HSA material can be calculated based on the BET surface area listed in table 12 to be $TOSC_{\mathrm{theo}} = 454\,\mu\mathrm{mol}_{\mathrm{O_2}}/\mathrm{g}$, which should be the sum of released oxygen and oxygen equivalents of adsorbed hydrogen $n_{\mathrm{H_2}}$.

$$TOSC_{\mathrm{theo}} = TOSC_{500\,°\mathrm{C}} + 0.5\frac{n_{\mathrm{N_2}}}{m_{\mathrm{cat}}} \tag{50}$$

$$= 195\,\mu\mathrm{mol}_{\mathrm{O_2}}/\mathrm{g} + 0.5 \cdot 498\,\mu\mathrm{mol}_{\mathrm{H_2}}/\mathrm{g} \tag{51}$$

$$= 444\,\mu\mathrm{mol}_{\mathrm{O_2}}/\mathrm{g} \tag{52}$$

This value is close to the predicted value from calculation of $TOSC_{\mathrm{theo}}$, when the *BET* surface area S_{BET} is used in equation (49). Thus, these results suggest that the differences between measured $TOSC_{500\,°\mathrm{C}}$ and based on the BET surface area theoretically predicted $TOSC_{\mathrm{theo}}$ at high BET surface areas S_{BET} are caused by a fraction of the surface that cannot be reduced under oxygen release, but rather through hydrogen chemisorption, most probably as hydroxyl groups as suggested by Bernal et al..[144] To investigate the formation of hydroxyl groups *in situ*-DRIFTS reduction experiments were carried out for

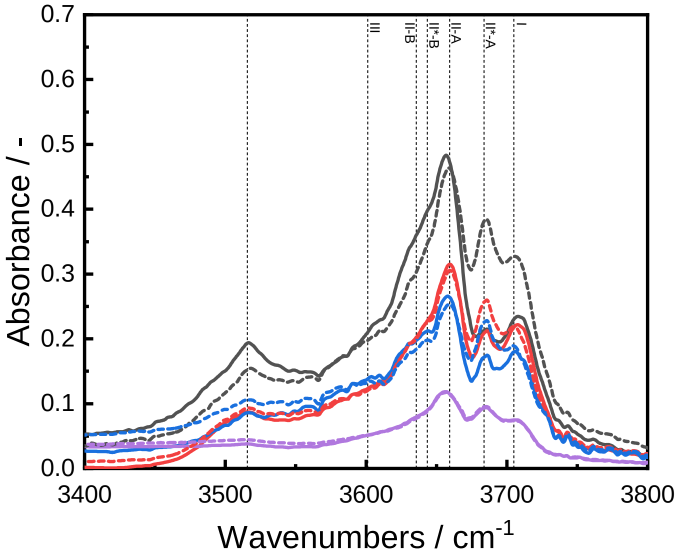

Figure 19: *In situ*-DRIFTS spectra of degassed HSA (——), UP-500 (——), AP50-500 (——) and AP5-700 (——) and after H_2 adsorption at 100 °C (-----).

four materials to investigate whether hydroxyl groups are actually formed.

It is evident from figure 19 that different OH species are present on the surface of the oxides. Badri et al. investigated the formation of hydroxyl groups on ceria surfaces.[256] Their observed features are very similar to the ones observed in this study. Aside from monodentate hydroxyl groups ($\nu_{\mathrm{OH(I)}} = 3710\,\mathrm{cm}^{-1}$) they observed also bridging bidentate hydroxyl groups ($\nu_{\mathrm{OH(II)}} = 3660\,\mathrm{cm}^{-1}$) as well as tridentate hydroxyl groups ($\nu_{\mathrm{OH(III)}} = 3600\,\mathrm{cm}^{-1}$) on oxidized surfaces. For high surface area samples it can also be observed that the spectral feature of the bidentate hydroxyl group is characterized by a doublet structure with $\nu_{\mathrm{OH(II-A)}} = 3660\,\mathrm{cm}^{-1}$ and $\nu_{\mathrm{OH(II-B)}} = 3640\,\mathrm{cm}^{-1}$. The authors attributed the OH(II-B) to bridging hydroxyl groups in the vicinity of oxygen vacancies. The two bands shift to higher wavenumbers with $\nu_{\mathrm{OH(II*-A)}} = 3681\,\mathrm{cm}^{-1}$ and $\nu_{\mathrm{OH(II*-B)}} = 3647\,\mathrm{cm}^{-1}$ when the oxide is reduced with oxygen vacancy formation.[142,144,256]

After degassing, hydrogen was introduced at 100 °C. From figure 19 it can be observed that the spectra in the hydroxyl range are changed differently between the four materials investigated after hydrogen introduction. Whereas little to no change is observed for the small surface area sample AP5-700, the change became more pronounced for UP-500 and the largest change was observed for the HSA ceria sample. When looking at the individual bands of the HSA sample in figure 19, the one with the highest surface area, an increase in intensity of the OH-I and OH-II*-A species is observed, while the band attributed to the OH-II-A species has not changed much, and OH-II-B and OH-II*-B decrease slightly in intensity. For materials with intermediate surface areas (UP-15 and AP40-500), the band of monodentate OH-I groups is not changed upon hydrogen adsorption, with the OH-II*-A feature increased substantially again. At the same time intensities of II-A, II-B and II*-B decreased only slightly. In contrast, the low surface area ceria showed almost no change in hydroxyl band intensities after hydrogen adsorption. Already Badri et al. demonstrated that it is possible to dissociatively adsorb hydrogen on the surface of ceria materials already at 100 °C.[256] In their study, the authors found that upon hydrogen adsorption, terminal and bridging OH groups are formed. It was reported by Binet et al. that upon reduction and oxygen vacancy formation a band at 2127 cm^{-1} is observed, which was attributed to an electronic transition in Ce^{III}, allowed through crystal field effects in the vicinity to oxygen vacancies.[257] This band, however, is not observed after hydrogen adsorption at 100 °C, pointing towards adsorption without reduction, which is also in line with previous studies.[258] Thus, different mechanisms of hydrogen dissociation have to be considered. Whereas, homolytic dissociation, as proposed by Wu et al., would lead to neutral species heterolytic dissociation would lead to a formation of hydride and a proton species on the surface.[259] In the study of Binet et al., a band at 1700 cm^{-1} was observed, which was attributed to a charge transfer process at point defects as shown in reaction 22.

$$\text{Ce}^{\text{III}} - \text{v}_{\text{O}} - \text{Ce}^{\text{IV}} \rightleftharpoons \text{Ce}^{\text{IV}} - \text{v}_{\text{O}} - \text{Ce}^{\text{III}} \qquad [\text{R } \mathbf{22}]$$

For the high surface are materials, for which a deviation was observed between the redox-active surface area and the BET surface area, it was found, that upon hydrogen adsorption the charge transfer related band at 1700 cm^{-1} did decrease in intensity. Instead of a reduction, this points towards a reoxidation of the surface through homolytic dissociative adsorption coupled with a SET, as proposed by Li et al.[259] The presence of dissociative homolytic adsorption of hydrogen on the ceria surface would also explain the increase in hydroxyl species OH-II-A, while OH-II-B species do decrease in intensity. When the hydrogen-hydrogen bond is homolytically split, one hydroxyl group is formed while a hydride is formed by a SET from the point defect to the second hydrogen atom, thus oxidizing the otherwise not oxidizable point defect. These findings are in perfect agreement with the study published by Li et al. who showed using electron spin resonance experiments, that upon hydrogen exposure the concentration of Ce^{III} in the sample is decreased, through a single-electron transfer from a Ce^{III} to an adsorbed hydrogen ion.[259] This is shown in figure 20.

A shown in figure 20 the ceria oxidation through a SET from a point defect to an adsorbed hydrogen atom decreases the number of Ce^{III} on the surface, leading to a decreased number

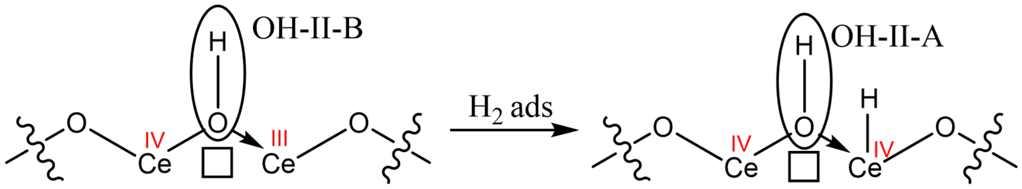

Figure 20: Proposed reaction during homolytic dissociation of H_2 on the surface of defective (Ce^{III}) containing ceria in line with findings by Li et al.[259]

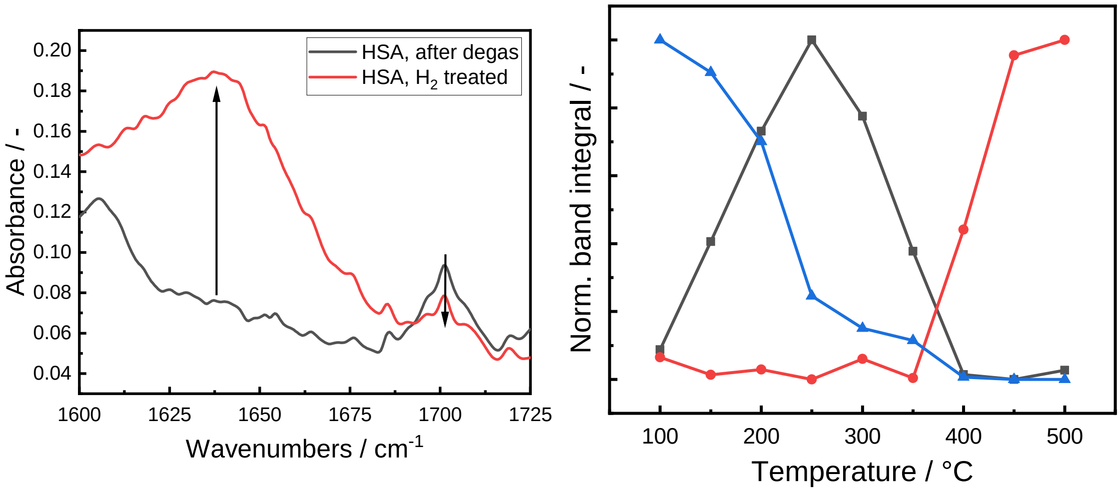

Figure 21: DRIFTS spectra of HSA sample after degas (——) and after hydrogen adsorption at 100 °C (——) (left) and normalized band intensity of the mixed hydroxide band at 1630 cm^{-1} (—■—),the charge transfer band at 1700 cm^{-1} (—■—) and oxygen vacancy band at 2127 cm^{-1} (—●—) band (right)

of hydroxyl groups in the vicinity of such species (OH-II-B), while more bidentate hydroxyl groups OH-II-A are present between two Ce^{IV} ions. This also explains why the Ce(III) charge transfer band at 1700 cm^{-1} is decreased. Hydrogen adsorption also changes the DRIFTS spectrum through the emergence of a broad but intense band at around 1630 cm^{-1} as shown in figure 21.

The emerging band at 1630 cm^{-1} was already seen by Allen et al. who prepared mixed Ce^{III} and Ce^{IV} hydroxides. This band, however, was absent when pure Ce^{III} and Ce^{IV} hydroxides were analyzed.[260] The charge transfer related band, as well as the mixed hydroxyl band are only observed for materials showing high surface areas. One might explain this tentatively by the presence of hydroxyl groups that are associated with point defects. When tracking at different temperatures the fate of the Ce^{III}/Ce^{IV} hydroxyl band at 1630 cm^{-1}, the charge transfer related band at 1700 cm^{-1} as well as the electronic Ce^{III} band, for Ce^{III} surrounded by oxygen vacancies, at 2127 cm^{-1}, an interesting trend can be observed. Normalized band integrals as a function of temperature for the HSA material are shown in figure 21 (right).

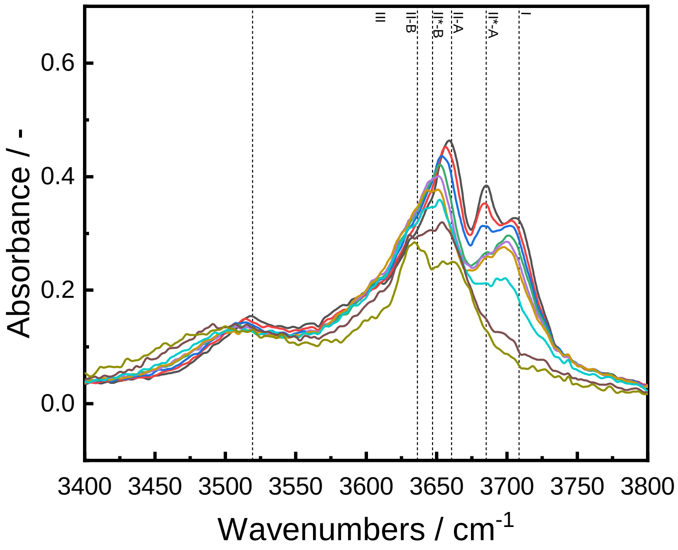

Figure 22: *In situ*-DRIFTS spectra during reduction of HSA sample after 1 h of isothermal treatment under hydrogen flow at 100 °C (—), 150 °C (—), 200 °C (—), 250 °C (—), 300 °C (—), 350 °C (—), 400 °C (—), 450 °C (—) and 500 °C (—) in the OH-region

After dissociative hydrogen adsorption at 100 °C, the band related to mixed valent hydroxyl bands ($\nu = 1630\,\mathrm{cm^{-1}}$) is the most prevalent one among the three bands. With increasing temperature the intensity of this band decreases. On the other hand, the charge-transfer band between Ce^{III} and Ce^{IV} (*c.f.* reaction 22) increases, with a maximum value at around 250 °C, before it decreases again. Simultaneously, after 350 °C, the Ce^{III} electronic transition band associated with oxygen vacancies gains intensity. These results are in line with literature studies.[257] To understand this decrease in intensity with increasing temperature, the intensities observed in the hydroxyl wavenumber range were examined during the reduction process. These are shown for the HSA sample in figure 22.

When comparing the intensities of the different hydroxyl groups during reduction, it is not surprising that the intensity of the bands related to hydroxyl group vibrations changes. There is little change, but a slight decrease in the band intensity of the OH-II-A and OH-II*-A and at the same time an increase in OH-II-B and OH-II*-B band intensity up to 200 °C. Between 200 °C and 350 °C, the intensity loss, especially for the OH-II-A and later also terminal hydroxyl groups, is observed. Above 350 °C the intensity of the band related to terminal OH-I groups decreases quickly with increasing temperature, which was also observed by Badri et al..[256] While also the band intensities are lowered for the bidentate hydroxide species, intensity of OH-II-A and OH-II*-A are affected more than the bands OH-II-B and OH-II*-B. As discussed above the bridging OH feature OH-II-B is attributed to hydroxyl groups in the vicinity of oxygen vacancies. This is hardly a surprise since with increasing reduction the number of oxygen vacancies is increased. Time resolved

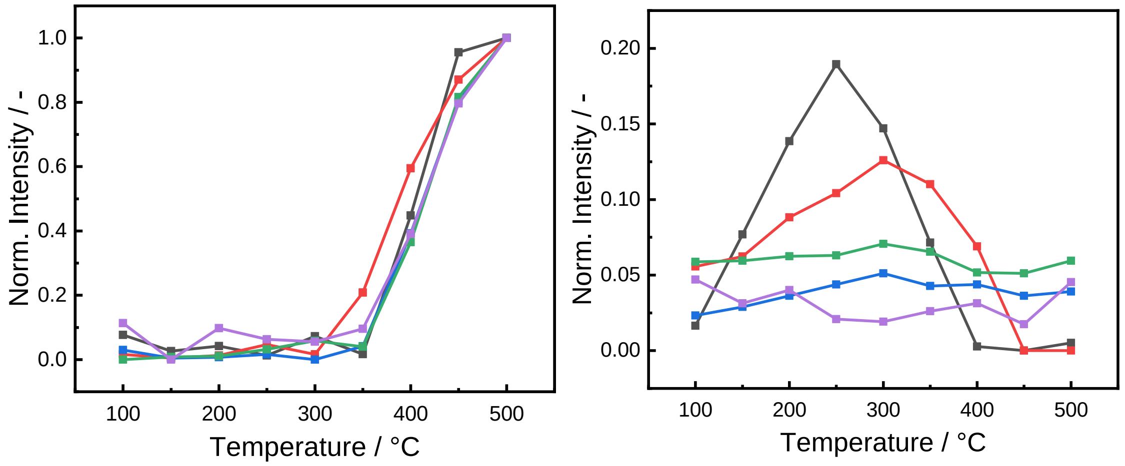

Figure 23: Band integral of the electronic Ce$^{\mathrm{III}}$ transition associated to oxygen vacancies 2127 cm^{-1} (left), and the charge-transfer band at 1700 cm^{-1} (right) for HSA (—■—), UP-500 (—■—), AP50-500 (—■—), AP25-500 (—■—) and AP5-700 (—■—). Intensities are normalized to the band at 2127 cm^{-1} and thus the contribution of different surface areas is accounted for, as the formation of oxygen vacancies is a surface process for ceria

measurements published in the literature showed that upon initial hydrogen introduction the OH-II-B band vanishes, which was explained by reduction through water formation, while the OH-II*-B band reappeared when approaching the maximum reduction degree.[256] Evacuation experiments described in literature showed that it was exactly the presence of this OH-II*-B band which is attributable to the reversible reduction, i.e. reduction without water formation.[256,261] The reduction behavior of the other oxides behaved comparable to the here discussed material (Spectra are shown in figure 55, 56 and 57). The fact that intensity only slightly decreases in the hydroxyl range below temperatures of 200 °C, while rapidly decreasing above that point is in agreement with the cerium related electron transitions observed in the *in situ* DRIFTS spectra, whose temperature related intensity profile is shown in figure 21. The fact that the charge transfer band at 1700 cm^{-1}, which lost intensity during hydrogen adsorption, increased in intensity can be explained when comparing these results to literature studies. In the study of Li et al. it was reported that the reoxidation of point defects is reversed at around 200 °C.[259] This coincides well with the observed increase of the charge transfer band, as the cerium reduction of Ce$^{\mathrm{IV}} - \mathrm{H}^{-}$ to Ce$^{\mathrm{III}} - \mathrm{H}$ would increase the number of Ce$^{\mathrm{III}} - v_{\mathrm{O}} - \mathrm{Ce}^{\mathrm{IV}}$ moieties on the surface. The oxygen vacancy related feature at 2127 cm^{-1} is only observed when the temperature is increased to above 350 °C. Comparing the materials, this increase is rather similar. It is not surprising that formation of oxygen vacancies, which can be considered to be Ce$^{\mathrm{III}} - v_{\mathrm{O}} - \mathrm{Ce}^{\mathrm{III}}$ species, coincides with a decrease in the band related to Ce$^{\mathrm{III}} - v_{\mathrm{O}} - \mathrm{Ce}^{\mathrm{IV}}$.

In figure 23 the temperature dependence of the band at 2127 cm^{-1}, which is related to

Ce^{III} ions associated with oxygen vacancies, and the band at $1700\,cm^{-1}$ related to charge-transfer processes in mixed valent point defects $Ce^{III} - v_O - Ce^{IV}$ is shown. The band integrals are normalized to the respective band at $2127\,cm^{-1}$ at 500 °C. In that way, since the oxygen vacancy formation is limited to the surface, the integral of the $1700\,cm^{-1}$ is expressed in relation to the amount of oxygen vacancies and with it surface area. Thus, the contribution of different surface areas is compensated by this normalization and different materials can be compared directly. It can be seen that the amount of oxygen vacancies increases at around 350 °C similarly among the different materials. This is, as mentioned before in line with the findings of Badri et al.[256] However, if the intensities of the charge transfer transition of mixed valent point defects is compared between the materials it can be observed, that while the HSA and UP-500 material do show this transition, the spectra of the other materials do not show that specific transition during the reduction process. This shows clearly that while point defects are reoxidizable through hydrogen homolytic dissociative adsorption followed by a SET from Ce^{III} to the adsorbed hydrogen atom, after the reversibility of the ceria oxidation at around 200 °C, similarly to findings by Li et al., point defects can be deduced as an explanation for the deviating behavior from the predicted redox-active surface area.

As the hydroxyl band intensity mostly differs in intensity between the different materials due to a difference in surface area, the hypothesis of reversible reduction was probed. To do so, the samples were, after reduction at 500 °C, subsequently degassed in a nitrogen stream. It is assumed, that when reduction yields only oxygen vacancies, the spectrum in the hydroxyl group range should not change after reduction and degassing. If, however, hydroxyl groups are indeed formed during reduction, the desorption should not be complete at 500 °C, in line with H_2-TPD measurements shown in figure 18, and therefore a positive difference between the spectrum after the final and the initial degassing should be observable. The entire DRIFTS spectra for the different samples are shown in figure 58, while the hydroxyl group range is plotted in figure 24.

Figure 24 shows that for materials with high surface areas more hydroxyl groups were present after reduction with hydrogen at 500 °C and subsequent degassing in N_2. For these materials a difference between the predicted $TOSC_{\text{theo}}$ and measured $TOSC_{500\,°\text{C}}$ was observed. For materials with low surface areas and low deviation between measured and predicted $TOSC$ values, no additional hydroxyl groups were detected. This finding strengthens the assumption that the so called reversible reduction, reduction without water formation, coupled with presence of point defects is most probably the reason for the observed deviation from the predicted values. These centers would thus not be active in reactions which will be catalyzed through a MvK mechanism. Thus, for high surface area

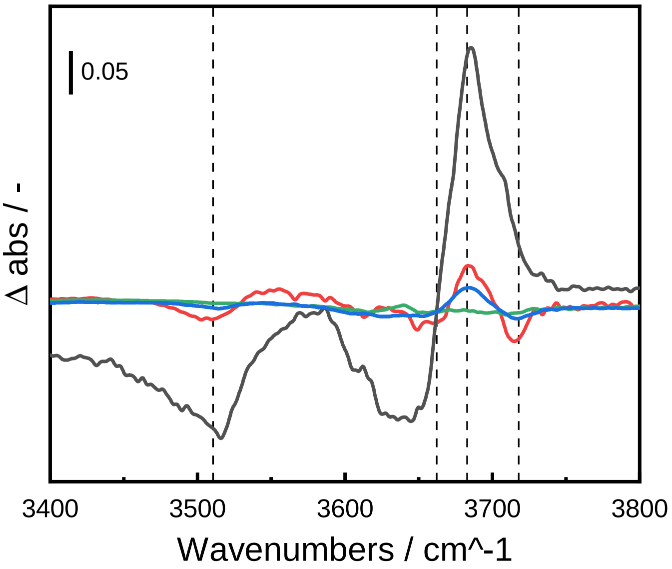

Figure 24: Difference spectra between samples after desorption following reduction and initial degassed sample in the hydroxyl spectral range for HSA (——), UP-500 (——), AP50-500 (——) and AP5-700 (——)

cerium oxides it is not sufficient to normalize reaction rates by using the BET surface area when investigating structure-property relationships, but rather the actual active surface area in the MvK mechanism S_{MvK} has to be used. This active surface area can be calculated based upon the measured $TOSC_{500\,^{\circ}\mathrm{C}}$ using a transformed version of equation (49), given in equation (53)

$$S_{\mathrm{MvK}} = 2 \cdot TOSC_{500\,^{\circ}\mathrm{C}} \cdot a^2 \cdot \mathrm{N_A}. \tag{53}$$

The DRIFTS measurements revealed, in accordance with several literature studies, that there are different processes that happen as a function of temperature. An attempt has been made to summarize these in one reaction scheme, which can be found in in figure 25.

As shown in figure 25, the combined results of this study show that hydrogen adsorbs dissociatively in a homolytic manner on ceria at 100 °C. This homolytic splitting of a H-H bond leads to the formation of two neutrally charged hydrogen atoms on the surface and the reversible oxidation of point defects on the ceria surface below 200 °C through formation of a hydride. This process is reversed at temperatures above 200 °C. Afterwards, reduction proceeds through oxygen vacancy formation. Point defects do not participate in the oxygen release, leading to a decrease in released oxygen ions per surface area.

It was attempted to find the reason why the MvK active surface area S_{MvK} differs from

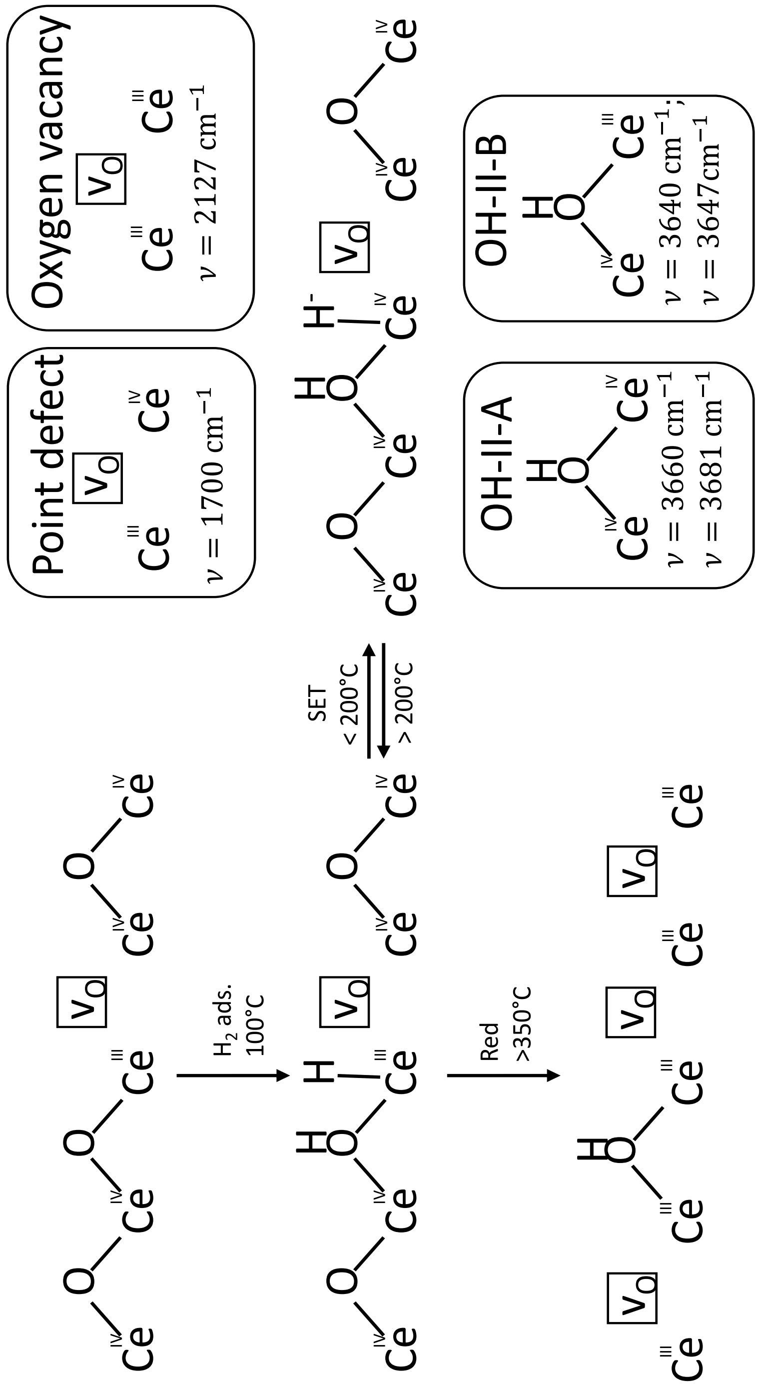

Figure 25: Proposed reaction mechanism based on the DRIFTS results obtained

the specific surface area S_{BET}. The reduction of ceria coincides with an increase in the lattice parameter due to the larger ionic radius of Ce^{III} compared to the prevalent Ce^{IV} ion present in stoichiometric CeO_2. It is reported that smaller particles exhibit a larger lattice parameter, which is believed to stem from an increased number of surface point defects caused by the increase in surface-to-bulk ratio and therefore a lower stabilizing effect of the bulk.[262] These point defects, which as described above would lead to a decrease in oxygen release capability, would be prevalent in small sized cerium oxides. As small crystallites below $D < 5$ nm do not contribute significantly to the measured XRD pattern, a crystallite surface S_{cryst} was calculated according to equation 54

$$S_{\text{cryst}} = \frac{A_{\text{cryst}}}{V_{\text{cryst}} \cdot \rho_{\text{CeO}_2}}. \tag{54}$$

The crystallites were approximated as spheres which enabled the calculation of A_{cryst} and V_{cryst} according to eq.(55) and (56). The density of ceria, ρ_{CeO_2}, can be calculated using the molar mass of cerium, M_{Ce}, and oxygen, M_{O}, according to equation (57).

$$A_{\text{cryst}} = 4\pi \left(\frac{D}{2}\right)^2 \tag{55}$$

$$V_{\text{cryst}} = \frac{4}{3}\pi \left(\frac{D}{2}\right)^3 \tag{56}$$

$$\rho_{\text{CeO}_2} = \frac{4M_{\text{Ce}} + 8M_{\text{O}}}{a^3 \cdot \text{N}_\text{A}} \tag{57}$$

The calculated values for S_{cryst} of the different materials are listed in table 12. It can be observed that the calculated crystallite surface S_{cryst} differs significantly from the measured total surface area S_{BET} for some of the materials. In figure 26 the measured $TOSC_{500\,°\text{C}}$ are plotted as a function of the with eq.(54) calculated and in table 12 listed values for S_{cryst} $TOSC_{500\,°\text{C}}\,(S_{\text{cryst}})$ as well as the previously shown plot of measured $TOSC_{500\,°\text{C}}$ values as a function of the specific surface area S_{BET}.

It can be observed that the measured $TOSC_{500\,°\text{C}}$ values as a function of the calculated crystallite surface area S_{cryst} correspond reasonably well with the theoretically calculated value $TOSC_{\text{theo}}$. This is in contrast to the plot of the same values as a function of the specific surface area S_{BET} obtained from physisorption experiments. Also, when the values of the MvK active surface area S_{MvK} are compared to the values calculated based upon

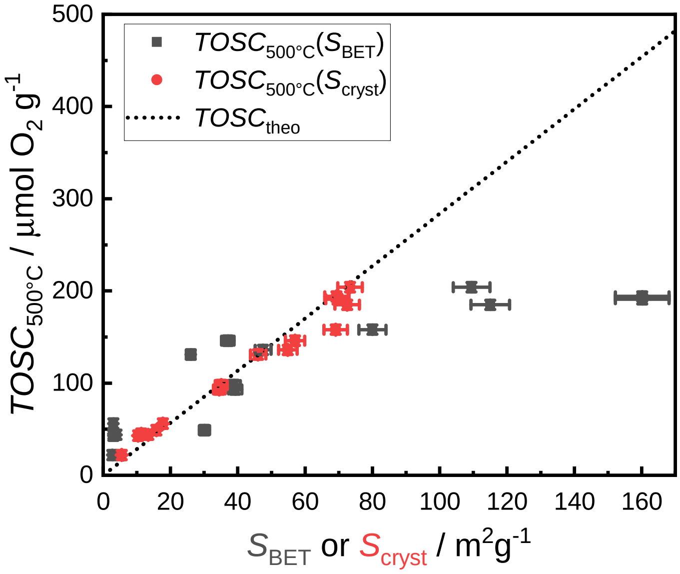

Figure 26: Measured $TOSC_{500\,°\mathrm{C}}$ values as a function of BET surface area S_{BET} (■) and crystallite surface area S_{cryst} (●) as well as theoretical oxygen storage capacity as function of surface area calculated with equation (49) (·········).

the crystallite size it can be observed that one can estimate the surface area that can reversibly release oxygen through the crystallite size D. This also hints at the fact that small crystallites might be responsible for the deviation of $TOSC_{500\,°\mathrm{C}}\,(S_{\mathrm{BET}})$ from the theoretically predicted values $TOSC_{\mathrm{theo}}$. As crystallites become smaller the crystallite size distribution gets ever closer to the detection limit of XRD, which is usually given with $D = 5\,\mathrm{nm}$.[263] Thus, when large surface areas are present for nonporous materials as investigated here, and therefore small crystallites, a fraction of the crystallites can not be detected by XRD, while still contributing to the overall surface area which is measured by N_2 physisorption. When these small crystallites are not able to release oxygen reversibly during reduction, one would observe the present correlation. The presence of such small crystallites was therefore subsequently investigated with high-resolutions transmission electron microscopy (TEM) imaging. Representative TEM images are shown in figure 27.

It can be seen from the images depicted in figure 27 that although there are large crystallites present, also very small crystallites can be found in the material. These domains with a size of less than 5 nm will, as discussed above, not contribute to the diffraction pattern in a significant way. And thus, the TEM pictures strengthen the assumption that small crystallites, showing a larger concentration of point defects on the surface,[264] are most probably the reason for a lower MvK active surface area, because they are not able to release oxygen.

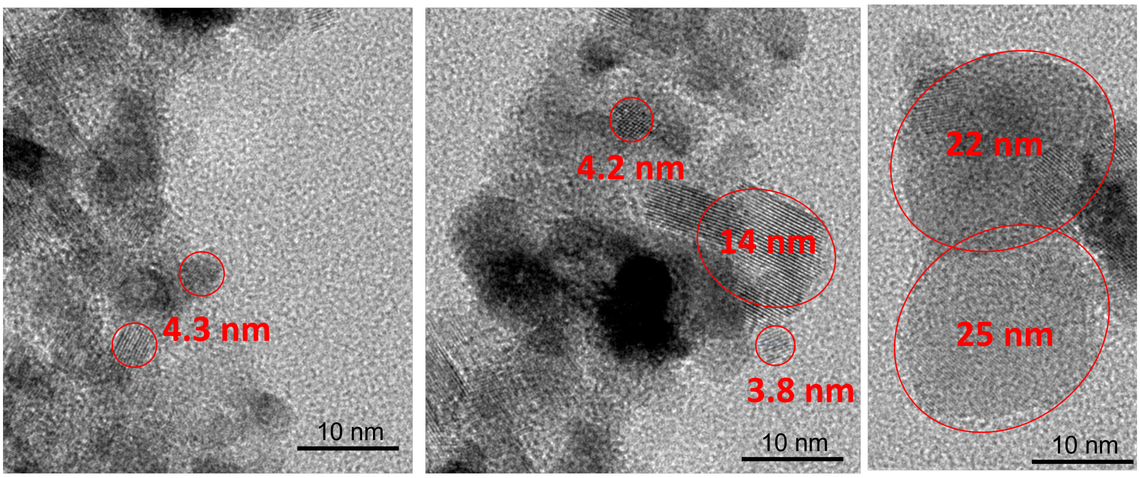

Figure 27: TEM images of crystallite structure of CeO_2-64

Overall, these studies show that when investigating ceria redox catalysts for catalytic applications in which the oxygen release is a vital step in the reaction mechanism the normalization of kinetic data using the specific surface area S_{BET} is not appropriate. Instead, the surface that can reversibly release oxygen during reduction has to be used for the normalization of rates. The deviation between total surface area S_{BET} and the *Mars-van-Krevelen* active surface area S_{MvK} can most probably be attributed to small crystallites, showing larger amounts of point defects. The presented results suggest that these small crystallites are reduced without forming oxygen vacancies and releasing oxygen. Instead during reduction hydroxyl groups, which were detected by *in situ*-DRIFTS, are formed, which can release hydrogen during desorption. The presented results suggest that the crystallite surface area S_{cryst} calculated from the crystallite size D extracted by *Rietveld* refinement can be used as a descriptor for S_{MvK}. This is also important for doped cerium oxides, since in such systems the surface and bulk reduction can not be separated anymore by the right choice of reduction temperature, making the experimental determination of S_{MvK} difficult.

10. Investigation of Structure-Property Relationships of Ceria Catalysts in CO Oxidation

Cerium oxide materials are used as oxygen storage materials in exhaust gas catalysis. As previously discussed, there are usually precious metals present that facilitate reactant activation and increase low temperature activity. However, it is difficult to study structure-property relationships of cerium oxide supports in their platinum-loaded state as the platinum dispersion is known to change during catalysis.[205,213] For this reason, different approaches are followed in this work to understand the role of cerium oxide in such systems. First, CO oxidation activity of bare ceria supports was investigated. Afterwards the same ceria supports were loaded with platinum in a highly dispersed state to suppress agglomeration. In this way it was attempted to gain new insights into the role of ceria and its material properties during CO oxidation.

10.1. Material Preparation and Characterization

Various materials were prepared with the aim to span a wide range of material properties to investigate structure-property relationships in the oxidation of CO. The materials were prepared as indicated by the systematic nomenclature introduced in the chapters before and given for every material prepared in table 13. After preparation the materials were thoroughly characterized. TOSC values were measured according to chapter 7.11.2, with the obtained TPR profiles shown in the appendix figure 66, after which the oxygen pulse chemisorption was carried out. Using equation (53), the *Mars-van-Krevelen* active surface area S_{MvK} was also calculated. It was previously established that the S_{MvK} is the important parameter that determines the active surface area in oxidation catalysis following the MvK mechanism. Materials are thus referred to as CeO_2-S_{MvK}. The systematic nomenclature describing the preparation conditions under which the materials were prepared are listed in table 13.

Table 13: Prepared materials for CO oxidation experiments and their measured $TOSC_{500\,°\mathrm{C}}$ with therefrom calculated S_{MvK} using equation (53).

Name	Systematic name	$TOSC_{500\,°\mathrm{C}}$ / µmol g^{-1}	S_{MvK} / m^2 g^{-1}
CeO_2-64	HSA	180	64
CeO_2-54	UP15-500	152	54
CeO_2-41	AP40-500	117	41
CeO_2-34	AP25-500	97	34
CeO_2-15	HUP-700	41	15
CeO_2-10	AP5-700	28	10

While XRD coupled with *Rietveld* refinement was used to obtain information about the crystal properties of the prepared materials (diffractograms shown in figure 62), specific BET surface areas were determined using N_2 physisorption (isotherms shown in figure 63).

Raman spectroscopy was conducted to investigate the defectivity of the oxygen sublattice (spectra are shown in figure 64). XPS measurements were carried out as well to assess the concentration of Ce$^{\text{III}}$ ions close to the surface. It is described in literature that the high degree of freedom during fit of the complex CeÒ$3d$ XP spectrum makes a reliable quantitative analysis challenging.[238] For that reason the spectrum of a prepared $CeAlO_3$ standard was used to analyze the Ce$^{\text{III}}$ contribution for the different samples through linear combination of the spectra. As discussed previously the Ce$3d$-XP spectra of nanocrystalline ceria are characterized by 10 peaks related to Ce$^{\text{III}}$ (v_0, u_0, v', u') and Ce$^{\text{IV}}$ $(v, u, v'', u''', v''', u''')$.[239] Although it was attempted to minimize the error through usage of the $CeAlO_3$ standard material, the error in oxidation state analysis is very sensitive to the way spectra are measured and fitted and thus errors tend to be high.[238,239,265] Spectra are shown in figure 65. The obtained results of the material characterization are summarized in table 14.

Table 14: Prepared materials for CO oxidation experiments and their material parameters from ^{a}XRD and *Rietveld* refinement, ^{b}N_2 physisorption, ^{c}Raman analysis and ^{d}XPS analysis

Name	a^a / nm	D^a / nm	S^a_{cryst} / $m^2\,g^{-1}$	S^b_{BET} / $m^2\,g^{-1}$	I_{600}/I^c_{464} -	Ce$^{\text{III}}$/Ce^d -
CeO_2-64	0.54112	12.0	70	160	0.0119	0.26
CeO_2-54	0.54141	9.7	86	109	0.0069	0.24
CeO_2-41	0.54119	11.9	57	71	0.0041	0.15
CeO_2-34	0.54133	14.6	57	37	0.0026	0.16
CeO_2-15	0.5412	40.8	20	22	0.0012	0.18
CeO_2-10	0.54118	68.4	12	8	0.0010	0.16

After preparation and characterization of the different ceria materials platinum loading was carried out using a SEA approach. This approach is based upon the selective adsorption of the employed metal salt on the oxide surface. This is the reason for the reported high dispersion of metal centers, all the way down to atomic dispersion.[266] The adsorption sites are generated by utilization of the amphoteric nature of oxide surfaces.[267] At ambient conditions oxide surfaces exhibit surface hydroxyl groups. These groups can be protonated or deprotonated at a given pH depending on the acidity or basicity of the oxide surface. The point at which the oxide is in its neutral state is known as *PZC*.[232] If an oxide is dispersed in a solution with a pH above the *PZC*, the surface is deprotonated, leading to a negative surface charge. Therefore it can be used as an adsorption site for cations. Accordingly, knowledge about the *PZC* is paramount for such a synthetic procedure. The so-called

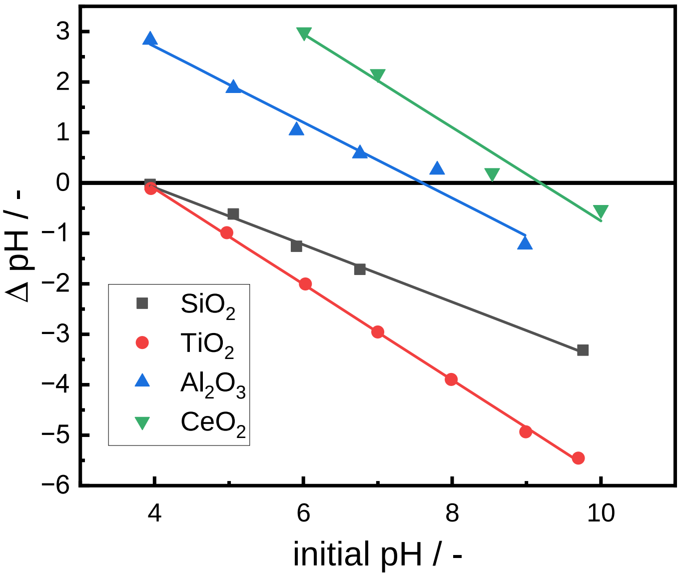

Figure 28: pH difference ΔpH as a function of the initial pH $pH_{initial}$ for SiO_2 ■ ($PZC = 4$), TiO_2 ● ($PZC = 4$), Al_2O_3 ▲ ($PZC = 8$) and CeO_2 (HSA) ▼ ($PZC = 9$)

salt addition method was used to identify the *PZC* of cerium oxides used in this work (*c.f* chapter 6.2.2). Different oxides were used to verify the methodology. The measured pH differences ΔpH for SiO_2, TiO_2, Al_2O_3 as well as for the CeO_2 sample of interest (HSA) are plotted as a function of the initial pH, $pH_{initial}$, in figure 28.

The measured PZC values obtained in this work are comparable to published PZC for these metal oxides ($PZC_{SiO_2} = 3.8$, $PZC_{TiO_2} = 3.8$, $PZC_{Al_2O_3} = 7.8$[232]), enabling the use of this methodology to study the PZC of ceria. The obtained value for the PZC of ceria of $PZC_{CeO_2} \approx 9$ means that during platinum loading a pH above 9 has to be maintained in order to adsorb the positive $Pt(NH_3)_4^{2+}$ ions. With that in mind, the different prepared oxides could be loaded. According to Resasco et al., in order to get stable single atoms on ceria, very low surface specific loadings have to be chosen.[221] In this study the authors showed that for a surface area specific loading, SD_A, of $SD_A = 0.03\,N_{Pt}/nm^2$ somewhat stable atomic dispersion can be achieved using SEA. As described in chapter 6.2.1 it was attempted to achieve a SD_A comparable to their study. With the given BET surface areas, mass specific loadings and with it the needed amount of TAPN were calculated. The obtained mass specific loadings and together with them the surface specific site densities are listed in table 15.

When comparing the obtained values for SD_A in table 15 with the target value of SD_A of $SD_A = 0.03\,N_{Pt}/nm^2$ it is evident that the obtained values are lower across all materials. This can be explained by co-adsorption of platinum salt on the glass surface of the flask. From figure 28 is can be seen that SiO_2, the main component of laboratory glass, has a

Table 15: Results for the platinum loading. $\omega_{\mathrm{Pt},SD_\mathrm{A}}$ with $SD_\mathrm{A} = 0.03\,\mathrm{N_{Pt}/nm^2}$ was calculated using $\omega_{\mathrm{Pt},SD_\mathrm{A}} = SD_\mathrm{A} \cdot N_\mathrm{A}^{-1} \cdot S_\mathrm{BET} \cdot M_\mathrm{Pt}$. Measured values $\omega_{\mathrm{Pt},measured}$ were obtained using ICP-MS, while values marked with * were calculated on basis of the respective ICP-OES value and corrected using the calibration equation equation (81).

Material	S_BET / $\mathrm{m^2\,g^{-1}}$	$\omega_{\mathrm{Pt},SD_\mathrm{A}=0.03\,\mathrm{N_{Pt}/nm^2}}$ / -	$\omega_{\mathrm{Pt},measued}$ / -	SD_A / $\mathrm{N_{Pt}/nm^2}$
CeO_2-64	160	1.56×10^{-3}	0.63×10^{-3}	0.012
CeO_2-54	109	1.06×10^{-3}	0.47×10^{-3}	0.013
CeO_2-41	71	0.69×10^{-3}	$0.34 \times 10^{-3*}$	0.015
CeO_2-34	37	0.36×10^{-3}	0.15×10^{-3}	0.013
CeO_2-15	22	0.21×10^{-3}	0.13×10^{-3}	0.019
CeO_2-10	9	0.08×10^{-3}	0.02×10^{-3}	0.007

PZC around $PZC = 4$. Thus, by using a pH value of 9 to charge the surface of ceria negatively to adsorb the positively charged platinum ion, the glass is also negatively charged. Therefore the difference can be traced back to the competitive adsorption of platinum on the wall of the flask and the dispersed redox oxide. As the surface specific loadings are comparable between each other, the lower loading values do not hamper the applicability of these materials in the study, as the SD_A is lower than the proposed value of $SD_\mathrm{A} = 0.03\,\mathrm{N_{Pt}/nm^2}$ by Resasco et al. .[221]

As already described in chapter 4.2.1 the use of SAC requires a thorough analysis of the catalysts to show that atomic dispersion was actually achieved during the preparation and that it is still maintained throughout catalysis. One of the most frequently used techniques to show that the atoms are atomically dispersed is STEM. A HAADF-STEM image of the CeO_2-54 sample is shown in figure 29.

As the materials were measured in HAADF-STEM mode, the contrast is inverted compared to classical bright-field STEM where normally heavier atoms appear darker compared to lighter atoms. Therefore, platinum ($M_\mathrm{Pt} = 195.1\,\mathrm{g\,mol^{-1}}$) should appear brighter compared to cerium ions ($M_\mathrm{Ce} = 140.1\,\mathrm{g\,mol^{-1}}$). During STEM imaging no platinum clusters were observed. Instead, atomically dispersed Pt ions were observable on the surface. A representative picture of which is shown in figure 29. A contrast line was drawn along the lattice planes to showcase this more clearly. The lines are shown in figure 70 in the appendix. Another important aspect is the positioning of the platinum ions on the ceria support. Based on the distance between the atoms, which were extracted based on the

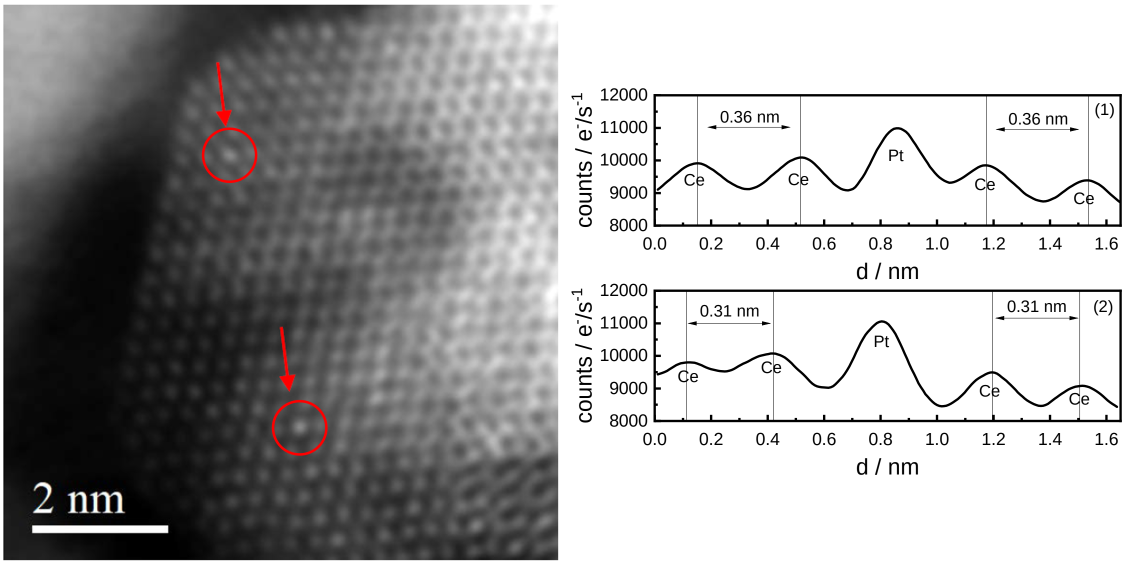

Figure 29: HAADF-STEM image of CeO_2-54 (left). Arrows indicate platinum ions. Intensity line profile along lattice plane with higher intensity for Pt ion compared to Ce ions (right), lines are shown in the appendix in figure 70.

line scans it can be concluded that platinum is coordinated on the (111) surface of cerium oxide, where the ideal Ce-Ce distance is 0.33 nm. The STEM images do suggest that the platinum ions are coordinated to ceria at lattice positions where usually ceria should be situated. Since in the calcined state platinum is reported to be present in the oxidation state IV,[221] this can be written in the *Kröger-Vink notation* as $\mathrm{Pt}_{\mathrm{Ce}}^{x}$.

To investigate the coordination environment of the platinum ions as well as the oxidation state, XAS measurements were carried out. The results are plotted in figure 30.

Comparing the white line intensities, the intensity of the absorption edge in XAS, of the pristine materials to the platinum references, the above assumption is supported. The white line intensity of the Pt-CeO_2 samples is similar to the one obtained for a PtO_2 standard material. As the white line intensity is indicative of the oxidation state of the ions on the samples, this suggests that after loading and calcination the platinum ions are indeed present in the $\mathrm{Pt}^{\mathrm{IV}}$ state. It is therefore not surprising that the platinum ions can be found at Ce-defects $v_{\mathrm{Ce}}^{''''}$ in the lattice as isovalent dopants $\mathrm{Pt}_{\mathrm{Ce}}^{x}$. This is consistent with published literature results, which showed that Pt-SAC catalysts show a $\mathrm{Pt}^{\mathrm{IV}}$ oxidation state and are located at ceria defect sites.[221,268] Using DFT calculations it was also shown by Kinch, Cabrera, and Ishikawa that the most stable adsorption site for single platinum atoms are on ceria defect sites.[269] Exposing the samples to a reduction treatment at 300 °C did lead to a reduction in white line intensity, which can be related to a loss in oxidation state. Comparing the obtained intensity to a $\mathrm{Pt}^{\mathrm{II}}$ reference sample, Pt(acac)$_2$, it can be seen that the reduced samples do exhibit similar white line intensities. This is in line with the reports

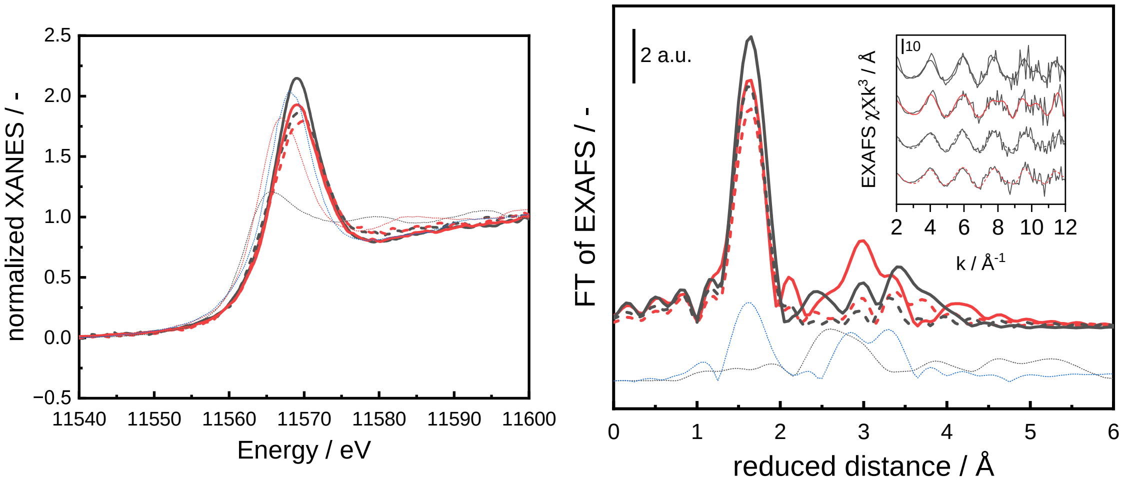

Figure 30: Pt $L3$-edge XAS results of CeO_2-64 (——) and CeO_2-54 (——) before (solid) and after 3 h reduction at 300 °C in 10 % H_2 in N_2 (dashed) compared to platinum foil (········), $Pt(acac)_2$ (········) and PtO_2 (········) in the XANES region (left) and Fourier transformation of the experimental EXAFS spectra which is shown in the insert (right).

of Resasco et al. who showed the same behavior for their SAC.[221] Juxtaposing the Fourier-transformed EXAFS spectra of the reference samples with the results obtained for the platinum-loaded ceria materials in figure 30, it can be seen that the first coordination shell of the prepared Pt-CeO_2 material does not resemble the platinum foil, but rather is similar to cubic PtO_2. Especially the most prevalent coordination at a distance of 1.97 Å, as extracted through EXAFS simulation, is comparable to values obtained for PtO_2, which show a Pt−O distance of 1.99 Å. The bond length does not change significantly either between the oxidized and reduced sample. When looking at the coordination number of the sample, although reduction slightly (≈ 0.3) decreases the extracted value, simulation of the EXAFS spectra show that roughly a coordination number of 4.0 ± 0.5 is present for materials before and after reduction. These results are consistent with literature.[164,221,268] Although it is usually necessary to investigate the second shell to see whether Pt−Pt scattering paths are present, it is not possible with the obtained measurement data. Due to the low platinum loading the low signal-to-noise ratio makes it impossible to calculate dependable values for contributions of R larger than 2.5 Å. The Pt−Pt scattering would be expected at 2.77 Å.[221] Also, as these samples were reduced *ex situ* and stored under ambient conditions, these results solely show that there is little contribution of platinum clusters to the measured X-ray absorption spectra and no large platinum clusters are present, in accordance with TEM images discussed before. These would exhibit, after harsh reduction at 300 °C, an oxidation state close to Pt^0, as shown by Resasco et al.[221] However, small clusters formed during the reductive treatment might get reoxidized when taken out of the hydrogen stream, although samples were cooled down in hydrogen.

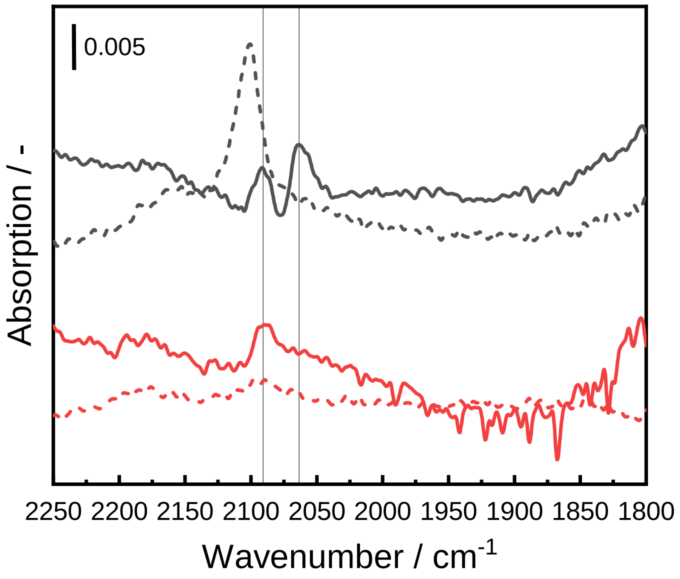

Figure 31: CO-DRIFTS spectra for degassed Pt-loaded ceria materials (——) and after reduction with 10 % H_2 in N_2 for 3 h at 300 °C (- - - -) for Pt-CeO_2-64 (——) and Pt-CeO_2-54 (——)

By using CO-DRIFTS, it is possible to show whether platinum species are indeed isolated on the surface, since the CO stretching vibration of CO is highly sensitive to the center it is coordinated to, as discussed in chapter 4.2.1. For analysis two different materials were chosen. CO was adsorbed on the surface, then any weakly bound CO was purged from the surface using nitrogen and finally DRIFTS spectra were measured. Afterwards the materials were reduced for 3 h at 300 °C *in situ* with 10 % H_2 in N_2, before cooling down to 25 °C and adsorption of CO as described in chapter 7.8. The DRIFTS spectra, obtained after subtraction of the spectra of the degassed sample, are shown in figure 31.

Looking at the CO-DRIFTS measurements shown in figure 31, the weak intensities are apparent for the two samples investigated. This is on the one hand caused by the low surface-specific loading, but also by the weak interaction of CO with isolated Pt ions.[221] Before reduction, the Pt-CeO_2-64 sample shows a band at 2100 cm^{-1}. This is consistent with studies, which traced this band back to CO adsorption on isolated, ionic Pt^{x}_{Ce} sites.[153,165,166] After reduction the band splits into two bands, one at 2090 cm^{-1} and one at 2064 cm^{-1}. The red-shift of 10 cm^{-1} can be explained by a change in the oxidation state of platinum substituted in the ceria lattice.[164,165,217,270] The band at 2064 cm^{-1} might result from platinum ions whose coordination environment did change. It was suggested by Wang et al. that when Pt^{II} single atoms on top of a CeO_2(111) surface, a CO stretching vibration of 2070 cm^{-1} would be expected.[165] Maurer et al. however calculated that Pt^{II} adsorbed on the (111) surface would lead to a stretching vibration of 2090 cm^{-1}, similar to the substituted Pt^{x}_{Ce} one, whereas Pt species adsorbed on the (110) facet would result in a much lower frequency of around 2043 cm^{-1}. The observed shift might stem from platinum ions stabilized on ceria defect sites, showing similar adsorption behaviors compared to Pt adsorbed on the $CeO_2(110)$ facet.[217] Further reduction would lead to a further red-shift of the band. Jiang et al. argued that metallic Pt atoms on the surface would exhibit values lower than 2000 cm^{-1}, which is why they attributed their low-frequency bands to partially reduced but still isolated $Pt^{\delta+}$.[164] The reduction might, however, have formed small metallic platinum clusters, which are easily reoxidizable.[221,228] These clusters would show comparable bands to the observed ones in the DRIFT spectra for Pt_1-CeO_2-64. These features however are absent for the sample Pt_1-CeO_2-54. The DRIFTS results suggest that after preparation the platinum species are present in their atomically dispersed state. However, harsh *in situ* reduction at 300 °C leads to reduction of the platinum species, which is in line with the previously discussed XANES results. The exact oxidation state of the platinum ions is hard to extract by using CO-DRIFTS only.[227] The results suggest that when reductive conditions as used in this work (300 °C using 10 % H_2 in N_2) are applied, the platinum ions are reduced almost to their metallic state. The linear adsorption modes are difficult to analyze precisely due to shifts caused by the support. One further hint to the presence of isolated platinum ions is the absence of any bridged CO bands. These bands are observed around 1999 cm^{-1}.[227,270,271] It was also reported by Kottwitz et al. that bridged CO on platinum nanoparticles shows a broad band at 1835 cm^{-1}.[226,268] Both features however were absent for the materials prepared here even after reduction of the samples. This means there is only a small amount, if any, of neighboring Pt−Pt sites after reduction. However the bridging CO band are known to exhibit lower intensities compared to linear adsorbed CO.[228] Thus, it might be the case that reduction at 300 °C in hydrogen forms small platinum-clusters on the surface of ceria, which are oxidized by the surface oxygen and thus, they do not show a significant contribution in the *ex situ* measured XANES spectrum.

XAS and CO-DRIFTS measurements point towards the fact that the prepared materials show isolated platinum ions in ceria vacancies on the surface after preparation. Reductive treatment, however, does seem to reduce the present platinum species. From the spectroscopic data presented here it is not clear, whether the platinum species are only reduced to Pt^{II} at 300 °C as proposed by Resasco et al. for isolated platinum species on ceria or whether a fraction is reduced entirely to Pt^0, forming small platinum clusters which are reoxidized under ambient conditions. The employed reaction conditions for CO oxidation experiments are significantly less reducing compared to the harsh reduction treatment employed during material analysis. This means that during catalysis the atomic dispersion is more likely to be retained compared to the harsh H_2 reduction.[213] Thus, it can be assumed that the isolated nature of the Pt ions in the as-prepared state should be stable under the reaction

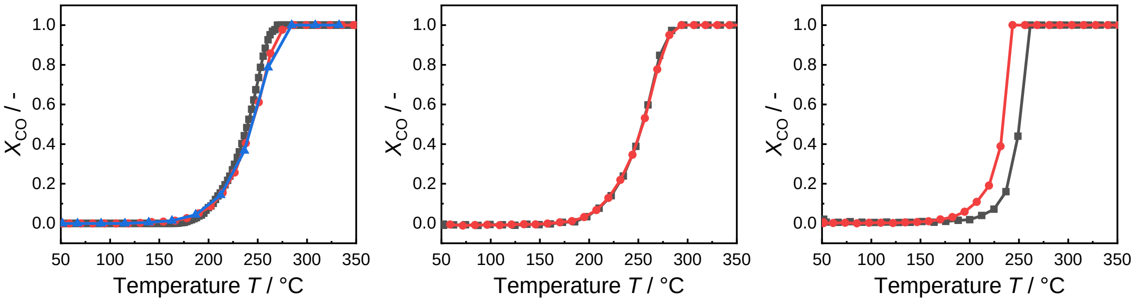

Figure 32: Multiple consecutive light-off runs for Pt_1-CeO_2-54 (left), Pt_1-CeO_2-41 (middle) and Pt0.025-Al_2O_3 (right). Run 1 (—■—), Run 2 (—●—) and Run 3 (—▲—). For the Pt_1-CeO_2-54 the heating rate was varied from 0.1 K min^{-1} (Run 1), to 0.5 K min^{-1} (Run 2) to 1 K min^{-1} (Run 3), no changes were observed due to altered heating rates.

conditions applied here. To probe this, multiple consecutive light-off curves were measured for Pt_1-CeO_2-54 and Pt_1-CeO_2-41 to show the stability of these catalysts under reaction conditions. The corresponding light-off curves are shown in figure 32.

As shown in figure 32 the light-off curves of the Pt_1-CeO_2 are highly comparable with light-off temperatures that do not deviate more than 2 K between each run. A platinum-loaded alumina reference sample, which was prepared using incipient wetness impregnation, is shown together with the results obtained for the platinum-loaded ceria materials. Whereas no change was observed for the platinum-loaded ceria materials between consecutive light-off runs, the light-off temperature was substantially lowered in the second run compared to the first one. This points towards a partial reduction of the platinum species of the platinum clusters on the alumina support. Usually for catalytic experiments Pt_1-CeO_2-54 samples are degassed in 20 % O_2 in N_2. This oxidative treatment was replaced by a reductive pretreatment, at the same temperature as employed during spectroscopic analysis, *i.e.* 3 h but using 0.5 % CO in N_2 as a reducing agent. After the reductive treatment, the sample was cooled down to the analysis temperature (light-off experiment: 50 °C; steady-state kinetic experiment 190 °C) before oxygen was added to yield the desired reaction mixture. Multiple consecutive light-off experiments and steady-state results are shown in figure 33.

Figure 33 shows that after reduction the light-off temperature is substantially shifted by 110 °C from 243 °C to 133 °C. In the following light-off runs, the light-off temperature does increase steadily (Run 2: 146 °C, Run 3: 152 °C and Run 4: 160 °C). This is in contrast to the results shown in figure 32, according to which the light-off curves did not change much between consecutive light-off cycles. This is further illustrated by comparing the obtained *Arrhenius*-type diagrams shown in figure 33. Whereas without a reducing treatment an activation energy of (105 ± 3) kJ mol^{-1} is obtained, in line with

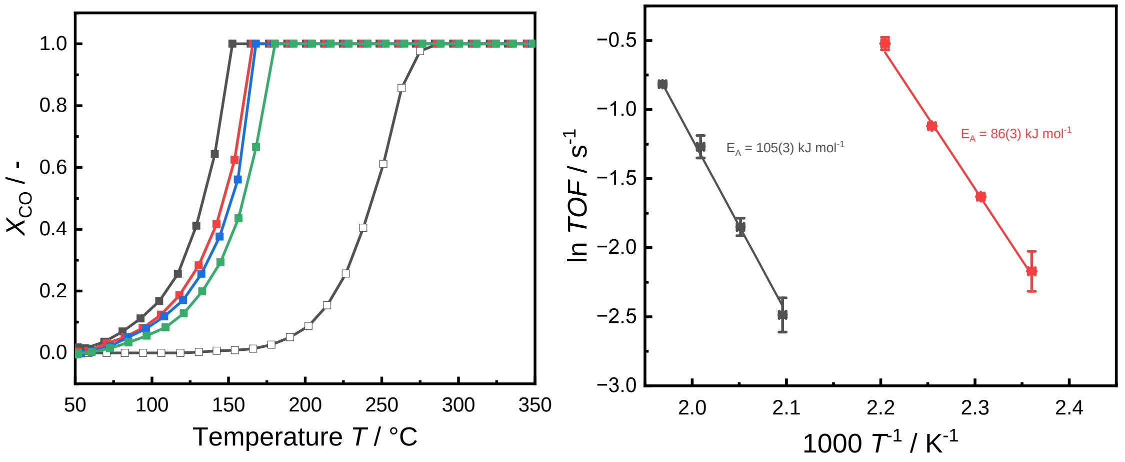

Figure 33: Successive (Run 1: —■—, Run 2: —■—, Run 3: —■— and Run 4: —■—) light-off curves after reducing treatment compared to light-off curve after oxidative treatment from figure 32 (—□—) (left) and *Arrhenius*-type plot obtained through steady-state kinetic experiments using Pt_1-CeO_2-54 after oxidative (■; $E_A = (105 \pm 3)\,\mathrm{kJ\,mol^{-1}}$) and reductive (■; $E_A = (86 \pm 3)\,\mathrm{kJ\,mol^{-1}}$) pre-treatment (right)

results obtained by Resasco et al.,[221] the sample after reductive pretreatment shows an activation energy of $(86 \pm 3)\,\mathrm{kJ\,mol^{-1}}$, which is more in line with small platinum clusters on ceria.[209] Also, the activity is enhanced by a factor of 20 (ox: $TOF_{200\,°C} = 0.07\,\mathrm{s^{-1}}$, red: $TOF_{200\,°C} = 1.43\,\mathrm{s^{-1}}$). This points towards the presence of small metallic clusters, which are known to be highly active after harsh reduction.[205] The fact that the activity decreases through successive light-off runs suggests that these clusters are probably reoxidized and redispersed very slowly. Thus, the chosen experimental conditions are oxidative enough to lead to a redispersion behavior, rather than sintering. This explains why the light-off curves are highly reproducible when an oxidative treatment is applied prior to the reaction.

To conclude, the spectroscopic, imaging and reaction-based analysis results presented here show that the prepared Pt_1-CeO_2 catalysts actually posses isolated platinum ions dispersed over the surface. The very low loading, in accordance with literature, enables the stabilization of the isolated state even at high temperatures up to 400 °C under the applied reaction conditions. However, the platinum ions on the surface are reduced to their metallic state under highly reductive atmospheres, as shown in DRIFTS and indirectly through CO light-off experiments. As the employed experimental conditions during CO oxidation are significantly less reducing due to the overstoichiometric presence of oxygen, the isolated platinum atoms can be considered to be stable in their isolated state during catalysis, which was shown during consecutive light-off cycles, enabling the derivation of ceria-based activity descriptors.

10.2. Redox Analysis of Cerium Oxide and Platinum-Loaded Cerium Oxide Compounds

After the previously discussed preparation and thorough characterization, the prepared unloaded and platinum-loaded materials were subsequently analyzed using TPR to characterize their redox properties. First, TPR profiles of the different unloaded platinum materials were measured and are depicted in figure 34.

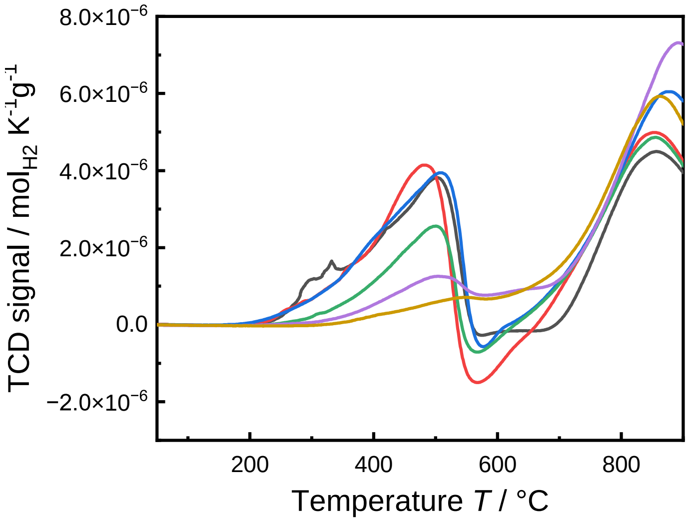

Figure 34: H_2-TPR profiles of CeO_2-64 (——), CeO_2-54 (——), CeO_2-41 (——), CeO_2-34 (——), CeO_2-15 (——) and CeO_2-10 (——)

The prepared materials show the typical reduction behavior of ceria: a low temperature reduction feature related to reduction of the surface and a high temperature reduction process, which is traced back to bulk reduction, which was already described in chapter 3.1.1. Congruent to the results discussed in chapter 9, BET surface area does not correlated with the integral of the observed surface reduction feature. Another thing which is evident from the TPR measurements shown in figure 34 is that the larger the crystallites are, the higher the temperature required for reduction of the surface is. This could be seen as a hint towards a higher activation energy for the surface reduction caused by a change of material properties. The hydrogen desorption feature around 550 °C, related to desorption of hydrogen previously adsorbed as discussed in chapter 9.1, was also evident for the high-surface area materials in congruence with the previous discussion.

When platinum is loaded onto the support, the reduction profiles change noticeably. In figure 35 the TPR profiles of the platinum-loaded samples are shown.

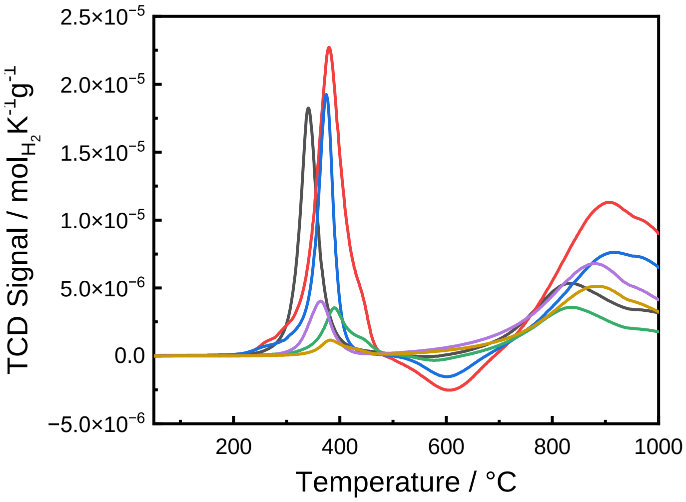

Figure 35: H_2 TPR profiles of Pt_1-CeO_2-64 (——), Pt_1-CeO_2-54 (——), Pt_1-CeO_2-41 (——), Pt_1-CeO_2-34 (——), Pt_1-CeO_2-15 (——) and Pt_1-CeO_2-10 (——)

After platinum loading the surface reduction peak maximum is shifted to lower temperatures for all materials, while the onset seems to be comparable between the loaded and unloaded samples. Not only is the reduction maximum shifted, but the reduction feature is also narrower, pointing to improved reduction kinetics, which is known for platinum-loaded ceria materials.[137] When comparing the different materials with each other it can be deduced, that the temperatures where the reduction maximum is observed (360 °C to 390 °C) are similar for all the materials, except for Pt_1-CeO_2-64, which is shifted to lower temperatures (340 °C). This hints towards comparable active sites between the different materials. The similarity between the materials can be explained by similar area specific loadings of the samples as well as similar active sites due to the atomic dispersion of platinum on the samples, as shown in chapter 10.1. The reason that the Pt_1-CeO_2-64 sample shows an earlier reduction maximum might be an earlier formation of platinum clusters as also shown in the DRIFTS experiments in figure 31. Comparing the feature attributable to hydrogen desorption between the platinum-loaded and the plain ceria samples, it can be observed that the intensity of the reversible reduction feature, discussed in detail in chapter 9.1, is more clearly seen in the Pt-loaded samples, since now the processes of surface reduction with hydrogen and desorption of hydrogen, through the shift of the reduction maximum to lower temperatures, are more separated and do not overlay as much. When atomically dispersed platinum is present in the samples the reduction behavior should not be dependent on the surface specific loading anymore, since the single platinum sites do not interact. To show this, the CeO_2-64 sample was loaded with a lower surface specific loading of platinum. The obtained reduction profile is shown in the appendix in figure 68, which shows only a slight shift. This is in contrast to nanoparticle loaded ceria materials.[137]

10.3. CO Oxidation Catalyzed by bare Ceria

As discussed in chapter 1.1 it is necessary when investigating heterogeneously catalyzed reactions, in order to draw conclusions about the catalyst, to evaluate whether measured kinetics are the true microkinetics of the solid or whether mass transport superimposes and macrokinetics are measured. Mass transport limitations can be caused by film and pore diffusion leading to a decrease of the catalyst effectiveness factor (*c.f.* equation (2)). Different approaches can be taken to prove this, which were already described in chapter 1.2 and 1.3.

A test for pore diffusion limitation is given by the *Weisz-Prater Criterion*, shown in equation (3). For the CO oxidation the criterion Ψ is calculated with equation (58)

$$\Psi = \frac{\left(\frac{d_{\text{cat}}}{2}\right)^2 \cdot r_{\text{v}}}{D_{\text{eff,CO}} \cdot c_{\text{CO}}} \tag{58}$$

where D_{eff} is given by equation (4). The calculation of the effective diffusion coefficient requires knowledge about the pore structure of the system. For that purpose Hg intrusion porosimetry measurements were carried out, the results of which are shown in figure 36 and listed in table 20.

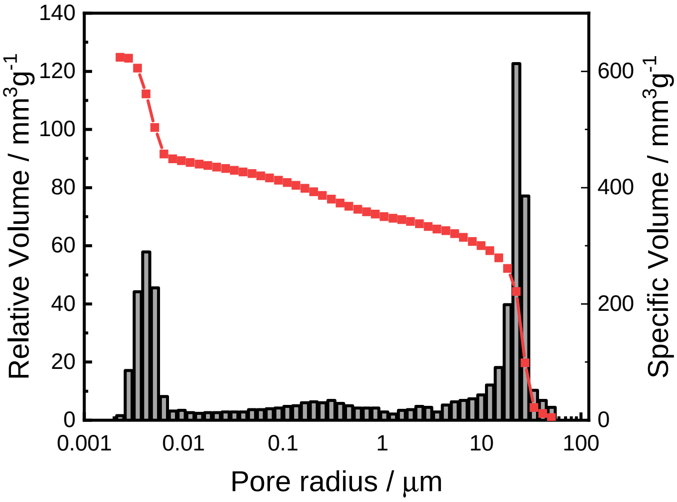

Figure 36: Mercury intrusion porosimetry results for CeO_2-64 $100\,\mu m \leq d_{\text{cat}} \leq 200\,\mu m$. The Hg porosimetry measurements yielded a surface area of $S_{\text{Hg}} = 102\,\text{m}^2\,\text{g}^{-1}$, total cumulative volume of $V_{\text{Hg}} = 0.635\,\text{ml}\,\text{g}^{-1}$, a bulk density of $\rho_{\text{Hg,bulk}} = 1.22\,\text{g}\,\text{ml}^{-1}$ and a porosity of $\epsilon = 0.774$

TEM images of the material showed that the material can be considered as non-porous primary particles which are aggregated (*c.f.* figure 27), forming voids rather than pores. Thus, the expression by Comiti and Renaud is used to calculate the tortuosity τ.[38] With the values for ϵ extracted from Hg intrusion porosimetry and a particle shape factor P given as $P = 0.49$, the tortuosity can be calculated using equation (9).[38]

$$\begin{aligned} \tau &= 1 - P \ln \epsilon && (59) \\ &= 1 - 0.49 \ln 0.774 && (60) \\ &= 1.13 && (61) \end{aligned}$$

Using differential experiments, the temperature dependence of the reaction rate r_m was determined. This enabled the calculation of the volume-specific reaction rate r_v. Free diffusion coefficients were calculated based on equation (5) and (6) for different temperatures. Subsequently these diffusion coefficients were used, employing equation (4) to calculate effective diffusion coefficients D_eff. Combined with the maximum particle diameter used in the catalytic experiments ($d_\mathrm{cat} = 200\ \mu\mathrm{m}$) as well as the previously calculated values for r_v, the *Weisz-Prater Criterion* was calculated. The obtained values are shown in figure 37 (left).

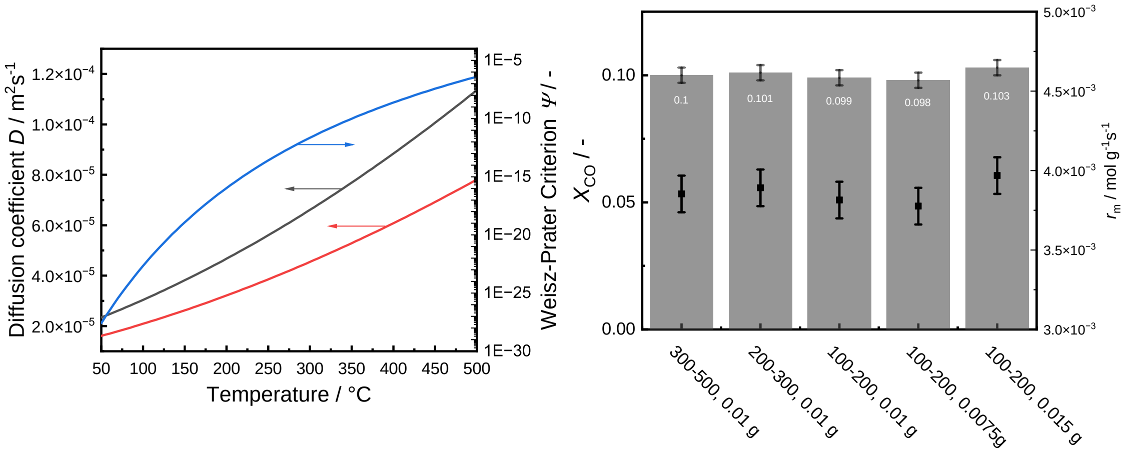

Figure 37: Calculated free diffusion coefficient $D_{\mathrm{CO}(0.1\ \mathrm{O}_2,\ 0.9\mathrm{N}_2)}$ of CO (——) and effective diffusion coefficients $D_{\mathrm{eff,CO}(0.1\ \mathrm{O}_2,\ 0.9\mathrm{N}_2)}$ (——) in a matrix of 0.1 O_2 and 0.9 N_2. Calculated *Weisz-Prater criterion* Ψ as a function of temperature (——) (left); Empirical studies for macrokinetic limitation for CeO_2-64 at 300 °C (right)

Pore diffusion limitation can be considered absent, with a pore effectiveness of more than 0.95, if Ψ values significantly lower than 1 are obtained.[17] This is indeed the case for all relevant temperatures in this work. Furthermore, since pore diffusion is absent, also film diffusion limitation is absent as well, as diffusion limitation starts with pore limitation before film diffusion is occuring.[18] Thus, it can be assumed that when measuring kinetics the measured reaction rate is dominated by the microkinetics, rather than the macrokinetics. It was also attempted to show this experimentally by varying the flow rate $\dot{V}$ while keeping the residence time constant, as well as varying the secondary particle size at constant residence times. The first variation is to show whether measured reaction rates are limited by film diffusion, whereas the second one aims to show the absence of pore diffusion experimentally. The experiments are designed in a way that when no mass transport limitations are present, the observed conversions and with it calculated reaction rates should be the same. The results of these experiments are also shown in figure 37. Indeed, the results are congruent with the calculations, showing that neither film diffusion, nor pore diffusion are present. Further experiments can thus be used to derive structure-property relationships without having to consider mass-transport processes.

It is notoriously difficult to compare the activity of polycrystalline materials between different studies. However, it is necessary to validate the activity measurements in this work. As mentioned before, it is possible to prepare facet-enriched ceria. These materials, due to their defined surface properties, can be used to compare results obtained in this work with literature. Cerium nanocubes were synthesized according to literature.[272] After preparation, the material was analyzed using N_2 physisorption as well as TEM, before measuring CO oxidation light-off curves. A TEM image shown in figure 38 shows the successful preparation of nanocubes, while N_2 physisorption revealed a surface area of $S_{\mathrm{BET}} = 25\,\mathrm{m}^2\,\mathrm{g}^{-1}$, which is the same BET surface area as measured in the published preparation recipe.[272]

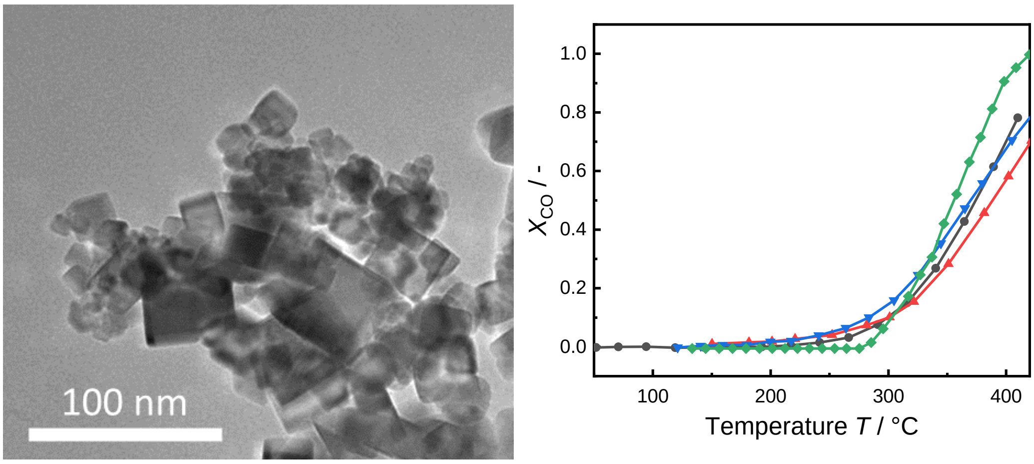

Figure 38: TEM image of prepared CeO_2-NC (left) and CO oxidation activity (right) of prepared CeO_2-NC (—●—) in comparison to studies of ceria nanocubes by Konsolakis and Lykaki[198] (—▲—), Wu, Li, and Overbury[194] (—▼—) and Lykaki et al.[244] (—■—).

In the representative TEM image depicted in figure 38, the cubic structure of the ceria nanocubes is evident showing that the preparation was successful and led to materials that can be compared to literature results. After preparation a light-off curve of the nanocubes in the experimental setup was measured. When comparing the measured CO oxidation light-off behavior of the prepared nanocubes, the results obtained here show highly comparable results to literature, as shown in figure 38. This proves that the self-built setup can be used to analyze activity of different ceria materials and compare these to literature results.

After investigation of the redox properties the prepared polycrystalline ceria materials were tested for their CO oxidation activity. Light-off curves of the different unloaded ceria materials were measured and are shown in figure 39.

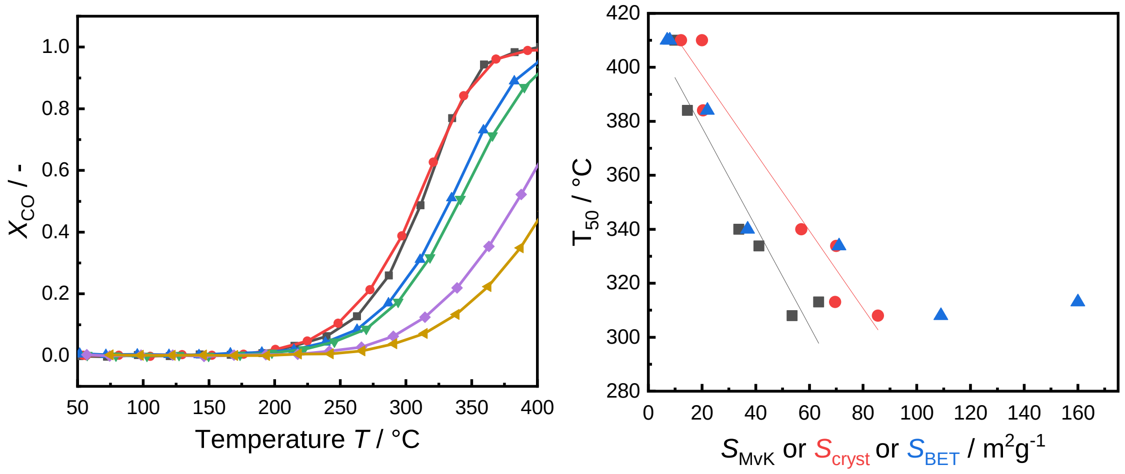

Figure 39: Light-off curves of different unloaded ceria materials CeO_2-64 (—■—), CeO_2-54 (—■—), CeO_2-41 (—■—), CeO_2-34 (—■—), CeO_2-15 (—■—), CeO_2-10 (—■—) (left) and light-off temperature T_{50} as a function of S_{MvK} (■), S_{cryst} (●) and S_{BET} (■) (right)

Comparing the measured light off curves with the H_2-TPR profiles of the different samples from figure 34 shows that the CO oxidation activity is closely related to the reduction onset of the different materials. This can easily be explained by the proposed MvK mechanism. As the oxidation of CO commences by reduction of the redox catalyst rather than direct oxidation through an ER or LH mechanism, the ceria lattice has to release oxygen in order to close the catalytic cycle. This explains why the reaction onset is directly related to the oxygen release properties of the ceria material.

The light-off curves shown in figure 39 were measured, as described in chapter 7.12.1, at constant modified residence times τ_{mod} of $\tau_{mod} = 120000\,g\,s\,m^{-3}$. Since the materials vary in their specific surface areas the active surface area in the reactor deviates between the measurements. When the light-off temperatures, the temperatures where a conversion

Table 16: Results of the CO oxidation experiments for the different cerium oxide materials, value marked with * are extrapolated values due to the temperature limitation of the used aluminum heating block of the reactor.

Sample	T_{50} / °C	$E_{\mathrm{A,app}}$ / kJ mol^{-1}	$TOF_{315\,°\mathrm{C}}$ /s^{-1}
CeO_2-64	313	76 ± 1	0.011
CeO_2-54	308	73 ± 1	0.010
CeO_2-41	334	79 ± 1	0.011
CeO_2-34	340	79 ± 2	0.007
CeO_2-15	384	81 ± 1	0.003
CeO_2-10	410*	94 ± 2	0.002

of $X_{\mathrm{CO}} = 0.5$ is reached, which are listed in table 16, are compared between the different materials, they show similar but slightly displaced linear trend which is obtained when plotting the light-off temperature as a function of the MvK active surface area and as a function of the crystallite surface area derived from crystallite size listed in table 13 and 14. This shows, although deviations are present, that the concept of a theoretical crystallite surface can be used to approximate the redox-active surface area. When these curves are compared to the light-off temperature as a function of the BET surface area it is evident that light-off temperature can not be described sufficiently by the measured BET surface area., which is also evident from figure 39 and consistent with the previously discussed results.

To investigate this further, steady-state kinetics investigations were carried out as described in chapter 7.12.2. To evaluate the temperature dependence of the reaction rate the natural logarithm of the mass specific reaction rate r_{m} is plotted as a function of the inverse absolute temperature T $1/T$in figure 40.

From the *Arrhenius*-type plots shown in figure 40, the apparent activation energies $E_{\mathrm{A,app}}$ can be extracted from the slope m_{fit} of the linear fit function using equation (62)

$$E_{\mathrm{A,app}} = -m_{\mathrm{fit}}\,\mathrm{R}. \tag{62}$$

The calculated values for the apparent activation energies are listed in table 16 while the errors were calculated from the standard deviation of the linear regression. Comparing the

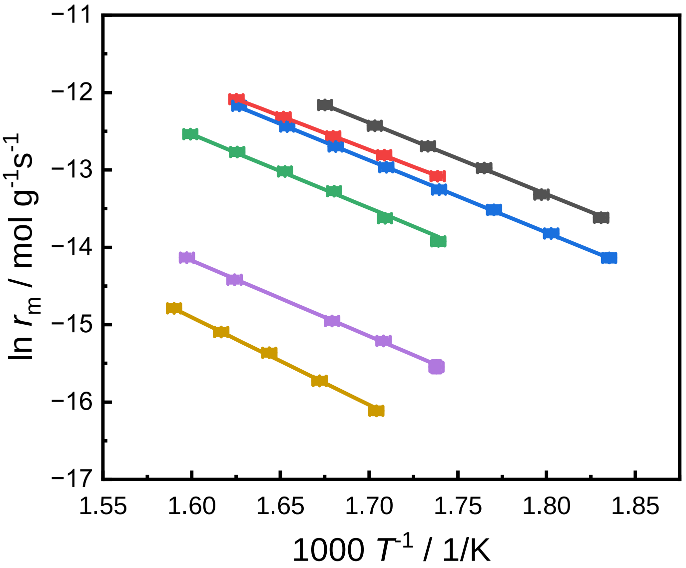

Figure 40: *Arrhenius*-type plot of steady state kinetic measurements of CeO$_2$-64 (⬛), CeO$_2$-54 (🟥), CeO$_2$-41 (🟦), CeO$_2$-34 (🟩), CeO$_2$-15 (🟪) and CeO$_2$-10 (🟨) and linear fit used to calculated activation energies listed in table 16

activation energies it is evident that the material properties do influence the CO oxidation activity. Compared to reported literature values, the values obtained are mostly comparable to other studies on polycrystalline ceria materials. Only CeO$_2$-10 showed a slightly higher value compared to the values reported in literature. Aneggi et al. and Kim et al. reported activation energy values of about 85 kJ mol^{-1} for their material with large crystallites and low surface area samples.[119,273] However, it was shown that their high temperature treatment led to a surface faceting in their materials, since very low surface areas and large crystallites were only obtained with temperatures above 700 °C which is given as the threshold for surface restructuring.[119] In this study it was attempted to remain below this threshold to avoid surface restructuring. Therefore, the higher activation energies might be a result of large crystallites without enriching the surface with highly active facets.

The vast difference in mass specific reaction rates plotted in figure 40 can in part be explained by the different *Mars-van-Krevelen* active surface areas S_MvK which the oxides exhibit (*c.f.* table 14). Therefore it is necessary to compare the site specific reaction rates, represented by the *TOF*. These can be calculated from the mass specific reaction rates r_m using equation (43). As the measured TOSC$_{500\,°\mathrm{C}}$ values represent a mass specific site density SD_m the difference in active surface area between the materials is accounted for by the TOF calculation, which is expressed as mole of converted CO per mole of surface oxygen centers per second. The site specific turnover rates are plotted in figure 41.

Comparing the mass specific and site specific reaction rates in figure 40 and 41 the differ-

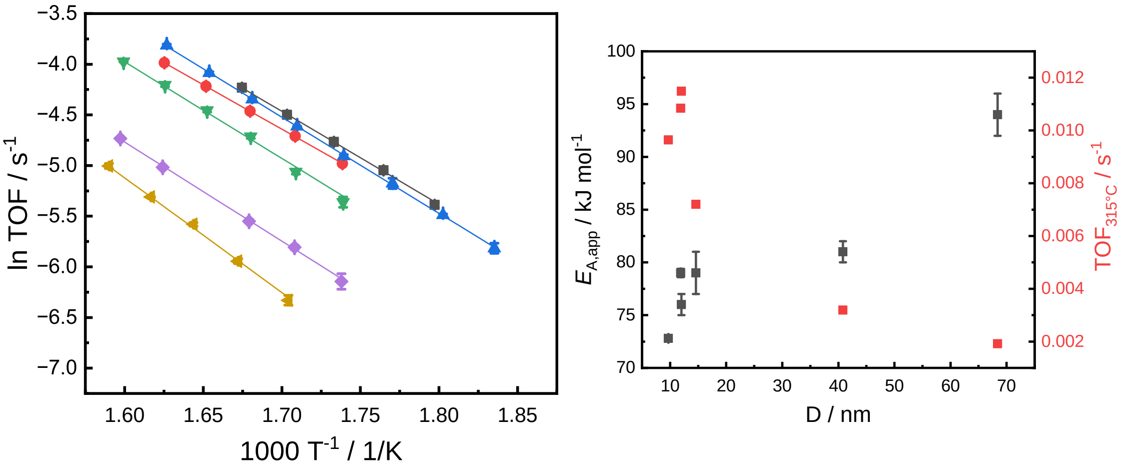

Figure 41: *Arrhenius*-type plot of steady-state kinetic measurements of CeO_2-64 (■), CeO_2-54 (🟥), CeO_2-41 (🟦), CeO_2-34 (🟩), CeO_2-15 (🟪) and CeO_2-10 (🟨) (left) and plot of the extracted activation energy $E_{\mathrm{A,app}}$ (■) and $TOF_{315\,°\mathrm{C}}$ (🟥) as a function of the crystallite size.

ence between the materials got smaller, since now the contribution of different surface areas is accounted for. However, there are still differences between the materials observable. As discussed previously, it was reported in literature that high temperature calcination might lead to more active exposed surface sites, through surface faceting.[119] This can not be observed in the results obtained here. Instead, materials calcined at higher temperatures, so materials with larger crystallites, showed lower site specific activity compared to materials calcined at low temperatures. This is in line with theoretical calculations, predicting that the oxygen vacancy formation energy decreases with decreasing particle size.[274,275] When comparing the activation energies between the materials, listed in table 16, and the respective material properties from table 14, a somewhat good correlation can be found between the crystallite size and the activation energy as well as the turnover frequency. The dependence of E_{A} is plotted as a function of D in figure 41. The results show that with increasing crystallite size, the activation energy does indeed, as predicted in literature, increase. This is at the same time accompanied by a decrease in site-specific turnover rate at 315 °C. As discussed previously, separating the strain and size distributions in nanocrystalline materials is difficult as these do indeed influence each other. When comparing the activation energy and site-specific turnover rates as a function of the bulk defect concentration extracted from *Raman* spectroscopy I_{600}/I_{464}, which is also shown in the appendix in figure 67, a correlation can be observed as well. The most sensible explanation for the observed dependencies would be the aforementioned decrease in vacancy formation energy with decreasing crystallite size, whereas the intrinsic activity might be better described as a function of the defect concentration. With an increase in defects the $\mathrm{Ce{-}O}$ bond length is increased, leading to an easier removal of oxygen, which was also shown for ammonia oxidation.[276] The observed plateauing of the turnover frequency with increasing defect concentration might be explainable by the fact that if the defect concentration is too high, the extraction of oxygen might be decreased again through strain effects in the material.[172]

To investigate this further, partial pressure dependencies of reaction rates were probed, since there is almost no data published on the reaction order of cerium oxide materials. The studies published, suggest a reaction order between 0.5 to 1 for CO and 0 for O_2 for unloaded ceria.[189,193] This was investigated for three different ceria materials to see how the partial pressure dependence of the reaction rate changes with material properties.

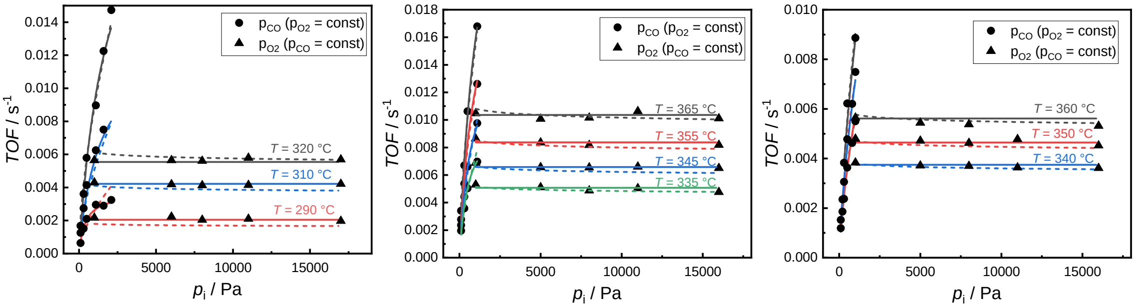

Figure 42: Partial pressure dependence of the site specific reaction rate TOF for CeO_2-54 (left), CeO_2-34 (middle) and CeO_2-10 (right). ▲ variation of oxygen partial pressure at constant $p_{CO} = 500\,\mathrm{Pa}$ and ● variation of CO partial pressure at constant $p_{O_2} = 11000\,\mathrm{Pa}$ at different temperatures. - - - - represents a power-law fit (equation (63)) of the reaction rate, while —— is a fit based on an *Eley-Rideal* mechanism (equation (64)) for different indicated temperatures.

The dependencies of the TOF on the partial pressure depicted in figure 42 shows that the reaction orders obtained are comparable to the ones published in literature for all materials measured. Whereas a reaction order of $n_{O_2} = 0$ is roughly observed for all materials independent of the temperature, the reaction rate is strongly influenced by the CO concentration. Using a double logarithmic plot of the obtained reaction rates as a function of partial pressure, it could be observed that indeed the reaction order n_{O_2} is independent of the temperature approximately 0, whereas the CO reaction order increases with increasing temperature. Based on the general power law description equation (10) to describe the partial pressure dependence of the reaction rate r and the *Arrhenius* equation (equation (11)) to describe the temperature dependence of the reaction, the measured reaction rates were fitted using equation (63)

$$r = k_0 \cdot e^{\frac{E_A}{RT}} \cdot p_{CO}^{n_{CO}} \cdot p_{O_2}^{n_{O_2}} \quad . \tag{63}$$

The result of this fit is plotted in figure 42 as the dashed line. As the power law kinetics can not describe a dependence of the reaction orders on temperature, but assumes a constant reaction orders, it is hardly surprising that the fit obtained for the different temperatures is not optimal. Therefore a mechanistic model was used to fit the reaction data obtained in differential mode. Generally, the MvK is proposed for ceria-based catalysts as described in chapter 3.3. However, the independence of the reaction rate on p_{O_2} under the chosen lean conditions does not allow to model the contribution of oxygen partial pressure on the reaction rate. Therefore, an ER mechanism was used to fit the reaction data as it was already proposed for CO oxidation catalyzed by other ceria containing systems.[193] This assumes the reoxidation of the ceria is significantly faster than the surface reduction step, which is known from literature.[190] The expression used for the fit is shown in equation (64)

$$r = \frac{k_0\, \mathrm{e}^{\frac{E_\mathrm{A}}{\mathrm{R}T}} \cdot K_\mathrm{CO} p_\mathrm{CO} \cdot p_{\mathrm{O}_2}^{n_{\mathrm{O}_2}}}{1 + K_\mathrm{CO} p_\mathrm{CO}}. \tag{64}$$

When fitting the reaction rate as a function of the partial pressure dependence using a power law approach (c.f. equation (10)) an insufficient description of the reaction rate for the different temperatures was obtained. This is not surprising since the partial pressure dependence of the reaction is, as previously discussed, a function of temperature, which is not considered when describing the kinetics using equation (63). Since equation (64) can describe this temperature dependence and also has more degrees of freedom (six parameters fitted) compared to the power law (four parameters fitted) it is hardly surprising that a better fit is obtained when using equation (64). The parameters obtained through fitting with the ER rate equation in equation (64) are given in table 17 and were used to simulate light-off curves for the different materials, which are shown in figure 43.

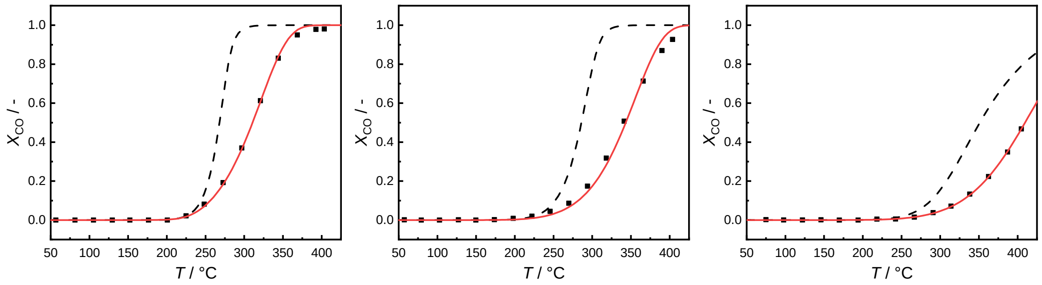

Figure 43: Simulated light-off curves using equation (64) and parameters obtained from the partial pressure dependence listed in table 17 (*c.f.* figure 42) (----) and measured CO conversion as a function of temperature (■). Fitted expression using equation (65), considering CO_2 competitive adsorption (——) for CeO_2-54 (left), CeO_2-34 (middle) and CeO_2-10 (right)

Comparing simulated and measured light-off curves shown in figure 43 it is evident that, although the reaction onset is described mostly correct, the simulated curve shows a steeper increase in CO conversion with temperature compared to the measured one. As the ramping speed with $1\,\mathrm{K\,min^{-1}}$ is slow enough a hysteresis due to too high ramping speeds is unlikely. The rates in figure 42 and were measured in differential mode. Since conversion is kept below $X_{\mathrm{CO}} = 0.1$, the CO_2 partial pressure is comparatively low. Therefore CO_2 desorption might be a possible limiting factor for the reactivity at higher conversions. To probe this, CO_2 desorption experiments on prereduced ceria were carried out. The measured CO_2 desorption profiles are shown in figure 44.

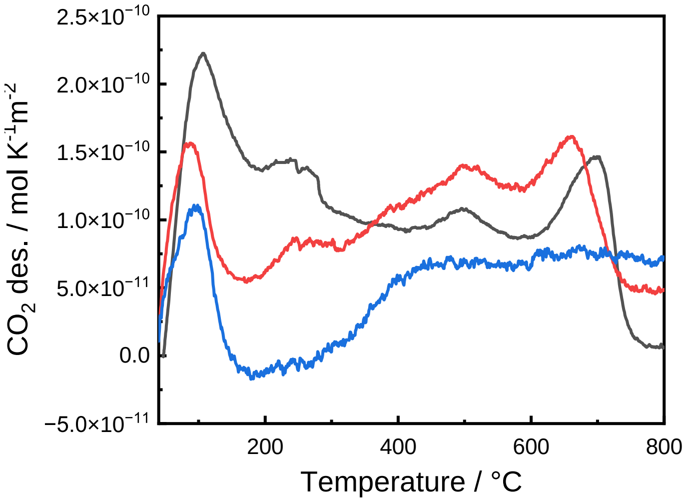

Figure 44: CO_2 desorption profiles of prereduced (*c.f.* chapter 7.11.3) CeO_2-54 (——), CeO_2-34 (——) and CeO_2-10 (——)

Ceria materials are known to exhibit basic surface properties, enabling the formation of surface carbonates upon CO_2 adsorption. This strong adsorption behavior is also evident in figure 44. There are multiple distinct features in the desorption profile. A low temperature feature around 100 °C, a feature at around 250 °C as well as high temperature features at 500 °C and 650 °C were observed. IR studies by Binet et al. suggest that desorption around 100 °C might be related to bidentate carbonates, whereas monodentate carbonates decompose at around 200 °C and polydentate carbonates at even higher temperatures.[261] Solely a desorption feature at 100 °C is reported for fully oxidized ceria materials. The artificial introduction of La^{III} ions in the study of Bernal et al. however led to similar CO_2 desorption profiles observed for the profiles measured for reduced ceria here.[277] Similar to La^{III}, the Ce^{III} ions formed through reduction of ceria exhibit significantly stronger *Lewis* basicity compared to Ce^{IV}. Thus, this strong CO_2 adsorption behavior of ceria catalysts points towards a possible competitive adsorption between CO_2 and CO, resulting in a

Table 17: Estimated parameters by using equation (64) and equation (65) for the different materials

Material	k_0	$E_{\mathrm{A,app}}$	A_{CO}	Q_{CO}	$n_{\mathrm{O_2}}$	$A_{\mathrm{CO_2}}$	$Q_{\mathrm{CO_2}}$
	$\mathrm{s^{-1}}$	$\mathrm{kJ\,mol^{-1}}$	$\mathrm{s^{-1}}$	$\mathrm{kJ\,mol^{-1}}$	-	$\mathrm{s^{-1}}$	$\mathrm{kJ\,mol^{-1}}$
CeO_2-54	3.26×10^{11}	148.4	1.19×10^{-12}	98.2	0.0	7.00×10^{-12}	110.2
CeO_2-34	1.66×10^{9}	130.7	5.09×10^{-11}	88.3	0.0	4.00×10^{-12}	120.0
CeO_2-10	6.16×10^{8}	126.4	4.43×10^{-11}	86.7	0.0	6.00×10^{-12}	120.4

product inhibiting behavior. This was tested by adding a CO_2 adsorption term to the kinetic expression in equation (64), yielding equation 65:

$$r = \frac{k_0 \cdot \mathrm{e}^{-\frac{E_{\mathrm{A,app}}}{RT}} \cdot K_{\mathrm{CO}} p_{\mathrm{CO}} \cdot p_{\mathrm{O_2}}}{1 + K_{\mathrm{CO}} p_{\mathrm{CO}} + K_{\mathrm{CO_2}} p_{\mathrm{CO_2}}} \quad . \tag{65}$$

Equation (65) considers the oxidation reaction to be still irreversible as the CO_2 reduction rate $r_{\mathrm{CO_2-red}}$ can be considered very slow compared to the CO oxidation rate $r_{\mathrm{CO-ox}}$ at the investigated temperatures. But by introducing a term considering the CO_2 competitive adsorption, the reaction rate decreases with increasing CO_2 partial pressure $p_{\mathrm{CO_2}}$. Using the measured light-off curves, the adsorption term of CO_2 was fitted while the other parameters were held constant according to the values determined by fitting equation (64). Through integration of the rate law, conversions for different temperatures were calculated and plotted in figure 43. It can be shown that just by adding the CO_2 adsorption term, the light-off behavior can be fitted comparatively well. The obtained additional parameters $A_{\mathrm{CO_2}}$ and $Q_{\mathrm{CO_2}}$ from the fit are also listed in table 17.

Since only the terms for CO_2 adsorption were fitted, this rate law is still able to describe the partial pressure dependence measurements shown in figure 42. When comparing the different parameters in table 17, obtained through fitting of the measured steady-state rates as well as fitting the light off curves by CO_2 adsorption, trends in some of the parameters can be observed. First, the physical meaningfulness of the obtained heat of adsorption values has to be established. Adsorption CO_2 on CeO_2 differs between the oxidized and reduced states. It is known that reduction of a reducible support leads to an increase in *Lewis* basicity, due to formation of two unpaired electrons.[278,279] It is therefore not surprising that the adsorption strengths of CO_2 differ between reduced and oxidized ceria. Using

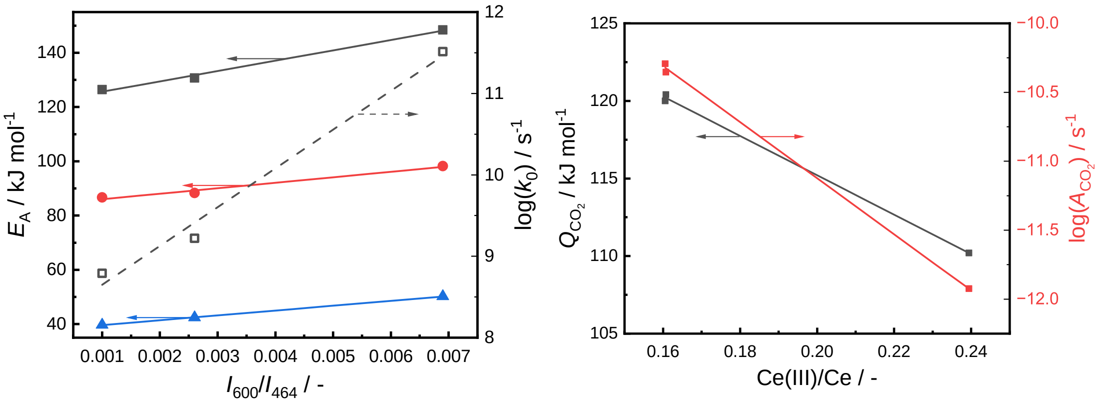

Figure 45: Activation energy E_A (■), adsorption energy of CO, Q_{CO}, (●) and difference $E_A - Q_{CO}$ (▲) as well as logarithm of pre-exponential factor $\log k_0$ (□) as a function of the intensity ratio of the bulk defect concentration (I_{600}/I_{464}) (left) and adsorption energy of CO_2 (■) and preexpontential factor $\log A_{CO_2}$ (■) as a function of the surface defect concentration measured through XPS (right).

DFT calculations, CO_2 adsorption energies can be calculated. Cheng et al. calculated adsorption energies of CO_2 on reduced ceria of 100 kJ mol^{-1} and 119 kJ mol^{-1} depending on the vacancy association state.[280] This is similar to values published by Kumari et al. who postulated an adsorption energy of 123 kJ mol^{-1}.[281] These values are similar to the values obtained by fitting the kinetic measurements shown in table 17. It was also discussed in literature that desorption of CO_2 only occurs upon reoxidation of the reduced oxide.[282] However, experimental studies also showed that while adsorbed carboxylates do reoxidize the support readily at low temperatures, surface carbonates do limit the reoxidation of the oxide support.[283] These literature findings all align well with the results obtained here. For cerium oxides, the *rds* is frequently reported to be the oxygen vacancy formation.[284,285] A thorough DFT study showed that surface carbonate formation (*i.e.* carbon monoxide activation) and oxygen vacancy formation do have similar activation barriers of 44 kJ mol^{-1} and 45 kJ mol^{-1}. When $p_{CO}K_{CO} \ll 1$, essentially assuming a first reaction order regarding CO, the activation energy can be calculated as the difference between E_A and Q_{CO}.[193] This yields values between 40 kJ mol^{-1} and 50 kJ mol^{-1} for the kinetic parameters in table 17, which is close to the theoretically predicted value by Kim et al.[273]

Using the material parameters for the different materials listed in table 14 together with the obtained kinetic parameters in table 17, structure-property relationships can be derived. Plotting the different activation and adsorption energies against I_{600}/I_{464}, representing the bulk defect concentration given by *Raman* experiments, as well as against the surface Ce(III) concentration from XPS measurements yield the plots shown in figure 45. It can be seen that the activation energy, as well as the heat of adsorption of CO can be well described by the bulk defect concentration. With increasing bulk defect concentration E_A,

Q_{CO} as well as k_0 all increase as well. Defects in the ceria lattice usually lead to an increase in lattice expansion, which is described to lead to a larger barrier for the reduction,[172] which can explain the larger activation energy. The increase of the pre-exponential factor k_0 and heat of adsorption of CO with increasing bulk defect concentration might be attributable to the increased *Lewis* basicity of the oxide with increasing defect concentration.[279] Increased *Lewis*-basicity would lead to stronger backbonding to CO. The kinetic parameters extracted for CO_2 adsorption on the other hand can be described quite well with the results from XPS. It was previously discussed that the desorption of formed CO_2 or adsorption of CO_2 from the gas phase might hamper the reoxidation rate. However, it is known that oxygen can adsorb and be activated on surface point defect Ce^{III} sites.[178,179,286] Thus, the trend might be explained by a higher degree of oxygen activation and an increase in reactive oxygen species leading to reoxidation through their surface mobility and thus, lower inhibition through CO_2 with increasing surface defect concentration.

Comparing the trend extracted from the *Arrhenius*-type plots with the activation and adsorption energies obtained through the mechanistic fits discussed above, an inverse relationship with the defect concentration is observed. This points towards the assumption, that it is not enough to use the apparent activation energy, obtained by using *Arrhenius*-type plots, to derive structure-property relationships, but rather requires a more in-depth analysis of the obtained reaction rates. It was also assumed that CO_2 adsorption was negligible at low conversions during the kinetic experiments in differential mode due to the very low CO_2 concentration. However, this as well as the assumption of 0th order towards CO during differential kinetic analysis of the measurement data, introduces errors in the analysis. Thus, co-feed experiments with an additional CO_2 dosing are required to further strengthen the assumptions made here.

10.4. CO Oxidation Catalyzed by Platinum-Loaded Ceria Catalysts

As described in chapter 4.2 it is difficult to derive structure-property relationships from nanoparticle loaded cerium oxides because of the highly dynamic behavior of the Pt-Ce interface due to redispersion of platinum under oxidizing conditions.[205,213] Although single-platinum atoms are known to be less active than metallic platinum clusters due to their lower electron density, it should still yield important insights into how the ceria material does influence the CO oxidation kinetics during TWC operation. In combustion engine cars, water is always present in the exhaust gas due to the combustion of alkanes. Aside from present molecular oxygen, water can act as an oxidant for reduced ceria materials.[141,171]

Since water reduction does not require the breakage of the stable oxygen double bond, the reduction of water was reported to be the preferred way of reoxidation during reaction. The aim of this work was to attempt to assess whether the material parameters of the ceria support influence the degree to which presence of water does influence the activity of the materials.

As described previously a SEA approach was employed to prepare atomically dispersed platinum centers on the different cerium oxides. Structural and spectroscopic investigation of these materials revealed that the platinum species are indeed atomically dispersed, and stay in their atomically dispersed state under the chosen lean reaction conditions (*c.f.* chapter 10.1). Thus, kinetic data can be normalized by the total number of platinum atoms on the surface of the catalyst as the dispersion is 1 for SACs. With a stable atomic dispersion and therefore constant platinum-cerium interface, it is possible to derive structure-property relationships related to the oxide, since differences in activity can now be traced back solely to the oxide support. Congruent to the investigation of bare ceria materials discussed in chapter 10.3 initial activity tests were done based on light-off experiments. In order to assess how water influences the activity related to the material properties of the oxide, these experiments were carried out in dry as well as wet feed gas. The obtained light-off curves are shown in figure 46.

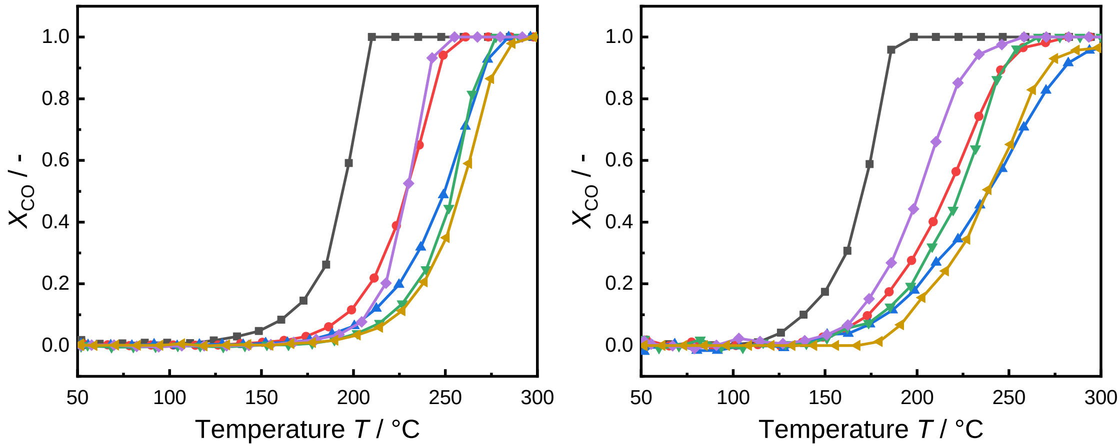

Figure 46: Light-off curves of different platinum-loaded ceria materials CeO_2-64 (—■—), CeO_2-54 (—■—), CeO_2-41 (—■—), CeO_2-34 (—■—), CeO_2-15 (—■—), and CeO_2-10 (—■—) with dry feed gas (left) and wet feed gas (right), light-off temperatures T_{50} are listed in table 18.

Comparing the light-off curves between the unloaded ceria materials in figure 39 and the light-off behavior after platinum loading in figure 46, the light-off temperatures T_{50} shift significantly to lower temperatures as shown in table 18. Not only does the light-off temperature itself change, but the slope of the light-off curve becomes steeper as

Table 18: Light-off temperatures of CeO_2 (*c.f.* table 16) and Pt_1-CeO_2 catalysts in dry and wet feeds

Material	$T_{50,\text{unloaded}}$ / °C	$T_{50,\text{dry}}$ / °C	$T_{50,\text{wet}}$ / °C
Pt_1-CeO_2-64	313	194	170
Pt_1-CeO_2-54	308	229	217
Pt_1-CeO_2-41	334	250	239
Pt_1-CeO_2-34	340	254	223
Pt_1-CeO_2-15	384	229	202
Pt_1-CeO_2-10	410	258	239

well, compared to the unloaded oxide. When comparing the obtained light-off behavior with values from literature listed in table 6, the obtained T_{50} values are congruent with literature values (*c.f.* table 5 and 6). Therefore, as discussed in chapter 4.2, the light-off temperatures observed for the here prepared materials are around 100 K higher compared to Pt-nanoparticle loaded ceria materials.[213]

When comparing the actual obtained light-off temperatures, which are listed in table 18, it is evident that between the unloaded and loaded materials the T_{50} values shift differently for the different oxide supports which hints towards a change in activity due to the respective oxide properties. When water is added to the feed gas, the light-off temperatures are only slightly lowered. This phenomenon was already reported in literature.[171] However, comparing the shift observed for materials prepared in this work, which varies around 20 K, to literature values the reported shifts are larger in Wang et al. study, who reported a shift of 70 K. The authors of that study used highly-loaded materials, which showed very low light-off temperatures. This points towards the presence of small platinum clusters in their materials.[217,221] It is known that metallic clusters which are formed under CO oxidation conditions, activate CO more effectively compared to Pt_1-CeO_2 materials. Thus, the influence of the reoxidation becomes even more pronounced, which might explain the smaller shift observed in the data presented here. Negligible WGS activity was found during their kinetic experiments below 200 °C, which is in line with other published results on highly-dispersed platinum-loaded ceria.[165,287] Wang et al. proposed a mechanism through which CO oxidation rate would be increased by water as a mediator (water-mediated MvK).[171] Using DFT calculations coupled with experiments they proposed dissociation of water atop of a cerium ion, forming two hydroxyl groups, one vicinal and one lattice hydroxyl group. The vicinal OH group subsequently reacts with the CO adsorbed on the platinum single site forming a carboxyl intermediate. The carboxyl group is subsequently dehydrated through the lattice hydroxyl group initially formed by water adsorption, thus releasing CO_2 and H_2O, forming an oxygen vacancy which subsequently can be refilled.[171] This is in direct contrast to a mechanism following the WGS activity, also reported for Pt_1-CeO_2 catalysts.[288] In comparison to the mechanism proposed by Wang et al., WGS is accompanied by consumption of water and formation of hydrogen through reaction 23

$$CO + H_2O \rightleftharpoons CO_2 + H_2 \cdot \qquad [R\ \mathbf{23}]$$

The difference between the two mechanisms is therefore the observed consumption of water. While the water-mediated MvK mechanism for CO oxidation does not coincide with net water consumption, the WGS reaction would be accompanied by a stoichiometric conversion of water to H_2 following reaction (23). However, as the formed hydrogen would subsequently be reoxidized due to the lean experimental conditions the contributions of the different mechanisms would require separate WGS experiments, which were not carried out.

The changed slope of the light-off curves in the presence of water points towards a change in activation energy. The difference between the different ceria materials points towards a change in influenceability of the reaction rate based on the material parameters of the oxide. To investigate this further, steady-state kinetic investigations of the platinum-loaded samples were carried out in dry and wet feeds. From the measured CO conversions, site specific turnover rates TOF were calculated using equation (38) to (42). By plotting the natural logarithm of the obtained TOF against the reciprocal absolute temperature, *Arrhenius*-type plots were obtained through these experiments as depicted in figure 47.

Comparing site specific turnover rates as a function of temperature obtained for materials prepared in this work to literature values, it can be observed that the TOF values obtained here are in good agreement with published literature (*c.f.* figure 71). Between the different materials in this work, it is evident that most of the materials exhibit similar slopes as a function of temperature. When activation energies are calculated from the obtained fits, which are listed in table 19, indeed the calculated activation energies $E_{\mathrm{A,app}}$ are similar between the materials at $(100 \pm 5)\,\mathrm{kJ\,mol^{-1}}$, except for material Pt_1-CeO_2-10. As already discussed in context of the light-off experiments the high activation energies obtained for these materials can be traced back to the lower electron density of platinum and therefore decreased activating capability of the single-platinum atoms compared to metallic Pt^0 found in clusters and particles. Especially as Pt clusters and nanoparticles are reported to be

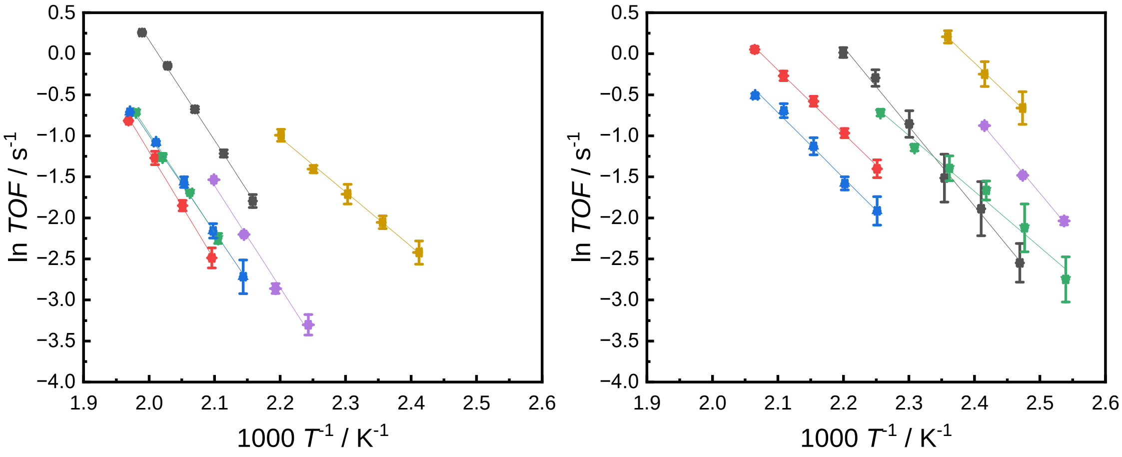

Figure 47: *Arrhenius*-type plots for different Pt_1 ceria materials CeO_2-64 (⬛), CeO_2-54 (🟥), CeO_2-41 (🟦), CeO_2-34 (🟩), CeO_2-15 (🟪) and CeO_2-10 (🟨) with dry feed (left) and wet feed (right)

reduced even under oxygen surplus to Pt^0.[205,209] Obtained values also align with published studies.[221] The similarity of activation energies extracted from the *Arrhenius*-type plots between the different materials points towards a *rds* connected to the Pt_1 active site, as these sites are comparable between the materials. Wang et al. calculated an activation barrier of $E_{A,app} = 100\,\mathrm{kJ\,mol^{-1}}$ for the reaction between CO adsorbed on Pt_1 centers with lattice oxygen of ceria.[165] This is congruent with the values obtained for the fits in figure 47 and listed in table 19. The only material that behaves differently is Pt_1-CeO_2-10 which exhibits an activation energy that is substantially lower compared to the other materials. One possible explanation is that high-temperature treatment is known to restructure the surface in a way that yields highly active (100) facets on the surface. Studies on single platinum atoms on ceria focused on introducing surface restructuring around the platinum ions propose that high-temperature treatment yields a coordination environment around the single platinum ions similar to platinum ions on a (100) facet, which can also be found on surface defects. These platinum ions are reported to exhibit lower activation energies, similar to the material measured here. Thus, it is perceivable that the restructuring of the surface before platinum loading yielded these adsorption sites, leading to more active Pt_1 ions on the surface.[164,223,289] However, the structural rearrangement would have also been evident in the studies focusing on the bare ceria support, as these also show enhanced CO oxidation activity without platinum being present. However, the samples calcined at 700 °C when tested in their unloaded state did not show increased site specific activity. Another explanation for the observed very low activation barrier is, that stabilization of single platinum ions on the surface was not possible on this support and platinum clusters were formed. As the employed method uses cerium defect sites, whose concentration is lowered for large crystalline samples, to anchor platinum ions in their atomically dispersed

Table 19: Results of kinetic investigations of Pt_1-CeO_2 catalysts in dry and wet feeds

Material	$E_{\mathrm{A,dry}}/\mathrm{kJ\,mol^{-1}}$	$E_{\mathrm{A,wet}}/\mathrm{kJ\,mol^{-1}}$	$TOF_{200\,°\mathrm{C,dry}}/\mathrm{s^{-1}}$	$TOF_{170\,°\mathrm{C,wet}}/\mathrm{s^{-1}}$
Pt_1-CeO_2-64	102 ± 2	80 ± 3	0.38	0.63
Pt_1-CeO_2-54	110 ± 4	64 ± 2	0.16	0.24
Pt_1-CeO_2-41	98 ± 4	66 ± 4	0.09	0.14
Pt_1-CeO_2-34	101 ± 4	56 ± 4	0.35	0.50
Pt_1-CeO_2-15	103 ± 8	79 ± 4	1.14	1.87
Pt_1-CeO_2-10	55 ± 2	63 ± 3	1.79	2.67

state, the area-specific platinum loading has to be smaller compared to the area-specific ceria-defect density. When less defects are present on the surface than introduced platinum ions the stabilization would not occur and thus, highly active platinum clusters would most probably form. Generally it can be assumed that the larger the crystallites, the lower the number of surface defects are, which could be a possible reason for this observation.

When the steady-state plots of CO oxidation with dry and wet feeds in figure 47 are compared, a shift to higher reaction rates in the presence of water can be observed. This, as discussed before, was expected and also shown by light-off experiments discussed previously. Compared to the results obtained under dry feed conditions deviations in the slope of the *Arrhenius*-type diagram can be observed. Calculation of the apparent activation energies $E_{\mathrm{A,app}}$ for the different materials makes this also evident. However, it has to be pointed out that the margin of error is increased with water in the feed due to inconsistencies of water concentration in the feed. When the calculated activation energies, listed in table 19, are compared between the experiments in dry and wet feeds, a decrease in activation energy between $10\,\mathrm{kJ\,mol^{-1}}$ to $50\,\mathrm{kJ\,mol^{-1}}$ is observed between the materials. This difference in activation energy between dry and wet feeds was previously found by Wang et al. as well. They traced it back to a water-mediated MvK mechanism in which the reoxidation of formed oxygen vacancy through reduction was refilled by water, forming hydroxyl groups, which subsequently were able to form carboxyl intermediates.[171] This formation had, according to their DFT calculations, roughly $30\,\mathrm{kJ\,mol^{-1}}$ decreased activation barrier. Thus, it is most likely that the same mechanism is prevalent for the present materials, leading to the decrease in activation energy. It was already discussed that the presence of water enables the reaction to proceed through the WGS reaction. Literature proposes activation energies of WGS reactions catalyzed by highly-dispersed platinum species on ceria to exhibit activation barriers of around $(70 \pm 5)\,\mathrm{kJ\,mol^{-1}}$.[287,290–292] However, no significant

WGS activity was found in these studies below 210 °C. Since most measurement points for the determination of activation energies were measured in the present work below that temperature ($1000/T = 2.07\,\mathrm{K}^{-1}$), it can be assumed, that the contribution of the WGS reaction is negligible. Thus, the activities probed here are most probably dominated by the water-mediated MvK mechanism proposed by Wang et al.[171]

When comparing the activation energies that were extracted from the *Arrhenius*-type diagrams, no clear correlation with the material parameters in table 14 can be found. This is also true for the magnitude in light-off temperature decrease. The simplified *Arrhenius*-type analysis, where the measured reaction rate is used to extract the activation energies does not yield the true activation energy of the surface reaction. This was well shown in the discussion of the material-parameter dependence of unloaded ceria redox catalysts discussed before. Therefore, if multiple processes influence the reaction rate, this simplified view on reaction kinetics is not sufficient anymore and a mechanistic model is required. It is known that the redox-active support might change the electronic properties of the platinum ions.[293] As the transition state in the water-mediated MvK mechanism is described to be a vicinal hydroxyl group reacting with adsorbed CO on the platinum ions, the hydroxyl density might influence the reaction rate as well. Also, as discussed above, the contribution of the WGS reaction is not entirely clear here.

The extracted TOF values at 220 °C for the dry feed measurements and 150 °C for measurements with water containing feeds are plotted as a function of the bulk defect concentration measured by *Raman* spectroscopy and represented by I_{600}/I_{464} are plotted in fig. 48 .

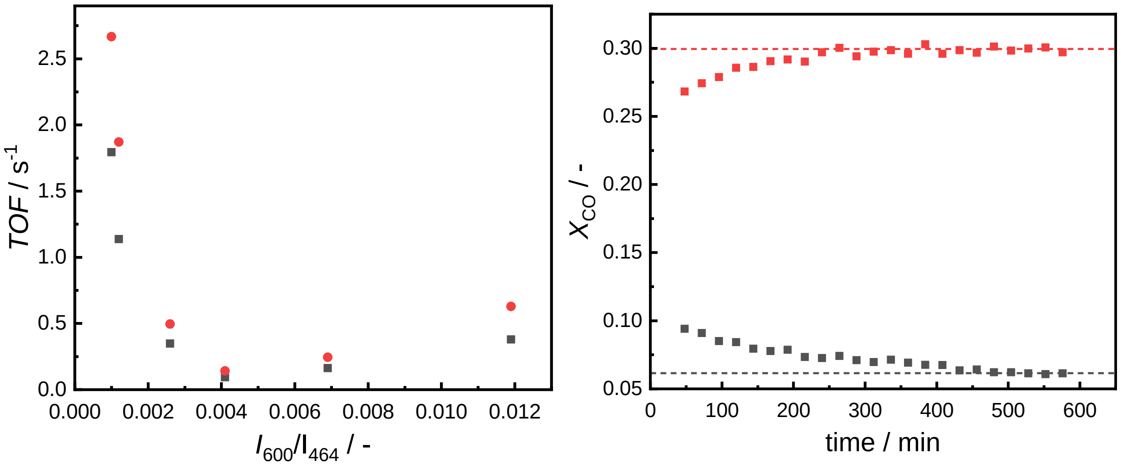

Figure 48: TOF values for different materials for dry ($TOF_{220°}$ ■) and wet feed ($TOF_{150\,°C}$ ●) (left) and conversion during the induction period of Pt_1-CeO_2-64 at 220 °C for wet (■) and dry feeds (■) (right)

When looking at the site specific rates, TOF, as a function of the bulk defect concentration extracted from *Raman* spectroscopy I_{600}/I_{464} for dry and wet feeds in figure 48, similar trends can be observed independently of whether water is present or not. Whereas high TOF values are observed for materials which exhibit low defect concentrations, a minimum of activity is observed, while highly defective materials again show an increase in activity. This suggests that there might be two different processes that dictate the reactivity depending on the respective defect concentration. This might be caused by materials with higher defect concentration having higher electron density at the platinum ions, enabling a better activation of CO, while at low defect concentrations, the formation of the vicinal hydroxyl group might be easier. Both would influence the observed reaction rate but in an opposite manner, making the analysis of the combined effect difficult. Also, when looking at the conversion over time during the equilibration period before kinetic testing, an interesting picture arises. Whereas feeds without water start with high activity, which subsequently decreases, when testing the same sample in a wet feed the activity increases during equilibration. The latter might be explainable by converting vicinal lattice oxygen into hydroxyl groups, whereas for the dry feed this points to an equilibration of the reduction degree around the platinum ion. In their oxidized state, the surroundings of the platinum ions are fully oxidized, whereas there are oxygen vacancies formed during catalysis, which due to the low temperature cannot be refilled fast enough through reoxidation, leading to a decrease in reaction rate. This also shows that it is necessary to look into the reoxidation of ceria materials when looking into platinum-loaded materials and their structure-property relationships. This, along with the possible presence of the WGS reaction, requires further detailed study of partial pressure dependencies in order to derive material-based activity descriptors.

The results presented show that among the different catalysts similar processes occur, which determine the activity of Pt_1-CeO_2 catalysts. Congruent with literature the data presented here suggests that activation energy is determined by the reaction of adsorbed CO on Pt_1 sites and ceria lattice oxygen. Intrinsic activities of the different materials show that at high as well as low defect concentrations activities are high, whereas at intermediate ones they are low. Whereas water increases the activity, it does not change this dependency. It was shown that the oxide support does indeed influence the activity of the materials substantially, however, a clear description of structure-activity descriptors in their platinum-loaded state is difficult due to the complex nature of the reaction system. Carrying out measurements for the partial pressure dependence of the reaction rate coupled with the use of a two-center LH kinetic expression should provide the necessary results to disentangle the different contributions on the reaction rates and activation energies and set up models with which activities of different platinum-loaded ceria materials can be predicted. These investigations show that the use of low loaded Pt-CeO_2 catalysts can be used to investigate the role of the oxide supports in redox catalysis.

Part VI.

Conclusion

The aim of this work was to investigate structure-property relationships of different cerium oxide catalysts. First, the interplay of preparation parameters and resulting material properties was investigated. Precipitation, as one of the most used wet chemical preparation techniques for metal oxide catalysts, was selected as the preparation method of choice. It is known that precipitation is a process that is highly sensitive to its process parameters. In order to vary material properties of ceria materials over a wide range, the precipitation temperature, T_{prec}, dependence was investigated. It was found that higher precipitation temperatures led to an increase in specific BET surface area and decrease of crystallite size. Using pH experiments, this was traced back to an increase in nucleation rate at higher temperatures, leading to smaller crystallites exhibiting higher surface areas. Redox investigations, to probe the interplay between material properties and the redox-active or MvK active surface area were carried out next. While literature often assumes that the redox-active surface area is equivalent to the BET surface area, the results obtained in this work suggest something else. Through oxygen pulse chemisorption experiments, it was found that at large BET surface areas the MvK-active surface area deviates substantially from the BET surface area obtained from N_2 physisorption experiments. H_2-TPD experiments as well as *in situ*-DRIFTS were used to trace this back to reduction of the surface without formation of oxygen vacancies, but rather hydroxyl groups for small crystallites. Since these sites cannot release oxygen, they are not active during MvK catalysis. Therefore, the presented results show that it is of paramount importance that obtained kinetic results are not simply normalized by the BET surface area, but rather using the MvK active surface area. It was also found that it is possible to use a calculated crystallite surface area, S_{cryst} based on the crystallite size, D, extracted by *Rietveld* refinement, as a descriptor for the MvK active surface area. This is especially important when direct measurement of the redox active surface area can not easily be realized, *e.g.* for doped ceria materials.

Subsequently CO oxidation experiments were used as a model reaction to probe the influence of the material properties on catalytic activity of ceria materials. It was found that the bulk oxygen point defect concentration measured by *Raman* spectroscopy probably determines the activity of ceria-based materials in CO oxidation. This is in line with other studies in literature. By measuring partial pressure dependencies and using mechanism based models, the results suggest that for bare ceria catalysts, CO_2 desorption and readsorption of previously formed CO_2 causes an inhibition of the CO oxidation. Defect concentration did lead to an increase not only in the preexponential factor of the rate expression but also in the activation energy and heat of adsorption of CO. First results, which have to be supported by further measurements, pointed towards a decreased heat of adsorption of CO_2 with decreasing number of surface defects, while also the preexponential factor decreased.

Single-platinum ions supported on different ceria materials were employed to investigate whether these systems can be used to derive structure-property relationships of platinum-loaded systems. By using a SEA approach it was possible to prepare different ceria materials with comparable area-specific loadings. These catalysts showed atomic dispersion after preparation. The atomic dispersion was shown to be stable under the lean conditions used for catalytic experiments. It was however shown that when harsh reducing conditions were applied, *i.e.* reduction at 300 °C in 10 % H_2 in N_2, cluster formation did most probably occur. Kinetic measurements of these materials showed that, although the catalytic active center was comparable between the different catalysts, differences in activity could be observed. As atomic dispersion was present this could be solely traced back to the influence of the oxide support. When using oxygen as the oxidant during catalysis, activation energies were similar between the different materials. However, turnover rates did change between materials, which could, similar to the results obtained for the unloaded ceria materials, be traced to the bulk defect concentration. This also did not change when water was introduced to the feed. Although the overall activity increased, similar trends were observed for TOF values as a function of the bulk defect concentration. Although it could not be ruled out that WGS plays a role during the catalytic experiments, the influence of water in the temperature range in which the catalytic experiments were carried out, the water-mediated MvK seems to be prevalent. Concluding, it can be stated that it is possible to use low-loaded platinum single-atom catalysts as a means to derive structure-property relationships of the ceria support in platinum-loaded ceria catalysts.

Part VII.

Outlook

In this work it was shown that for redox-active oxides the physical surface area might differ from the active surface area in catalysis. Although for the investigated CO oxidation this contribution through reduction by hydroxyl group formation was not beneficial, many other reactions could benefit from it. Especially selective oxidations, where total oxidation is a competing reaction, such as oxidative dehydrogenation of propane to propene might be able to take advantage of this phenomenon. Especially the stabilization of these sites as well as their kinetic characterization might open new pathways to carry out selective oxidation reactions using ceria catalysts.

While good correlation between the activity of unloaded ceria materials and respective material parameters were found, the data set obtained during this work is limited. In order to derive reliable structure-property relationships for these materials, partial pressure dependencies have to be extended to other materials. Also, artificial CO_2 dosing is necessary to really show whether CO_2 adsorption is causing a product inhibition in the CO oxidation rate at CeO_2. Using the derived structure-property relationships to predict CO oxidation activities could act as a way to verify these findings.

The experiments in this work showed that it is possible to use Pt_1-CeO_2 materials to probe the influenceability of the reaction rate by the support. Thorough measurement of partial pressure dependencies of the reaction rate need to be mechanistically modeled in order to derive the necessary activity descriptors. Although the results obtained in this work were congruent with literature, it was not probed how the derived structure-property relationships translate to nanoparticle loaded Pt-NP-CeO_2 systems. If these findings can be used to describe activities of nanoparticle-loaded ceria systems, they could be used to parameterize kinetic models for dynamic applications. This would enable the transfer of knowledge gained through these model systems to industrially relevant nanoparticle catalysts. It was shown that water does influence the reaction rate. Initial results point towards a water-mediated MvK mechanism, with no net water conversion. However, this has to be probed in more detail. It would be interesting to investigate whether in steady-state the water-mediated MvK mechanism is also prevalent at higher temperatures also in lean exhaust gases. The presented results suggest that there is a temperature range at which the reactivity changes to the WGS mechanism. This would mean that it is necessary to not only find structure-property relationships for LT-CO-Oxidation but also WGS activity.

Similar to the CO oxidation, there is little data available to how ceria materials do influence the WGS activity of Pt-loaded ceria catalysts.

References

(1) Ertl, G.; Gloyna, T. *Zeitschrift für Physikalische Chemie* **2003**, *217*, 1207–1220, DOI: `10.1524/zpch.217.10.1207.20496`.

(2) Ertl, G. *Angewandte Chemie International Edition* **2009**, *48*, 6600–6606, DOI: `10.1002/anie.200901193`.

(3) Schlögl, R. *Angewandte Chemie International Edition* **2015**, *54*, 3465–3520, DOI: `10.1002/anie.201410738`.

(4) Roduner, E. *Chemical Society reviews* **2014**, *43*, 8226–8239, DOI: `10.1039/C4CS00210E`.

(5) Dumesic, J. A.; Huber, G. W.; Boudart, M. In *Handbook of heterogeneous catalysis*, Ertl, G., Ed., 2nd, completely rev. and enl. ed. / edited by Gerhard Ertl ... [et al.]; Wiley-VCH and [Chichester : John Wiley: Weinheim, 2008, DOI: `10.1002/9783527610044.hetcat0001`.

(6) Deutschmann, O.; Knözinger, H.; Kochloefl, K.; Turek, T. In *Ullmann's encyclopedia of industrial chemistry*, 7. edition, release 2015; Wiley-VCH: Weinheim and Wiley online library, 2010, DOI: `10.1002/14356007.a05_313.pub3`.

(7) Heck, R. M.; Farrauto, R. J. *Applied Catalysis A: General* **2001**, *221*, 443–457, DOI: `10.1016/S0926-860X(01)00818-3`.

(8) Lambert, C. K. *Nature Catalysis* **2019**, *2*, 554–557, DOI: `10.1038/s41929-019-0303-x`.

(9) Farrauto, R. J.; Heck, R. M. *Catalysis Today* **2000**, *55*, 179–187, DOI: `10.1016/S0920-5861(99)00237-0`.

(10) Deutschmann, O.; Grunwaldt, J.-D. *Chemie Ingenieur Technik* **2013**, *85*, 595–617, DOI: `10.1002/cite.201200188`.

(11) Brinkmeier, C.; Eigenberger, G.; Bernnat, J.; Tuttlies, U.; Schmeißer, V.; Opferkuch, F. *Chemie Ingenieur Technik* **2005**, *77*, 1333–1355, DOI: `10.1002/cite.200500111`.

(12) Trovarelli, A. *Catalysis Reviews* **1996**, *38*, 439–520, DOI: `10.1080/01614949608006464`.

(13) Trovarelli, A.; Leitenburg, C. d.; Boaro, M.; Dolcetti, G. *Catalysis Today* **1999**, *50*, 353–367, DOI: `10.1016/S0920-5861(98)00515-X`.

(14) Beurer, A.-.-.-K.; Kirchhof, M.; Bruckner, J. R.; Frey, W.; Baro, A.; Dyballa, M.; Giesselmann, F.; Laschat, S.; Traa, Y. *ChemCatChem* **2021**, *13*, 2407–2419, DOI: `10.1002/cctc.202100229`.

(15) DiCosimo, R.; McAuliffe, J.; Poulose, A. J.; Bohlmann, G. *Chemical Society reviews* **2013**, *42*, 6437–6474, DOI: `10.1039/c3cs35506c`.

(16) Bertini, I., *Inorganic and bio-inorganic chemistry ; Vol. 2*; Encyclopedia of life support systems 6, Chemical sciences engineering and technology resources; EOLSS Publ: Oxford, 2009; 486 pp.

(17) Levenspiel, O., *Chemical reaction engineering*, 3. ed.; Wiley: Hoboken, NJ, 1999; 668 pp.

(18) Emig, G.; Klemm, E., *Chemische Reaktionstechnik*, 6., neu bearbeitete Auflage; Springer-Lehrbuch, Emig, Gerhard (VerfasserIn) Klemm, Elias (VerfasserIn) Hungenberg, Klaus-Dieter (MitwirkendeR); Springer Vieweg: Berlin and Heidelberg, 2017; 600 pp., DOI: `10.1007/978-3-662-49268-0`.

(19) Chambers, R. P.; Boudart, M. *Journal of Catalysis* **1966**, *6*, 141–145, DOI: `10.1016/0021-9517(66)90118-7`.

(20) Mears, D. E. *Industrial & Engineering Chemistry Process Design and Development* **1971**, *10*, 541–547, DOI: `10.1021/i260040a020`.

(21) Weisz, P. B.; Prater, C. D. In *Advances in catalysis*, Frankenburg, W. G., Komarewsky, V. I., Rideal, E. K., Eds.; Advances in Catalysis v.6, Vol. 6; Elsevier: Burlington, 1954, pp 143–196, DOI: `10.1016/S0360-0564(08)60390-9`.

(22) Weissberg, H. L. *Journal of Applied Physics* **1963**, *34*, 2636–2639, DOI: `10.1063/1.1729783`.

(23) Blanc, A. *Journal de Physique Théorique et Appliquée* **1908**, *7*, 825–839, DOI: `10.1051/jphystap:019080070082501`.

(24) Marrero, T. R.; Mason, E. A. *Journal of Physical and Chemical Reference Data* **1972**, *1*, 3–118, DOI: `10.1063/1.3253094`.

(25) Massman, W. J. *Atmospheric Environment* **1998**, *32*, 1111–1127, DOI: `10.1016/S1352-2310(97)00391-9`.

(26) Barrande, M.; Bouchet, R.; Denoyel, R. *Analytical Chemistry* **2007**, *79*, 9115–9121, DOI: `10.1021/ac071377r`.

(27) Carman, P. C. *Transactions of the Institution of Chemical Engineers* **1937**, 150–167, DOI: `10.1016/S0263-8762(97)80003-2`.

(28) Carman, P. C., *Flow of Gases through Porous Media.* London: Butterworths Scientific Publications, 1956.

(29) Carniglia, S. *Journal of Catalysis* **1986**, *102*, 401–418, DOI: `10.1016/0021-9517(86)90176-4`.

(30) Fick, A. *Annalen der Physik* **1855**, *170*, 59–86, DOI: `10.1002/andp.18551700105`.

(31) León y León, C. A. *Advances in Colloid and Interface Science* **1998**, *76-77*, 341–372, DOI: `10.1016/S0001-8686(98)00052-9`.

(32) Lowell, S.; Shields, J. E.; Thomas, M. A.; Thommes, M., *Characterization of porous solids and powders, Surface area, pore size and density*, 4. ed., 1. reprint with some corr; Particle technology series, Vol. 16; Springer: Dordrecht, 2006; 347 pp.

(33) Manickam, S. S.; Gelb, J.; McCutcheon, J. R. *Journal of Membrane Science* **2014**, *454*, 549–554, DOI: `10.1016/j.memsci.2013.11.044`.

(34) Zhang, W.; Yang, C.; Liu, W.; Wang, H.; Wei, S.; Qi, J.; Bai, P.; Jin, B.; Xu, L. *Applied Catalysis B: Environmental* **2021**, *293*, 120199, DOI: `10.1016/j.apcatb.2021.120199`.

(35) Flores-López, S. L.; Ramírez-Montoya, L. A.; Casal, M. D.; Montes-Morán, M. A.; Menéndez, J. A.; Arenillas, A. *Carbon* **2021**, *171*, 921–930, DOI: `10.1016/j.carbon.2020.09.079`.

(36) Zalc, J. M.; Reyes, S. C.; Iglesia, E. *Chemical Engineering Science* **2004**, *59*, 2947–2960, DOI: `10.1016/j.ces.2004.04.028`.

(37) Armatas, G. S. *Chemical Engineering Science* **2006**, *61*, 4662–4675, DOI: `10.1016/j.ces.2006.02.036`.

(38) Comiti, J.; Renaud, M. *Chemical Engineering Science* **1989**, *44*, 1539–1545, DOI: `10.1016/0009-2509(89)80031-4`.

(39) Atkins, P. W.; de Paula, J.; Keeler, J. J., *Atkins' physical chemistry*, Eleventh edition, Atkins, Peter W. (VerfasserIn) de Paula, Julio (VerfasserIn) Keeler, James J. (VerfasserIn) Atkins, Peter W. (VerfasserIn) de Paula, Julio (VerfasserIn) Keeler, James J. (VerfasserIn); Oxford University Press: Oxford and New York, 2018; 908 pp.

(40) Langmuir, I. *Transactions of the Faraday Society* **1922**, *17*, 607–620, DOI: `10.1039/TF9221700607`.

(41) Eley, D. D.; Rideal, E. K. *Nature* **1940**, *146*, 401–402, DOI: `10.1038/146401d0`.

(42) Eley, D. D. *Proceedings of the Royal Society of London. Series A, Containing Papers of a Mathematical and Physical Character* **1941**, *178*, 452–464, DOI: `10.1098/rspa.1941.0067`.

(43) Prins, R. *Topics in Catalysis* **2018**, *61*, 714–721, DOI: `10.1007/s11244-018-0948-8`.

(44) Langmuir, I. *Journal of the American Chemical Society* **1918**, *40*, 1361–1403, DOI: `10.1021/ja02242a004`.

(45) Anstrom, M. *Journal of Catalysis* **2003**, *213*, 115–125, DOI: `10.1016/S0021-9517(02)00031-3`.

(46) Hinshelwood, C. N., *The Kinetics of Chemical Change in Gaseous Systems*; Clarendon Press: 1926.

(47) Engel, T.; Ertl, G. In *Advances in Catalysis*, Eley, D. D., Pines, H., Weisz, P. B., Eds.; Academic Press: 1982; Vol. 28, pp 1–78, DOI: `10.1016/S0360-0564(08)60133-9`.

(48) Ertl, G. *Surface Science* **1994**, *299-300*, 742–754, DOI: `10.1016/0039-6028(94)90694-7`.

(49) Baxter, R. J.; Hu, P. *The Journal of Chemical Physics* **2002**, *116*, 4379–4381, DOI: `10.1063/1.1458938`.

(50) Vannice, M. A., *Kinetics of Catalytic Reactions*; Springer Science+Business Media Inc: Boston, MA, 2005, DOI: `10.1007/b136380`.

(51) Vannice, M. A. *Catalysis Today* **2007**, *123*, 18–22, DOI: `10.1016/j.cattod.2007.02.002`.

(52) Mars, P.; van Krevelen, D. W. *Chemical Engineering Science* **1954**, *3*, 41–59, DOI: `10.1016/S0009-2509(54)80005-4`.

(53) Doornkamp, C.; Ponec, V. *Journal of Molecular Catalysis A: Chemical* **2000**, *162*, 19–32, DOI: `10.1016/S1381-1169(00)00319-8`.

(54) Dhall, A.; Self, W. *Antioxidants (Basel, Switzerland)* **2018**, *7*, DOI: `10.3390/antiox7080097`.

(55) Das, S.; Dowding, J. M.; Klump, K. E.; McGinnis, J. F.; Self, W.; Seal, S. *Nanomedicine (London, England)* **2013**, *8*, 1483–1508, DOI: `10.2217/nnm.13.133`.

(56) Hosseini, M.; Mozafari, M. *Materials* **2020**, *13*, 3072, DOI: `10.3390/ma13143072`.

(57) Gnanam, S.; Rajendran, V. *Journal of Alloys and Compounds* **2018**, *735*, 1854–1862, DOI: `10.1016/j.jallcom.2017.11.330`.

(58) Huang, X.; Zhang, K.; Peng, B.; Wang, G.; Muhler, M.; Wang, F. *ACS Catalysis* **2021**, *11*, 9618–9678, DOI: `10.1021/acscatal.1c02443`.

(59) Bellardita, M.; Fiorenza, R.; Palmisano, L.; Scirè, S. In *Cerium Oxide (CeO2)*, Scire, S., Ed.; Metal Oxides Ser; Elsevier: San Diego, 2020, pp 109–167, DOI: `10.1016/B978-0-12-815661-2.00004-9`.

(60) Xie, S.; Wang, Z.; Cheng, F.; Zhang, P.; Mai, W.; Tong, Y. *Nano Energy* **2017**, *34*, 313–337, DOI: `10.1016/j.nanoen.2017.02.029`.

(61) Ling, Y.; Wang, X.; Ma, Z.; Wei, K.; Wu, Y.; Khan, M.; Zheng, K.; Shen, S.; Wang, S. *Journal of Materials Science* **2020**, *55*, 1–23, DOI: `10.1007/s10853-019-03876-z`.

(62) Lim, C.; Alavijeh, A. S.; Lauritzen, M.; Kolodziej, J.; Knights, S.; Kjeang, E. *ECS Electrochemistry Letters* **2015**, *4*, F29–F31, DOI: `10.1149/2.0081504eel`.

(63) Mori, T.; Ou, D. R.; Zou, J.; Drennan, J. *Progress in Natural Science: Materials International* **2012**, *22*, 561–571, DOI: `10.1016/j.pnsc.2012.11.010`.

(64) Chockalingam, R.; Amarakoon, V. R.; Giesche, H. *Journal of the European Ceramic Society* **2008**, *28*, 959–963, DOI: `10.1016/j.jeurceramsoc.2007.09.031`.

(65) Wang, J.; Chen, H.; Hu, Z.; Yao, M.; Li, Y. *Catalysis Reviews* **2015**, *57*, 79–144, DOI: `10.1080/01614940.2014.977059`.

(66) Li, P.; Chen, X.; Li, Y.; Schwank, J. W. *Catalysis Today* **2019**, *327*, 90–115, DOI: `10.1016/j.cattod.2018.05.059`.

(67) Montini, T.; Melchionna, M.; Monai, M.; Fornasiero, P. *Chemical Reviews* **2016**, *116*, 5987–6041, DOI: `10.1021/acs.chemrev.5b00603`.

(68) Shannon, R. D.; Prewitt, C. T. *Acta Crystallographica Section B Structural Crystallography and Crystal Chemistry* **1969**, *25*, 925–946, DOI: `10.1107/s0567740869003220`.

(69) Mullins, D. R. *Surface Science Reports* **2015**, *70*, 42–85, DOI: `10.1016/j.surfrep.2014.12.001`.

(70) Wyckoff, R. W. G., *Crystal structures*, 2nd ed.; Interscience Publ: New York and NY [u.a.], 1963.

(71) Hong, S. J.; Virkar, A. V. *Journal of the American Ceramic Society* **1995**, *78*, 433–439, DOI: `10.1111/j.1151-2916.1995.tb08820.x`.

(72) Nolan, M.; Grigoleit, S.; Sayle, D. C.; Parker, S. C.; Watson, G. W. *Surface Science* **2005**, *576*, 217–229, DOI: `10.1016/j.susc.2004.12.016`.

(73) ZINKEVICH, M.; DJUROVIC, D.; ALDINGER, F. *Solid State Ionics* **2006**, *177*, 989–1001, DOI: `10.1016/j.ssi.2006.02.044`.

(74) Namai, Y.; Fukui, K.-i.; Iwasawa, Y. *The journal of physical chemistry. B* **2003**, *107*, 11666–11673, DOI: `10.1021/jp030142q`.

(75) Nörenberg, H.; Briggs, G. A. D. *Physical Review Letters* **1997**, *79*, 4222–4225, DOI: `10.1103/PhysRevLett.79.4222`.

(76) Vegard, L. *Zeitschrift fr Physik* **1921**, *5*, 17–26, DOI: `10.1007/bf01349680`.

(77) Kim, D.-J. *Journal of the American Ceramic Society* **1989**, *72*, 1415–1421, DOI: `10.1111/j.1151-2916.1989.tb07663.x`.

(78) Sayle, T. X. T.; Parker, S. C.; Catlow, C. R. A. *Journal of the Chemical Society, Chemical Communications* **1992**, 977, DOI: `10.1039/C39920000977`.

(79) Nolan, M.; Fearon, J. E.; Watson, G. W. *Solid State Ionics* **2006**, *177*, 3069–3074, DOI: `10.1016/j.ssi.2006.07.045`.

(80) Nolan, M.; Watson, G. W. *The journal of physical chemistry. B* **2006**, *110*, 16600–16606, DOI: `10.1021/jp062499a`.

(81) Devaiah, D.; Reddy, L. H.; Park, S.-E.; Reddy, B. M. *Catalysis Reviews* **2018**, *60*, 177–277, DOI: `10.1080/01614940.2017.1415058`.

(82) Mullin, J. W. In *Ullmann's encyclopedia of industrial chemistry*, 7. edition, release 2015; Wiley-VCH: Weinheim and Wiley online library, 2010, DOI: `10.1002/14356007.b02_03`.

(83) Kashchiev, D.; van Rosmalen, G. M. *Crystal Research and Technology* **2003**, *38*, 555–574, DOI: `10.1002/crat.200310070`.

(84) Schwarz, J. A.; Contescu, C.; Contescu, A. *Chemical Reviews* **1995**, *95*, 477–510, DOI: `10.1021/cr00035a002`.

(85) Whitehead, C. B.; Özkar, S.; Finke, R. G. *Materials Advances* **2021**, *2*, 186–235, DOI: `10.1039/D0MA00439A`.

(86) Chu, D. B. K.; Owen, J. S.; Peters, B. *The journal of physical chemistry. A* **2017**, *121*, 7511–7517, DOI: `10.1021/acs.jpca.7b08368`.

(87) Volmer, M.; Weber, A. *Zeitschrift für Physikalische Chemie* **1926**, *119U*, 277–301, DOI: `10.1515/zpch-1926-11927`.

(88) Becker, R.; Döring, W. *Annalen der Physik* **1935**, *416*, 719–752, DOI: `10.1002/andp.19354160806`.

(89) Frenkel, J. *The Journal of Chemical Physics* **1939**, *7*, 538–547, DOI: `10.1063/1.1750484`.

(90) Oxtoby, D. W. *Accounts of Chemical Research* **1998**, *31*, 91–97, DOI: `10.1021/ar9702278`.

(91) Kaščiev, D., *Nucleation, Basic theory with applications*, Transferred to digital printing; Butterworth Heinemann: Oxford, 2003; 529 pp., DOI: `51578`.

(92) Polte, J. *CrystEngComm* **2015**, *17*, 6809–6830, DOI: `10.1039/C5CE01014D`.

(93) Whitehead, C. B.; Özkar, S.; Finke, R. G. *Chemistry of Materials* **2019**, *31*, 7116–7132, DOI: `10.1021/acs.chemmater.9b01273`.

(94) LaMer, V. K.; Dinegar, R. H. *Journal of the American Chemical Society* **1950**, *72*, 4847–4854, DOI: `10.1021/ja01167a001`.

(95) Farkas, L. *Zeitschrift für Physikalische Chemie* **1927**, *125U*, 236–242, DOI: `10.1515/zpch-1927-12513`.

(96) Voorhees, P. W. *Journal of Statistical Physics* **1985**, *38*, 231–252, DOI: `10.1007/BF01017860`.

(97) Cui, Y.; Fang, R.; Shang, H.; Shi, Z.; Gong, M.; Chen, Y. *Journal of Alloys and Compounds* **2015**, *628*, 213–221, DOI: `10.1016/J.JALLCOM.2014.12.149`.

(98) Chen, H.-I.; Chang, H.-Y. *Ceramics International* **2005**, *31*, 795–802, DOI: `10.1016/J.CERAMINT.2004.09.006`.

(99) Chen, P.-L.; Chen, I.-W. *Journal of the American Ceramic Society* **1993**, *76*, 1577–1583, DOI: `10.1111/J.1151-2916.1993.TB03942.X`.

(100) De Lima Batista, A. M.; Miranda, M. A. R.; Martins, Fátima Itana Chaves Custódio; Morilla Santos, C.; Sasaki, J. M. *Powder Diffraction* **2018**, *33*, 21–25, DOI: `10.1017/S0885715617001208`.

(101) Zhou, X.-D.; Huebner, W.; Anderson, H. U. *Applied Physics Letters* **2002**, *80*, 3814–3816, DOI: `10.1063/1.1481244`.

(102) Kirk, N. B.; Wood, J. V. *Journal of Materials Science* **1995**, *30*, 2171–2175, DOI: `10.1007/BF00353051`.

(103) Alifanti, M.; Baps, B.; Blangenois, N.; Naud, J.; Grange, P.; Delmon, B. *Chemistry of Materials* **2003**, *15*, 395–403, DOI: `10.1021/cm021274j`.

(104) Vidmar, P.; Fornasiero, P.; Kašpar, J.; Gubitosa, G.; Graziani, M. *Journal of Catalysis* **1997**, *171*, 160–168, DOI: `10.1006/jcat.1997.1784`.

(105) Kaneko, K.; Inoke, K.; Freitag, B.; Hungria, A. B.; Midgley, P. A.; Hansen, T. W.; Zhang, J.; Ohara, S.; Adschiri, T. *Nano Letters* **2007**, *7*, 421–425, DOI: `10.1021/nl062677b`.

(106) Si, R.; Zhang, Y.-W.; Li, S.-J.; Lin, B.-X.; Yan, C.-H. *The journal of physical chemistry. B* **2004**, *108*, 12481–12488, DOI: `10.1021/jp048084b`.

(107) Hirano, M.; Kato, E. *Journal of the American Ceramic Society* **1996**, *79*, 777–780, DOI: `10.1111/j.1151-2916.1996.tb07943.x`.

(108) Ghahramani, Z.; Arabi, A. M.; Shafiee Afarani, M.; Mahdavian, M. *International Journal of Applied Ceramic Technology* **2020**, *17*, 1514–1521, DOI: `10.1111/ijac.13365`.

(109) Zarezadeh Mehrizi, M.; Ahmadi, S.; Beygi, R.; Asadi, M. *Russian Journal of Non-Ferrous Metals* **2018**, *59*, 111–116, DOI: `10.3103/S1067821218010170`.

(110) Vinothkumar, G.; Amalraj, R.; Babu, K. S. *Ceramics International* **2017**, *43*, 5457–5466, DOI: `10.1016/j.ceramint.2017.01.053`.

(111) Hidalgo, J.; Roussel, P.; Okuno, H.; Delahaye, T.; Rouvière, J. L.; Leturcq, G. *Hydrometallurgy* **2022**, *207*, 105774, DOI: `10.1016/j.hydromet.2021.105774`.

(112) Yadav, T. P.; Srivastava, O. N. *Ceramics International* **2012**, *38*, 5783–5789, DOI: `10.1016/j.ceramint.2012.04.025`.

(113) Trovarelli, A.; Zamar, F.; Llorca, J.; Leitenburg, C. d.; Dolcetti, G.; Kiss, J. T. *Journal of Catalysis* **1997**, *169*, 490–502, DOI: `10.1006/jcat.1997.1705`.

(114) Soren, S.; Jena, S. R.; Samanta, L.; Parhi, P. *Applied Biochemistry and Biotechnology* **2015**, *177*, 148–161, DOI: `10.1007/s12010-015-1734-8`.

(115) Mahmoud, W. E.; Faidah, A. *Journal of the European Ceramic Society* **2012**, *32*, 3537–3541, DOI: `10.1016/j.jeurceramsoc.2012.05.003`.

(116) Godinho, M.; Ribeiro, C.; Longo, E.; Leite, E. R. *Crystal Growth & Design* **2008**, *8*, 384–386, DOI: `10.1021/cg700872b`.

(117) Dahle, J. T.; Arai, Y. *International Journal of Environmental Research and Public Health* **2015**, *12*, 1253–1278, DOI: `10.3390/ijerph120201253`.

(118) Pujar, M. S.; Hunagund, S. M.; Desai, V. R.; Patil, S.; Sidarai, A. H. *AIP Conference Proceedings* **2018**, *1942*, 050026, DOI: `10.1063/1.5028657`.

(119) Aneggi, E.; Llorca, J.; Boaro, M.; Trovarelli, A. *Journal of Catalysis* **2005**, *234*, 88–95, DOI: `10.1016/j.jcat.2005.06.008`.

(120) Letichevsky, S.; Tellez, C. A.; Avillez, R. R. d.; Silva, M. I. P. d.; Fraga, M. A.; Appel, L. G. *Applied Catalysis B: Environmental* **2005**, *58*, 203–210, DOI: `10.1016/j.apcatb.2004.10.014`.

(121) Schüth, F.; Hesse, M.; Unger, K. K. In *Handbook of heterogeneous catalysis*, Ertl, G., Ed., 2nd, completely rev. and enl. ed. / edited by Gerhard Ertl ... [et al.]; Wiley-VCH and [Chichester : John Wiley: Weinheim, 2008; Vol. 37, p 291, DOI: `10.1002/9783527610044.hetcat0008`.

(122) Shaw, W. H. R.; Bordeaux, J. J. *Journal of the American Chemical Society* **1955**, *77*, 4729–4733, DOI: `10.1021/ja01623a011`.

(123) Alexandrova, A. N.; Jorgensen, W. L. *The journal of physical chemistry. B* **2007**, *111*, 720–730, DOI: `10.1021/jp066478s`.

(124) Polino, D.; Parrinello, M. *The journal of physical chemistry. B* **2019**, *123*, 6851–6856, DOI: `10.1021/acs.jpcb.9b05271`.

(125) Li, J.-G.; Li, X.; Sun, X.; Ikegami, T.; Ishigaki, T. *Chemistry of Materials* **2008**, *20*, 2274–2281, DOI: `10.1021/cm7033257`.

(126) Ntainjua N., E.; Garcia, T.; Solsona, B.; Taylor, S. H. *Catalysis Today* **2008**, *137*, 373–378, DOI: `10.1016/j.cattod.2007.12.140`.

(127) García, T.; Solsona, B.; Taylor, S. H. *Applied Catalysis B: Environmental* **2006**, *66*, 92–99, DOI: `10.1016/j.apcatb.2006.03.003`.

(128) Garcia, T.; Solsona, B.; Taylor, S. H. *Catalysis Letters* **2005**, *105*, 183–189, DOI: `10.1007/s10562-005-8689-2`.

(129) Yu, J. C.; Zhang, L.; Lin, J. *Journal of Colloid and Interface Science* **2003**, *260*, 240–243, DOI: `10.1016/S0021-9797(02)00168-6`.

(130) Pengpanich, S.; Meeyoo, V.; Rirksomboon, T.; Bunyakiat, K. *Applied Catalysis A: General* **2002**, *234*, 221–233, DOI: `10.1016/S0926-860X(02)00230-2`.

(131) Hirano, M.; Kato, E. *Journal of the American Ceramic Society* **1999**, *82*, 786–788, DOI: `10.1111/j.1151-2916.1999.tb01838.x`.

(132) Matijević, E.; Hsu, W. P. *Journal of Colloid and Interface Science* **1987**, *118*, 506–523, DOI: `10.1016/0021-9797(87)90486-3`.

(133) Chen, J.-C.; Chen, W.-C.; Tien, Y.-C.; Shih, C.-J. *Journal of Alloys and Compounds* **2010**, *496*, 364–369, DOI: `10.1016/j.jallcom.2010.01.151`.

(134) Dai, Y.; Lu, P.; Cao, Z.; Campbell, C. T.; Xia, Y. *Chemical Society reviews* **2018**, *47*, 4314–4331, DOI: `10.1039/C7CS00650K`.

(135) Perrichon, V.; Laachir, A.; Abouarnadasse, S.; Touret, O.; Blanchard, G. *Applied Catalysis A: General* **1995**, *129*, 69–82, DOI: `10.1016/0926-860X(95)00089-5`.

(136) Montini, T.; Bañares, M. A.; Hickey, N.; Di Monte, R.; Fornasiero, P.; Kašpar, J.; Graziani, M. *Phys. Chem. Chem. Phys.* **2004**, *6*, 1–3, DOI: `10.1039/b312684f`.

(137) Kamiuchi, N.; Haneda, M.; Ozawa, M. *Catalysis Today* **2014**, *232*, 179–184, DOI: `10.1016/j.cattod.2013.10.044`.

(138) Li, J.; Liu, X.; Zhan, W.; Guo, Y.; Guo, Y.; Lu, G. *Catal. Sci. Technol.* **2016**, *6*, 897–907, DOI: `10.1039/c5cy01571e`.

(139) Laachir, A.; Perrichon, V.; Badri, A.; Lamotte, J.; Catherine, E.; Lavalley, J. C.; El Fallah, J.; Hilaire, L.; Le Normand, F.; Quéméré, E.; Sauvion, G. N.; Touret, O. *Journal of the Chemical Society, Faraday Transactions* **1991**, *87*, 1601–1609, DOI: `10.1039/FT9918701601`.

(140) Lykaki, M.; Pachatouridou, E.; Iliopoulou, E.; Carabineiro, S. A. C.; Konsolakis, M. *RSC Advances* **2017**, *7*, 6160–6169, DOI: `10.1039/C6RA26712B`.

(141) Bickel, J.; Odendall, B.; Eigenberger, G.; Nieken, U. *Chemical Engineering Science* **2017**, *160*, 34–53, DOI: `10.1016/j.ces.2016.11.016`.

(142) El Fallah, J.; Boujana, S.; Dexpert, H.; Kiennemann, A.; Majerus, J.; Touret, O.; Villain, F.; Le Normand, F. *The Journal of Physical Chemistry* **1994**, *98*, 5522–5533, DOI: `10.1021/j100072a020`.

(143) Bernal, S.; Calvino, J. J.; Cifredo, G. A.; Rodriguez-Izquierdo, J. M. *The Journal of Physical Chemistry* **1995**, *99*, 11794–11796, DOI: `10.1021/j100030a025`.

(144) Bernal, S.; Calvino, J. J.; Cifredo, G. A.; Gatica, J. M.; Omil, J. A. P.; Pintado, J. M. *Journal of the Chemical Society, Faraday Transactions* **1993**, *89*, 3499, DOI: `10.1039/FT9938903499`.

(145) Baker, R. T.; Bernal, S.; Blanco, G.; Cordón, A. M.; Pintado, J. M.; Rodríguez-Izquierdo, J. M.; Fally, F.; Perrichon, V. *Chemical Communications* **1999**, 149–150, DOI: `10.1039/a808203k`.

(146) Bernal, S.; Calvino, J. J.; Cifredo, G. A.; Rodríguez-Izquierdo, J. M.; Perrichon, V.; Laachir, A. *Journal of the Chemical Society, Chemical Communications* **1992**, 460–462, DOI: `10.1039/C39920000460`.

(147) Bernal, S. *Journal of Catalysis* **1992**, *137*, 1–11, DOI: `10.1016/0021-9517(92)90134-4`.

(148) Bernal, S.; Calvino, J. J.; Cifredo, G. A.; Laachir, A.; Perrichon, V.; Herrmann, J. M. *Langmuir* **1994**, *10*, 717–722, DOI: `10.1021/la00015a020`.

(149) Li, C.; Sakata, Y.; Arai, T.; Domen, K.; Maruya, K.-i.; Onishi, T. *Journal of the Chemical Society, Faraday Transactions 1: Physical Chemistry in Condensed Phases* **1989**, *85*, 929, DOI: `10.1039/F19898500929`.

(150) Li, C.; Sakata, Y.; Arai, T.; Domen, K.; Maruya, K.-i.; Onishi, T. *Journal of the Chemical Society, Faraday Transactions 1: Physical Chemistry in Condensed Phases* **1989**, *85*, 1451, DOI: `10.1039/F19898501451`.

(151) Zaki, M. I.; Knözlngem, H. *Spectrochimica Acta Part A: Molecular Spectroscopy* **1987**, *43*, 1455–1459, DOI: `10.1016/S0584-8539(87)80030-2`.

(152) Bazin, P.; Saur, O.; Lavalley, J. C.; Daturi, M.; Blanchard, G. *Physical Chemistry Chemical Physics* **2005**, *7*, 187, DOI: `10.1039/B414159H`.

(153) Dutta, G.; Gupta, A.; Waghmare, U. V.; Hegde, M. S. *Journal of Chemical Sciences* **2011**, *123*, 509–516, DOI: `10.1007/s12039-011-0089-0`.

(154) Zhou, K.; Wang, X.; Sun, X.; Peng, Q.; Li, Y. *Journal of Catalysis* **2005**, *229*, 206–212, DOI: `10.1016/j.jcat.2004.11.004`.

(155) Trovarelli, A.; Llorca, J. *ACS Catalysis* **2017**, *7*, 4716–4735, DOI: `10.1021/acscatal.7b01246`.

(156) Yang, Z.; Woo, T. K.; Hermansson, K. *Chemical Physics Letters* **2004**, *396*, 384–392, DOI: `10.1016/j.cplett.2004.08.078`.

(157) Boronin, A. I.; Slavinskaya, E. M.; Figueroba, A.; Stadnichenko, A. I.; Kardash, T. Y.; Stonkus, O. A.; Fedorova, E. A.; Muravev, V. V.; Svetlichnyi, V. A.; Bruix, A.; Neyman, K. M. *Applied Catalysis B: Environmental* **2021**, *286*, 119931, DOI: `10.1016/j.apcatb.2021.119931`.

(158) Wei, D.-Y.; Yue, M.-F.; Qin, S.-N.; Zhang, S.; Wu, Y.-F.; Xu, G.-Y.; Zhang, H.; Tian, Z.-Q.; Li, J.-F. *Journal of the American Chemical Society* **2021**, *143*, 15635–15643, DOI: `10.1021/jacs.1c04590`.

(159) Kopelent, R.; van Bokhoven, J. A.; Szlachetko, J.; Edebeli, J.; Paun, C.; Nachtegaal, M.; Safonova, O. V. *Angewandte Chemie* **2015**, *127*, 8852–8855, DOI: `10.1002/ange.201503022`.

(160) Cargnello, M.; Doan-Nguyen, V. V. T.; Gordon, T. R.; Diaz, R. E.; Stach, E. A.; Gorte, R. J.; Fornasiero, P.; Murray, C. B. *Science (New York, N.Y.)* **2013**, *341*, 771–773, DOI: `10.1126/science.1240148`.

(161) Holmgren, A.; Andersson, B.; Duprez, D. *Applied Catalysis B: Environmental* **1999**, *22*, 215–230, DOI: `10.1016/S0926-3373(99)00047-8`.

(162) Martínez-Arias, A.; Coronado, J. M.; Cataluña, R.; Conesa, J. C.; Soria, J. *The journal of physical chemistry. B* **1998**, *102*, 4357–4365, DOI: `10.1021/jp9805306`.

(163) Wan, W.; Geiger, J.; Berdunov, N.; Lopez Luna, M.; Chee, S. W.; Daelman, N.; López, N.; Shaikhutdinov, S.; Roldan Cuenya, B. *Angewandte Chemie International Edition* **2022**, *61*, e202112640, DOI: `10.1002/anie.202112640`.

(164) Jiang, D.; Yao, Y.; Li, T.; Wan, G.; Pereira-Hernández, X. I.; Lu, Y.; Tian, J.; Khivantsev, K.; Engelhard, M. H.; Sun, C.; García-Vargas, C. E.; Hoffman, A. S.; Bare, S. R.; Datye, A. K.; Hu, L.; Wang, Y. *Angewandte Chemie International Edition* **2021**, *60*, 26054–26062, DOI: `10.1002/anie.202108585`.

(165) Wang, H.; Liu, J.-X.; Allard, L. F.; Lee, S.; Liu, J.; Li, H.; Wang, J.; Wang, J.; Oh, S. H.; Li, W.; Flytzani-Stephanopoulos, M.; Shen, M.; Goldsmith, B. R.; Yang, M. *Nature Communications* **2019**, *10*, 3808, DOI: `10.1038/s41467-019-11856-9`.

(166) Nie, L.; Mei, D.; Xiong, H.; Peng, B.; Ren, Z.; Hernandez, X. I. P.; DeLaRiva, A.; Wang, M.; Engelhard, M. H.; Kovarik, L.; Datye, A. K.; Wang, Y. *Science (New York, N.Y.)* **2017**, *358*, 1419–1423, DOI: `10.1126/science.aao2109`.

(167) Esteves, P.; Wu, Y.; Dujardin, C.; Dongare, M. K.; Granger, P. *Catalysis Today* **2011**, *176*, 453–457, DOI: `10.1016/j.cattod.2010.10.068`.

(168) Adamski, A.; Tabor, E.; Gil, B.; Sojka, Z. *Catalysis Today* **2007**, *119*, 114–119, DOI: `10.1016/j.cattod.2006.08.003`.

(169) Granger, P.; Esteves, P.; Kieger, S.; Navascues, L.; Leclercq, G. *Applied Catalysis B: Environmental* **2006**, *62*, 236–243, DOI: `10.1016/j.apcatb.2005.07.015`.

(170) Djéga-Mariadassou, G.; Fajardie, F.; Tempère, J.-F.; Manoli, J.-M.; Touret, O.; Blanchard, G. *Journal of Molecular Catalysis A: Chemical* **2000**, *161*, 179–189, DOI: `10.1016/S1381-1169(00)00334-4`.

(171) Wang, C.; Gu, X.-K.; Yan, H.; Lin, Y.; Li, J.; Liu, D.; Li, W.-X.; Lu, J. *ACS Catalysis* **2017**, *7*, 887–891, DOI: `10.1021/acscatal.6b02685`.

(172) Rink, J.; Meister, N.; Herbst, F.; Votsmeier, M. *Applied Catalysis B: Environmental* **2017**, *206*, 104–114, DOI: `10.1016/j.apcatb.2016.12.052`.

(173) Che, M.; Tench, A. J. In *Advances in Catalysis*, Eley, D. D., Pines, H., Weisz, P. B., Eds.; Academic Press: 1982; Vol. 31, pp 77–133, DOI: `10.1016/S0360-0564(08)60453-8`.

(174) Choi, Y. M.; Abernathy, H.; Chen, H.-T.; Lin, M. C.; Liu, M. *Chemphyschem : a European journal of chemical physics and physical chemistry* **2006**, *7*, 1957–1963, DOI: `10.1002/cphc.200600190`.

(175) Soria, J.; Martínez-Arias, A.; Conesa, J. C. *Journal of the Chemical Society, Faraday Transactions* **1995**, *91*, 1669–1678, DOI: `10.1039/FT9959101669`.

(176) Huang, M.; Fabris, S. *Physical Review B* **2007**, *75*, 081404, DOI: `10.1103/PhysRevB.75.081404`.

(177) Zhao, Y.; Teng, B.-T.; Wen, X.-D.; Zhao, Y.; Chen, Q.-P.; Zhao, L.-H.; Luo, M.-F. *The Journal of Physical Chemistry C* **2012**, *116*, 15986–15991, DOI: `10.1021/jp3016326`.

(178) Schilling, C.; Ganduglia-Pirovano, M. V.; Hess, C. *The Journal of Physical Chemistry Letters* **2018**, *9*, 6593–6598, DOI: `10.1021/acs.jpclett.8b02728`.

(179) Paier, J.; Penschke, C.; Sauer, J. *Chemical Reviews* **2013**, *113*, 3949–3985, DOI: `10.1021/cr3004949`.

(180) Yang, C.; Yu, X.; Heißler, S.; Weidler, P. G.; Nefedov, A.; Wang, Y.; Wöll, C.; Kropp, T.; Paier, J.; Sauer, J. *Angewandte Chemie International Edition* **2017**, *56*, 16399–16404, DOI: `10.1002/anie.201709199`.

(181) Etim, U. J.; Bai, P.; Gazit, O. M.; Zhong, Z. *Catalysis Reviews* **2021**, 1–187, DOI: `10.1080/01614940.2021.1919044`.

(182) Ganduglia-Pirovano, M. V.; Hofmann, A.; Sauer, J. *Surface Science Reports* **2007**, *62*, 219–270, DOI: `10.1016/j.surfrep.2007.03.002`.

(183) Duncan, K. L.; Wang, Y.; Bishop, S. R.; Ebrahimi, F.; Wachsman, E. D. *Journal of Applied Physics* **2007**, *101*, DOI: `10.1063/1.2559601`.

(184) Kofstad, P. *Phase Transitions* **1996**, *58*, 75–93, DOI: `10.1080/01411599608242395`.

(185) Tuller, H. L.; Bishop, S. R. *Chemistry Letters* **2010**, *39*, 1226–1231, DOI: `10.1246/cl.2010.1226`.

(186) Keating, P. R. L.; Scanlon, D. O.; Morgan, B. J.; Galea, N. M.; Watson, G. W. *The Journal of Physical Chemistry C* **2012**, *116*, 2443–2452, DOI: `10.1021/jp2080034`.

(187) Smith, T.; Moxon, S.; Tse, J. S.; Skelton, J. M.; Cooke, D. J.; Gillie, L. J.; Da Silva, E. L.; Harker, R. M.; Storr, M. T.; Parker, S. C.; Molinari, M. *Journal of Physics: Energy* **2023**, *5*, 025004, DOI: `10.1088/2515-7655/acbb29`.

(188) Bunluesin, T.; Gorte, R. J.; Graham, G. W. *Applied Catalysis B: Environmental* **1997**, *14*, 105–115, DOI: `10.1016/S0926-3373(97)00016-7`.

(189) Breyesse, M.; Guenin, M.; Claudel, B.; Latreille, H.; Veron, J. *Journal of Catalysis* **1972**, *27*, 275–280, DOI: `10.1016/0021-9517(72)90268-0`.

(190) Breyesse, M.; Claudel, M. G. B.; Veron, J. *Journal of Catalysis* **1973**, *28*, 54–62, DOI: `10.1016/0021-9517(73)90178-4`.

(191) Djéga-Mariadassou, G.; Boudart, M. *Journal of Catalysis* **2003**, *216*, 89–97, DOI: `10.1016/S0021-9517(02)00099-4`.

(192) Capdevila-Cortada, M.; Vilé, G.; Teschner, D.; Pérez-Ramírez, J.; López, N. *Applied Catalysis B: Environmental* **2016**, *197*, 299–312, DOI: `10.1016/j.apcatb.2016.02.035`.

(193) Liu, W.; Flytzanistephanopoulos, M. *Journal of Catalysis* **1995**, *153*, 317–332, DOI: `10.1006/jcat.1995.1133`.

(194) Wu, Z.; Li, M.; Overbury, S. H. *Journal of Catalysis* **2012**, *285*, 61–73, DOI: `10.1016/j.jcat.2011.09.011`.

(195) Boaro, M.; Leitenburg, C. d.; Dolcetti, G.; Trovarelli, A. *Journal of Catalysis* **2000**, *193*, 338–347, DOI: `10.1006/jcat.2000.2887`.

(196) Liu, X.; Zhou, K.; WANG, L.; Wang, B.; Li, Y. *Journal of the American Chemical Society* **2009**, *131*, 3140–3141, DOI: `10.1021/ja808433d`.

(197) Lykaki, M.; Pachatouridou, E.; Carabineiro, S. A.; Iliopoulou, E.; Andriopoulou, C.; Kallithrakas-Kontos, N.; Boghosian, S.; Konsolakis, M. *Applied Catalysis B: Environmental* **2018**, *230*, 18–28, DOI: `10.1016/j.apcatb.2018.02.035`.

(198) Konsolakis, M.; Lykaki, M. *Catalysts* **2021**, *11*, 452, DOI: `10.3390/catal11040452`.

(199) Lee, K. J.; Kim, Y.; Lee, J. H.; Cho, S. J.; Kwak, J. H.; Moon, H. R. *Chemistry of Materials* **2017**, *29*, 2874–2882, DOI: `10.1021/acs.chemmater.6b05098`.

(200) Zhou, H.-P.; Zhang, Y.-W.; Si, R.; Zhang, L.-S.; Song, W.-G.; Yan, C.-H. *The Journal of Physical Chemistry C* **2008**, *112*, 20366–20374, DOI: `10.1021/jp807091n`.

(201) Cui, R.; Lu, W.; Zhang, L.; Yue, B.; Shen, S. *The Journal of Physical Chemistry C* **2009**, *113*, 21520–21525, DOI: `10.1021/jp9065168`.

(202) Tschope, A.; Liu, W.; Flytzanistephanopoulos, M.; Ying, J. Y. *Journal of Catalysis* **1995**, *157*, 42–50, DOI: `10.1006/jcat.1995.1266`.

(203) Ying, J. Y.; Tschöpe, A. *The Chemical Engineering Journal and the Biochemical Engineering Journal* **1996**, *64*, 225–237, DOI: `10.1016/S0923-0467(96)03142-9`.

(204) Li, J.; Zhang, Z.; Gao, W.; Zhang, S.; Ma, Y.; Qu, Y. *ACS Applied Materials & Interfaces* **2016**, *8*, 22988–22996, DOI: `10.1021/acsami.6b05343`.

(205) Gänzler, A. M.; Casapu, M.; Maurer, F.; Störmer, H.; Gerthsen, D.; Ferré, G.; Vernoux, P.; Bornmann, B.; Frahm, R.; Murzin, V.; Nachtegaal, M.; Votsmeier, M.; Grunwaldt, J.-D. *ACS Catalysis* **2018**, *8*, 4800–4811, DOI: `10.1021/acscatal.8b00330`.

(206) Liu, H.-H.; Wang, Y.; Jia, A.-P.; Wang, S.-Y.; Luo, M.-F.; Lu, J.-Q. *Applied Surface Science* **2014**, *314*, 725–734, DOI: `10.1016/j.apsusc.2014.06.196`.

(207) Singh, J.; Alayon, E. M. C.; Tromp, M.; Safonova, O. V.; Glatzel, P.; Nachtegaal, M.; Frahm, R.; van Bokhoven, J. A. *Angewandte Chemie International Edition* **2008**, *47*, 9260–9264, DOI: `10.1002/anie.200803427`.

(208) Gatla, S.; Aubert, D.; Agostini, G.; Mathon, O.; Pascarelli, S.; Lunkenbein, T.; Willinger, M. G.; Kaper, H. *ACS Catalysis* **2016**, *6*, 6151–6155, DOI: `10.1021/acscatal.6b00677`.

(209) Maurer, F.; Beck, A.; Jelic, J.; Wang, W.; Mangold, S.; Stehle, M.; Di Wang; Dolcet, P.; Gänzler, A. M.; Kübel, C.; Studt, F.; Casapu, M.; Grunwaldt, J.-D. *ACS Catalysis* **2022**, *12*, 2473–2486, DOI: `10.1021/acscatal.1c04565`.

(210) Meunier, F. C.; Cardenas, L.; Kaper, H.; Šmíd, B.; Vorokhta, M.; Grosjean, R.; Aubert, D.; Dembélé, K.; Lunkenbein, T. *Angewandte Chemie International Edition* **2021**, *60*, 3799–3805, DOI: `10.1002/anie.202013223`.

(211) Ke, J.; Zhu, W.; Jiang, Y.; Si, R.; Wang, Y.-J.; Li, S.-C.; Jin, C.; Liu, H.; Song, W.-G.; Yan, C.-H.; Zhang, Y.-W. *ACS Catalysis* **2015**, *5*, 5164–5173, DOI: `10.1021/acscatal.5b00832`.

(212) Pereira-Hernández, X. I.; DeLaRiva, A.; Muravev, V.; Kunwar, D.; Xiong, H.; Sudduth, B.; Engelhard, M.; Kovarik, L.; Hensen, E. J. M.; Wang, Y.; Datye, A. K. *Nature Communications* **2019**, *10*, 1358, DOI: `10.1038/s41467-019-09308-5`.

(213) Gänzler, A. M.; Casapu, M.; Vernoux, P.; Loridant, S.; Cadete Santos Aires, F. J.; Epicier, T.; Betz, B.; Hoyer, R.; Grunwaldt, J.-D. *Angewandte Chemie (International ed. in English)* **2017**, *56*, 13078–13082, DOI: `10.1002/anie.201707842`.

(214) Flynn, P. C.; Wanke, S. E. *Journal of Catalysis* **1974**, *34*, 390–399, DOI: `10.1016/0021-9517(74)90052-9`.

(215) Flynn, P. C.; Wanke, S. E. *Journal of Catalysis* **1974**, *34*, 400–410, DOI: `10.1016/0021-9517(74)90053-0`.

(216) Nagai, Y.; Dohmae, K.; Ikeda, Y.; Takagi, N.; Tanabe, T.; Hara, N.; Guilera, G.; Pascarelli, S.; Newton, M. A.; Kuno, O.; Jiang, H.; Shinjoh, H.; Matsumoto, S. *Angewandte Chemie International Edition* **2008**, *47*, 9303–9306, DOI: `10.1002/anie.200803126`.

(217) Maurer, F.; Jelic, J.; Wang, J.; Gänzler, A.; Dolcet, P.; Wöll, C.; Wang, Y.; Studt, F.; Casapu, M.; Grunwaldt, J.-D. *Nature Catalysis* **2020**, *3*, 824–833, DOI: `10.1038/s41929-020-00508-7`.

(218) Ye, X.; Wang, H.; Lin, Y.; Liu, X.; Cao, L.; Gu, J.; Lu, J. *Nano Research* **2019**, *12*, 1401–1409, DOI: `10.1007/s12274-019-2351-6`.

(219) Jones, J.; Xiong, H.; DeLaRiva, A. T.; Peterson, E. J.; Pham, H.; Challa, S. R.; Qi, G.; Oh, S.; Wiebenga, M. H.; Pereira Hernández, X. I.; Wang, Y.; Datye, A. K. *Science (New York, N.Y.)* **2016**, *353*, 150–154, DOI: `10.1126/science.aaf8800`.

(220) Dvořák, F.; Farnesi Camellone, M.; Tovt, A.; Tran, N.-D.; Negreiros, F. R.; Vorokhta, M.; Skála, T.; Matolínová, I.; Mysliveček, J.; Matolín, V.; Fabris, S. *Nature Communications* **2016**, *7*, 10801, DOI: `10.1038/ncomms10801`.

(221) Resasco, J.; DeRita, L.; Dai, S.; Chada, J. P.; Xu, M.; Yan, X.; Finzel, J.; Hanukovich, S.; Hoffman, A. S.; Graham, G. W.; Bare, S. R.; Pan, X.; Christopher, P. *Journal of the American Chemical Society* **2020**, *142*, 169–184, DOI: `10.1021/jacs.9b09156`.

(222) Daelman, N.; Capdevila-Cortada, M.; López, N. *Nature Materials* **2019**, *18*, 1215–1221, DOI: `10.1038/s41563-019-0444-y`.

(223) Lu, Y.; Zhou, S.; Kuo, C.-T.; Kunwar, D.; Thompson, C.; Hoffman, A. S.; Boubnov, A.; Lin, S.; Datye, A. K.; Guo, H.; Karim, A. M. *ACS Catalysis* **2021**, *11*, 8701–8715, DOI: `10.1021/acscatal.1c01900`.

(224) Ding, K.; Gulec, A.; Johnson, A. M.; Schweitzer, N. M.; Stucky, G. D.; Marks, L. D.; Stair, P. C. *Science (New York, N.Y.)* **2015**, *350*, 189–192, DOI: `10.1126/science.aac6368`.

(225) Jeong, H.; Shin, D.; Kim, B.-S.; Bae, J.; Shin, S.; Choe, C.; Han, J. W.; Lee, H. *Angewandte Chemie International Edition* **2020**, *59*, 20691–20696, DOI: `10.1002/anie.202009776`.

(226) Happel, M.; Mysliveček, J.; Johánek, V.; Dvořák, F.; Stetsovych, O.; Lykhach, Y.; Matolín, V.; Libuda, J. *Journal of Catalysis* **2012**, *289*, 118–126, DOI: `10.1016/j.jcat.2012.01.022`.

(227) Aleksandrov, H. A.; Neyman, K. M.; Hadjiivanov, K. I.; Vayssilov, G. N. *Physical Chemistry Chemical Physics* **2016**, *18*, 22108–22121, DOI: `10.1039/C6CP03988J`.

(228) Meunier, F. C. *The Journal of Physical Chemistry C* **2021**, *125*, 21810–21823, DOI: `10.1021/acs.jpcc.1c06784`.

(229) Su, Y.-Q.; Wang, Y.; Liu, J.-X.; Filot, I. A.; Alexopoulos, K.; Zhang, L.; Muravev, V.; Zijlstra, B.; Vlachos, D. G.; Hensen, E. J. *ACS Catalysis* **2019**, *9*, 3289–3297, DOI: `10.1021/acscatal.9b00252`.

(230) An, K.; Alayoglu, S.; Musselwhite, N.; Plamthottam, S.; Melaet, G.; Lindeman, A. E.; Somorjai, G. A. *Journal of the American Chemical Society* **2013**, *135*, 16689–16696, DOI: `10.1021/ja4088743`.

(231) Jiao, L.; Regalbuto, J. R. *Journal of Catalysis* **2008**, *260*, 329–341, DOI: `10.1016/j.jcat.2008.09.022`.

(232) Kosmulski, M., *Surface charging and points of zero charge*; Surfactant Science Ser, Vol. v.145, Kosmulski, Marek (MitwirkendeR); Taylor & Francis: Boca Raton, 2009; 1064 pp.

(233) Toby, B. H.; von Dreele, R. B. *Journal of Applied Crystallography* **2013**, *46*, 544–549, DOI: `10.1107/S0021889813003531`.

(234) Kim, S.; Merkle, R.; Maier, J. *Surface Science* **2004**, *549*, 196–202, DOI: `10.1016/j.susc.2003.12.002`.

(235) Scherrer, P. *Nachrichten von der Gesellschaft der Wissenschaften zu Göttingen, Mathematisch-Physikalische Klasse* **1918**, *1918*, 98–100.

(236) Holzwarth, U.; Gibson, N. *Nature Nanotechnology* **2011**, *6*, 534, DOI: `10.1038/nnano.2011.145`.

(237) Dinnebier, R. E.; Billinge, S. J. L., *Powder Diffraction*; Royal Society of Chemistry: Cambridge, 2008, DOI: `10.1039/9781847558237`.

(238) Sims, C. M.; Maier, R. A.; Johnston-Peck, A. C.; Gorham, J. M.; Hackley, V. A.; Nelson, B. C. *Nanotechnology* **2019**, *30*, 085703, DOI: `10.1088/1361-6528/aae364`.

(239) Romeo, M.; Bak, K.; El Fallah, J.; Le Normand, F.; Hilaire, L. *Surface and Interface Analysis* **1993**, *20*, 508–512, DOI: `10.1002/sia.740200604`.

(240) Aneggi, E.; Boaro, M.; Leitenburg, C. d.; Dolcetti, G.; Trovarelli, A. *Journal of Alloys and Compounds* **2006**, *408-412*, 1096–1102, DOI: `10.1016/j.jallcom.2004.12.113`.

(241) Li, J.; Guo, C.; Ma, Y.; Wang, Z.; Wang, J. *Acta Materialia* **2015**, *90*, 10–26, DOI: `10.1016/j.actamat.2015.02.030`.

(242) McBride, J. R.; Hass, K. C.; Poindexter, B. D.; Weber, W. H. *Journal of Applied Physics* **1994**, *76*, 2435–2441, DOI: `10.1063/1.357593`.

(243) Yashima, M.; Arashi, H.; Kakihana, M.; Yoshimura, M. *Journal of the American Ceramic Society* **1994**, *77*, 1067–1071, DOI: `10.1111/j.1151-2916.1994.tb07270.x`.

(244) Lykaki, M.; Stefa, S.; Carabineiro, S.; Pandis, P.; Stathopoulos, V.; Konsolakis, M. *Catalysts* **2019**, *9*, 371, DOI: `10.3390/catal9040371`.

(245) Graham, G. W.; Weber, W. H.; Peters, C. R.; Usmen, R. *Journal of Catalysis* **1991**, *130*, 310–313, DOI: `10.1016/0021-9517(91)90113-I`.

(246) Weber; Hass; McBride *Physical review. B, Condensed matter* **1993**, *48*, 178–185, DOI: `10.1103/physrevb.48.178`.

(247) Pijolat, M.; Prin, M.; Soustelle, M.; Touret, O.; Nortier, P. *Journal of the Chemical Society, Faraday Transactions* **1995**, *91*, 3941, DOI: `10.1039/ft9959103941`.

(248) Giordano, F.; Trovarelli, A.; Leitenburg, C. d.; Giona, M. *Journal of Catalysis* **2000**, *193*, 273–282, DOI: `10.1006/jcat.2000.2900`.

(249) Yao, H. *Journal of Catalysis* **1984**, *86*, 254–265, DOI: `10.1016/0021-9517(84)90371-3`.

(250) Madier, Y.; Descorme, C.; Le Govic, A. M.; Duprez, D. *The journal of physical chemistry. B* **1999**, *103*, 10999–11006, DOI: `10.1021/jp991270a`.

(251) Rossignol, S.; Gérard, F.; Mesnard, D.; Kappenstein, C.; Duprez, D. *J. Mater. Chem.* **2003**, *13*, 3017–3020, DOI: `10.1039/B306726B`.

(252) Iglesias, I.; Baronetti, G.; Mariño, F. *Solid State Ionics* **2017**, *309*, 123–129, DOI: `10.1016/j.ssi.2017.07.008`.

(253) Emig, G.; Liauw, M. A. *Topics in Catalysis* **2002**, *21*, 11–24, DOI: `10.1023/A:1020543729259`.

(254) Richter, O.; Mestl, G. *Catalysts* **2019**, *9*, 435, DOI: `10.3390/catal9050435`.

(255) Bekheet, M. F.; Grünbacher, M.; Schlicker, L.; Gili, A.; Doran, A.; Epping, J. D.; Gurlo, A.; Klötzer, B.; Penner, S. *CrystEngComm* **2019**, *21*, 145–154, DOI: `10.1039/C8CE01726C`.

(256) Badri, A.; Binet, C.; Lavalley, J.-C. *Journal of the Chemical Society, Faraday Transactions* **1996**, *92*, 4669, DOI: `10.1039/FT9969204669`.

(257) Binet, C.; Badri, A.; Lavalley, J.-C. *The Journal of Physical Chemistry* **1994**, *98*, 6392–6398, DOI: `10.1021/j100076a025`.

(258) Wu, Z.; Cheng, Y.; Tao, F.; Daemen, L.; Foo, G. S.; Nguyen, L.; Zhang, X.; Beste, A.; Ramirez-Cuesta, A. J. *Journal of the American Chemical Society* **2017**, *139*, 9721–9727, DOI: `10.1021/jacs.7b05492`.

(259) Li, Z.; Werner, K.; Qian, K.; You, R.; Płucienik, A.; Jia, A.; Wu, L.; Zhang, L.; Pan, H.; Kuhlenbeck, H.; Shaikhutdinov, S.; Huang, W.; Freund, H.-J. *Angewandte Chemie International Edition* **2019**, *58*, 14686–14693, DOI: `10.1002/anie.201907117`.

(260) Allen, G. C.; Wood, M. B.; Dyke, J. M. *Journal of Inorganic and Nuclear Chemistry* **1973**, *35*, 2311–2318, DOI: `10.1016/0022-1902(73)80295-7`.

(261) Binet, C.; Daturi, M.; Lavalley, J.-C. *Catalysis Today* **1999**, *50*, 207–225, DOI: `10.1016/S0920-5861(98)00504-5`.

(262) Tsunekawa, S.; Sivamohan, R.; Ito, S.; Kasuya, A.; Fukuda, T. *Nanostructured Materials* **1999**, *11*, 141–147, DOI: `10.1016/S0965-9773(99)00027-6`.

(263) Holder, C. F.; Schaak, R. E. *ACS Nano* **2019**, *13*, 7359–7365, DOI: `10.1021/acsnano.9b05157`.

(264) Schweke, D.; Mordehovitz, Y.; Halabi, M.; Shelly, L.; Hayun, S. *Advanced materials (Deerfield Beach, Fla.)* **2018**, *30*, e1706300, DOI: `10.1002/adma.201706300`.

(265) Paparazzo, E. *Journal of Materials Chemistry A* **2021**, *9*, 23722–23725, DOI: `10.1039/D1TA00387A`.

(266) Miller, J. T.; Schreier, M.; Kropf, A.; Regalbuto, J. R. *Journal of Catalysis* **2004**, *225*, 203–212, DOI: `10.1016/j.jcat.2004.04.007`.

(267) Schreier, M.; Regalbuto, J. R. *Journal of Catalysis* **2004**, *225*, 190–202, DOI: `10.1016/j.jcat.2004.03.034`.

(268) Kottwitz, M.; Li, Y.; Palomino, R. M.; Liu, Z.; Wang, G.; Wu, Q.; Huang, J.; Timoshenko, J.; Senanayake, S. D.; Balasubramanian, M.; Lu, D.; Nuzzo, R. G.; Frenkel, A. I. *ACS Catalysis* **2019**, *9*, 8738–8748, DOI: `10.1021/acscatal.9b02083`.

(269) Kinch, R. T.; Cabrera, C. R.; Ishikawa, Y. *The Journal of Physical Chemistry C* **2009**, *113*, 9239–9250, DOI: `10.1021/jp810021e`.

(270) Xie, P.; Pu, T.; Nie, A.; Hwang, S.; Purdy, S. C.; Yu, W.; Su, D.; Miller, J. T.; Wang, C. *ACS Catalysis* **2018**, *8*, 4044–4048, DOI: `10.1021/acscatal.8b00004`.

(271) Qiao, B.; Wang, A.; Yang, X.; Allard, L. F.; Jiang, Z.; Cui, Y.; Liu, J.; Li, J.; Zhang, T. *Nature Chemistry* **2011**, *3*, 634–641, DOI: `10.1038/nchem.1095`.

(272) Hu, Z.; Liu, X.; Meng, D.; Guo, Y.; Guo, Y.; Lu, G. *ACS Catalysis* **2016**, *6*, 2265–2279, DOI: `10.1021/acscatal.5b02617`.

(273) Kim, K.; Yoo, J. D.; Lee, S.; Bae, M.; Bae, J.; Jung, W.; Han, J. W. *ACS Applied Materials & Interfaces* **2017**, *9*, 15449–15458, DOI: `10.1021/acsami.7b01844`.

(274) Migani, A.; Vayssilov, G. N.; Bromley, S. T.; Illas, F.; Neyman, K. M. *Chemical Communications* **2010**, *46*, 5936–5938, DOI: `10.1039/C0CC01091J`.

(275) Sayle, T. X. T.; Caddeo, F.; Zhang, X.; Sakthivel, T.; Das, S.; Seal, S.; Ptasinska, S.; Sayle, D. C. *Chemistry of Materials* **2016**, *28*, 7287–7295, DOI: `10.1021/acs.chemmater.6b02536`.

(276) Yu, X.; Wu, X.; Chen, Z.; Huang, Z.; Jing, G. *Molecular Catalysis* **2019**, *476*, 110512, DOI: `10.1016/j.mcat.2019.110512`.

(277) Bernal, S.; Blanco, G.; El Amarti, A.; Cifredo, G.; Fitian, L.; Galtayries, A.; Martín, J.; Pintado, J. M. *Surface and Interface Analysis* **2006**, *38*, 229–233, DOI: `10.1002/sia.2224`.

(278) Wu, Y.; Dujardin, C.; Lancelot, C.; Dacquin, J. P.; Parvulescu, V. I.; Cabié, M.; Henry, C. R.; Neisius, T.; Granger, P. *Journal of Catalysis* **2015**, *328*, 236–247, DOI: `10.1016/j.jcat.2015.02.001`.

(279) Metiu, H.; Chrétien, S.; Hu, Z.; Li, B.; Sun, X. *The Journal of Physical Chemistry C* **2012**, *116*, 10439–10450, DOI: `10.1021/jp301341t`.

(280) Cheng, Z.; Sherman, B. J.; Lo, C. S. *The Journal of Chemical Physics* **2013**, *138*, 014702, DOI: `10.1063/1.4773248`.

(281) Kumari, N.; Haider, M. A.; Sinha, N.; Basu, S. *ECS Transactions* **2015**, *68*, 155–166, DOI: `10.1149/06803.0155ecst`.

(282) Song, Z.; Liu, W.; Nishiguchi, H. *Catalysis Communications* **2007**, *8*, 725–730, DOI: `10.1016/j.catcom.2006.08.048`.

(283) Staudt, T.; Lykhach, Y.; Tsud, N.; Skála, T.; Prince, K. C.; Matolín, V.; Libuda, J. *The Journal of Physical Chemistry C* **2011**, *115*, 8716–8724, DOI: `10.1021/jp200382y`.

(284) Yang, C.; Yin, L.-L.; Bebensee, F.; Buchholz, M.; Sezen, H.; Heissler, S.; Chen, J.; Nefedov, A.; Idriss, H.; Gong, X.-Q.; Wöll, C. *Physical Chemistry Chemical Physics* **2014**, *16*, 24165–24168, DOI: `10.1039/C4CP02372B`.

(285) Davó-Quiñonero, A.; López-Rodríguez, S.; Chaparro-Garnica, C.; Martín-García, I.; Bailón-García, E.; Lozano-Castelló, D.; Bueno-López, A.; García-Melchor, M. *Catalysts* **2021**, *11*, 1556, DOI: `10.3390/catal11121556`.

(286) Wang, Y.-J.; Dong, H.; Lyu, G.-M.; Zhang, H.-Y.; Ke, J.; Kang, L.-Q.; Teng, J.-L.; Sun, L.-D.; Si, R.; Zhang, J.; Liu, Y.-J.; Zhang, Y.-W.; Huang, Y.-H.; Yan, C.-H. *Nanoscale* **2015**, *7*, 13981–13990, DOI: `10.1039/C5NR02588E`.

(287) Fu, Q.; Saltsburg, H.; Flytzani-Stephanopoulos, M. *Science (New York, N.Y.)* **2003**, *301*, 935–938, DOI: `10.1126/science.1085721`.

(288) Ammal, S. C.; Heyden, A. *ACS Catalysis* **2019**, *9*, 7721–7740, DOI: `10.1021/acscatal.9b01560`.

(289) Song, B.; Si, S.; Soleymani, A.; Xin, Y.; Hagelin-Weaver, H. E. *Nano Research* **2022**, *15*, 5922–5932, DOI: `10.1007/s12274-022-4251-4`.

(290) Kalamaras, C. M.; Americanou, S.; Efstathiou, A. M. *Journal of Catalysis* **2011**, *279*, 287–300, DOI: `10.1016/j.jcat.2011.01.024`.

(291) Zhai, Y.; Pierre, D.; Si, R.; Deng, W.; Ferrin, P.; Nilekar, A. U.; Peng, G.; Herron, J. A.; Bell, D. C.; Saltsburg, H.; Mavrikakis, M.; Flytzani-Stephanopoulos, M. *Science (New York, N.Y.)* **2010**, *329*, 1633–1636, DOI: `10.1126/science.1192449`.

(292) Yang, M.; Liu, J.; Lee, S.; Zugic, B.; Huang, J.; Allard, L. F.; Flytzani-Stephanopoulos, M. *Journal of the American Chemical Society* **2015**, *137*, 3470–3473, DOI: `10.1021/ja513292k`.

(293) Geiger, J.; López, N. *The Journal of Physical Chemistry C* **2022**, *126*, 13698–13704, DOI: `10.1021/acs.jpcc.2c03710`.

List of Figures

List of Tables

Part VIII.

Appendix

A. Commissioning of Synthesis Setup

During commissioning of the precipitation setup the temperature of the reactor as well as the piston pump for ammonia addition was calibrated. As discussed in chapter 6.1 the temperature of the precipitation reactor was controlled using a thermostat. The set temperature was calibrated using two thermocouples in the reactor, whose temperature difference ΔT was always smaller than $\Delta T \leq 0.3\,\mathrm{K}$. The reactor was filled with $0.6\,\mathrm{l}$ of water, equivalent to the preparations. After setting a temperature at the thermostat T_{set} and an one hour long equilibration, the temperature was measured. This was repeated for the other temperatures. Thermal equilibrium was checked by repeating the calibration by starting at a high temperature and decreasing the temperature. The resulting calibration plots are shown in figure 49.

During precipitation an ammonia solution was added to the reaction solution using a piston pump with a constant flow rate $\dot{V}$. The pump was calibrated by setting a flow rate $\dot{V}_{\mathrm{set}}$ for a given time into a tarred vial. Dividing the pumped mass of water by the set time gave the measured flow rate $\dot{V}_{\mathrm{meas}}$ by approximating the water density $\rho_{\mathrm{H_2O}} = 1\,\mathrm{g\,ml^{-1}}$. Values were averaged over three measurements. The resulting plot is shown in figure 49.

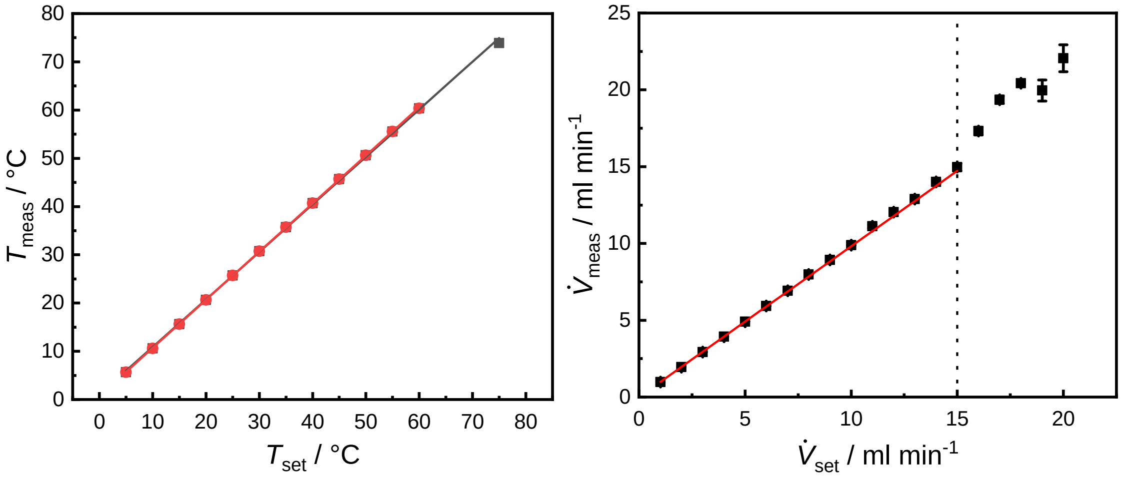

Figure 49: Temperature calibration measurements and fit of the synthesis reactor (■) with fit equation (66) and the pH reactor (●) with calibration equation (67) (left) and calibration of the piston pump used for ammonia addition (right) with fit equation shown in equation (68)

From figure 49 the following fit functions were obtained for the synthesis reactor (equation (66)) and the pH reactor (equation (67))

$$T_{\text{meas,syn. reactor}} = (0.985 \pm 0.006) \cdot T_{\text{set,syn. reactor}} + (1.0 \pm 0.2)\,^{\circ}\text{C} \tag{66}$$

$$T_{\text{meas,pH reactor}} = (0.997 \pm 0.002) \cdot T_{\text{set,ph reactor}} + (0.72 \pm 0.07)\,^{\circ}\text{C}. \tag{67}$$

From the calibration of the piston pump it was evident that the pumping head installed only worked linearly up to a flow rate of $15\,\text{ml}\,\text{min}^{-1}$. The linear fit function, with its y-intercept set to $y = 0$ obtained for set flow rates $\dot{V}_{\text{set}} = 1\,\text{ml}\,\text{min}^{-1}$ to $15\,\text{ml}\,\text{min}^{-1}$, is shown in equation (68)

$$\dot{V}_{\text{meas}} = (0.981 \pm 0.002) \cdot \dot{V}_{\text{set}}. \tag{68}$$

B. Diffractogram of LaB_6 Standard

A certified LaB_6 (NIST-SRM660c) was measured to create the instrument function that was used to account for the instrument contribution to angular position of the reflections as well as their lineshape. An exemplary diffractogram is shown in figure 50

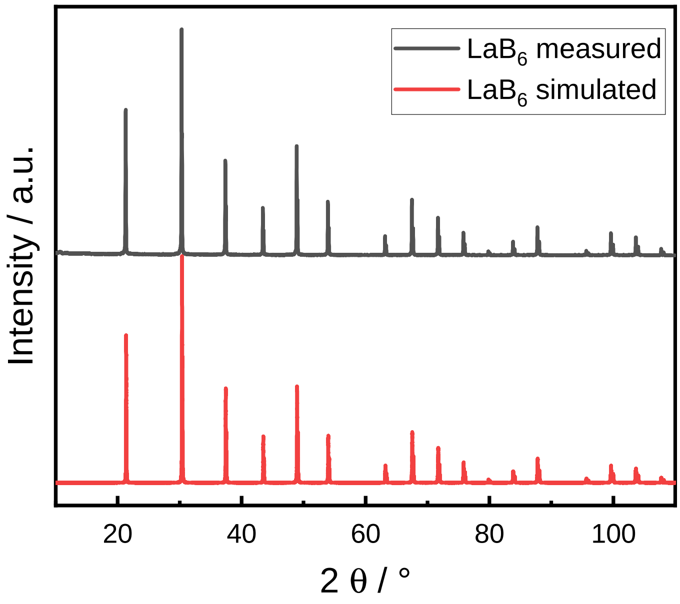

Figure 50: Measured and simulated diffractogram of NIST-SRM660c used for caluclation of the instrument function

C. H_2 Calibration for TPR Experiments

A copper(II) oxide was used to calibrate the TCD signal. The oxidation state of the commercial copper(II) oxide was first validated by TGA. 20 mg were placed in a sample crucible before degasing it in synthetic air at 300 °C. After cooling down to 150 °C the flow was switched to Ar and the sample was purged free of oxygen for 2 h. Afterwards the gas was switched to 50 ml min^{-1} of 5 % H_2 in N_2 before equilibrating the mass for 1 h. Afterwards the sample was heated to 500 °C where the sample was again held for 2 h before cooling it down to 150 °C. After cool down the mass was equilibrated for 2 h. The relative mass loss $\Delta\omega$ was calculated based on the mass right before the temperature ramp and after the mass equilibration after reduction at the end of the experiment.

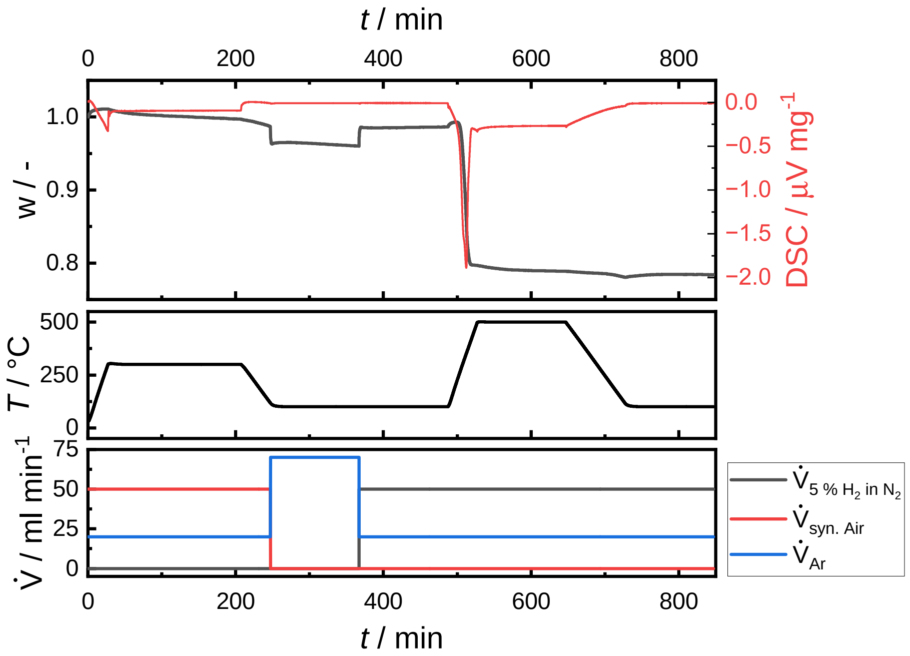

Figure 51: DTA experiment to verify oxidation state of copper standard used subsequently for calibration of TCD signal

With the relative remaining mass w the molecular weight of copper M_{Cu} and oxygen M_{O}, the stoichiometry x of Cu_xO can be calculated using equation (71)

$$x = \frac{\frac{M_{\mathrm{Cu}}}{w} - M_{\mathrm{Cu}}}{M_{\mathrm{O}}} \tag{69}$$

$$= \frac{\frac{63.456\,\mathrm{g\,mol^{-1}}}{0.7985} - 63.456\,\mathrm{g\,mol^{-1}}}{16\,\mathrm{g\,mol^{-1}}} \tag{70}$$

$$= 1.002. \tag{71}$$

This results shows that the copper standard is copper(II) oxide as well as the fact that all copper centers can be reduced, enabling the calibration of the TCD signal for TPR experiments.

After verifying the presence of CuO, the hydrogen consumption during TPR experiments was calibrated by measuring TPR profiles of 2.5 mg, 5 mg and 10 mg of CuO. After degassing and oxidizing the samples at 300 °C for 1 h, temperature was cooled down to 100 °C before switching to 10 vol. % of H_2 in N_2 and applying a temperature ramp of $10\,\mathrm{K\,min^{-1}}$ to 450 °C and following the hydrogen consumption using the inbuilt TCD. Water was removed from the gas stream by passing the gas after the sample cell through a dry ice/acetone cool trap before detection. The resulting H_2-TPR profiles are shown in figure 52. The TPR profiles were integrated and the integral A_{TCD} was plotted against the amount of consumed hydrogen, which was calculated using equation (72)

$$n_{\mathrm{H_2}} = n_{\mathrm{CuO}} = \frac{m_{\mathrm{sample}} \cdot w_{\mathrm{degas}}}{M_{\mathrm{CuO}}}. \tag{72}$$

The calibration plot is also shown in figure 52.

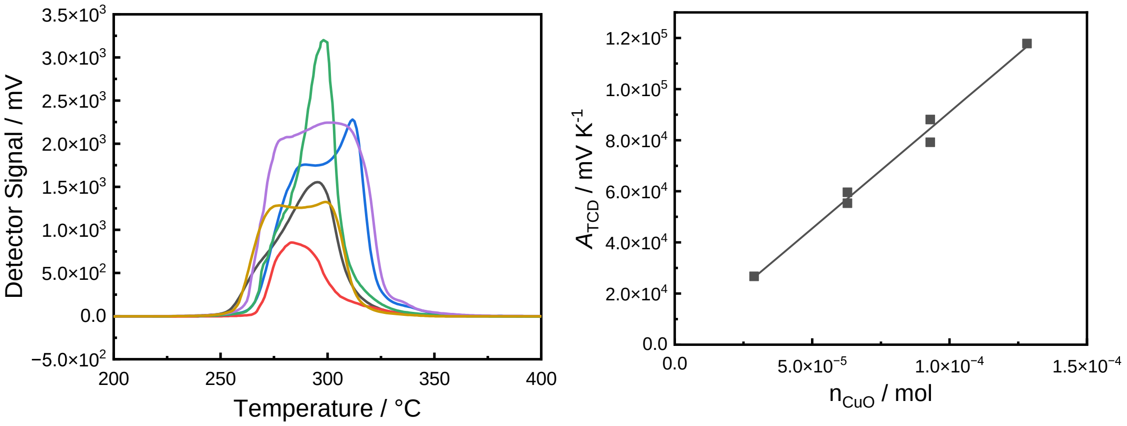

Figure 52: H_2-TPR profiles of CuO with 2.5 mg (—), 5 mg (—) and 10 mg (—) and plot of the integrated peak area A_{TCD} (■) as a function of n_{H_2}, fit function is given in equation (73)

The fit function of $A_{\mathrm{TCD}}\left(n_{H_2}\right)$, with y-intercept being set to 0 is shown in equation (73)

$$A_{\mathrm{TCD}}\left(n_{H_2}\right) = (6.75 \pm 0.09) \times 10^{8}\,\mathrm{mV\,K\,mol^{-1}} \cdot n_{H_2}. \tag{73}$$

D. CO_2 Calibration for TPD Experiments

As described in chapter 7.11.3 the TCD signal during CO_2 desorption was calibrated. The resulting plot is shown in figure 53.

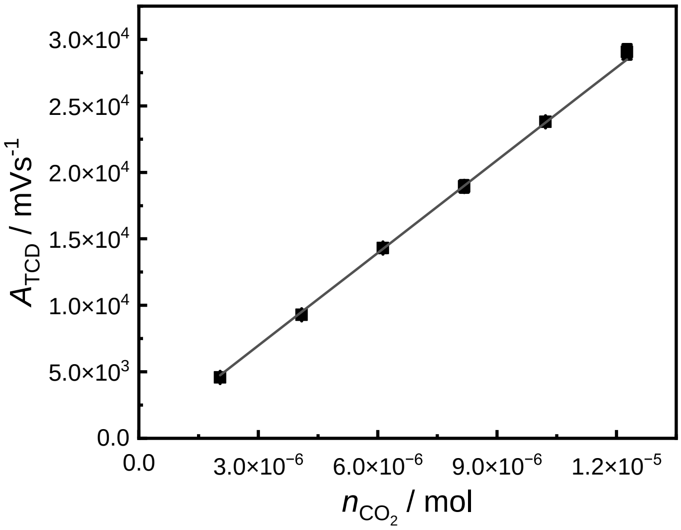

Figure 53: Calibration curve for the CO_2 desorption signal for TPD experiments

The fit function obtained to quantify the CO_2 desorption signal is shown in equation (74)

$$A_{\mathrm{TCD}}\left(n_{\mathrm{CO_2}}\right) = (2.32 \pm 0.02) \times 10^{9}\,\mathrm{mV\,s^{-1}\,mol^{-1}} \cdot n_{\mathrm{CO_2}}. \tag{74}$$

E. Investigation of Reducibility

The DRIFTS results of the other materials are shown in figure 54, 55, 56 and 57.

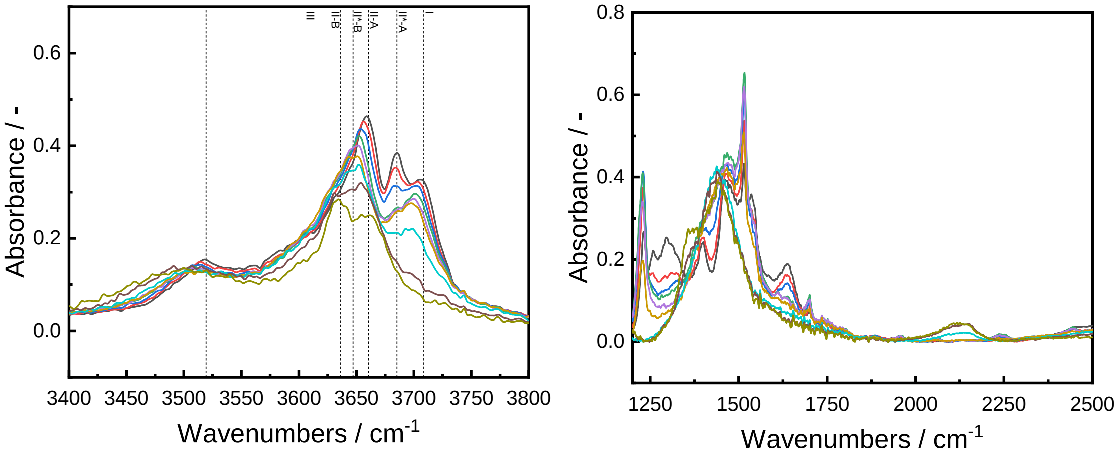

Figure 54: *In situ*-DRIFTS spectra during reduction of HSA sample after 1 h of isothermal treatment under hydrogen flow at 100 °C (—), 150 °C (—), 200 °C (—), 250 °C (—), 300 °C (—), 350 °C (—), 400 °C (—), 450 °C (—) and 500 °C (—) in the OH-region (left) and the low frequency region (right)

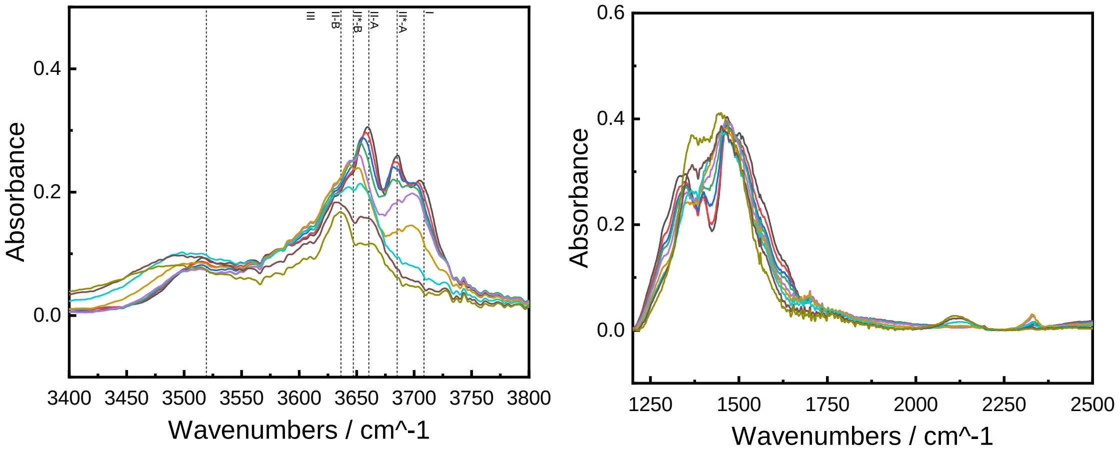

Figure 55: *In situ*-DRIFTS spectra during reduction of UP-500 sample after 1 h of isothermal treatment under hydrogen flow at 100 °C (——), 150 °C (——), 200 °C (——), 250 °C (——), 300 °C (——), 350 °C (——), 400 °C (——), 450 °C (——) and 500 °C (——) in the OH-region (left) and the low frequency region (right)

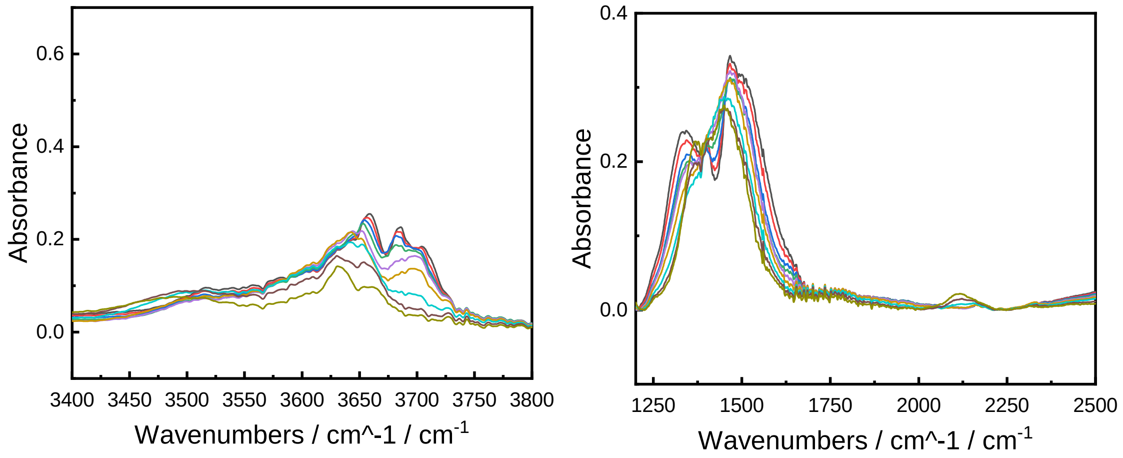

Figure 56: *In situ*-DRIFTS spectra during reduction of AP50-500 sample after 1 h of isothermal treatment under hydrogen flow at 100 °C (—), 150 °C (—), 200 °C (—), 250 °C (—), 300 °C (—), 350 °C (—), 400 °C (—), 450 °C (—) and 500 °C (—) in the OH-region (left) and the low frequency region (right)

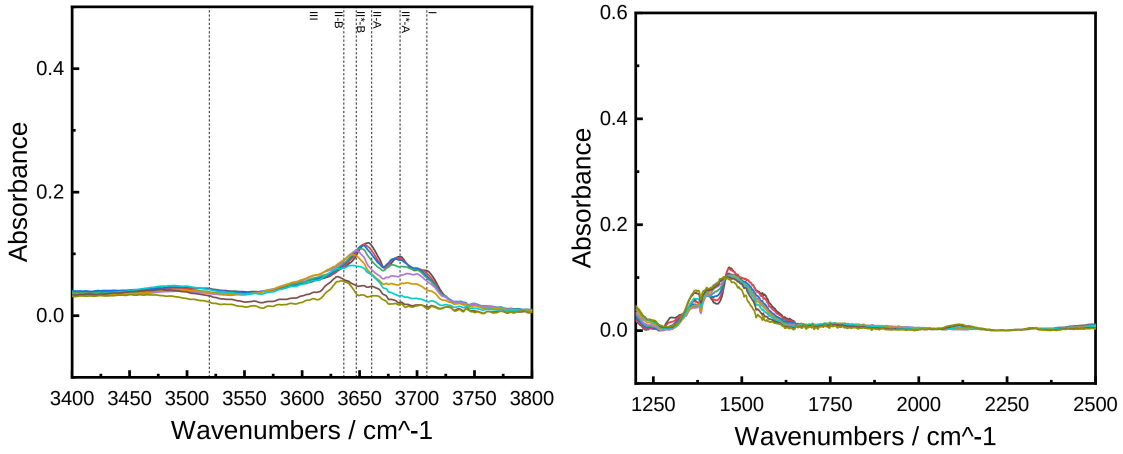

Figure 57: *In situ*-DRIFTS spectra during reduction of AP5-700 sample after 1 h of isothermal treatment under hydrogen flow at 100 °C (—), 150 °C (—), 200 °C (—), 250 °C (—), 300 °C (—), 350 °C (—), 400 °C (—), 450 °C (—) and 500 °C (—) in the OH-region (left) and the low frequency region (right)

Spectra after initial degas and desorption after reduction are shown in figure 58.

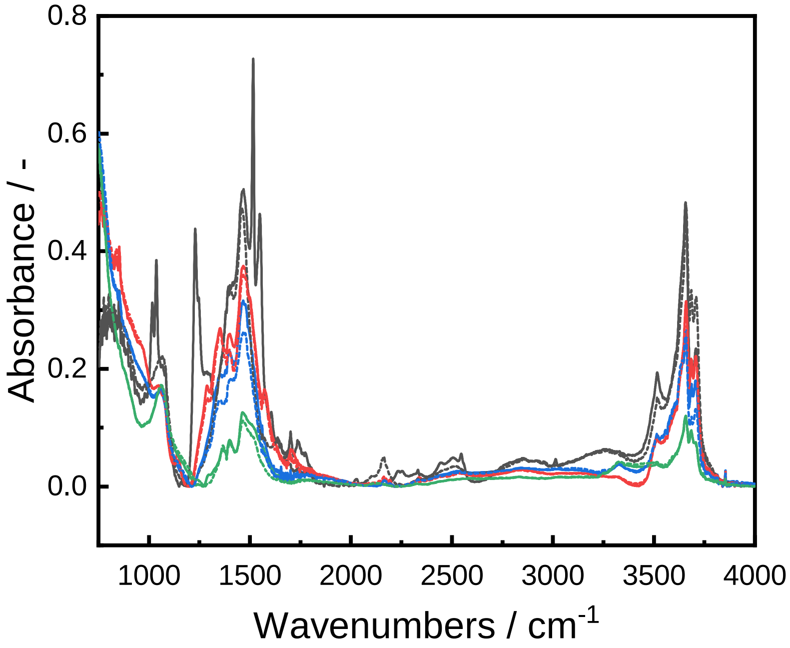

Figure 58: *In situ*-DRIFTS spectra after initial degas (——) and after reduction with successive desorption (- - - -) for HSA (——), UP15-500 (——), AP50-500 (——) and AP5-700 (——)

F. GC-system

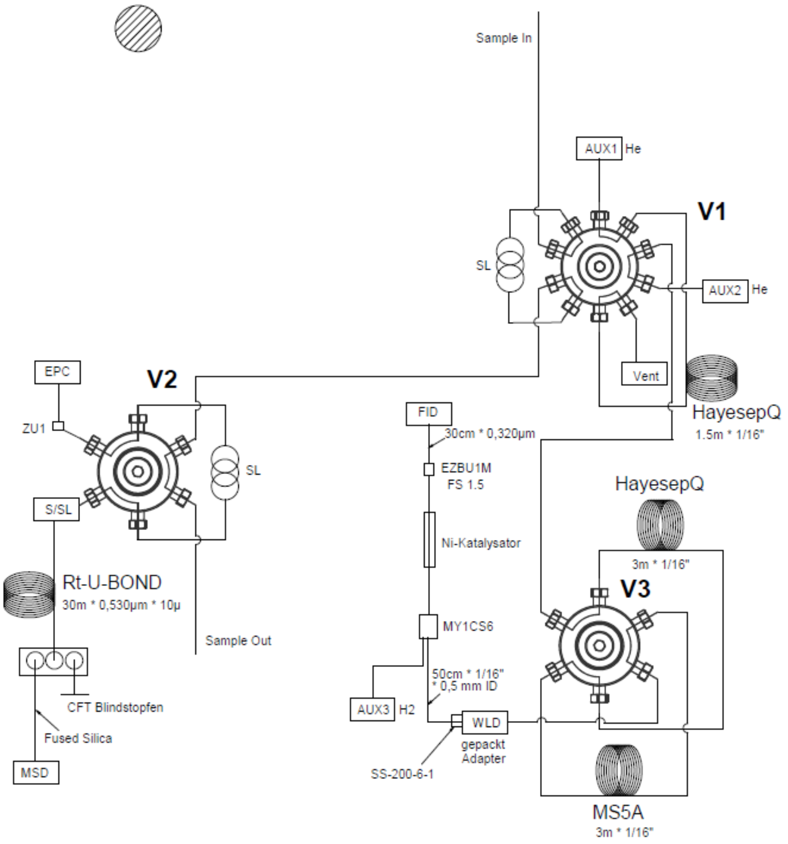

Figure 59: Column and detector system of GC-MS

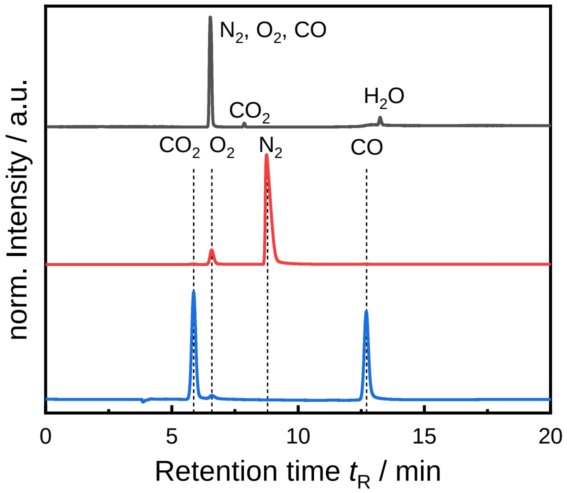

Figure 60: Exemplary chromatograms with MS (——), TCD (——) and FID (——) of GC-MS system, retention times t_R are listed in table 10.

Exemplary Calibration of GC-MS System

As described in sec. 7.12, the GC-MS was calibrated repeatedly over the course of this work. One exemplary calibration for CO (FID), CO_2 (FID), O_2 (TCD), N_2 (TCD) and H_2O (MS) is shown in figure 61.

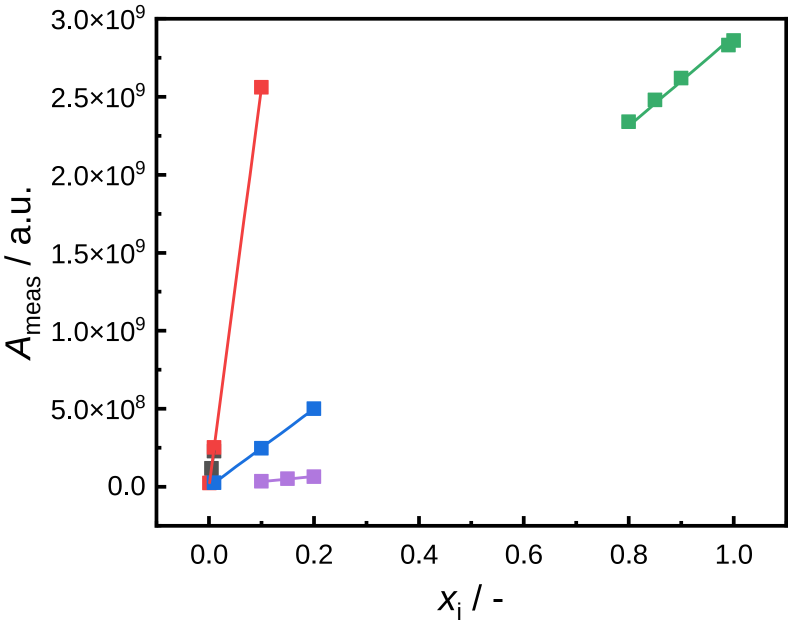

Figure 61: Calibration plot of exemplary calibration of GC-MS system for CO_2 (FID) (⬛), CO (FID) (🟥), O_2 (TCD) (🟦), N_2 (TCD) (🟩) and H_2O (MS) (🟪)

The intercepts of the calibration functions were set to 0. With that, the following calibration equations for the different compounds were obtained. The slopes of the calibration plots shifted only slightly over the course of this work.

$$A_{\mathrm{CO,FID}} = (2.56 \pm 0.01) \times 10^{10}\,\mathrm{pA\,min^{-1}} \cdot x_{\mathrm{CO}} \tag{75}$$

$$A_{\mathrm{CO_2,FID}} = (2.30 \pm 0.03) \times 10^{10}\,\mathrm{pA\,min^{-1}} \cdot x_{\mathrm{CO_2}} \tag{76}$$

$$A_{\mathrm{O_2,TCD}} = (2.50 \pm 0.02) \times 10^{9}\,\mathrm{\mu V\,min^{-1}} \cdot x_{\mathrm{O_2}} \tag{77}$$

$$A_{\mathrm{N_2,TCD}} = (2.89 \pm 0.02) \times 10^{9}\,\mathrm{\mu V\,min^{-1}} \cdot x_{\mathrm{N_2}} \tag{78}$$

$$A_{\mathrm{H_2O,MS}} = (3.34 \pm 0.08) \times 10^{8}\,\mathrm{min^{-1}} \cdot x_{\mathrm{H_2O}} \tag{79}$$

$$\tag{80}$$

G. Characterization of CeO_2 Materials Used for Investigations of CO Oxidation Activity

Materials used for CO oxidation experiments were thoroughly characterized. XRD patterns with the respective *Rietveld* calculated pattern and residual are plotted in figure 62, while N_2-physisorption isotherms are shown in figure 63 on basis of which S_{BET} values were calculated, *Raman* spectra of the samples are shown in figure 64, while Ce$3d$ XPS spectra are shown in figure 65 and the TPR profiles of the materials before O_2 chemisorption are shown in figure 66.

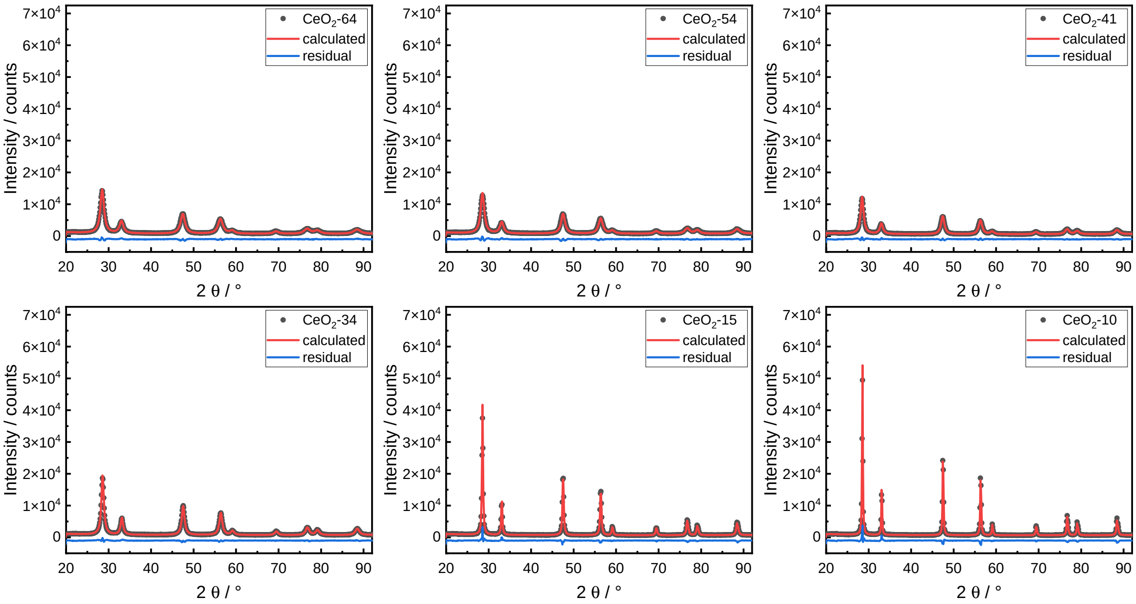

Figure 62: Measured X-ray diffractograms (●) and associated calculated diffraction pattern (——) and residual (——) from *Rietveld* refinement for materials used in the CO oxidation experiments, results of the structural refinement are listed in table 14.

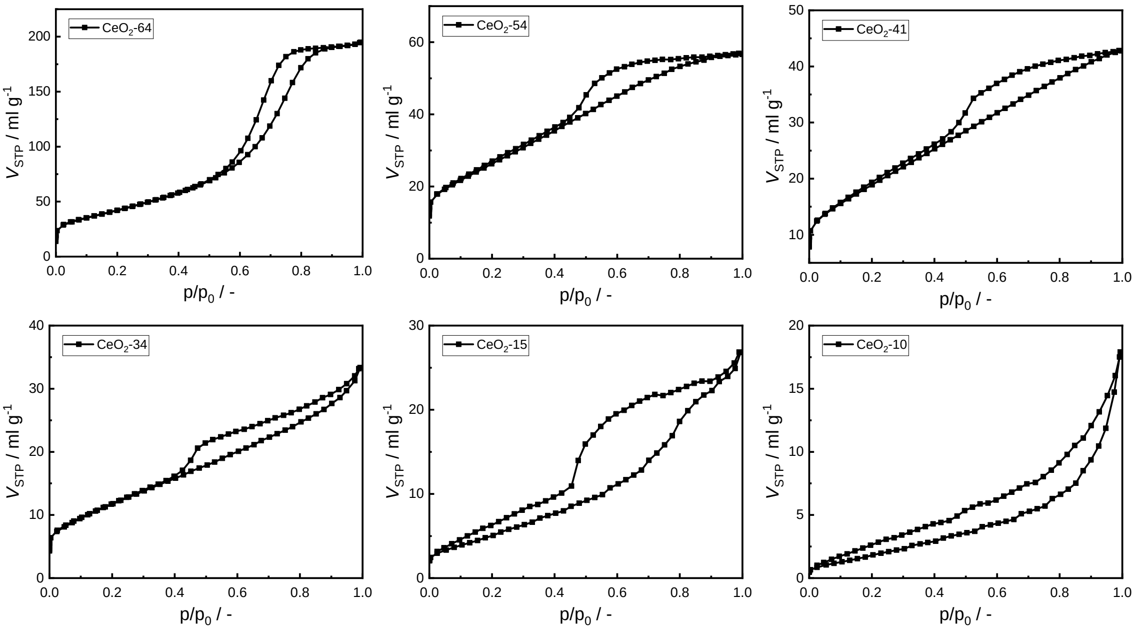

Figure 63: N_2 physisorption isotherms obtained from N_2 physisorption for materials used in the CO oxidation, he extracted surface areas are listed in table 14.

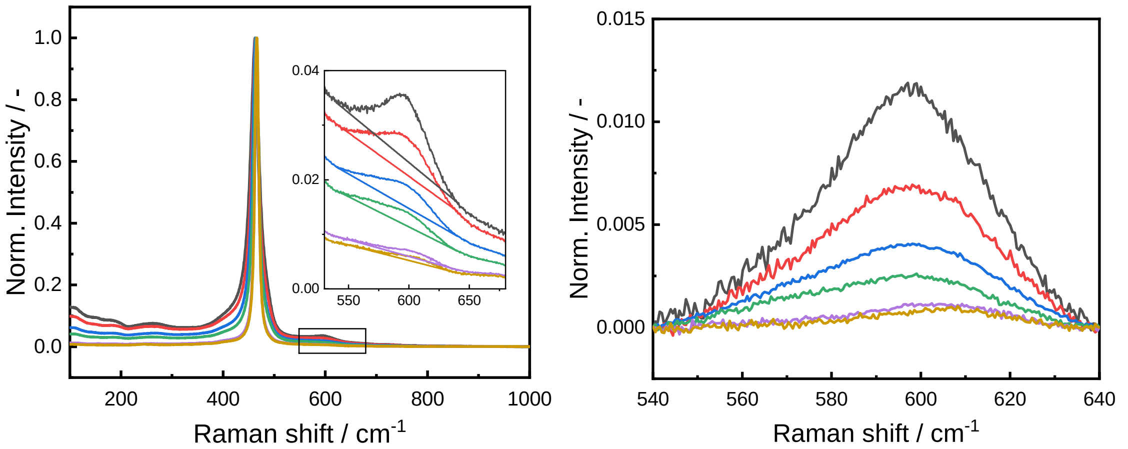

Figure 64: Normalized *Raman* spectra of the prepared materials used in CO oxidation (left) and baseline subtracted defect related feature for quantification (right), CeO_2-64 (——) , CeO_2-54 (——), CeO_2-41 (——) , CeO_2-34 (——) , CeO_2-15 (——) and CeO_2-10 (——)

The obtained kinetic parameters could not only be described as a function of crystallite size D but also as a function of the bulk defect concentration extracted from *Raman* spectra as shown in figure 67.

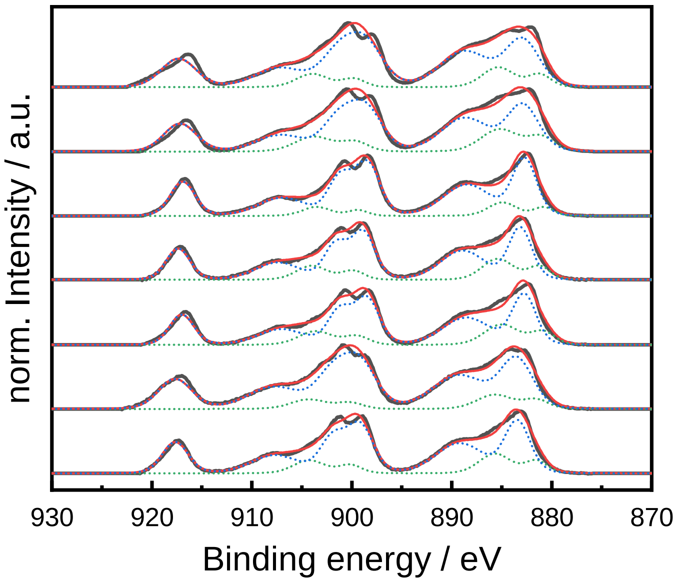

Figure 65: Ce$3d$ spectra of the different materials investigated in CO oxidation for CeO$_2$-64 to CeO$_2$-10 from top to bottom

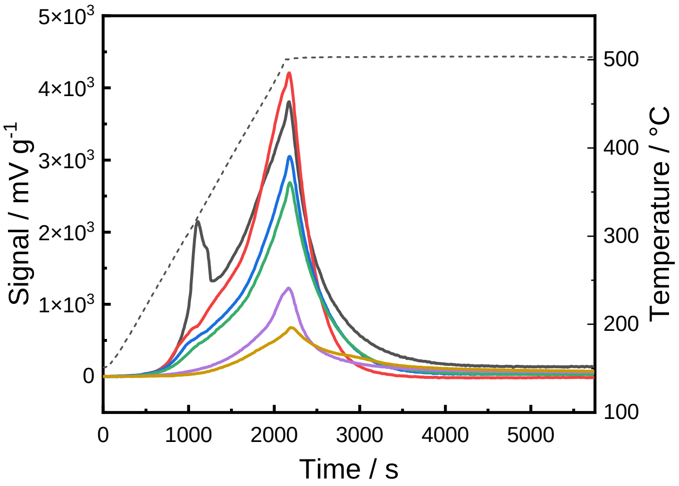

Figure 66: TPR profiles of CeO$_2$-64 (——), CeO$_2$-54 (——), CeO$_2$-41 (——), CeO$_2$-34 (——), CeO$_2$-15 (——) and CeO$_2$-10 (——) as well as the temperature (- - - -), after the reduction oxygen pulse chemisorption were carried out to measure $TOSC_{500\,°\mathrm{C}}$ values.

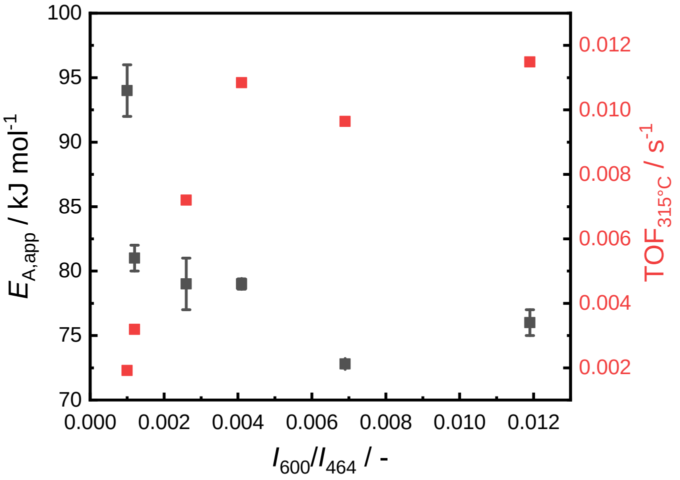

Figure 67: Extracted activation energies $E_{\mathrm{A,app}}$ (——) and $TOF_{315\,°\mathrm{C}}$ (——) from steady-state kinetic investigations shown in figure 41 as a function of defect concentration I_{600}/I_{464} extracted from *Raman* spectroscopy

TPR Analysis of Materials with Different Surface Specific Loading

To see whether the same trend as in nanoparticle loaded ceria materials is present where reduction temperature is a function of loading, a control sample was prepared. While the ”standard” Pt-CeO$_2$-64 sample has a surface specific platinum loading of $SD_{\mathrm{A}} = 0.012\,\mathrm{N_{Pt}/nm^2}$, the reference sample exhibits a surface specific loading of $SD_{\mathrm{A}} = 0.007\,\mathrm{N_{Pt}/nm^2}$. The measured reduction profiles are plotted in figure 68.

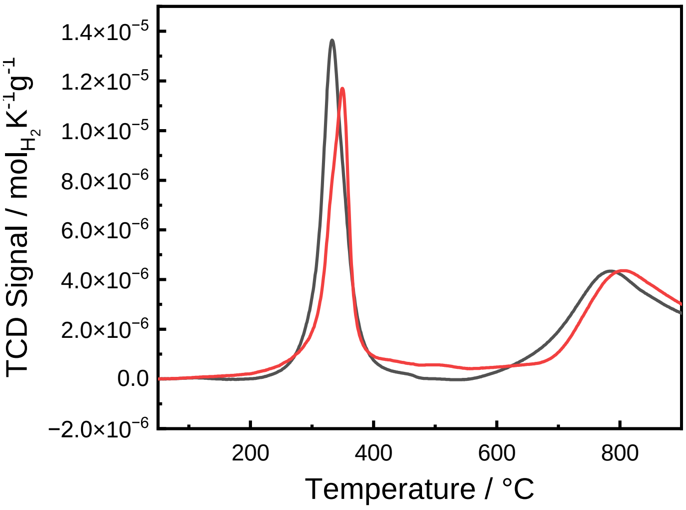

Figure 68: TPR profiles of Pt-CeO$_2$-64 samples with $SD_{\mathrm{A}} = 0.012\,\mathrm{N_{Pt}/nm^2}$ (——) and $SD_{\mathrm{A}} = 0.007\,\mathrm{N_{Pt}/nm^2}$ (——).

Figure 68 shows that although the mass specific loading is almost halved, the reduction maximum is only shifted by 10 K. This proofs that the materials are in a range where the reduction temperature is mostly independent of the surface loading, which is in contrast to nanoparticle loaded cerium oxides.[137]

Correction of ICP-OES Values

The low loading of the prepared Pt$_1$-CeO$_2$ materials did lead to substantial errors in the determination of platinum content through ICP-OES, because the values were at the lower detection limit. For that ICP-MS measurements were carried out at the *Fraunhofer IGB* with the same solutions as ICP-OES measurement. The results of which are shown in figure 69.

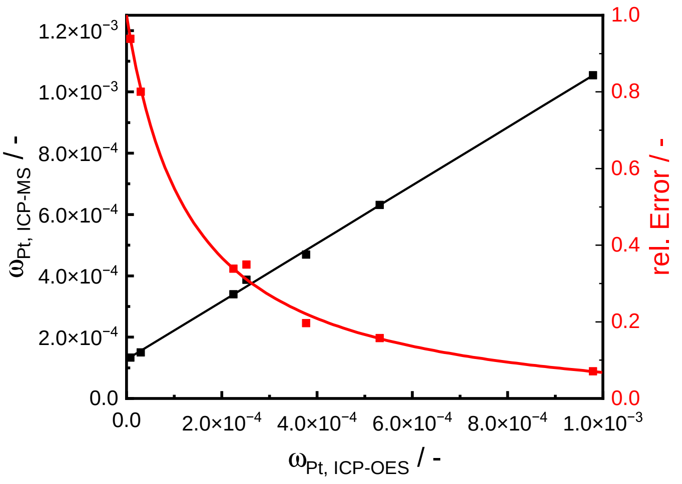

Figure 69: Actual platinum weight fraction as measured by ICP-MS $\omega_{\mathrm{Pt,ICP-MS}}$ as a function of the measured weight fraction from ICP-OES $\omega_{\mathrm{Pt,ICP-OES}}$ (■) and relative error (🟥).

From figure 69 it is evident that there is a systematic error in the measured $\omega_{\mathrm{Pt,ICP-OES}}$ when using ICP-OES at very low Pt contents. When assuming the ICP-MS value for the platinum weight fraction to be the real platinum value ω_{Pt} this error can be corrected using the linear fit function obtained, whose fit function is given in equation (81)

$$\omega_{\mathrm{Pt}} = (1.27 \pm 0.07) + (0.95 \pm 0.02)\,\omega_{\mathrm{Pt,ICP-OES}}. \tag{81}$$

STEM Analysis of Pt-iso Materials.

Intensity line scans are shown in figure 29. The lines scanned for this are shown in figure 70.

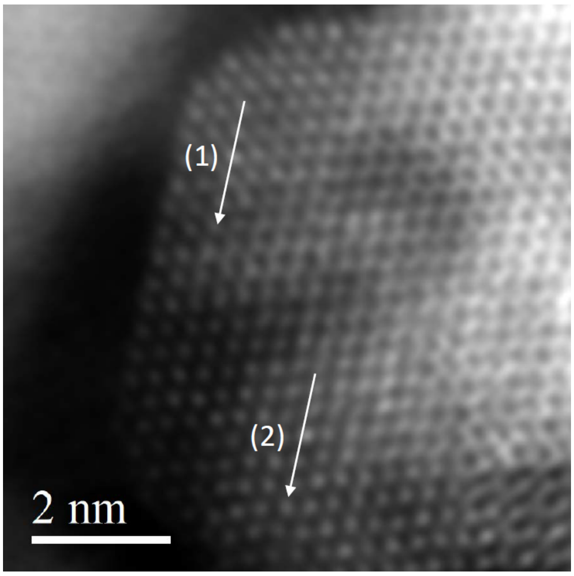

Figure 70: Lines scanned for intensity line profiles

Comparison of Obtained TOFs with Literature Values

The obtained values in this work are juxtaposed in figure 71 with literature values shown in figure 3.

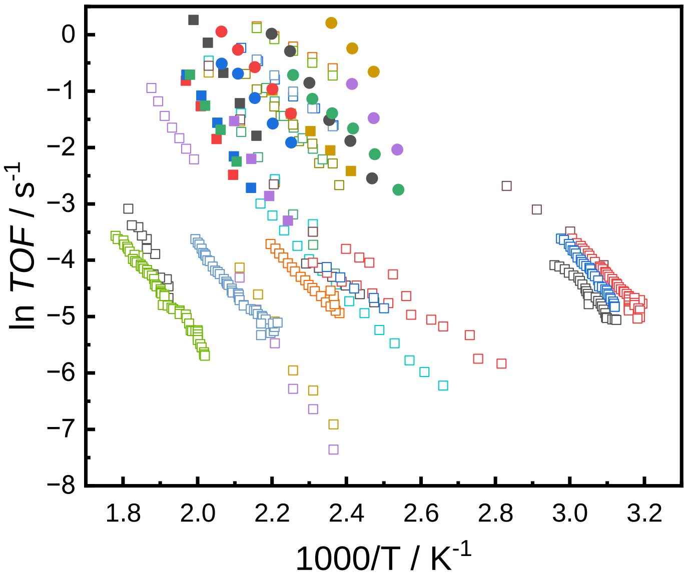

Figure 71: Comparison of literature TOF values (□) with results obtained in this work for Pt$_1$-CeO$_2$-64 (■), Pt$_1$-CeO$_2$-54 (🟥), Pt$_1$-CeO$_2$-41 (🟦), Pt$_1$-CeO$_2$-34 (🟩), Pt$_1$-CeO$_2$-15 (🟪) and Pt$_1$-CeO$_2$-10 (🟨) for dry (■) and wet (●) feeds

H. Calculation of Effective Diffusion Coefficient

The effective diffusion coefficient D_{eff} was calculated with equation (4). First, the free diffusion coefficient of CO in the reaction gas $D_{\mathrm{CO,(0.1\ O_2,\ 0.9\ N_2)}}\,(T, 1.05\,\mathrm{bar})$ was calculated according to *Blanc's law* (*c.f.* equation (5)) based on the free diffusion coefficients of CO in N$_2$ $D_{\mathrm{CO,\ N_2}}\,(T, 1.05\,\mathrm{bar})$ and O$_2$ $D_{\mathrm{CO,\ O_2}}\,(T, 1.05\,\mathrm{bar})$. With equation (6) and values at STP published by Massman which are $D_{\mathrm{CO,\ N_2}}\,(0\,°\mathrm{C}, 1\,\mathrm{bar}) = 1.804 \times 10^{-5}\,\mathrm{m^2\,s^{-1}}$ and $D_{\mathrm{CO,\ O_2}}\,(0\,°\mathrm{C}, 1\,\mathrm{bar}) = 1.817 \times 10^{-5}\,\mathrm{m^2\,s^{-1}}$[25] the values shown in table 20 were obtained.

Using the expression for the mass-specific reaction rate r_{m} for CeO$_2$-64 from figure 40 and the bulk density value $\rho_{\mathrm{bulk}} = 1.22 \times 10^{7}\,\mathrm{g\,m^{-3}}$ extracted from mercury porosimetry shown in figure 36 were used to calculate the volume-specific reaction rate according to equation (82)

$$r_{\mathrm{V}} = r_{\mathrm{m}} \cdot \rho_{\mathrm{bulk}}. \tag{82}$$

The calculated values are listed in table 20. Subsequently the *Weisz-Prater criterion* was calculated according to equation (58).

Table 20: Calculated values for $D_{\mathrm{CO},(0.1\ \mathrm{O_2} 0.9\ \mathrm{N_2})}\ (T, 1.05\,\mathrm{bar})$, D_{eff}, r_{V} and Ψ between 50 °C to 450 °C

T / / °C	$D_{\mathrm{CO},(0.1\ \mathrm{O_2},\ 0.9\ \mathrm{N_2})}$ / / $\mathrm{m^2\,s^{-1}}$	D_{eff} / $\mathrm{m^2\,s^{-1}}$	r_{V} / $\mathrm{mol\,m^{-3}\,s^{-1}}$	Ψ -
50	2.34×10^{-5}	1.61×10^{-5}	4.72×10^{-23}	2.61×10^{-28}
100	3.04×10^{-5}	2.09×10^{-5}	5.10×10^{-18}	2.18×10^{-23}
150	3.82×10^{-5}	2.62×10^{-5}	3.57×10^{-14}	1.21×10^{-19}
200	4.67×10^{-5}	3.21×10^{-5}	3.84×10^{-11}	1.07×10^{-16}
250	5.60×10^{-5}	3.85×10^{-5}	1.09×10^{-8}	2.52×10^{-14}
300	6.61×10^{-5}	4.54×10^{-5}	1.15×10^{-6}	2.26×10^{-12}
350	7.69×10^{-5}	5.29×10^{-5}	5.77×10^{-5}	9.74×10^{-11}
400	8.84×10^{-5}	6.08×10^{-5}	1.62×10^{-3}	2.37×10^{-9}
450	1.01×10^{-4}	6.92×10^{-5}	2.85×10^{-2}	3.68×10^{-8}